High-Throughput Computational Screening of MOFs for Carbon Dioxide Capture and Hydrogen Purification

by

Gökay Avcı

A Dissertation Submitted to the
Graduate School of Sciences and Engineering
in Partial Fulfillment of the Requirements for
the Degree of

Doctor of Philosophy

in

Materials Science and Engineering

KOÇ ÜNİVERSİTESİ

December 02, 2021

High-Throughput Computational Screening of MOFs for Carbon Dioxide Capture and Hydrogen Purification

Koç University

Graduate School of Sciences and Engineering

This is to certify that I have examined this copy of a doctoral dissertation by

Gökay Avcı

and have found that it is complete and satisfactory in all respects, and that any and all revisions required by the final

examining committee have been made.

Committee Members:

_____

Prof. Seda Keskin Avcı (Advisor)

_____

Assoc. Prof. İlknur Eruçar

_____

Assoc. Prof. Mehmet Sayar

_____

Asst. Prof. Betül Uralcan

_____

Assoc. Prof. Uğur Ünal

Date: 02/12/2021

To my dear parents Lutfi and Naime and my dear sister Yıldız, and to my cat Vega.

ABSTRACT

High-Throughput Computational Screening of MOFs for Carbon Dioxide Capture and Hydrogen Purification

Gökay Avcı

Doctor of Philosophy in Materials Science and Engineering

December 02, 2021

Metal organic frameworks (MOFs) constitute a novel class of porous materials that are formed by the combination of inorganic nodes and organic linkers. The number of newly synthesized MOFs increases exponentially each year, and it is not feasible to experimentally test the gas separation performances of each MOF adsorbent and membrane. Therefore, a computational approach that can identify the promising MOFs out of thousands of materials is essential. In this thesis, by performing high-throughput computational screening, CO_2/H_2 separation performances of MOF adsorbents and membranes were investigated in detail, and the top promising MOFs were identified.

In the first part of this thesis, molecular simulations were performed to identify adsorption- and membrane-based CO_2/H_2 separation performances of 3857 unique MOFs. Results showed that all 3857 MOFs were CO_2 selective when considered as adsorbents, whereas 899 MOFs overcame the performances of polymeric membranes as H_2 selective membranes. H_2/CO_2 selectivities and H_2 permeabilities of MOF membranes varied between 2.1×10^{-5}-6.3 and 2.30-1.7×10^{6} Barrer, respectively. Structure-performance relationships revealed that MOFs with pore size <7.5 Å performed well as CO_2 selective adsorbents whereas MOFs with pore size >15 Å were more suitable to be used as H_2 selective membranes.

In the second part of this thesis, Grand Canonical Monte Carlo (GCMC) and Equilibrium Molecular Dynamics (EMD) simulations were performed on the updated MOF database to identify adsorption and membrane-based CO_2/H_2 separation performances of 10221 unique MOFs. The applicability of Ideal Adsorbed Solution Theory to MOFs for CO_2/H_2 separation at temperature and pressure swing adsorption conditions, and the effects of inaccessible local pores, catenation in the frameworks, and presence of impurities (CO, CH_4 and H_2O) in gas mixture on the selectivity, working capacity, and regenerability of MOFs were examined. MOFs that are recently synthesized and added to the updated MOF database were shown to have higher CO_2/H_2 selectivities and working capacities than the previously reported MOFs.

In the third part of this thesis, new MOFs were designed by using in-silico metal exchange techniques and CO_2/H_2 and CO_2/CH_4 separation performances of these MOFs were studied. Results showed that the type of the metal site affects the CO_2/H_2 selectivities of MOFs. As a result, CO_2/H_2 selectivity of a commonly studied MOF in the literature, HKUST-1, was significantly enhanced by 11% and 38% when Cu metal was exchanged with Cr and Cd metals, respectively. The exchange of Zn with V increased the selectivity of HIFTOG02 from 119 to 355.

Overall, results showed that high-throughput computational screening techniques introduced in this thesis can be used to (i) shortlist potentially promising MOFs among thousands of MOFs for pre-combustion CO_2 capture, (ii) identify the structural properties of the promising MOFs with high CO_2/H_2 separation performances, (iii) design new MOFs with exceptional CO_2 capture and H_2 purification properties. The results presented in this thesis will serve as a catalyst for future computational and experimental studies on MOFs which will efficiently capture and sequester CO_2.

ÖZETÇE

Karbon Dioksit Yakalama ve Hidrojen Saflaştırma Süreçlerinde Kullanılmak Üzere Metal-Organik Gözenekli Yapıların Gaz Ayırma Performanslarının Kapsamlı Hesaplamalı Taraması

Gökay Avcı

Malzeme Bilimi ve Mühendisliği, Doktora

02 Aralık 2021

Metal-organik gözenekli yapılar (metal organic framework, MOF) organik ve inorganik yapıtaşlarından oluşan yeni bir gözenekli malzeme sınıfıdır. Her geçen yıl yeni sentezlenmiş MOFların sayısı artmaktadır ve her bir yeni MOFun adsorbent ve membran özelliklerini deneysel yöntemler kullanarak ölçmek pratik olmamaktadır. Bu sebeple, binlerce MOF içerisinden yüksek performanslı MOFların ve özelliklerinin saptanması için hesaplamalı bilimlere dayalı bir yöntem geliştirilmesi elzemdir. Bu tezde, moleküler modellemeye dayanan hesaplamalı tarama yöntemleri kullanılarak MOFların adsorbent ve membran olarak CO_2/H_2 ayırma potansiyelleri incelenmiştir.

Tezin ilk kısmında, moleküler modelleme teknikleri kullanılarak 3857 farklı yapıdaki MOFun CO_2/H_2 adsorpsiyon- ve membran-temelli ayırma potansiyelleri incelenmiştir. Sonuçlar 3857 MOFun CO_2 seçici adsorbent özelliğinde olduğunu, 899 MOFun ise H_2 seçici membran olarak polimer membranlardan daha iyi performans verebildiğini göstermiştir. MOF membranların H_2/CO_2 seçicilikleri ve H_2 geçirgenlikleri sırasıyla 2.1×10^{-5}-6.3 ve 2.30-1.7×10^{6} Barrer arasında hesaplanmıştır. MOFların yapı-performans ilişkileri gözenekleri 7.5 Å'dan küçük olan MOFların CO_2 seçici adsorbent olarak, gözeneği 15 Å'dan büyük olan MOFların ise H_2 seçici membran olarak iyi performans verebildiğini göstermiştir.

Tezin ikinci kısmında, en güncel MOF veri tabanındaki 10221 MOF ayıklanmış, Grand Kanonik Monte Carlo (GCMC) ve Denge Halindeki Molekül Dinamikleri (EMD) tekniklerinden elde edilen sonuçlar ile MOFların CO_2/H_2 ayrımında kullanılmak üzere adsorbent ve membran performansları hesaplanmıştır. Sıcaklık ve basınç değişimli sistemlerde İdeal Adsorblanmış Solüsyon Teorisi'nin (Ideal Adsorbed Solution Theory, IAST) MOFlara uygulanabilirliği, ulaşılamayan gözeneklerin ve örgülü yapıların, ayrıca gaz karışımındaki safsızlıkların (CO, CH_4 ve H_2O) MOFların seçiciliğine, çalışma kapasitesine ve yenilenebilirliğine etkisi incelenmiştir. Yeni sentezlenmiş ve veri tabanına eklenmiş MOFların önceki MOFlara kıyasla daha yüksek CO_2 seçiciliği ve çalışma kapasitesine sahip olduğu gösterilmiştir.

Tezin üçüncü kısmında, bilgisayar ortamında tasarlama teknikleri ile MOFların metalleri değiştirilerek yeni MOFlar tasarlanmış, CO_2/H_2 ve CO_2/CH_4 ayırma potansiyelleri incelenmiştir. Simülasyonlardan elde ettiğimiz sonuçlar MOFların metal tipinin CO_2/H_2 seçiciliğini etkilediğini göstermiştir. Literatürde sıkça çalışılmış MOFlardan Cu metaline sahip HKUST-1'in metali Cr ve Cd ile değiştirildiğinde bu MOF'un CO_2/H_2 seçiciliğinde sırasıyla %11 ve %38 oranlarında artış gözlemlenmiştir. Zn-HIFTOG02'nin metali V ile değiştirildiğinde seçiciliği 119'dan 355'e yükselmiştir.

Sonuç olarak, bu tezde sunulan hesaplamalı tarama metotları ile (i) yanma öncesi CO_2/H_2 ayrımını yüksek performansla gerçekleştirecek MOFların binlerce MOF içerisinden ayıklanabileceği (ii) en yüksek CO_2/H_2 ayırma performansı veren MOFların yapısal özelliklerinin belirlenebileceği (iii) CO_2 yakalama ve H_2 saflaştırma performansı yüksek yeni MOFların tasarlanabileceği gösterilmiştir. Bu sonuçların CO_2 yakalama ve hapsetme performansı üstün yeni MOFların tasarlanmasını kolaylaştırıcı bir katalizör görevi görmesi beklenmektedir.

ACKNOWLEDGMENTS

I would like to present my gratitude to everyone that has directly or indirectly contributed to the inception of this thesis.

I have always been interested about the way things worked in this world which led me to pursue a career in science and engineering, so that I could contribute to essential solutions for grand puzzles of human society. At the start of this journey, I was discouraged occasionally since people seemed to be more interested in following what other people did with their lives rather than following the path of their inner motivations and childhood dreams. I would like to thank to my advisor Prof. Seda Keskin Avcı for giving me the freedom and opportunity to conduct research with the curiosity of a child while simultaneously honing my weaknesses, I am much more confident in being organized and diligent thanks to her effort and care as an awesome advisor. I feel exceptionally lucky and fortunate to grow as a researcher in her group and guidance.

I would like to thank to my dear thesis defense committee Assoc. Prof. İlknur Eruçar, Assoc. Prof. Mehmet Sayar, Asst. Prof. Betül Uralcan and Assoc. Prof. Uğur Ünal for showing interest in my work.

Financial support provided by the European Research Council (ERC) under the European Union's Horizon 2020 research and innovation programme (ERC-2017-Starting Grant, grant agreement no.756489-COSMOS) is also acknowledged cordially.

I thank all of NEMO members and Koc University friends as they have been great of my life in KU. I thank Dr. Ilknur Eruçar for assisting me at hard times and for showing awesome techniques and methods in research. Thank you Sadiye for teaching me intricacies of molecular simulations and giving sound feedback to some of my crazy research ideas with an open mind. I thank Cido, Hilal, Ömer, Önder, Özge, Zeeshan, Safiyye, Harun, Mert, Vahid, Ayda any other past and future NEMO members for sharing a great friendship environment.

I thank all my close friends who supported me through this thesis, Selim, Emir, Kerem, İrem, Sedat, Kaan, Cansu.

I extend the list of my supporters to whomever I could not think of while writing this thesis. I hope the presence of this thesis will make this earth a more manageable place to live and prosper.

TABLE OF CONTENTS

LIST OF TABLES

LIST OF FIGURES

ABBREVIATIONS

Å	Angstrom
APS	Adsorbent Performance Score
ASA	Accessible Surface Area
EqEq	Extended QeQ charge equilibration
cif	crystal information file
CO_2	Carbon dioxide
CoRE	Computation-Ready Experimental
CSD	Cambridge Structure Database
DDEC	Density Derived Electrostatic and Chemical
DFT	Density Functional Theory
D_i^0	diffusivity at infinite dilution (where i represents CO_2 or H_2)
$D_{self,i}$	self-diffusivity (where i represents CO_2 or H_2)
E	energy
EMD	Equilibrium Molecular Dynamics
EQeq	Extended charge equilibration
GCMC	Grand Canonical Monte Carlo
FC-Qeq	formal charge Qeq
k	Boltzmann constant
K	Kelvin
K_i^0	Henry's constant for species i
LCD	Largest Cavity Diameter
MEPO	MOF-electrostatic potential optimized
MMM	Mixed Matrix Membrane
MOF	Metal Organic Framework
N_i	gas uptake for species i
NVT	canonical ensemble
OPLS	Optimized Potentials for Liquid Simulations
P	Pressure
P_i	permeability of gas species i
P_{MOF}	gas permeability in MOF
PLD	Pore Limiting Diameter
Pqeq	Periodic charge equilibration
q	partial charge of an atom
Qeq	Charge equilibration
r	distance between two atoms
R%	Percent regenerability
REPEAT	repeating electrostatic potential extracted atomic
S_{ads}	Adsorption selectivity
S_{diff}	Diffusion selectivity
S_{mem}	Membrane selectivity
SQE	split-charge equilibration
T	Temperature
TraPPE	Transferable Potentials for Phase Equilibria
U_{LJ}	Lennard-Jones potential
U_{elec}	Electrostatic potential
V	Volume
ZIF	zeolitic imidazolate framework
ΔN	working capacity

ε	energy parameter of an atom
ε_0	dielectric constant
μ	chemical potential
π	number pi
σ	size parameter of an atom
ϕ	porosity

Chapter 1

INTRODUCTION

While this thesis was prepared, a global pandemic was in progress and the shift in paradigms through the world challenged us all in many aspects of our lives. We had to change the way we worked, change the way we communicated, and change the way we continued our lives. This thesis is written such that we can harness this wind of change and alter the way we treat the environment by reducing or eliminating the environmental damage we inflict as we strive to build a better society for all. Although green energy frontiers such as wind, solar, nuclear, and fusion energy have become more visible in the mainstream, still, most of the electricity production in the world is supplied from oil and coal plants.[1] Jansen et al.[2] commented that existing and future coal plants, which had a historically bad reputation for high toxic gas/fume emission history, can be converted into power plants that can potentially be established as carbon neutral. This conversion necessitates the discovery of novel materials which can purify, sequester, and store greenhouse gases such as carbon dioxide (CO_2) in a capital and time-intensive manner. Therefore, the introduction of such a technology to the existing energy production techniques will further accelerate our transition to a carbon-neutral society for better future generations.

In a gas mixture of unlike molecules, the thermodynamic tendency for gas pairs to stay together is greater than their tendency to travel apart from each other due to the favorable enthalpic and entropic conditions.[3] Traditionally separation methods such as absorption, adsorption, chemical looping, gas hydration, and membrane-based gas separation have been commonly employed in separating gas mixtures, to take advantage of the industrial conditions.[4] These techniques can be boiled down to two main approaches, (i) adsorption-based and (ii) membrane-based gas separation.

In adsorption-based gas separation, a certain gas species has a greater thermodynamic tendency to adsorb than the latter gas species within a certain temperature and pressure range, such that altering the temperature and/or pressure of the adsorbent results in the enrichment of the desired gas phase as the product.[5] Adsorption is an

exothermic process therefore gas molecules with more favorable energetics and interactions with the adsorbate have a stronger tendency to adsorb on a substrate material. Adsorption-based processes are usually energy-intensive because either a significant temperature or pressure change must be provided to take advantage of the potentially different gas compositions at different thermodynamic conditions. Any material with a surface can act as an adsorbent, but porous solids are preferred to be used as adsorbents due to their high amount of accessible surface areas. Materials in which porosity can be well controlled are commonly selected as adsorbents such as activated carbon, silica gel derivatives, zeolites, and polymers.[6] Adsorption-based gas separation techniques are limited by the physical adsorption capacity of the adsorbent and due to the cyclic operating conditions materials with low adsorption capacity can result in hindered performances.[7] Therefore, determining the best physical and chemical property combinations for an adsorbent-gas pair is essential for industrial applications.

In membrane-based gas separation, the kinetic energy of the continuous gas streams is the main driving force, where the difference in the diffusion rates of different gas species over a specific area can be harvested with the aid of pressure and/or concentration gradients.[8] In an ideal membrane, the membrane should (i) be able to maintain its stability in potentially harsh chemical environments of the gas mixture, (ii) have an anti-fouling mechanism to prevent clogging induced performance decrease, (iii) have a certain degree of processability and mechanical stability such that it can be designed as thin as possible to reduce the material cost, and (iv) have a high surface area to assist in modularization of a membrane unit.[9] Traditionally, polymer membranes are used to separate gases, but they are prone to plasticization and fouling due to the disentanglement of polymer chains over time.[10]

Metal organic frameworks (MOFs) are an emerging class of porous materials that possess a wide range of crystal types and tunable chemical and physical properties. They are made out of metal nodes and organic linkers in which the orientation and coordination of these connections concert the chemical and physical properties of MOFs.[11] The structure of MOFs can be modulated by changing the combination of metal nodes and organic linkers at the precursor stage, or MOFs can be post-synthetically modified.[12] Recently, this tunability in the chemistry space resulted in a Cambrian explosion of new and novel MOF types that can be experimentally realized and new MOF classes and types are discovered each year, such as isoreticular metal organic frameworks (IRMOFs),

zeolitic imidazolate frameworks (ZIFs), and Bio-MOFs.[13-15] Each new MOF that has been synthesized is curated and deposited to the Cambridge Structural Database (CSD) where the crystal structure is digitized and made ready for computational analysis and database curation purposes.[16] The number of structures deposited to the CSD has exceeded 1 million and the number of MOFs deposited to the CSD has well exceeded 120000.[16] Testing each and every one of these materials is theoretically possible but it is not practical since not every structure is promising in terms of its gas adsorption and separation properties. Therefore, in this thesis, the performances of MOF adsorbents and membranes were investigated using high-throughput computational screening for CO_2 separation and H_2 purification.

This thesis is divided into seven chapters. Chapter 1 is the Introduction, Chapter 2 is the literature review of the following three topics: CO_2 capture, screening the updated MOF database, and design of new MOFs as high performing adsorbents. In Chapter 3, details of the molecular simulation techniques and the parameters implemented for performance prediction approaches can be found. Specific computational details (carbon dioxide separation, screening of the updated MOF database, and design of new MOFs as high performing adsorbents), results, and discussions of each chapter are presented in Chapters 4, 5, and 6, together with the conclusions for each chapter. Chapter 7 provides an outlook for future studies.

Chapter 2

LITERATURE REVIEW

2.1 Metal Organic Frameworks (MOFs)

MOFs are composed of inorganic metal-oxo node complexes that form covalent bonds with organic moieties which in turn result in a continuous framework in 1-2-3-dimensional space. Due to the discovery of new classes of MOFs and the recent surge in the number of MOFs reported in the databases, there has been a debate over which materials can accurately be classified as MOFs.[17] We will consider a material as MOF if it has been classified into the "non-disordered MOF database" as curated by the CSD.[17] MOFs can have an exotic range of linker and node combinations and this immense number of chemical combinations lead to MOFs realized with a wide range of surface areas (500-10500 m^2/g) and pore volumes up to 4.40 cm^3/g.[18] MOFs are commonly synthesized with solvothermal, hydrothermal, or microwave-assisted synthesis techniques.[19] Microwave-assisted techniques are more favorable in terms of the absence of residual solvent molecules which can be bound or unbound to the MOF, whereas solvothermal techniques can be easily modified and a series of MOFs can be synthesized systematically with a similar synthetical recipe.[20] To digitize the spatial orientation and position of MOF atoms and make the transition from experimental to computational studies, X-Ray Diffraction techniques are used and information such as the atomic coordinates, unit cell angles, and crystal topology are written to a crystallographic information file (cif). This cif file can be easily visualized and post-processed with software such as Mercury or iRASPA as shown in **Figure 2.1** and interpreted by a simulation software such as Zeo++ or RASPA to conduct molecular simulations.[21-23] Cifs are the most important bridge between experimental and computational studies since any imperfections from XRD pre-processing such as the degree for uncertainty of atomic positions and partial occupancy information are also included.

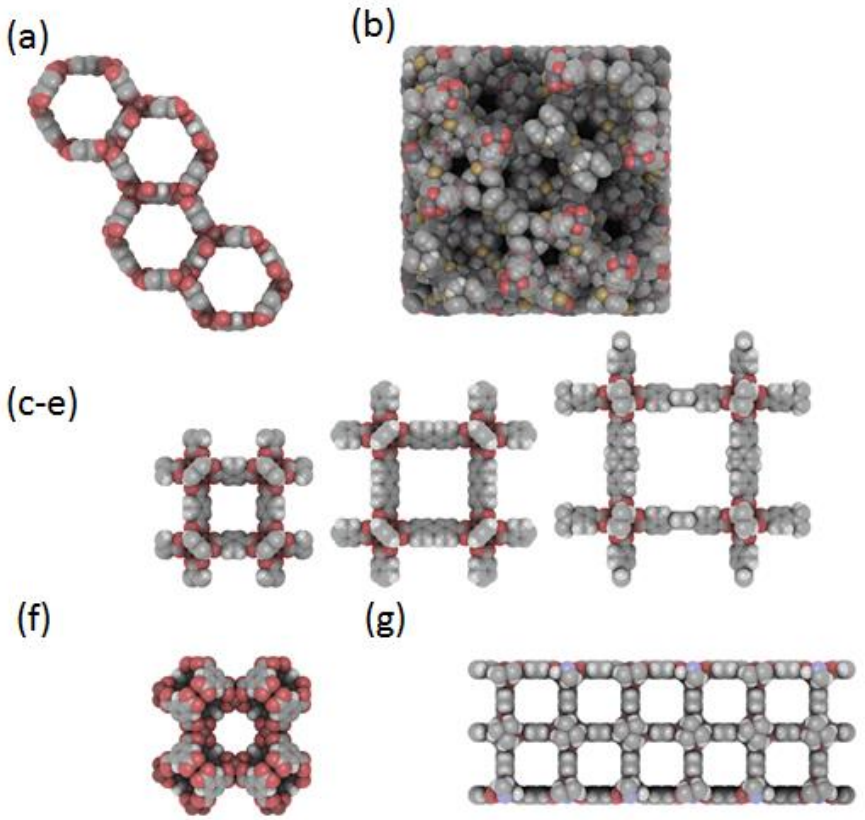

Figure 2.1. Graphical representation of diversity in MOF structures: (a) Mg-DOBDC,[24] (b) MIL-101,[25] (c-e) IRMOF-1, IRMOF-10, IRMOF-16,[26] (f) Cu-BTC[27] and (g) D-MOF.[28]

A recent report by Eddaoudi et al.[29] showed that millions of different types of MOFs can be accessible through synthetic routes although a small fraction of this potential has been experimentally realized so far, with over 100000 MOFs reported to the CSD database until its inception. Out of these thousands of MOFs, one of them has the highest potential for CO_2/H_2 separation but it is not feasible to test every single MOF experimentally, thus computational approaches can potentially identify the most promising MOFs in a time-efficient manner. Computation-ready and open-public MOF databases are available in the literature which facilitate the investigation of many MOFs for gas adsorption and separation applications. MOF database curation is a tedious task since any structural disorder or misreported structures, the presence/absence of residual gas molecules/solvent molecules, missing atoms, and/or extra framework ions must be correctly treated to conduct molecular simulations.[30] Several public MOF databases were formed to address these issues with their unique approaches. Initially, in 2014, 5109

MOFs were curated in a computation-ready experimental MOFs (CoRE MOFs) database which were exclusively 3-dimensional and a 2.4 Å pore size cutoff was used to enable gas molecules larger than Helium to pass through the MOFs.[31] CoRE MOF database was revisited in 2019 and a further classification was made with 14142 all-solvent-removed MOFs, and 13156 unbound solvent removed MOFs. This update was necessary since CoRE MOF database was curated in-house and there was a need for manual interpretation of special cases, reconstruction of MOFs with partial occupancies, and inclusion of MOFs that were not previously added to the CSD.[32] The challenge of constructing a MOF database is that every type of crystal, whether be it MOF, covalent organic framework, zeolite, or organic molecule is deposited into the CSD and a well-thought algorithm is essential to identify MOFs out of different chemical classes. To address these issues, Moghadam and co-workers established a more transparent definition of a MOF by using 7 different identification criteria, established a non-disordered MOF dataset under CSD, and included a solvent removal script that can easily remove a predefined list of solvents.[17] These two database curation approaches are both important since some MOFs require manual interpretation as applied in the case of CoRE MOF database whereas CSD database is quarterly updated, and new structures are deposited into the non-disordered MOF dataset. To compare the advantages and drawbacks of these two databases, our group compared the simulation results for CH_4/H_2 separation for MOFs deposited into CoRE MOF 2014 and non-disordered CSD MOF subset. MOFs are deposited with a 6 letter reference code (refcode) and we identified that MOFs deposited into these two databases with the same refcodes could have significantly different selectivities since they were reported with different structural representations in the two databases.[33] Overall, it is vital to make sure that the cif file completely represents the correct chemical and physical structure of a MOF.

2.2 CO_2/H_2 separation

Separating CO_2 from H_2 is important since more than 40% of world energy use comes from coal plants.[34] Attention towards cleaner fuels such as H_2, which can be easily produced by coal plants, has increased and different classification types regarding the source of hydrogen have been made such as “blue hydrogen” or “green hydrogen”.[35] Blue hydrogen is produced in steam reforming plants such as coal plants whereas green hydrogen is produced predominantly by an electrolysis process supplied from green energy sources.[35] Therefore, separating H_2 gas from CO_2 is vitally

important to supply the increasing electricity demand produced from power plants by steam generators and conversion of blue hydrogen to green hydrogen to efficiently supply fuel cells in cars. Traditionally, coal plants integrated distillation-based techniques such as selexol adsorption to sequester CO_2 but this process is highly energy-intensive and a substantial amount of energy is lost in the process of CO_2 recovery from liquid absorption.[36] Adsorption-based separation is currently possible with zeolites and carbon-based adsorbents such as MCM-41, however, large adsorbent beds are required which imposes both economic and engineering challenges for easy installation and maintenance of these units.[37, 38] Low selectivity, low surface area, and porosity of traditional porous materials such as activated carbon and zeolites prohibit the potential for high performing adsorbents and membranes. Research on new class of materials that can separate H_2 from CO_2 has therefore remained an unsolved puzzle.

Pre-combustion gas plants are an essential source of energy production through burning H_2 to obtain high-energy water steam.[39] In a pre-combustion plant, a mixture of carbon dioxide, carbon monoxide, steam, and hydrogen are reacted in a catalytic reactor through a conversion process that results in a hydrogen-rich fuel called syngas which is processed through a water-gas shift reaction (WGSR).[40] This output of WSGR is composed of a high-pressure mixture of CO_2 and H_2 which has ubiquitous utilities such as in boilers, furnaces, engines, turbines, and hydrogen fuel cells.[41] The main constituents of the WSGR mixture are CO_2, H_2, and water vapor, where water vapor can be captured in an efficient way which leaves a mixture of CO_2 and H_2.[42] Traditionally, this excess CO_2 is captured with liquid solvents such as selexol, methanol, and methyldiethanolamine which is currently 50% more costly than the energy efficiency target of the Department of Energy of United States.[43] This low energy efficiency of liquid absorption techniques stems from high amounts of energy required for regeneration which is partly due to the low selectivity and CO_2 capture capacity of these solvents and partly due to energy intensity to remove a gas phase from a liquid phase. This necessitates the discovery of new materials which have both high selectivity and high CO_2 capture capacity to efficiently capture CO_2 from CO_2/H_2 mixture.

CO_2 adsorption capacities of MOFs have been widely investigated due to their unique physical and chemical properties, which could not be obtained with zeolites and polymers.[44, 45] Advances in synthesis techniques and iterations over previously reported MOFs led to the formation of many MOF families, such as Cu-Cu paddlewheel

MOFs inspired from Cu-BTC, IRMOFs inspired from MOF-5, ZIF family inspired from ZIF-8, and MOFs with hexagonal 2D channels in which Mg-MOF-74 served as a template.[46] Usually, experimental CO_2 adsorption capacities are measured at 1 bar, 273 K or 298 K. 1 bar, 273 K adsorption studies are less relevant for the experimental conditions studied in this thesis, yet CO_2 adsorption up to 38.5 wt% has been reported for SNU-5 for this condition.[47] At 1 bar, 298 K, Mg-MOF-74 has one of the highest reported CO_2 adsorption capacities of 27.5 wt%,[48] whereas, at ambient temperature and pressure, CO_2 adsorption decreases to 19.8 wt% for Cu-BTC,[49] 8.5 wt% for MOF-5,[50] and 4.3 wt% for ZIF-8.[51] Subsequently, many more MOFs have been synthesized and MOFs like MOF-177, with CO_2 capture capacity up to 71 wt% were reported due to its ultrahigh porosity at 50 bar, 298 K.[52] When we compare these values of MOFs with traditional adsorbents such as zeolites, we observe that MOFs have exceptional CO_2 adsorption capacities. 10-membered ring zeolites had 4.8 wt% CO_2 adsorption capacity, whereas a commonly studied zeolite 13X was measured to have 4.2 wt% CO_2 adsorbed at 1 bar, 298 K.[53, 54] Thus, MOFs are promising materials to replace traditional materials such as zeolites in CO_2 capture.

There is an abundant number of studies related to the gas separation with MOFs that focus on their CO_2 capture potential,[46] yet there has been a limited number of studies investigating CO_2/H_2 separation. Experimental studies were conducted to measure the single-component adsorption isotherms of CO_2 and H_2 at various conditions ranging from 0.01-60 bar and 138-313 K for CO_2 and 0.01-120 bar and 77-403 K for H_2, respectively. Herm et al.[55] reported IAST calculated CO_2/H_2:20/80 mixture selectivities for several MOFs; 6 for Be-BTB, 17 for Cu-BTTri, and 400 for Mg_2(dobdc) at 40 bar, 313 K. Since measuring a gas adsorption isotherm for each MOF is extremely time consuming, only a handful of experimental studies on MOFs have well characterized adsorption isotherms for CO_2 and H_2. To overcome this experimental hurdle, computational studies have been conducted to explore the CO_2 capture potential of new MOFs. Molecular simulation has been commonly employed to reveal the CO_2 and H_2 adsorption in MOFs together with CO_2/H_2 mixture separation performance. [56, 57]

Although CO_2 composition in the syngas is the dominant phase compared to H_2, membrane-based separation techniques have been investigated to purify H_2 from CO_2 in the synthesis gas (syngas) mixture. Membrane technologies are especially attractive for H_2 purification in syngas mixture since (i) the gas stream is already at a high pressure (1-

35 bar) which intrinsically provides the necessary driving force, (ii) the potential high surface area of the membrane can significantly assist in miniaturization of the membrane unit, and (iii) membrane units can be easily integrated to existing syngas power plants, therefore, reducing cost. Currently, state-of-the-art membranes are conventional polymeric membranes and ceramic membranes based on zeolites, which suffer from low performances due to their low selectivity and low permeability values.[10, 58, 59] MOFs have been shown to overcome these shortcomings of the previous generations of membranes due to their high surface areas and high porosities.[18, 60]

In membrane-based H_2 purification, a suitable combination between gas permeability and membrane selectivity is targeted for efficient pre-combustion CO_2 capture. Conventional membrane materials such as polymers do not have the desired combination between high selectivity and high permeability, and they suffer from plasticization problems over pre-combustion separation conditions.[61, 62] Due to the physical chemistry restraints, polymers with high gas solubility usually have high selectivity but they have limited permeability whereas polymers with low gas solubility give high permeability but gas selectivity is hindered as stated by Robeson.[63] For example, Polyimide(1,1-6FDA-DIA)[64] has an experimental H_2/CO_2 membrane selectivity of 8.05 but suffer from an extremely low H_2 permeability of 31.4 Barrer, whereas Poly(trimethylsilylpropyne)[65] was reported to have a low experimental H_2/CO_2 membrane selectivity of 0.53, but with a high H_2 permeability of 23300 Barrer. For MOF membranes, this trade-off between gas permeability and selectivity does not necessarily hold due to exceptional surface area and unique physical properties of MOFs which enable efficient gas transport and separation.[66]

2.3 MOF Databases

Compiling consistent and clean MOF databases is essential for high-throughput computational studies. Until the early 2010s, crystallographic information files (cif) of MOFs had to be searched manually by going through each experimental article. Due to the lack of publicly available MOF structures, the growth of studies upon molecular simulations of MOFs was stagnated in the early years. Goldsmith et al.[67] curated the first MOF database by identifying 40000 MOFs retrieved from the CSD and 16000 MOFs were discarded due to problems in the crystal file such as the presence of disordered atoms or missing hydrogen atoms. However, this database was not available as open-public. Later in 2014, CoRE MOF database was established and made publicly available by Snurr

and coworkers. This was a major step in establishing a standard for MOF databases since over 60000 MOFs were (i) categorized according to their dimensionality, (ii) processed such that missing hydrogens and any missing structural features such as extra framework ions were treated, (iii) unbound solvent molecules were removed to create the computation-ready, experimental (CoRE) MOF database.[31] There was also a minor update to CoRE MOF which included 2932 Density Derived Electrostatic and Chemical (DDEC)-charged CoRE MOFs.[68] The DDEC method retrieved the point charges from DFT-based calculations which provide an accurate representation of charge distribution in MOFs.[69] Furthermore, another minor update included DDEC-charged CoRE MOF that ended up with 879 MOFs which were also geometry optimized according to Density Functional Theory (DFT) calculations.[70]

The only major impediment for the CoRE MOF database was that it was not updated for the most recent set of MOFs that were deposited into the CSD. Therefore, in 2017, Jimenez and co-workers, integrated a pre-compiling and screening script into the CSD that would remove the unbound solvents and structures with disorder coupled with manual crystal controls curated by the CSD scientists.[17] This study enabled the curation of a compounding non-disordered MOF database that was updated every quarter. Recently, Simon et al. discussed the ideal properties of a MOF database which included (i) retention of structural integrity after solvent removal, (ii) MOF phase change after solvent removal, and (iii) preservation of original MOF chemistry after automatic processing and categorization of MOFs.[71] Curating a MOF database is a tedious task and it is challenging to satisfy these conditions since an approach that checks all boxes is intrinsically hindered due to the extremely diverse structure of MOFs and due to the rigor applied to separate MOFs from all other non-MOF structures from CSD.

A recent answer to this challenging task of database curation was from an updated version of the CoRE MOF database. The number of MOFs in the database was increased to over 14000, an option to remove bound or unbound solvents was added, and topology-based crystal generation was employed to reconstruct structures with a disorder.[72] The pore structures and physical properties were analyzed among 14000 MOFs and it was found that MOFs with terephthalic linkers were observed to be the most common with 344 hits and pcu topology was the most common topology with 26.7%. Moghadam et al.[13] added targeted classification techniques to CSD and distinguished zirconium oxide-based MOFs, ZIF-like MOFs, IRMOF-like MOFs and Copper-Copper

paddlewheel type MOFs in addition to the classification of certain functional groups such as alkyl groups, halogen groups, and polar groups. It should be noted that since all MOF databases are mostly retrieved from CSD, the majority of the MOFs in each database is common. Therefore, Altintas et al.[73] recently compared the CH_4 and H_2 adsorption and CH_4/H_2 selectivity of CoRE MOF database and CSD non-disordered MOF subset database (CSDSS DB) and found that adsorption simulations from each database can differ significantly due to the different pre-processing steps in each database. 387 common MOFs with different treatments from CoRE MOF and CSDSS DB were identified and MOFs from CoRE MOF dataset were shown to overestimate H_2 and CH_4 adsorption due to missing extra framework ions and missing ligands.[73] In this thesis, we chose to focus on the CSDSS DB since this database is updated quarterly, thus additional MOF structures can be screened more efficiently.

Updating the MOF databases can potentially reveal previously hidden insights and information upon the characteristics of MOFs. In addition to the MOFs being "ordered, truly crystalline" structures as stated in the milestone paper of Hoskins and Robson,[74] they can also have important properties such as presence of interpenetration and catenation, inclusion of non-heterogenous pore architecture that leads to the formation of pore pockets. Ryan and co-workers computationally showed that catenation can significantly enhance hydrogen adsorption of IRMOF-1 from 60 mg/kg to 80 mg/g at 77 K but catenation has negligible influence on hydrogen adsorption of IRMOF-1, IRMOF-16 and their catenated pairs at room temperature.[75] Due to the lack of known catenated pairs for MOFs, Sezginel et al.[76] generated a library of 6000 MOFs from 4.3 million MOF pairs and identified 1045 pairs that would form catenation and 18 hypothetical hetero-interpenetrated MOFs. This hypothetical database study was able to generate 1005 MOFs that were 3D to 3D penetrated in addition to 40 MOF structures that were not previously synthesized. Chong et al.[77] performed high-throughput screening on 11558 MOFs retrieved from CoRE MOF database and investigated the ratio of Henry's constants and uptakes of gases in MOFs for which these special pores were included and ignored within the calculations. 13 MOFs were found to have hidden adsorption sites that could be excavated with defect introduction and methane uptake of the most promising MOF increased from 23 STP/v to 58 STP/v at 1 bar 298 K.[77] Therefore, promising MOFs for CO_2 capture and H_2 purification can be identified with detailed analysis of their chemical and physical properties.

In this thesis, by screening the most recent and updated MOF database retrieved from CSD, we were able to identify a significant number of MOFs that would have catenation and would require pore blocking and investigate the influence of pore blocking and catenation.

2.4 Role of metal exchange on CO_2 capture performance of MOFs

The number of MOFs that have been synthesized has increased rapidly and this is partially due to the degree of redundancy in new MOF design. MOFs have metal oxide nodes which are connected by organic linkers that outcome as a continuous framework. Rather than designing a new MOF from scratch, a practical approach from both experimental and computational perspectives is to change the precursors for the metal nodes and/or linkers that can result in a new MOF with its unique chemical and physical properties. Among these two options, linker exchange is more challenging since the degree of exchange depends on the interaction energies between the metal node and the existing linker and the metal node and the new linker.[78] This process can be energetically unfavorable which may result in a failed linker exchange or the linker exchange can completely collapse the framework.

A more straightforward approach is to change the metal precursor before synthesis or perform a post-synthetic metal exchange.[79] Post-synthetic metal exchange is thermodynamically more favorable than synthesizing a MOF with a new metal node since in the first approach the MOF already has a predefined framework, reducing the probability of a framework collapse. Due to the strong electrostatic forces imposed by the metal atoms, metal exchange can significantly influence the gas adsorption of a MOF especially for polar adsorbents such as carbon dioxide, acetone, and methanol. Wu et al.[80] computationally investigated adsorption properties of methanol and acetone in M-HKUST-1 and found that adsorption capacities of MOFs generally follow the order of Ti>Fe>Cu>Co>Mo>Ru-HKUST-1. They discussed that adsorption performance of MOFs were dictated by the adsorbate-framework interactions at low pressures whereas structural properties such as pore volume and accessible surface area are the predominant factors for gas adsorption at high pressures. Yu et al.[81] computationally focused on four different M-HKUST-1 materials (M=Zn, Co, Ni, and Mg) and found that hydrated Co-, Ni- and Zn-HKUST-1 showed improved CO_2 adsorption compared to their non-hydrated counterparts. Coulombic interactions between CO_2 molecules and the electric field

created by the coordinated water molecules were found to be responsible for the increased CO_2 uptake in these MOFs. Koh et al.[82] used the DFT calculations and modified the Universal Force Field parameters to better fit CH_4 adsorption in M-HKUST-1 where 17 different metals were investigated. They showed that CH_4 adsorption increases with increasing metal point charge. In addition to HKUST-1, IRMOF-10 and MOF-74 series have been also studied to understand the role of metal type in gas adsorption capacities of MOFs. Borycz et al.[83] developed a force field to investigate the CO_2 adsorption in M-IRMOF-10 series where M corresponds to Mg, Ca, Fe, Cu, Zn, Ge, Sr, Cd, Sn, Ba. They reported that CO_2 adsorption of Ba-IRMOF-10 at low pressure was almost doubled compared to Zn-IRMOF-10 due to the larger ionic radii of Ba which was exposed more to CO_2 by reducing the steric hindrance. Park et al.[84] performed DFT calculations and showed that M-MOF-74 can be tuned in order to have a stronger binding affinity for CO_2 by metal substitution with Ti and V. Canepa et al.[85] examined the binding characteristics of single-component gases such as H_2, CO_2, CH_4, and H_2O in M-MOF-74 series having 25 different metal types using the DFT calculations and reported that CO_2 interactions were higher with Rh, Pd, Os, Ir, Pt metals compared to the rest of the metals.

Although there have been few studies investigating the influence of metal exchange on gas adsorption both from experimental and computational perspectives, still the literature for the impact of metal exchange upon mixture gas separation is scarce. Poor et al.[86] examined M-HKUST-1 (M=Mn, Fe, Co, Ni, and Zn) for anesthetic gas separation and proposed that Ni-HKUST-1 can improve the uptake and selectivity of Xe with respect to CO_2. Sholl and coworkers[87] investigated M-HKUST-1 and showed that material with Zn atom has the highest C_2H_2/C_2H_6 selectivity where impurities can also be sequentially filtered by the use of MOFs having metals such as Ru, Ti and Ni.[87] . Yuan et al. performed grand canonical Monte Carlo (GCMC) simulations for adsorption and separation of an equimolar CO_2/H_2 mixture on M-SIFSIX-3, where M = Cu, Zn, and Fe, and found that CO_2 molecules adsorb preferentially closer to the SIF_2^- anion, whereas H_2 molecules prefer to adsorb at the pore center. CO_2/H_2 selectivities of Cu, Zn, and Fe-SIFSIX-3 were computed as 300, 400, and 500, respectively, at 10 bar, 298 K.[88]

In this thesis, the influence of metal exchange on CO_2/H_2 adsorption selectivity is investigated by performing in-silico metal exchange on two MOFs: HKUST-1, a well-known common MOF and HATGUF, a MOF that has been identified as one of the top performers from our previous screening study.[89]

Chapter 3

COMPUTATIONAL METHODOLOGY

3.3 Molecular Simulations

3.3.1 Calculation of Structural Properties of MOFs

The physical and chemical properties of MOFs can vary drastically due to the number of structural combinations of linkers, metal nodes, and topologies they can possess, so it is important to characterize the structural properties of MOFs. Determination and calculation of physical properties can provide essential information to both experimental and computational studies. It is possible to calculate the structural properties of MOFs such as pore limiting diameter (PLD), largest cavity diameter (LCD), surface area, density and pore volume with a simulation software such as Zeo++.[21, 90] Zeo++, as the name implies, was originally designed for calculating physical properties of zeolites but was later extended for other porous materials such as MOFs. In an essence, a cif file is fed to the software which is converted to a cssr file and the software proceeds with a Voronoi representation of the structure file. With the conversion of the cif file to the Voronoi network representation, a 3 dimensional surface is defined for probabilistic calculations.[90] This step provides the transition from spherical representation of individual atoms to an interconnected mesh of atoms, therefore physical properties can be calculated with great accuracy and speed.

A nitrogen probe with a probe radius of 1.86 Å can be used for nitrogen accessible surface area calculations whereas a helium probe with 1.20 Å radius can be used to calculate the pore volume. Ray tracing technique can be used to calculate the general MOF pore landscape which in turn can be used for similarity index calculations.[21]

3.3.2 Grand Canonical Monte Carlo (GCMC) Simulations

In this thesis, a classical molecular simulation technique was used to define the energetic interactions between adsorbate and adsorbent atoms. In the physical world, atoms and molecules move in a continuous fashion.[91] On the other hand, computer simulations work in principles of computing clocks processing millions of operations per second and a discretization method is required to model the physical world. To make a

discretized model of the continuous movement of atoms such that computers will be able to process this information, probabilistic methods such as the Grand Canonical Monte Carlo (GCMC) method can be used.

In GCMC technique, a reservoir of atoms with a pre-defined concentration, a simulation box with a starting configuration of atomic coordinates, and energetic rules are required. Metropolis et al.[92] hypothesized Monte Carlo Sampling techniques and this method was eventually implemented to classical molecular simulations. In this method, selection between a pre-defined type of configurational states is proceeded in a random fashion and this move proposition is accepted or rejected based on energetic rules. Energy (E) of each possible configuration is calculated and the probability (p) of each viable configuration is determined with using $e^{-E/kT}$ where k is the Boltzmann constant and T is the temperature. The new configuration is accepted if the newly proposed energetical state has a lower energy than the initial configuration state. What makes the Monte Carlo sampling efficient for molecular simulations is that if the new configuration state has higher energy than the previous configuration, the algorithm has an acceptance probability of the higher energetic state in which the strength of this probability is concerted by the energetic relationship between the simulation box and the adsorbate reservoir. This way, the simulation will give a realistic representation of the natural continuous energetic landscape of a physical system without trying every single configurational state which can be physically realized. Also, assigning a probability to accept a higher energy configuration removes the problem of simulation being stuck at an energy well, thus most probable energy landscape of the simulation will be considered.

For Monte Carlo sampling and GCMC techniques, a thermodynamic system must be defined. In a thermodynamic system, macro-state (pressure, temperature) conditions are collectively represented by individual micro-states (atomic configurations, chemical potential, kinetic and potential energy of individual atoms) within a system. The average energetics of micro-states over time can be translated to macro-state conditions and the different configurations of micro-states form an ensemble. For example, in microcanonical ensemble (NVE), the number of atoms in the system, volume, and the total system energy are specified, whereas in Canonical ensemble (NVT), the number of atoms in the system, volume, and temperature are fixed. Grand Canonical ensemble (μVT ensemble), is a curation of microsystems which have the exact chemical potential μ, volume V, and temperature T. Therefore, to probe the macroscopic states of this system,

we can influence the external pressure, and/or we can add/remove atoms to change the N value. Volume of the simulation box and temperature are kept constant and the number of molecules inside the system are allowed to change until the chemical potential of the adsorbate and adsorbent reaches a meta-stable equilibrium.[93]

Results from GCMC simulations provide a good representation of gas adsorption in MOFs given that enough simulation steps are used. In each step, a Monte Carlo sampling is performed for each adsorbate present in the system that can potentially change the configuration of atomic positions and number of atoms within the system. At the first step, gas molecules are inserted into the MOF randomly, thus a certain amount of equilibration steps must be performed. Certain trial moves are provided for the adsorbate atoms such as insertion, deletion, translation, and rotation to capture the intrinsic molecular energetics of the system. These trial moves are represented in **Figure 3.1**. If the chemical potential of the MOF simulation box is much lower than the chemical potential of the gas reservoir, then insertion move becomes highly favorable. Gas molecules are favorably inserted to the system until there becomes a dynamic equilibrium between the simulation box and the reservoir box. The simulation is continued until the total energy and number of molecules within the system fluctuates within an acceptable range and the average number of molecules are taken as adsorption values. From the slope of the fluctuation in energy, isosteric heat of adsorption can be calculated.[94] Another important factor to consider in GCMC simulations is ergodicity. The system is ergodic if the original configuration can be retraced from a certain random step within the simulation. This ensures that ensemble average probabilities are equal to the corresponding time averages. Different GCMC algorithms and programs have been written such as Multipurpose Simulation Code (MUSIC), RASPA and Materials Studio Adsorption Module.[95-97] It is important to understand that each of these algorithms can have different weighting functions and set of algorithm rules to provide a healthy relationship between the physical accuracy of the simulation and time efficiency.

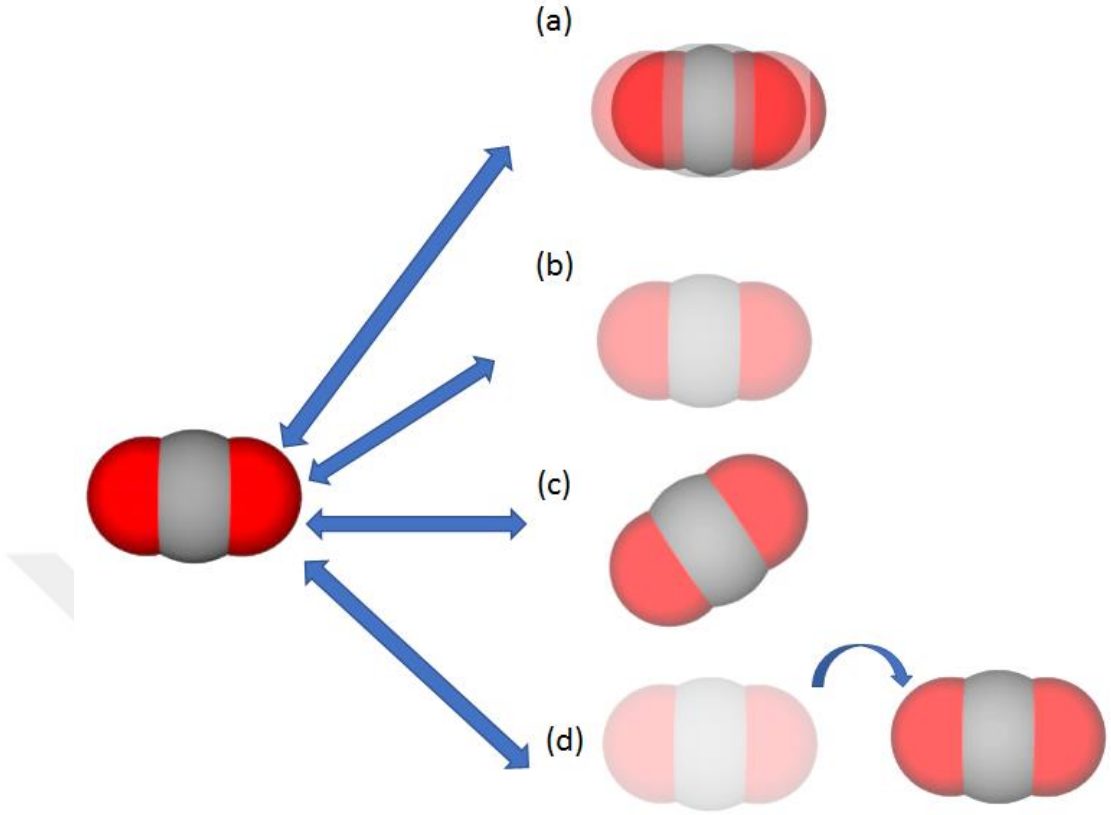

Figure 3.1. Representation of trial moves in a Monte Carlo simulation (CO_2 as the representative molecule): (a) translation, (b) addition/deletion, (c) rotation, (d) re-insertion, respectively.

For a GCMC simulation, the crystal structure of the MOF, a gas model, gas-MOF interaction parameters (force field parameters), temperature (T), pressure (P), and composition of the gas feed are used as the main input parameters. Unit cell parameters, including cell lengths and angles, symmetry identification, and fractional coordinates for MOF atoms are obtained from the cif and used in the GCMC.

In GCMC simulations, there is no concept of time, thus pairwise interactions are calculated to produce the Boltzmann distribution of particles within the simulation. This distribution is the outcome of energetic interactions between MOF and gas molecules and the parameters, σ, and ε, where σ represents the hard sphere radius of a gas molecule and ε represents the dispersion energy which is the sum of all bonded and non-bonded contributions. In adsorption simulations, the potential for MOF atoms and the introduced gas atoms are required as inputs. Therefore, parameters from classical force fields are used to model MOF atoms and gas atoms. To represent the intermolecular interactions between a pair of charged atoms, van der Waals forces are used together with Coulombic interactions. Lennard-Jones (LJ) 12-6 potential is an efficient method to compute the van

der Waals interactions in GCMC simulations.[98]

$$U_{LJ}=4\varepsilon_{ij}\left[\left(\frac{\sigma_{ij}}{r_{ij}}\right)^{12}-\left(\frac{\sigma_{ij}}{r_{ij}}\right)^{6}\right] \quad (3.1)$$

In Eqn. 3.1., U_{LJ} represents the LJ energy between two unlike particle (i and j), r is the total distance between two particles, ε_{ij} is the energy well depth, and σ_{ij} is the hard sphere radius. Since an unlike pair would have different σ and ε values, we can hypothetically treat them as a singular pair with Lorentz-Berthelot mixing rules. The arithmetic average of size parameters, $\left(\sigma_{ij}=\left(\sigma_i+\sigma_j\right)/2\right)$ and geometric average of energy parameters, $\left(\varepsilon_{ij}=\sqrt{\varepsilon_i\times\varepsilon_j}\right)$ give good approximations for treating the unlike gas-pairs. Although atoms can have multiple energy states and configurations, we can parametrize σ and ε values by retrieving pre-calculated constants from quantum chemistry-based calculations.[99] These classical force field approximations can be fine-tuned by including additional experimental thermodynamic data such as vapor-liquid equilibrium curves, thermal expansion coefficients or mechanical elasticity.[100, 101] Due to the diverse structure and geometries of MOFs, multiple types of force fields have been used such as Optimized Potentials for Liquid Simulations (OPLS), Universal Force Field (UFF), DREIDING, MOF-FF, QUICKFF which use various potentials such as Buch potential or approximation techniques to represent the MOF structure.[102, 103]

Electrostatic potential energy (U_{elec}) is commonly computed by using the Coulomb potential as shown in Eqn. 3.2 where ε_0, q_i and q_j show the dielectric constant, partial atomic charges of i and j, respectively. [98]

$$U_{elec}=\frac{1}{4\pi\varepsilon_0}\frac{q_i q_j}{r_{ij}} \quad (3.2)$$

From this equation we can understand that the strength of electrostatic interactions decreases with increasing distance and converges to zero at infinitely large distances. Electrostatic interactions have real and imaginary parts due to periodic boundary conditions. Although the charge of each MOF atom is not static and can be influenced with adsorbate interactions, using static partial charges give good approximations to the overall coulombic environment in most MOFs.[104] Partial charges of the gas molecule are included within the gas model whereas partial charges for MOF atoms are calculated using partial charge assignment methods. Density functional theory (DFT)-based partial charge assignment methods can be used to include a more detailed charge environment

in a MOF whereas time-efficient charge equilibration (Qeq) methods can be used with acceptable tolerance. Qeq methods rely on the neutral state oxidation potential and better estimations to the electrostatic potential of MOFs have been recently investigated.[105]

Periodic boundary conditions extend the simulation box with its replicas in three dimensions such that a small number of MOF atoms can be used to calculate intermolecular and intramolecular interactions.[98] In each time step or cycle, the interaction between every atom in the system has to be calculated and the simulation cost increases exponentially with increasing atom numbers. A minimum image convention is set to determine a good trade-off between simulation accuracy and speed.[98] Cut-off radius is set such that any interaction an atom can experience is within at least half the total cell length L.

Conditions of GCMC simulations such as pressure, temperature, and composition of the feed gas are retrieved from physical conditions. Pressure of adsorbates are converted into fugacity with Peng Robinson equation of state.[97] To keep the temperature constant while particles are added and retrieved from the system, a thermostat is used. Nosé-Hoover[106] and Andersen[107] thermostats give reliable and consistent temperature measurements through simulations with MOFs.

From the ensemble averages obtained from GCMC simulations, gas uptakes from single-component or mixture gas uptakes (N_i or N_i^{mix}, respectively), can be retrieved to calculate the adsorbent performance evaluation metrics of MOFs. Henry's constant (K^0) and heat of adsorption (ΔQ_{st}^0) values indicating the interaction affinity of single ghost gas molecule to the adsorbent at very low pressure is calculated with the Widom's particle insertion method.[108] In Widom's method, a particle is rolled on the surface of the MOF while the total surface of the MOF is probed with sufficient steps. Due to the infinite dilution conditions, the influence of gas-gas interactions are neglected with the Widom's particle insertion method.

3.3.3 Molecular Dynamics (MD) Simulations

Equilibrium Molecular Dynamics (EMD) simulations in the NVT ensemble can be performed to compute the diffusivity of gas molecules in a MOF. The Newton's equation of motion[109] is solved for finite time intervals and from the relationship between the positions and velocities of gas molecules, diffusivity data can be calculated. In an EMD simulation, initial configuration of the molecules is introduced as an input and the

molecular forces are computed based on the interaction parameters of the force field.

$$\frac{F_i}{m_i} = \frac{d^2r}{dt^2} \tag{3.3}$$

In Eqn. 3.3, Newton's equation of motion is defined where r is the position of the particle at time t, F_i is the force on component i, and m_i is the mass of the component i. To solve the Newton's equation of motion effectively, an algorithm is required to save computational time.

$$r(t + \Delta t) = r(t) + \Delta t v(t) + \frac{1}{2}\Delta t^2 a(t) \tag{3.4}$$

In Eqn. 3.4, the Velocity Verlet algorithm is shown where t is time, r is the position of the particle at time t, v is the velocity of the particle and a is the acceleration of the particle. The time step is chosen in such a way that the integration is accurate enough and the total energy of the system is conserved. The time step used in EMD simulations should be at least an order of magnitude faster than the fastest motion captured in the simulation.[97] If the time step is too low, then the EMD simulation can be computationally expensive, if the time step is too high, then the continuous motion of gas molecules can be discrete and problems such as overlap of atoms can occur. To simulate the motion of gas molecules in MOFs, a time step of 1 fs is usually preferred.[110]

During an EMD simulation, a thermostat algorithm is employed to keep the simulation temperature constant. Nosé-Hoover thermostat[106] is commonly used for EMD simulations whereas thermostats such Berendsen thermostat[111] are also suitable for certain MD simulations. As the molecules collide with each other and exchange momentum, certain molecules within the simulation become too fast or too slow and affect the temperature of the system, thus a normalizing algorithm for temperature is required. The overall momentum distribution of gas molecules is expected to converge to a Gaussian distribution, and the thermostat collectively normalizes the momentum of gas molecules at each time step so molecular dynamics at equilibrium can be observed.

Many different diffusion coefficients (Fickian-, Maxwell-Stefan-, and Onsager formulations)[97] can be defined to understand the dynamics of guest molecules in porous materials. In this thesis, the self-diffusivities of gases were utilized. The self-diffusivity ($D_{i,\,self}$) can be described as the individual motion of a certain gas molecule. In an isotropic 3D framework, self-diffusivity can be retrieved from the mean-squared displacement

(MSD) of the particles. An MD simulation with sufficient time window (≥1 ns) allows us to calculate the MSD of gas molecules. In crystalline materials, the MSDs become linear at long distances whereas the accuracy of MSD data rapidly decreases over increasing times. Therefore, it is convenient to fit the diffusivities averaged from different simulations. This MSD data is integrated over different time frames within the simulation with modified order-N algorithm. With plotting MSD versus simulation time, the diffusivity of gas components are obtained from the slope by using Einstein's equation.[112]

$$D^{S}_{i,\,self} = \frac{1}{2dN} \lim_{t\to\infty} \frac{d}{dt} \left\langle \left(\sum_{i=1}^{N} \left(r_i(t) - r_i(0) \right) \right)^2 \right\rangle \tag{3.5}$$

In Eqn. 3.5, r(t) is the position of the particle at time t, N is the number of particles, d is the number of spatial dimensions for diffusion (d= 1, 2, or 3 for one, two, or three dimensions, respectively) and the angular brackets represent the ensemble average. The order-n algorithm is convenient for measuring MSDs and it efficiently captures correlations over short, medium and long time frames. Finally, MOFs can have a wide range of pore sizes from 2-50 Å.[113] **Figure 3.2** shows that CO_2 and H_2 molecules both collide with each other and collide with pore walls.

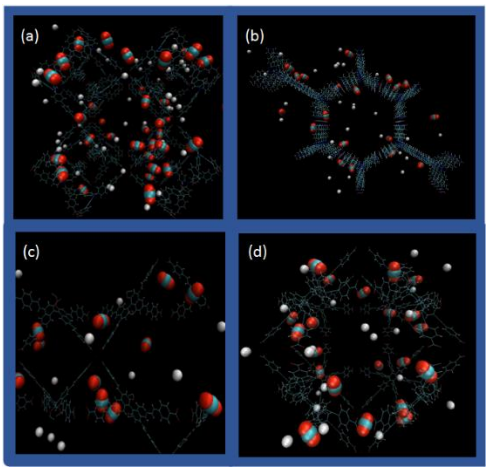

Figure 3.2. Representative MD simulation snapshots in (a) a 3-dimensional MOF, (b) a 2-dimensional MOF, (c) 1-dimensional MOF, (d) 3-dimensional MOF with large pores, respectively. White spheres represent H_2, whereas linear blue and red spheres represent CO_2 molecules.

Therefore, both molecular diffusion (the collision between gas molecules) and Knudsen diffusion (concerted by the collision of gas molecules to pore walls)[114] have influence on the diffusion characteristics of gases in MOFs.

3.4 Predicting Separation Performances of MOFs

3.4.1 Adsorption-Based Separation Performances of MOFs

Adsorbent performance evaluation metrics of MOFs were investigated for CO_2/H_2 separation in this thesis. Therefore, the metrics explained in this section will be based on the strongly adsorbed component of the system, which is CO_2. After computing the adsorbed CO_2 amounts for a MOF from a GCMC simulation, this data is processed to evaluate CO_2 separation performances of MOFs. Adsorbent performance evaluation metrics are commonly used for MOFs to model their real-world adsorption behavior when used as adsorbent beds. For example, CO_2 working capacity (ΔN_{CO_2}) is the total amount of CO_2 that can be captured due to a pressure or temperature swing within the system. It is simply the difference between the CO_2 uptakes at adsorption ($N_{CO_2,ads}$) and desorption ($N_{CO_2,des}$) pressure or temperature.

$$\Delta N_{CO_2} = N_{CO_2,ads} - N_{CO_2,des} \tag{3.3}$$

For systems with high selectivity such as CO_2/H_2, mixture adsorption data ($N_{CO_2}^{mix}$) can also be used to calculate the working capacity, although single component data is a better model for nitrogen purge step of an adsorbent bed.[115, 116] The gas uptakes at desorption condition is matched with the feed composition of the gas mixture, and we followed this convention within the thesis. It is also possible to model the adsorption condition with single-component CO_2 uptake due to highly pure CO_2 at the desorption step.[117]

Pressure swing adsorption (PSA), vacuum swing adsorption (VSA) and temperature swing adsorption (TSA) are industrial procedures where the adsorbent is exposed to the feed at the first stage until saturation, followed by CO_2 desorption at the lower pressure or higher temperature, while less strongly adsorbed gas is purified through an iterative process.[118] Percent regenerability (R%) is used to calculate how efficiently the adsorption capacity of a MOF is utilized through each adsorption and desorption cycle and calculated by the formula:

$$R\% = \left(\Delta N_{CO_2} / N_{CO_2,ads}\right) \times 100\% \tag{3.4}$$

An ideal MOF adsorbent for CO_2 capture and H_2 purification should have high R% values in addition to high $N_{CO_2,ads}$ and high ΔN_{CO_2}, so that it can capture a significant amount of

CO_2 between specified pressures for several times without a need to regenerate the adsorbent.

Adsorption selectivity (S_{ads}) is the ratio of the uptake of more strongly adsorbed gas component (CO_2) to the weakly adsorbed gas species (H_2) at adsorption pressure. It shows us the relative strength and affinity of gas molecules with a MOF adsorbent to separate any impurities. Ideal selectivity can be defined as the ratio of Henry's constants for different gas species ($K^0_{CO_2}$ and $K^0_{H_2}$) or the ratio of single-component gas uptakes obtained from GCMC simulations as follows where N_{CO_2} is the adsorbed amount of CO_2 and N_{H2} is the adsorbed amount of less strongly adsorbed gas, H_2.

$$S_{ads,\,ideal} = K^0_{CO_2}/K^0_{H_2} \text{ or } S_{ads,\,ideal} = N_{CO_2}/N_{H_2} \tag{3.5}$$

Computational identification of ideal selectivity is rather simple and requires less time compared to mixture selectivity. Therefore, it is frequently used as an initial screening criterion to identify the most promising MOF adsorbents based on their selectivities. However, under real operating conditions, in the presence of other gas components and impurities in the gas feed, collaborative and competitive gas adsorption can be observed.[119, 120] For example, electrostatic interactions or pore topology can strongly favor adsorption of CO_2 molecules, and the other molecules need to compete with CO_2 for the available adsorption sites. Collaborative effects such as CO_2-CO_2 interactions can attract more CO_2 molecules into the framework. To take these effects into account, mixture selectivity should be considered. It can be calculated using the ratio of adsorbed gas amounts obtained from mixture GCMC simulation normalized with bulk composition of the gas mixture as shown in Eqn. 3.6 (x_{CO_2} represents the mole fraction of adsorbed CO_2, x_{H_2} represents the mole fraction of less-strongly adsorbed gas H_2, y_{CO_2} represents bulk feed composition of gas species CO_2 and y_{H_2} represents bulk feed composition of H_2).

$$S_{ads,(CO_2,H_2)} = \frac{x_{CO_2}/x_{H_2}}{y_{CO_2}/y_{H_2}} \tag{3.6}$$

Experimental investigation of mixture gas adsorption for various compositions of a gas mixture is challenging due to the lack of proper instrumentation and expertise to determine the gas mixture adsorption isotherms and also lack of time, human and financial resources.[121] Determination of the adsorption loadings for each gas species

through weight changes or pressure changes is also difficult. This requires using theoretical models that can predict mixture gas adsorption from single-component gas adsorption data. Ideal Adsorbed Solution Theory (IAST) predicts mixture adsorption isotherms from the single-component gas uptakes based on an adsorption model such as Langmuir model. It is based on the assumptions that all gas molecules have equal accessibility to the whole surface area of a homogeneous adsorbent, gases interact with the adsorbent similarly in strength, and there are no interactions between adsorbed gas molecules mimicking an ideal solution.[122] IAST method is shown to accurately work for gas adsorption in MOFs unless the MOF has an energetically heterogeneous surface.[123]

A good adsorbent is expected to provide a combination of high ΔN_{CO_2} and $S_{ads,(CO_2,H_2)}$. However, there is generally a trade-off between these two metrics.[124] Porous materials with large pore sizes generally exhibit high gas working capacities but due to the large pores both gas molecules can be adsorbed within the adsorbent leading to a decrease in adsorption selectivity. Therefore, other metrics combining working capacity and selectivity are developed to provide a better estimation of MOFs' performances. Adsorbent performance score (APS)[125] and PSA sorbent selection parameter (SSP)[116] can be defined as follows:

$$\text{APS (mol/kg)} = \Delta N_{CO_2} \times S_{ads,(CO_2,H_2)} \tag{3.7}$$

$$\text{SSP} = \frac{\Delta N_{CO_2}}{\Delta N_{H_2}} \times S_{ads,(CO_2,H_2)} \tag{3.8}$$

A recent work by Sholl's group[126] compared the predictions of adsorbent evaluation metrics (working capacity, adsorption selectivity, sorbent selection parameter, adsorbent performance score, regenerability) with the results of detailed process models (purity, recovery, productivity, energy) for dry CO_2/N_2 separation at sub-ambient temperatures at PSA conditions for 143 MOFs. Their results showed that ΔN_{CO_2} and APS are the two parameters that can best predict the process level rankings of MOFs for dry flue gas separation.

3.4.2 Membrane-Based Separation Performances of MOFs

Gas permeabilities of MOFs at infinite dilution (P_i^0) and ideal selectivities of MOF membranes were calculated using Eqn. 3.9 and 3.10.

$$P_i^0 = K_i^0 \times D_i^0 \tag{3.9}$$

$$S_{mem}^0 = P_i^0 / P_j^0 \tag{3.10}$$

Mixture permeabilities through MOF membranes were computed using Eqn. 3.11 where c_i, D_i and f_i correspond to adsorbed gas loading, self-diffusivity, and feed side partial pressure of the gas, respectively. Permeate side of the membrane was assumed to be vacuum.[127]

$$P_i^{mix} = c_i^{mix} \times D_i^{mix} / f_i \tag{3.11}$$

Gas permeabilities through MOFs can also be calculated using the following expression,[128]

$$P_i = \frac{\phi \times D_{i,self} \times c_i}{f_i} \tag{3.12}$$

where P_i, ϕ , $Di_{,self}$, c_i, f_i represent the permeability of the component i (mol/m/s/Pa), the porosity of MOFs, the self-diffusivity of the component i in the mixture (m^2/s), the concentration of component i at the upstream face of the membrane (mol/m^3) and the bulk phase fugacity of the component i (Pa), respectively. Mixture selectivities for MOF membranes were computed as the ratio of gas permeabilities as given in Eqn. 3.13.

$$S_{mem}^{mix} = P_i^{mix} / P_j^{mix} \tag{3.13}$$

3.5 Assumptions

Molecular simulations use intrinsic assumptions to provide a cost-effective way of representing real world physics and dynamics. In our molecular simulations, we implemented a generic force field, UFF), to capture the intermolecular interaction dynamics between adsorbates and MOF atoms.[103] This force field has been parametrized to represent the overall interaction dynamics between each set of atoms in the periodic table. UFF provides a good approximation for metals present in most of the MOFs such as Cu, Zn, Ni and Zr however, more specialized force fields such as UFF4MOF have been proposed for MOFs with complex geometries and MOFs with transition metals such as Cd, Ru and Zr.[129] Additionally, MOFs with open metal sites can have enhanced interactions with adsorbates where this behavior can be captured with specialized force fields and/or DFT based approaches.[130] Since our approach embedded a high-throughput computational screening method, special interactions were generalized with adopting UFF. Also, a good agreement between simulation and experimental isotherm data on commonly studied MOFs has been shown when UFF is

employed, validating the strength of these force fields in reproducing the valid electrostatic environment.[131] We were able to use the generic UFF in our simulations since we were able to reproduce experimental CO_2, H_2 and N_2 isotherms with our simulations over the range of pressure and temperatures of our process conditions at 0.1-10 bar and 298 K.

MOFs can have a wide range of structural imperfections such as linker defects, metal defects, intra-crystalline defects, collapsed pores in the microstructure regime, and impartial residual solvent retention which may lead to altered gas adsorption and diffusion dynamics.[132] MOFs are known to possess some degree of flexibility which can alter their gas adsorption performance.[133] Stimuli responsive MOFs can have significant flexibility which can be induced by temperature, pressure, or by an adsorbent guest. [134-138] Modeling flexible MOFs requires a flexible force field with additional stretching, bending, torsional potential terms together with the intermolecular interactions.[100] These force fields have poor transferability, thus in high-throughput computational screening studies, rigid framework assumption is made. In our simulations, we made a perfect crystal assumption with no defects and structural imperfections, which may lead to overestimation of MOF adsorption and diffusion performances. We retrieved the crystal structures of MOFs from the CSD database, and a major assumption is the structure proposed by the crystal scientist that deposited the CIF file to the CSD database curated a well-defined representation of the MOF. CSD database goes through a rigorous set of manual and automatic controls, yet some MOFs might still not be good representations of the proposed MOF structures.[13]

Chapter 4*

CO_2 SEPARATION FROM CO_2/H_2 MIXTURE

MOFs are promising candidates for separation of CO_2/H_2 mixture. Out of thousands of MOFs that have been synthesized so far, only few MOFs have been experimentally tested for CO_2/H_2 separation and it is essential to identify top performing MOF candidates with computational screening techniques. Therefore, to identify the adsorbent and membrane separation performance of MOFs for CO_2/H_2, high-throughput computational screening was performed by using Grand Canonical Monte Carlo (GCMC) and Molecular Dynamics (MD) simulation methods. The adsorbent performance evaluation metrics such as selectivity, working capacity, regenerability and adsorbent performance scores of 3857 MOFs were calculated. Performances of MOFs based on the simulation results were compared with the performances of commonly known materials such as zeolites to benchmark the potential of new MOFs identified in this study. Molecular dynamics simulations showed that MOFs, when considered as membranes, are highly permeable to H_2 and MOFs were even shown to surpass the upper bound limits established for polymers. Finally, the structure-performance relationships for 3857 MOFs were analyzed to serve as a map for further experimental and computational studies to identify MOFs with exceptional gas storage and membrane performances.

*The content of this chapter is taken from the published work (*Avci G., Velioglu S., and Keskin S. High-Throughput Screening of MOF Adsorbents and Membranes for H_2 purification and CO_2 capture. ACS Applied Materials & Interfaces*, 2018, *10(39), 33693–33706*: doi.org/10.1021/acsami.8b12746) and adapted for this thesis.[89]

4.1 Methodology

The most up to date MOF dataset that was integrated within the CSD at the time of this work was used in this part.[17] We used the python code as described in the literature and ended up with 54808 MOFs cleaned from their solvents.[17] The structural properties of MOFs including pore limiting diameter (PLD), largest cavity diameter (LCD), porosity (ϕ), and gravimetric surface area (SA) were calculated using Zeo++ software version 0.2.2.[21] SA was calculated by implementing a Monte Carlo probing technique where a nitrogen-sized (3.7 Å) probe molecule was allowed to be inserted inside the framework and the percentage of accepted moves was normalized to the cell volume. MOFs that failed to have any accessible gravimetric SA were eliminated and MOFs with PLD > 3.30 Å, which had kinetic diameters greater than both CO_2 and H_2 gas molecules were shortlisted for further evaluation, since both CO_2 and H_2 can travel freely within the pores of these MOFs. We then assigned Qeq charges to the MOFs to take Coulombic interactions into account, which was considered with Ewald summation, and eliminated 21 MOFs which did not have convergence in their point charges.[139] Overall, we ended up with 3857 different MOF structures.

Grand Canonical Monte Carlo (GCMC)[93] simulations are frequently used to compute binary adsorption isotherms of CO_2/H_2 mixtures in MOFs. UFF force field[103] was used to represent electrostatic interactions between MOF atoms and gas molecules and Lorentz-Berthelot mixing rules were obeyed to account for pairwise interactions. We selected this force field as it has been shown to give excellent agreement with the available experimental uptake data for CO_2 and H_2 for MOFs with different structures.[140, 141] Gas-gas and gas-MOF interactions were defined with the Lennard-Jones (LJ) potential. A three-site rigid molecule defined with LJ 12-6 potential was implemented to model CO_2 and partial charges which represent the molecule were distributed to the center of each side.[142] A single-site spherical LJ 12-6 potential was used to identify H_2.[102] CO was modeled with a single-site spherical LJ 12-6 potential,[143] and H_2O was modelled with the TIP4P representation.[144]

Gas adsorption was calculated at infinitely small pressure ranges, Henry's constant (K^0) of CO_2 and H_2 molecules were calculated at zero-pressure regime using 10^5 moves of Widom's particle insertion. Isosteric heat of adsorption values (ΔQ_{st}^0) were retrieved from Widom's particle insertion simulations. To account for GCMC simulations for different pressure regimes, we performed simulations for CO_2/H_2:15/85 mixture at 298 K

and 0.1, 1, and 10 bar. Four types of moves were implemented to simulate physical characteristics of gas molecules, reinsertion, swap, identity change and translation for H_2 molecule, and an additional rotation move was implemented to express the rotational freedom for CO_2 molecules. Peng-Robinson equation of state was used to calculate the corresponding pressure values at each resultant fugacity values retrieved from simulations. We set a truncation value of 13 Å to consider the periodic boundary conditions for each MOF simulation box, which was ensured to have at least 26 Å length at each dimension. For each 3857 MOFs, we carried out GCMC simulations with the set of conditions described above and ensured correct equilibration by setting 10000 simulation cycles where the first 5000 cycles were conducted to allow gas molecules reach favorable states, and the last 5000 cycles were separated for ensemble average calculations.

To set up a sensible computational experiment, we defined the pressure and temperature conditions based on industrial conditions commonly reported in the literature.[145] To simulate the PSA and VSA processes, adsorption and desorption pressures were taken as 10 (1) and 1 (0.1) bar accordingly at 298 K. Selectivity gives a measure to gauge the relative interaction strength of the strongly adsorbed gas (CO_2) to the weakly adsorbed one (H_2). High working capacity is desired for lower energy cost through less frequent regeneration cycles and smaller system volume.[146] We used the feed-gas composition for both the adsorption and desorption conditions following the literature.[115, 147, 148] From the difference in amount of CO_2 adsorbed in adsorption and desorption conditions, working capacity was calculated. Adsorbent performance score is the multiplication of selectivity and working capacity giving a composite metric. Regenerability shows how much CO_2 can be retrieved in each adsorbent bed cycle.

Single component self-diffusivities (D^0) of CO_2 and H_2 were calculated by switching off gas-gas intermolecular interactions in a simulation box with 30 gas molecules and the framework. A high accuracy was ensured by setting 10^6 cycles in the NVT ensemble using a time step of 1 fs for MD simulations. An average of diffusion slopes was taken for each dimension to calculate self-diffusion coefficients for each gas. Molecule per unit cell information was used to simulate mixture MD simulations at 1 bar and 298 K. All gas pair and gas-MOF interactions were considered to simulate the pressure conditions. The calculation details of adsorbent and membrane performance metrics are shown in **Table 4.1.**

Table 4.1. Performance metrics for MOF adsorbents and MOF membranes.

Metrics	Formula
Adsorption selectivity	$S^0_{ads,\ CO_2/H_2}=\frac{K^0_{CO_2}}{K^0_{H_2}}$
Mixture adsorption selectivity	$S^{mix}_{ads,\ CO_2/H_2}=\frac{N_{CO_2}}{N_{H_2}}/\frac{y_{CO_2}}{y_{H_2}}$
Working capacity	$\Delta N_i=N_{ads,\ i}-N_{des,\ i}$
Adsorbent performance score	$APS=S^{mix}_{ads,\ CO_2/H_2}\times\Delta N_{CO_2}$
Percent regenerability	$R\%=\frac{\Delta N_{CO_2}}{N_{ads,\ CO_2}}\times 100\%$
Diffusion selectivity	$S^0_{diff,\ H_2/CO_2}=\frac{D^0_{H_2}}{D^0_{CO_2}}$
Separation potential	$\Delta Q=Q_A\frac{\gamma_B}{1-\gamma_B}-Q_B$
Mixture diffusion selectivity	$S^{mix}_{diff,\ H_2/CO_2}=\frac{D^{mix}_{H_2}}{D^{mix}_{CO_2}}$
Membrane selectivity	$S^0_{mem,\ H_2/CO_2}=S^0_{ads,\ H_2/CO_2}\times S^0_{diff,\ H_2/CO_2}$
Mixture membrane selectivity	$S^{mix}_{mem,\ H_2/CO_2}=S^{mix}_{ads,\ H_2/CO_2}\times S^{mix}_{diff,\ H_2/CO_2}$
Permeability at infinite dilution	$P^0_i=K^0_i\times D^0_i$
Mixture permeability	$P^{mix}_i=\frac{N^{mix}_i\times D^{mix}_i}{f_i}$

N_{ads} : gas uptake in the mixture at 10 bar for PSA, 1 bar for VSA, 1 bar 298 K for TSA (mol/kg)
N_{des} : gas uptake in the mixture at 1 bar for PSA, 0.1 bar for VSA and 1 bar 473 K for TSA (mol/kg)
Q_i: volumetric uptake capacity of MOFs (mol/L)
γ_B: mole fraction of weakly adsorbing gas species in the feed mixture
i : gas species, CO_2 or H_2
j : gas species, CO_2 or H_2 for binary mixture, total composition of CO_2, CO, CH_4 and H_2O for quinary mixture
K^0: Henry's constant at infinite dilution (mol/kg/Pa)
D^0: self-diffusivity at infinite dilution (cm^2/s)
D^{mix}: self-diffusivity of gas species in the mixture (cm^2/s)
y: composition of the gas species in the bulk phase
f: partial pressure of gas species in the mixture (Pa)
1 Barrer = 3.348×10^{-16} mol×m/(m^2×s×Pa)

4.2 Results and Discussion

We validated the accuracy of our GCMC simulations and MD simulations to predict the CO_2 and H_2 uptake, the CO_2/H_2 selectivity and H_2/CO_2 permeability of CO_2 and H_2 in various MOFs such as NU-111, MOF-177, PCN-66, VEXTUO, Cu-BTC and MOF-5 by comparing the results we obtained from molecular simulations to that of experimental and computational data that were measured and calculated by different research groups.[55, 149-152] Experimental and computational CO_2 and H_2 isotherms are compared in **Figure 4.1**.

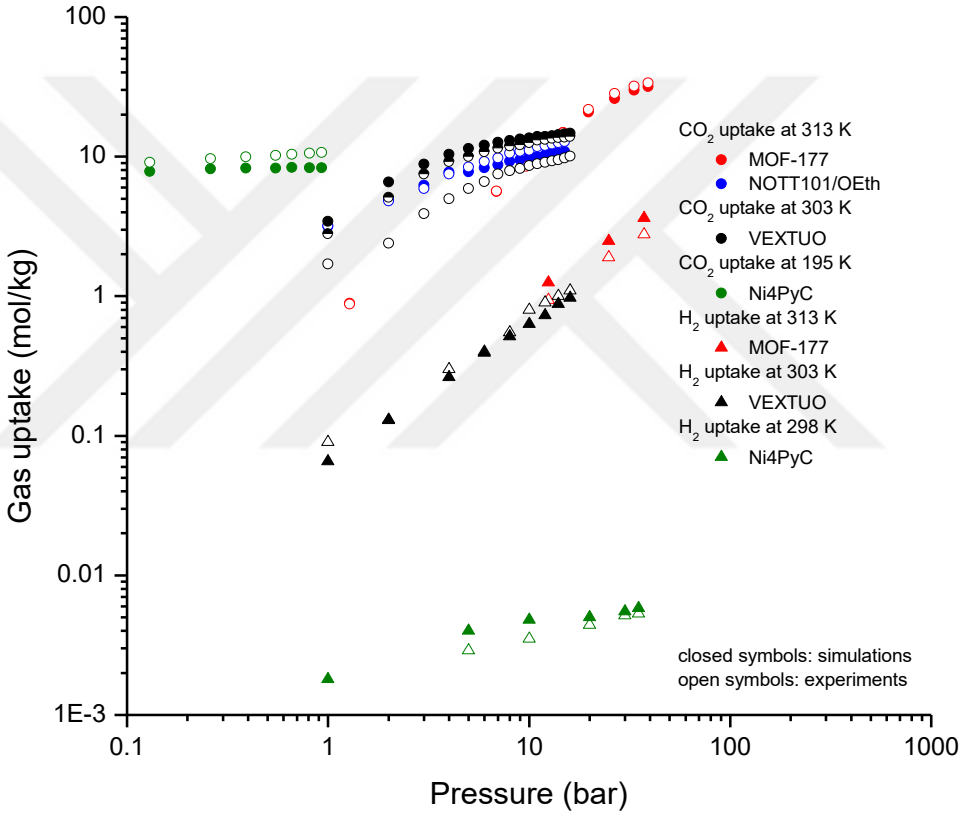

Figure 4.1. Comparison of adsorption isotherms of CO_2 and H_2 in commonly known MOFs. The closed symbols represent our simulations results, open symbols are the experimental data and the semi-closed symbol for VEXTUO represents the simulation data available for this MOF in the literature.[153]

We have validated the accuracy of our computational methodology to predict the adsorbent and membrane performances of MOFs for CO_2/H_2 mixture by conducting GCMC and MD simulations. Both the adsorption selectivity and permeability predictions through computational simulations showed an excellent agreement with experimental studies as shown by **Figure 4.2**. The details of experimental and computational conditions

for adsorption validation results are shown in **Table A.2** and membrane validation results are shown in **Table A.3** in **Appendix A**. Overall, we were able to show that through a wide range of temperature (298-313 K) and pressure (1-35 bar) our simulations were able to capture adsorption and membrane characteristics of a wide variety of MOFs.

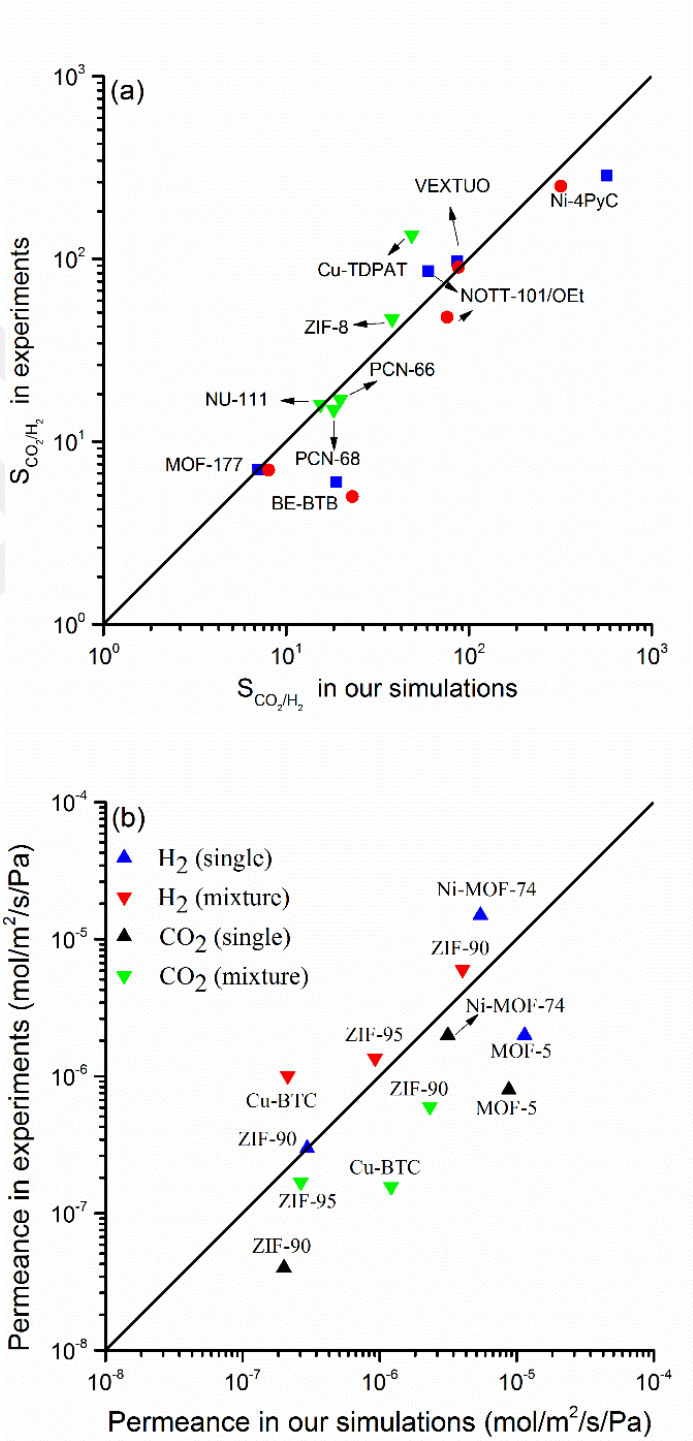

Figure 4.2. Comparison of experimental and simulated (a) adsorption selectivities of various MOFs and (b) gas permeances of MOF membranes. Details of the experimental data is given in **Appendix A3** and **Appendix A4**.

Motivated by the excellent agreements in our validation results, we continued our high-throughput simulations for 3857 MOFs and investigated their adsorption-based and membrane-based CO_2/H_2 separation performances. **Figure 4.3** shows the calculated CO_2/H_2 selectivity and CO_2 working capacity of MOFs at PSA and VSA conditions. For MOF adsorbents, both a high adsorption selectivity and working capacity are desired, such that the performance can be easily expressed by their multiplication which is shown by the adsorbent performance score (APS). The blue APS=400 mol/kg line and the red APS=2000 mol/kg line were drawn to aid the eye to distinguish promising MOFs from the rest of the screened MOFs. CO_2/H_2 selectivity of MOFs at PSA (VSA) condition were in a range of 2.43-24490 (2.47-84356), and CO_2 working capacities at PSA (VSA) were between 0.001 and 11.28 (0.008 and 4.60) mol/kg.

Although, an ideal adsorbent has both high working capacity and selectivity, this is not the case for most of the MOFs. For the materials with APS>2000 mol/kg, MOFs at PSA condition have a high working capacity but overall mediocre adsorption selectivities whereas at VSA condition have mediocre working capacity which is complemented with a high adsorption selectivity as shown in **Figure 4.3**. MOFs at VSA condition had a better combination of both adsorption selectivity and working capacity, which resulted in more MOFs marked as potentially promising compared to PSA condition. We calculated the CO_2/H_2 selectivity of these most promising MOFs as 280-20357 (798-84350), and CO_2 working capacities were in the range between 0.29-11.28 (0.028-4.60) mol/kg at PSA (VSA) condition as shown in **Figure 4.3(a)** (**Figure 4.3(b)**). From these results, we observed MOF adsorbents at PSA condition had slightly higher working capacities while these MOFs had similar adsorption selectivities compared to VSA condition. This is due to loading of greater number of gas molecules to each MOF at the pressure of 10 bar. Overall, MOFs can have exceptionally high APS both at PSA and VSA conditions.

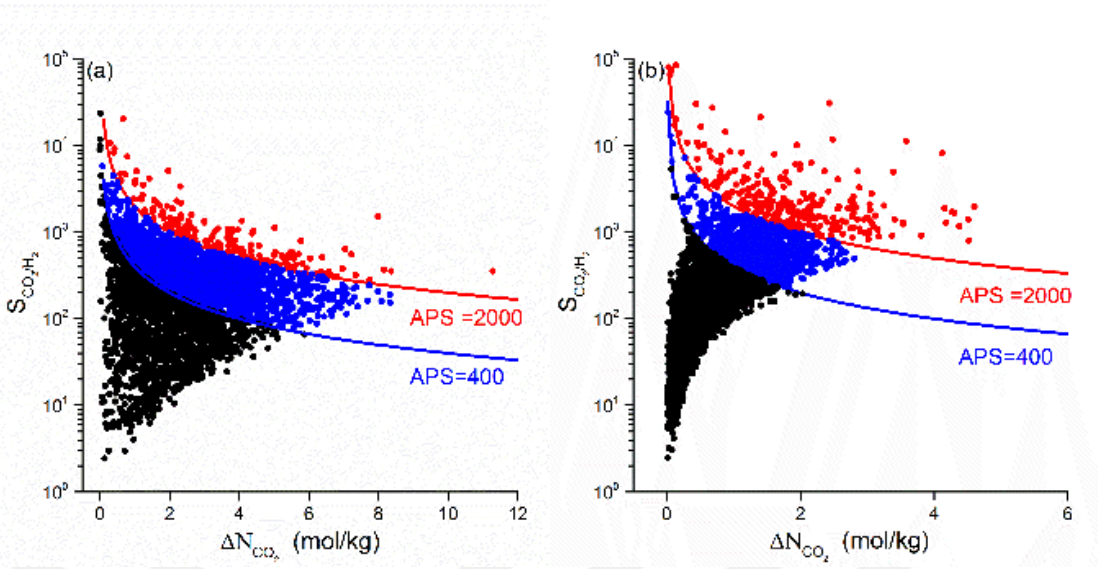

Figure 4.3. Relation between adsorption selectivity, working capacity and APS of MOFs for CO_2/H_2:15/85 mixture at (a) PSA and (b) VSA conditions. Black, blue, and red points represent MOFs with APS<400, 400<APS<2000, APS>2000, respectively.

It is reasonable to compare the performances of MOFs with that of traditional adsorbents such as zeolites. Fang et al.[154] examined the CO_2 working capacity of cationic zeolites for PSA and VSA processes and found that the highest CO_2 working capacities of the ten-membered ring (10MR) zeolites were reported as 1.95 and 2.03 mol/kg for PSA and VSA processes, respectively. When MOFs and zeolites are compared, 2137 and 166 MOFs outperform 10MR zeolites at PSA and VSA conditions. 11 MOFs exceed the performance of cationic zeolites with large pore volumes at PSA conditions whereas zeolites outperform MOFs if MOFs have large pore volumes at VSA conditions. Krishna[155] performed molecular simulations for many zeolites including NaY, CHA, FAU, LTA and reported that NaX and NaY are the most CO_2/H_2 selective materials with selectivities of 1510 and 550, respectively at 10 bar, 300 K for a CO_2/H_2:15/85 mixture. NaX and NaY zeolites have lower selectivities and lower APSs (~29.6 and ~27.1 mol/kg) compared to MOFs under PSA conditions. Both experimental studies for CO_2 uptakes of NaX (4.5 mol/kg) and NaY (3.9 mol/kg)[141, 156, 157] and simulations (~5.3 for NaX and ~4.8 mol/kg for NaY)[155] showed that these zeolites also have lower CO_2 uptakes than MOFs. Chung et al.[158] evaluated CO_2 working capacity, CO_2/H_2 adsorption selectivity and APS for 730 hypothetical MOFs (hMOFs). We identified 193 MOFs with CO_2/H_2 adsorption selectivities >1000 at 10 bar but there were only 6 hMOFs with selectivities >1000 and among them the highest selectivity was 2600. We found that 176 MOFs have APS>2000 mol/kg as illustrated in **Figure 4.3(a)** whereas

no hMOF was reported to have APS>1200 mol/kg. Overall, these comparisons showed that MOFs are either comparable or even better than the zeolites in adsorption-based CO_2/H_2 separations and they perform much better than hMOFs. It is worthy to note that higher performance of some hMOFs do not guarantee their synthesizability but give a promising outlook to the future of MOFs as adsorbents.

To identify the most promising MOFs, it is essential to investigate the adsorbent performance through multiple physically important metrics. We investigated the relation between R% and APS of MOFs in PSA and VSA conditions in **Figure 4.4**. Top 10 MOFs at PSA and VSA conditions are marked as red. The dashed line in **Figure 4.4**. shows the desired R% value (>85%) for MOFs, and MOFs with high APS and good regenerability values are considered as promising.[159] Although there are significant number of MOFs that have high APS values, only 1060 (2625) MOFs have R%>85% at PSA (VSA) conditions. Interestingly, the number of MOFs with low R% is much higher at PSA condition when compared to VSA condition. MOFs with low R% usually have very strong affinity towards CO_2, which results in overexpression of adsorption selectivity when compared to working capacity at APS calculation. Overall, it is important to include R% value to identify the most promising MOF adsorbents for CO_2/H_2 separation.

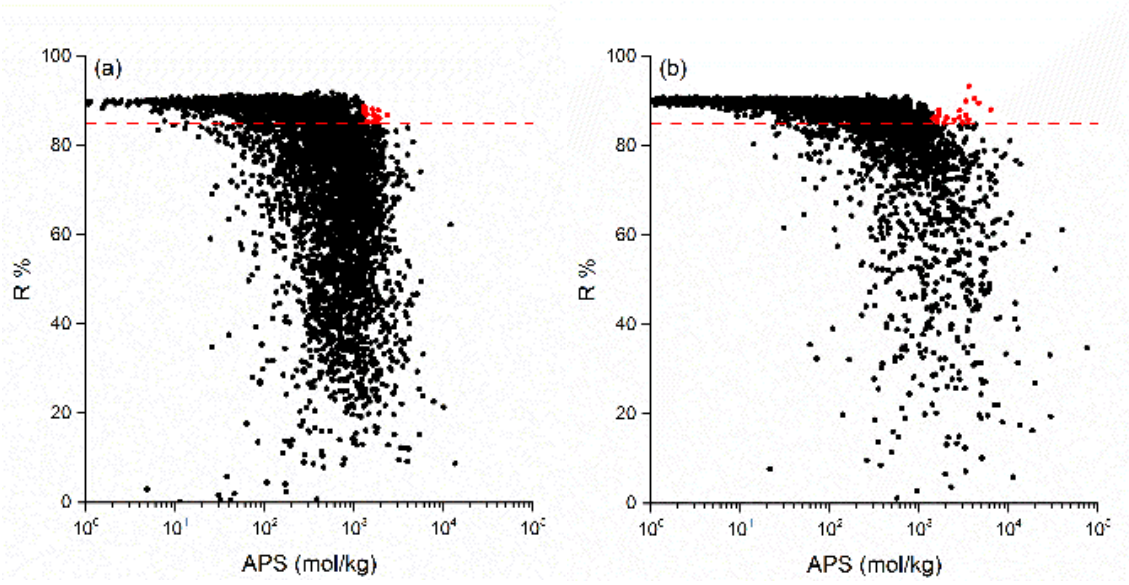

Figure 4.4. R% and APS of MOFs computed for CO_2/H_2:15/85 mixture for (a) PSA and (b) VSA conditions. The red dotted line shows the minimum desired R%=85%. The red data points represent the top MOF adsorbents with the highest APSs and R%>85%.

In high-throughput computational studies, it is important to investigate the top materials that were identified by adsorbent performance evaluation metrics. Therefore, we investigated the adsorbent performance metrics and physical properties of top 20 MOFs for the PSA and VSA processes as shown in **Table 4.2**. We identified DABWUA as the best adsorbent for PSA process, which had a CO_2/H_2 selectivity of 322 and R% of 87% at 10 bar and 298 K. DABWUA had narrow pores and an interconnected mesh of linkers which resulted in a narrow pore geometry with a PLD of 3.84 Å and LCD of 6.33 Å, therefore showed a high gas adsorption performance. Lässig et al.[160] experimentally reported CO_2 and H_2 uptakes of DABWUA, the top material of the PSA process, as 9.2 and 15.2 mol/kg at 273 and 77 K, respectively, at 1 bar. We carried out GCMC simulations at the same conditions and our results had very good agreement with experimental data, 9.7 and 17.4 mol/kg of CO_2 and H_2 uptakes, respectively. Although QUQQUP was 16th in terms of APS ranking among top 20 MOFs for PSA condition, it had the highest SA with 4342 m^2/g. This is due to four-connected structure of QUQQUP and co-presence of small and large pores enhancing the CO_2 adsorption. Identification of MOFs with high SA is especially important since experimentally synthesized MOFs can have significantly reduced surface area values, therefore hindering gas adsorption performance as discussed in the assumptions section of this thesis.

We identified DATKIU as the best adsorbent for VSA condition which has a selectivity of 1405 and R% of 88% at 1 bar and 298 K as shown in **Table 4.1**. DATKIU had a remarkable selectivity which can be explained by the presence of BF^{4-} extra framework ions present in the framework which significantly enhanced the CO_2 adsorption. Rest of the top MOFs for VSA condition was examined and 13 out of 20 MOFs had extra framework ions incorporated to the MOF structure, thus MOFs with extra framework ions have a higher chance of being identified as potentially promising for VSA condition. Experimental gas adsorption data was also available for one of the top MOFs of the VSA process, YAZFOW.[161] The CO_2 uptake of YAZFOW was experimentally reported as 6.3 mol/kg at 1 bar and 273 K, whereas we calculated its CO_2 adsorption as 7.5 mol/kg using GCMC simulations under the same pressure and temperature. YAZFOW is one of the seven top MOFs of VSA process without extra framework ions therefore we were able to get a good agreement between experimental data and our simulation results. Overall, we were able identify promising MOFs for CO_2 capture and validate our molecular simulation accuracy for the top MOFs.

Table 4.2. Separation performances of the top 20 MOFs (having the highest APSs and R%>85%) for PSA and VSA processes.

MOFs	APS (mol/kg)	$S^{mix}_{ads,\ CO_2/H_2}$	R%	LCD (Å)	PLD (Å)	ϕ	SA (m^2/g)
Pressure Swing Adsorption (PSA)							
DABWUA	2364.66	322.31	86.76	6.33	3.84	0.64	1367.86
HOWRES	1931.12	299.70	85.98	5.94	5.11	0.63	1511.89
ENATUJ	1872.19	241.81	87.88	5.92	5.35	0.69	2625.32
HUFHUN	1818.42	484.51	85.32	10.40	8.17	0.54	742.06
IJEFUZ	1797.25	287.58	86.42	6.27	5.40	0.65	2095.14
CECJAW	1737.22	292.02	86.12	5.62	4.51	0.65	2173.37
VARJEF	1715.09	233.07	86.43	7.50	4.27	0.63	2105.15
TUBTOB	1646.22	206.05	86.83	5.78	4.11	0.65	2672.89
AQEKUD	1614.35	221.62	88.07	4.87	4.21	0.70	2724.6
NULHEJ	1608.33	356.56	85.19	7.18	5.90	0.54	874.847
HASSUR	1393.04	250.94	85.24	7.03	5.33	0.63	1847.89
FOJWOS	1370.69	193.03	87.04	8.40	5.00	0.65	2302.56
LONVIV	1323.25	235.23	88.41	10.8	9.68	0.62	1042.60
UWOWEJ	1310.74	188.27	87.93	6.45	5.23	0.67	2998.37
XUNGIX	1299.81	177.96	88.31	8.23	4.89	0.66	3065.15
QUQQUP	1299.14	160.68	88.61	5.16	4.78	0.69	4342.4
CAXTEC	1298.04	215.68	87.73	10.87	5.27	0.63	1874.49
LEYGIH	1293.71	219.00	87.29	5.67	4.14	0.64	2102.15
HAFVUH	1293.23	219.80	88.60	7.25	7.14	0.60	1539.15
COQTEJ	1288.85	154.71	87.49	7.76	6.26	0.70	3263.67
Vacuum Swing Adsorption (VSA)							
DATKIU	6339.10	1404.82	88.05	5.74	4.50	0.64	2149.07
NIDBOS	4635.11	2060.24	89.50	5.46	5.27	0.48	539.12
HISJIE	4196.19	2401.78	90.47	6.28	5.58	0.43	361.15
EGELUY	3605.94	798.31	93.30	7.19	6.77	0.63	1554.21
AFEJOK	3569.22	1154.36	85.78	5.98	5.12	0.58	1257.63
GUKYUI	3353.50	1654.38	89.97	5.99	5.23	0.49	543.66
RAVNAE	3337.80	1650.24	86.83	4.58	4.25	0.53	376.57
PEJMOH	3055.10	1111.24	85.17	4.78	4.06	0.53	842.18
YAZFOW	2843.27	896.47	87.87	7.44	7.30	0.61	1108.06
RIGVOU	2834.71	2096.43	86.32	5.38	5.16	0.40	296.13
WOBQEL	2487.58	824.07	85.76	6.08	5.37	0.55	1053.12
UBIPAY	2044.71	923.13	86.27	4.39	3.96	0.49	651.70
BUHJUL	1922.78	790.80	85.18	5.38	4.57	0.51	880.20
OTAQUW	1670.33	969.23	87.02	5.80	4.62	0.52	886.78
CUSDIE	1646.45	629.68	88.00	13.09	5.58	0.67	1576.51
AMOYOR	1622.25	1003.13	86.63	4.84	4.51	0.47	470.55
YEVPIZ	1617.61	747.94	85.25	4.51	3.84	0.55	741.98
YARFII02	1526.45	756.33	86.45	5.48	4.20	0.52	809.62
EBIDAW	1456.33	693.99	85.94	5.45	4.04	0.54	830.57
TIXVON	1441.87	557.29	86.18	5.07	3.92	0.58	1034.39

At pre-combustion CO_2/H_2 separation conditions the gas stream might have trace amounts of water. Due to the polar structure of water molecules and potential hydrogen bonding configurations, trace amounts of water molecules can significantly alter adsorption dynamics thus adsorption selectivities of MOFs.[162, 163] This trace amount of water molecules usually compete with CO_2 for the most favorable adsorption sites and up to 0.1 wt% H_2O concentration has been shown to decrease CO_2/H_2 selectivity in a rht-MOF.[164] We considered the $CO_2/H_2/CO/CH_4/H_2O$:15/75/5/5/0.1 mixture at 10 bar to simulate a realistic condition with water vapor and investigated the performance of the top MOF of PSA process, DABWUA, and the top MOF of VSA process, DATKIU. CO_2 uptake and CO_2/H_2 selectivity were lower at binary condition at 8.45 mol/kg and 322 when compared to the water vapor condition which was computed as 6.28 mol/kg and 200, respectively. DATKIU was even more significantly influenced by the presence of water vapor with the selectivity decreasing from 1404 to 293 and working capacity decreasing from 5.12 mol/kg to 0.48 mol/kg. Due to the favorable adsorption sites of extra framework ions in DATKIU, water molecules were able to capture most of the adsorption sites therefore reducing overall CO_2 adsorption and its selectivity. Overall, these results showed that it is important to check whether a MOF has extra framework ions or any highly polar surface that can enhance coulombic interactions before simulating for CO_2/H_2 mixture with water molecules.

It is crucial to identify the common MOFs for different processes such as PSA and VSA which shows whether a MOF can be used for both processes simultaneously and/or interchangeably. Interestingly, there were no common promising MOFs for PSA and VSA processes, so we investigated how well the MOF rankings correlated with each other by computing Spearman's ranking correlation coefficient (SRCC) as shown in **Table 4.3**. SRCC measures how well the ranking in two distinct lists compare with each other by assigning a score between -1 and 1, where the score converges to 1 through existence of a unity in rankings whereas the score converges to -1 if no correlation exists. In **Table 4.3**, SRCC scores calculated for 3857 MOFs for PSA and VSA processes are shown in terms of selectivity, working capacity, APS and R%. SRCC scores are higher than 0.8 for all metrics except for R%, which shows that MOFs with high adsorbent performance metrics share common MOFs for PSA and VSA processes in terms of selectivity, working capacity and APS values. This result shows that all adsorbent performance metrics should be considered when most promising MOFs are identified, since as shown in previous

sections, promising MOFs at VSA condition with high R% have different structural characteristics entrenched within them such as presence of extra framework ions, whereas extra framework ions were absent in top MOFs at PSA condition as a main source for the low SRCC value for R%. High-throughput computational screening studies are usually performed at infinite dilution conditions to save computational energy and cost.[165] Our results showed that it is better to compare the adsorption performances of MOFs depending on their adsorption conditions as implied by the SRCC values. Overall, our screening approach was able to identify the top promising MOFs for both PSA and VSA processes.

Table 4.3. SRCC values for the MOF rankings of PSA and VSA processes.

Metrics used to rank MOFs	**SRCC**	**# of common MOFs in top 20 lists**
$S^{mix}_{ads,\,H_2/CO_2}$ (0.1 bar)	0.81	4
$S^{mix}_{ads,\,H_2/CO_2}$ (1 bar)	0.83	4
$S^{mix}_{ads,\,H_2/CO_2}$ (10 bar)	0.84	6
APS (mol/kg)	0.97	13
R%	0.50	1
ΔN_{CO_2}(mol/kg)	0.93	19
ΔN_{H_2}(mol/kg)	0.97	9

MOFs can be potentially promising materials as H_2 selective membranes due to their high surface areas and high porosity values. From a process-based perspective, H_2 selective membranes are more favorable since H_2 can travel faster than CO_2 in a syngas stream due to the smaller kinetic diameter of H_2 (2.96 Å) compared to the spherical kinetic diameter of CO_2 (3.3 Å). In **Figure 4.5**, we analyzed the adsorption, diffusion, and membrane selectivity of MOFs at infinite dilution conditions for H_2/CO_2 separation. In terms of adsorption, all 3857 MOFs are CO_2 selective since strong Coulombic interactions between framework and CO_2 molecules overcome the adsorption affinity of H_2 molecules with the framework. In terms of diffusion, all MOFs are H_2 selective due to the lower molecular weight of H_2 compared to CO_2. Diffusion selectivity of MOFs are color coded in **Figure 4.5**, where MOFs with low H_2/CO_2 diffusion selectivity are color coded with orange, MOFs with mediocre diffusion selectivity are color coded with green and MOFs with high diffusion selectivity are color coded with blue, respectively. Membrane

selectivity is the product of adsorption selectivity and diffusion selectivity of MOFs, therefore higher diffusion selectivity and lower adsorption selectivity values are favorable for a H_2 selective MOF membrane. 209 out of 3857 MOFs were H_2 selective, and as shown in **Figure 4.5**, only four MOFs that are H_2 selective are color coded with blue, whereas the vast majority of H_2 selective MOFs are color coded as orange, indicating H_2 selective MOFs have a combination of mediocre diffusion selectivity between 10^{-2} and 10^{-1} and low adsorption selectivity between 1-100, respectively. It should be noted that these 209 H_2 selective MOFs were selected at infinite dilution conditions and diffusion dynamics can change at finite pressures, which will be discussed in the upcoming section.

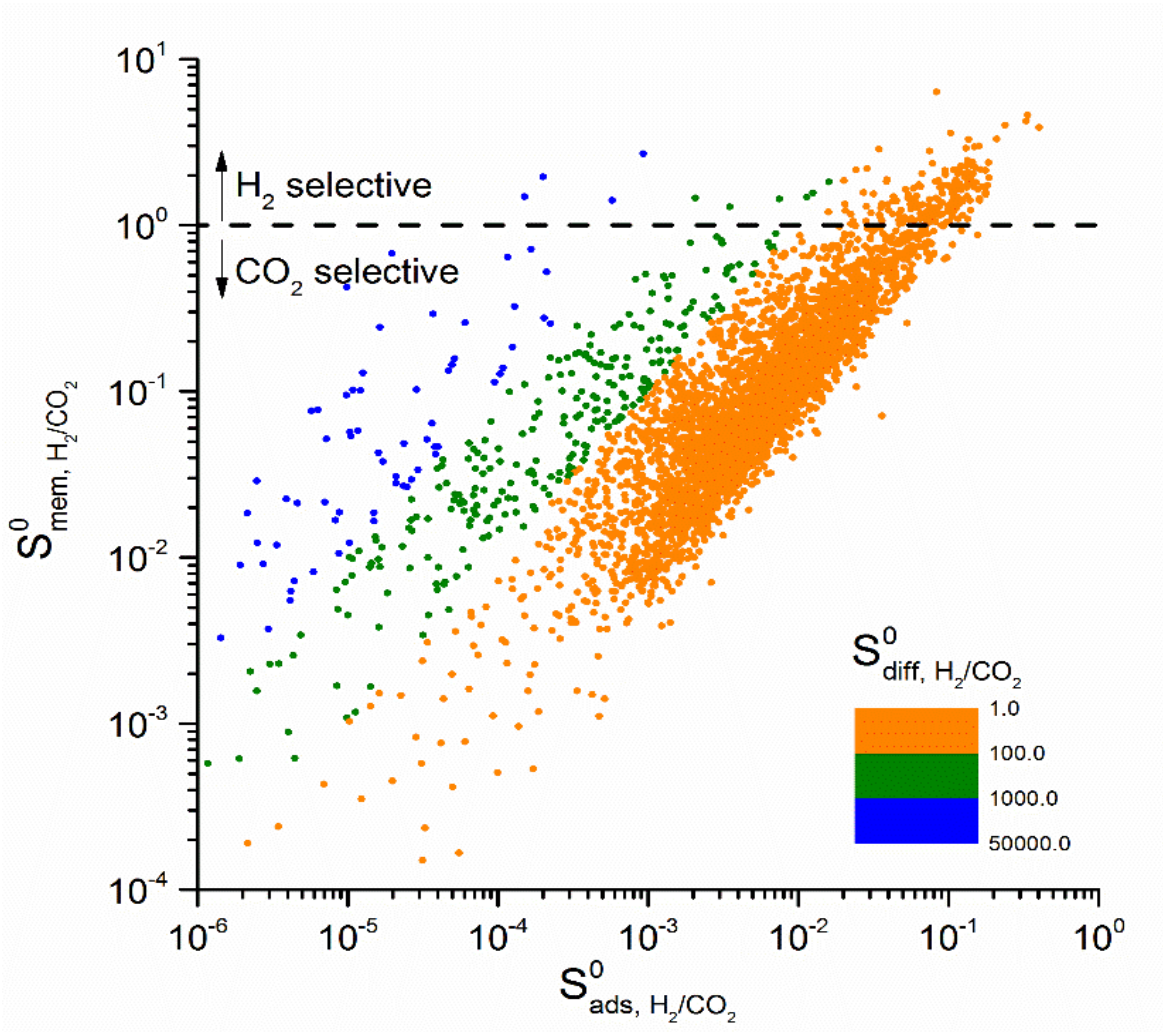

Figure 4.5. Comparison for adsorption, diffusion, and membrane selectivities computed at infinite dilution and 298 K.

Highly selective membranes with high permeability are desired for efficient MOF membranes. Motivated from the high diffusion selectivities that can be observed in MOFs, we showed the relationship between H_2 permeability and H_2/CO_2 selectivity of MOF membranes and marked the top MOF membranes in **Figure 4.6**. $S^0_{mem,\ H_2/CO_2}$ values were computed to be between 2.10×10^{-5} and 6.34 whereas $P^0_{H_2}$ values were calculated in the range of 229.33-1.67×10^6 Barrer. A significant number of MOFs (899) exceeds the upper bound which suggests that MOF membranes can replace traditional polymeric membranes in selective separation of H_2 from CO_2. A remarkable number of MOFs (1716) exhibits very high H_2 permeability, $P^0_{H_2}$ $>10^5$ Barrer, as shown by blue points in **Figure 4.6**. The solid line indicates the Robeson's upper bound, which was originally set to capture the trade-off between selectivity and permeability in polymers.[63] Since MOFs have unique structures with high surface areas and high porosities, they do not completely obey Robeson's upper bound as 899 out of 3857 MOFs were shown to surpass the upper bound. This is mainly due to diffusion selectivity of H_2 dominating the adsorption selectivity of CO_2 at infinite dilution condition. This phenomenon is strengthened for MOFs with porosity >0.8 and MOFs with large LCDs (>10 Å) since H_2 can travel more freely while the strong interaction between CO_2 molecules and the framework hinders the ability of CO_2 to freely travel in the large pores of these MOFs.

Two ZIF membranes acting as molecular sieves for H_2/CO_2 separation had high performances, but they were discarded from our MOF database due to their narrow pore sizes (<3.30 Å). H_2/CO_2 selectivities of these membranes were measured to be high, 8.4-13.6 for ZIF-7[60, 166] and 4.6-7.3 for ZIF-8,[167, 168] but their H_2 permeabilities were quite low, 6.7×10^2-3.4×10^3 Barrer for ZIF-7 and 2.8×10^3-2.2×10^4 Barrer for ZIF-8. This shows that sieving membranes suffer from poor permeabilities due to the lack of pore space in ZIF-7 and ZIF-8 and MOFs can purify H_2 without relying on molecular sieving mechanisms with poor gas transport properties as shown with ZIF membranes.

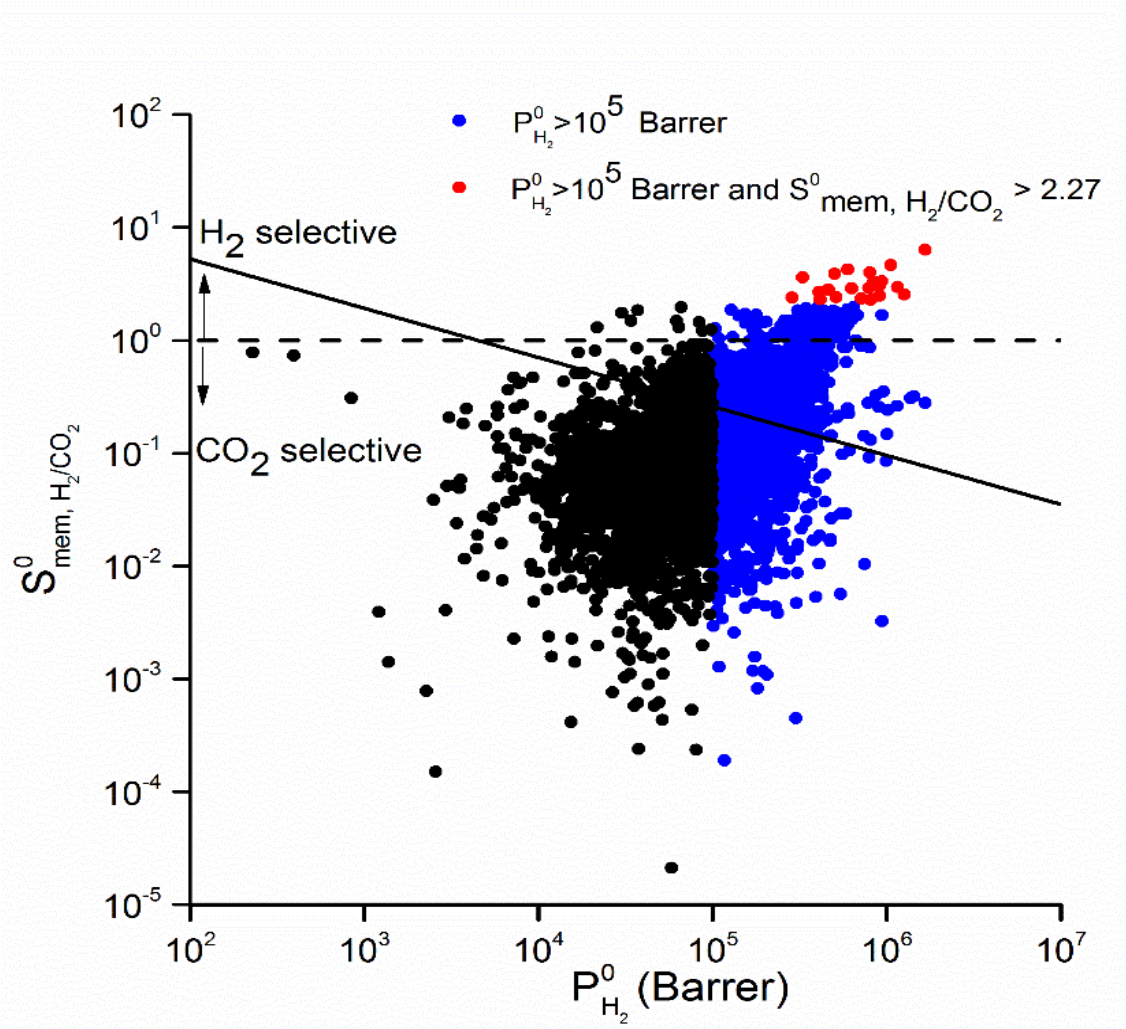

Figure 4.6. H_2/CO_2 selectivity and H_2 permeability of MOF membranes. Black dashed line indicates $S^0_{mem, H_2/CO_2}$=1. The black solid line represents the upper bound for H_2/CO_2 separation.

We ranked the MOF membranes having $P^0_{H_2}$>10^5 Barrer based on their H_2/CO_2 selectivity from the highest to the lowest and identified the top 20 MOFs based on this ranking and identified the structural properties in **Table 4.4**. The top 20 most promising MOF membranes offering H_2/CO_2 selectivity >2.27 and $P^0_{H_2}$ >10^5 Barrer were shown to have large pores and porosities well over 0.80, indicating that low densities and long free available travel distance for H_2 molecules substantially favored the diffusion of H_2 whereas CO_2 had lower diffusion coefficients due to strong electrostatic interactions with CO_2 and the MOF.

Table 4.4. Separation performances of the top 20 MOFs for membrane-based gas separation. This list consists of MOFs with $S^0_{mem,\ H_2/CO_2} > 2.27$ and $P^0_{H_2} > 10^5$ Barrer. MOFs are ranked based on $S^0_{mem,\ H_2/CO_2}$.

MOFs	LCD (Å)	PLD (Å)	ϕ	$D^0_{CO_2}$ (cm^2/s)	$D^0_{H_2}$ (cm^2/s)	$P^0_{CO_2}$ (Barrer)	$P^0_{H_2}$ (Barrer)	$S^0_{ads,\ CO_2/H_2}$	$S^0_{diff,\ H_2/CO_2}$	$S^0_{mem,\ H_2/CO_2}$
FOTNIN	33.63	28.54	0.91	1.78×10^{-4}	1.35×10^{-2}	2.63×10^{5}	1.67×10^{6}	12.00	76.05	6.34
XANLIJ	26.20	14.45	0.91	6.19×10^{-4}	8.44×10^{-3}	2.30×10^{5}	1.06×10^{6}	2.95	13.62	4.61
JULDAV	7.54	6.53	0.88	4.50×10^{-4}	5.74×10^{-3}	1.42×10^{5}	5.98×10^{5}	3.02	12.78	4.23
TURFIX	26.88	14.28	0.90	3.74×10^{-4}	6.24×10^{-3}	2.01×10^{5}	8.04×10^{5}	4.18	16.69	3.99
XIJNUA	16.10	15.60	0.82	5.38×10^{-4}	5.15×10^{-3}	1.30×10^{5}	5.03×10^{5}	2.47	9.58	3.88
WIDNEC	13.84	12.53	0.76	1.00×10^{-4}	3.46×10^{-3}	9.20×10^{4}	3.30×10^{5}	9.65	34.65	3.59
ECOKAJ	18.97	17.57	0.88	4.59×10^{-4}	7.25×10^{-3}	2.82×10^{5}	9.34×10^{5}	4.77	15.81	3.31
RUBYUK	16.11	12.67	0.87	2.77×10^{-4}	6.69×10^{-3}	2.57×10^{5}	8.47×10^{5}	7.33	24.10	3.29
HEXVEM	28.43	15.94	0.90	3.57×10^{-4}	6.68×10^{-3}	3.02×10^{5}	9.05×10^{5}	6.23	18.69	3.00
SAPBIW	28.19	23.24	0.88	4.65×10^{-4}	9.13×10^{-3}	3.92×10^{5}	1.16×10^{6}	6.65	19.63	2.95
RUTNOK	25.05	12.95	0.88	2.63×10^{-4}	5.81×10^{-3}	2.73×10^{5}	7.94×10^{5}	7.60	22.06	2.90
MOVPEU	16.16	14.92	0.77	7.10×10^{-5}	5.92×10^{-3}	2.19×10^{5}	6.30×10^{5}	28.95	83.23	2.87
BOGFIM	10.54	9.08	0.82	1.08×10^{-4}	4.03×10^{-3}	1.65×10^{5}	4.62×10^{5}	13.29	37.27	2.80
SOVGUF	7.99	7.06	0.79	8.36×10^{-4}	1.15×10^{-2}	5.00×10^{5}	1.26×10^{6}	5.44	13.75	2.53
RUBDUP	21.11	19.25	0.87	3.80×10^{-4}	6.94×10^{-3}	3.71×10^{5}	9.13×10^{5}	7.43	18.27	2.46
XANLEF	22.31	11.71	0.85	2.45×10^{-4}	4.03×10^{-3}	2.13×10^{5}	5.12×10^{5}	6.86	16.49	2.40
IZOWAW	18.36	8.13	0.76	2.29×10^{-4}	2.94×10^{-3}	1.21×10^{5}	2.87×10^{5}	5.39	12.80	2.38
TOVKOG	22.84	13.13	0.86	1.71×10^{-4}	5.11×10^{-3}	3.05×10^{5}	7.17×10^{5}	12.74	29.96	2.35
GESVAC	16.01	11.92	0.82	2.27×10^{-4}	3.64×10^{-3}	1.81×10^{5}	4.14×10^{5}	6.99	16.02	2.29
TOCJAY	24.08	19.56	0.85	3.42×10^{-4}	6.40×10^{-3}	3.56×10^{5}	8.08×10^{5}	8.23	18.69	2.27

MOFs can be promising candidates as CO_2/H_2 reverse selective membranes in syngas separation. Reverse selective membranes use the principle of purifying the main gas stream rather than purifying the retentate phase. The CO_2 permeability and CO_2/H_2 selectivity of top 20 reverse selective MOF membranes together with their physical properties are illustrated in **Table 4.5**. $S^0_{mem,\ CO_2/H_2}$ and $P^0_{CO_2}$ of these top MOFs were calculated to be in the range of 1.50×10^{-1}-4.25×10^{3} and 1.85×10^{4}-6.71×10^{8} Barrer, respectively. HESJOE was identified as the best reverse selective membrane with a high adsorption selectivity for CO_2 over H_2 since it had a combination of low porosity (0.51) together with a narrow pore limiting diameter of 3.99 Å and the largest pore diameter of 4.74 Å. The second reverse selective MOF membrane was identified as KAXQOR which can be explained with its high heat of adsorption for CO_2 due to the presence of a Ca-O network structure, which resulted in high CO_2 selectivity. MOFs are advantageous to be used as reverse selective membranes when compared to polymers since MOFs have strong and rigid framework structures and plasticization issues are not observed for MOFs in contrast to polymer membranes.[169] However, MOFs have been shown to lose stability in certain environments, so the long term stability controls must be performed.[170] The stability of MOFs can be calculated by DFT free energy calculations or long term experimental stability stress tests.[171] Among the top MOF membranes we identified, FOTNIN,[172] RUTNOK,[173] and TOVKOG[174] have common names of PCN-777, IRMOF-77, and PCN-285, respectively, in the literature. These MOFs were reported to be highly stable, encouraging further research on fabrication of membranes using these materials. Overall, MOFs are potentially promising candidates as reverse selective membranes.

Table 4.5. Separation performances of the top 20 reverse selective MOF membranes. This list consists of MOFs with $S^0_{mem,\ CO_2/H_2} > 600$ and $P^0_{CO_2} > 10^7$ Barrer. MOFs are ranked based on $S^0_{mem,\ CO_2/H_2}$.

MOFs	LCD (Å)	PLD (Å)	ϕ	$D^0_{CO_2}$ (cm^2/s)	$D^0_{H_2}$ (cm^2/s)	$P^0_{CO_2}$ (Barrer)	$P^0_{H_2}$ (Barrer)	$S^0_{ads,\ H_2/CO_2}$	$S^0_{diff,\ CO_2/H_2}$	$S^0_{mem,\ CO_2/H_2}$
HESJOE	4.74	3.99	0.51	1.91×10^{-4}	6.93×10^{-4}	2.77×10^{9}	5.85×10^{4}	5.81×10^{-6}	0.28	47429.63
KAXQOR	4.51	4.05	0.35	1.07×10^{-4}	7.70×10^{-4}	3.44×10^{8}	8.10×10^{4}	3.28×10^{-5}	0.14	4248.41
PEXSES	5.93	4.25	0.55	4.72×10^{-6}	3.29×10^{-4}	1.57×10^{8}	3.77×10^{4}	3.45×10^{-6}	0.01	4164.12
LOYMET	5.37	3.98	0.37	4.05×10^{-5}	3.37×10^{-4}	3.71×10^{7}	1.54×10^{4}	4.99×10^{-5}	0.12	2408.11
NADZID	5.01	4.70	0.48	7.74×10^{-5}	1.75×10^{-3}	6.72×10^{8}	3.03×10^{5}	1.99×10^{-5}	0.04	2219.82
LIFWON	5.03	3.91	0.51	3.14×10^{-4}	9.75×10^{-4}	1.43×10^{8}	7.61×10^{4}	1.72×10^{-4}	0.32	1876.65
KIPJUQ	7.29	6.98	0.46	2.12×10^{-6}	1.04×10^{-3}	8.08×10^{7}	4.64×10^{4}	1.17×10^{-6}	0.002	1740.74
NEWWAP	5.96	4.65	0.49	1.49×10^{-6}	4.81×10^{-4}	6.08×10^{7}	3.72×10^{4}	1.90×10^{-6}	0.003	1633.22
GUGNON	5.22	4.34	0.53	2.94×10^{-6}	4.06×10^{-4}	7.99×10^{7}	4.93×10^{4}	4.47×10^{-6}	0.007	1620.75
PEXROB	5.91	4.29	0.55	1.24×10^{-5}	2.27×10^{-4}	3.51×10^{7}	2.68×10^{4}	4.18×10^{-5}	0.05	1312.05
SAJFEO	6.63	6.00	0.60	2.00×10^{-5}	2.19×10^{-3}	1.90×10^{8}	2.06×10^{5}	9.93×10^{-6}	0.009	919.65
VAJTOR	4.13	3.84	0.43	2.19×10^{-4}	5.10×10^{-4}	3.05×10^{7}	3.37×10^{4}	4.74×10^{-4}	0.43	905.95
PEMGIZ	4.80	3.46	0.45	5.83×10^{-5}	6.97×10^{-4}	4.70×10^{7}	5.21×10^{4}	9.29×10^{-5}	0.08	900.94
NURVAZ	6.58	6.00	0.60	2.01×10^{-5}	2.08×10^{-3}	1.67×10^{8}	1.96×10^{5}	1.13×10^{-5}	0.01	855.79
HONCIY	4.83	4.32	0.40	1.04×10^{-4}	6.53×10^{-4}	1.45×10^{8}	1.71×10^{5}	1.88×10^{-4}	0.16	846.94
DEJMOV	4.53	4.16	0.44	5.97×10^{-6}	1.93×10^{-4}	1.15×10^{7}	1.62×10^{4}	4.37×10^{-5}	0.03	707.22
VOJMIS	6.54	4.23	0.55	4.15×10^{-6}	2.71×10^{-4}	2.26×10^{7}	3.34×10^{4}	2.27×10^{-5}	0.01	676.19
VUHJAK	5.35	4.69	0.38	8.24×10^{-5}	2.90×10^{-4}	2.19×10^{7}	3.28×10^{4}	4.26×10^{-4}	0.28	667.77
LUPQES	4.70	4.03	0.54	6.70×10^{-6}	6.27×10^{-4}	2.88×10^{7}	4.40×10^{4}	1.63×10^{-5}	0.01	655.93
LACFOM	4.63	4.04	0.35	5.73×10^{-5}	2.67×10^{-4}	2.06×10^{7}	3.24×10^{4}	3.37×10^{-4}	0.21	636.32

Up to this part, we have discussed the membrane performances of MOFs at infinite dilution condition, but it is also important to measure the membrane performances of MOFs at finite pressure conditions. Since it is computationally expensive to perform MD simulations at finite pressures, we performed mixture MD simulations for the top 20 MOF membranes. We used the same feed composition of CO_2/H_2 as the adsorption condition with 15/85 and the feed pressure was set to 1 bar. **Figure 4.7** shows that hydrogen and carbon dioxide permeabilities computed at infinite dilution (P^0) had a good agreement with permeabilities calculated at mixture condition (P^{mix}). We observed that H_2 permeabilities were slightly lower at mixture condition compared to infinite dilution condition since both molecules had free collision and hydrogen has lower molecular weight when compared to carbon dioxide, that resulted in decreased gas transport for the lighter molecule. Since the H_2/CO_2 membrane selectivities are calculated based on the ratio of gas permeabilities of the two pairs, infinite dilution calculations slightly overestimated the predictions for mixture conditions. Overall, these simulation data show that infinite dilution simulations are a cost-effective way to identify MOFs with high membrane performances at finite pressures.

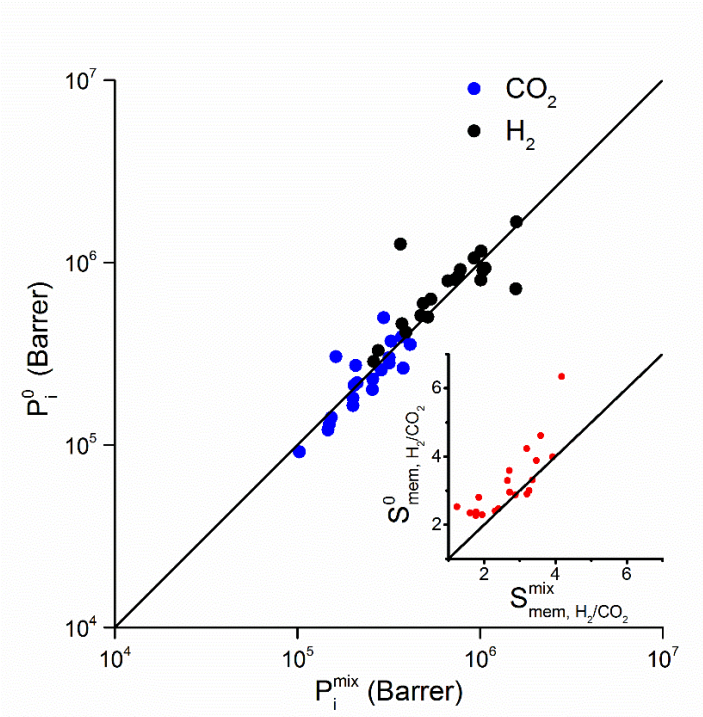

Figure 4.7. Comparison of gas permeabilities computed at infinite dilution ($P^0_{H_2}$ and $P^0_{CO_2}$) with the permeabilities computed for CO_2/H_2:15/85 binary mixture ($P^{mix}_{H_2}$ and $P^{mix}_{CO_2}$). The inset figure compares the selectivities computed at infinite dilution, $S^0_{mem,\,H_2/CO_2}$ with the mixture selectivities, $S^{mix}_{mem,\,H_2/CO_2}$.

Structure-performance relations show important correlations such that general structural characteristics of the most promising MOFs can be identified. First, we identified the correlation between porosity, LCD, and adsorption selectivity of MOFs at infinite dilution. The size of the bubbles was matched with adsorption selectivity values. MOFs with the highest CO_2/H_2 selectivities (>10000) are highly desirable and this was caused by the tight adsorption environment for CO_2 as proven by low LCDs (4.51-10.43 Å) and low porosities (0.36-0.65). Porous MOFs with porosity >0.8 and large pores with LCD >15 Å were calculated to have low adsorption selectivities, <100 as shown in **Figure 4.8.** These MOFs with large pores and high porosities had low selectivities which results in less electrostatic and Coulombic interactions; therefore, adsorption of both gases is diminished.

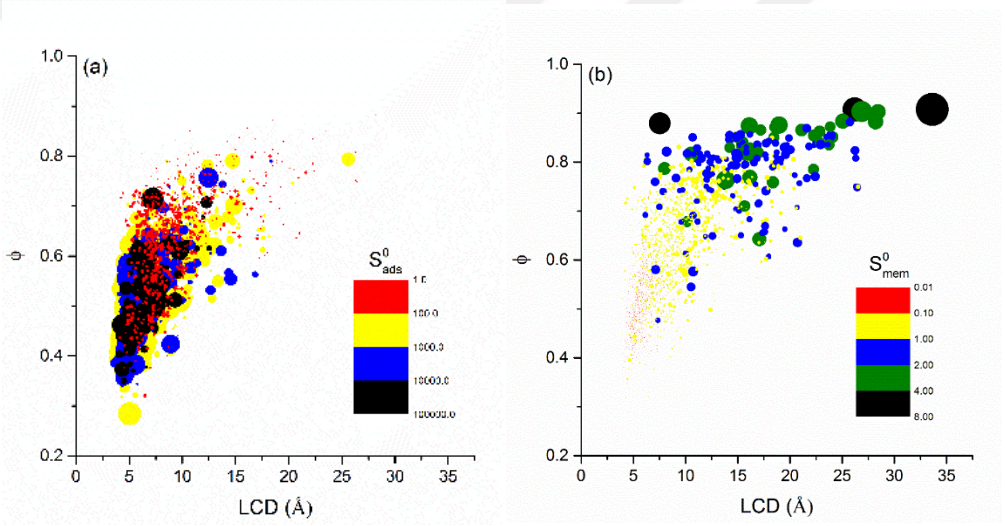

Figure 4.8. (a) Relation between porosities, pore sizes and CO_2/H_2 adsorption selectivities of MOFs. (b) Relation between porosities, pore sizes and H_2/CO_2 membrane selectivities of MOFs. Size of the bubbles represents selectivities of MOFs. Red, yellow, blue, and black region was scaled with a factor of 4.0×10^{-2}, 2.4×10^{-2}, 2.4×10^{-3}, and 2.4×10^{-4}, respectively in (a), scaling factor of 5 was used in (b) to have a clear representation.

The reduction in the MOF density also helped us to identify the most H_2 selective membranes which also had high LCDs. H_2 selective MOF membranes have 15<LCD<35 Å and 0.7<ϕ<1 as shown in **Figure 4.8**. The increase in membrane selectivity comes from two factors: (i) lower CO_2 adsorption selectivities due to lower gas-MOF interactions and (ii) unobstructed diffusion of H_2 molecules which dominates the unfavorable adsorption dynamics, hence result in high membrane selectivity in the large-pored materials. With the same rationale, MOFs with narrow pores (<7.5 Å) and small porosities (<0.6) shown

by red points are promising as reverse selective MOF membranes. Overall, performance of MOFs can be easily categorized with structure-performance relationships that can drastically accelerate the discovery of promising MOFs out of thousands of materials.

The top MOFs identified as adsorbents at PSA and VSA conditions and the top MOFs identified as H_2 selective membranes have essential structure-performance relationships. The effects of each structural property, namely PLD, LCD, SA, ϕ, and metal type on the performance of the top MOF adsorbents and membranes were analyzed in **Figure 4.9**. As expected, the top MOFs showed the same trend in PLD, and LCD as identified in **Figure 4.9** as MOFs with narrow pores had a higher probability of being identified as promising. We investigated the top 20 MOFs for PSA and VSA conditions and 18 out of 20 at PSA and 13 out of 19 MOFs at VSA condition had LCDs <7.5. On the contrary, 16 of the top 20 MOF membranes were shown to have PLDs (LCDs) >10 (15) Å, strengthening our argument in the previous section. Top MOF adsorbents usually had low SA <2000 m^2/g whereas top MOF membranes had significantly higher SA >3000 m^2/g. We then examined the type of the metal available in the MOF, but a clear structure-performance relation was not observed for PSA and VSA processes whereas most of the top MOF membranes have Zn as the metal type as shown in **Figure 4.9**.

The difference between the isosteric heats of adsorption of gas molecules computed at infinite dilution (ΔQ_{st}^0) cannot be accounted as a direct structural property, but it can be a useful parameter to assess the affinity of a MOF structure towards a specific gas. ΔQ_{st}^0 was high, $10<\Delta Q_{st}^0<20$ kJ/mol and $20<\Delta Q_{st}^0<30$ kJ/mol for the top adsorbents in PSA and VSA, whereas it was relatively low, $0<\Delta Q_{st}^0<20$ kJ/mol, for the top membranes. This is expected because if ΔQ_{st}^0 is large for MOFs, the MOF is strongly adsorbing CO_2 over H_2 and becoming a CO_2 selective adsorbent and CO_2 selective membrane (hence a weakly H_2 selective membrane). We finally used similarity index calculations[90, 175, 176] to compare surface texture and topology of the top MOFs. The similarity analysis of the top 20 MOFs in each process, PSA, VSA and membrane-based separation are illustrated in **Appendix A2**. SI >0.8 indicates the most similar materials whereas SI <0.3 shows the least similar structures. The SI computed for the MOF adsorbents for PSA and VSA were 0.68 and 0.74, respectively and the average SI computed for the top H_2 selective membranes was 0.57. These results suggest that topological structures of promising MOF adsorbents and membranes are quite similar.

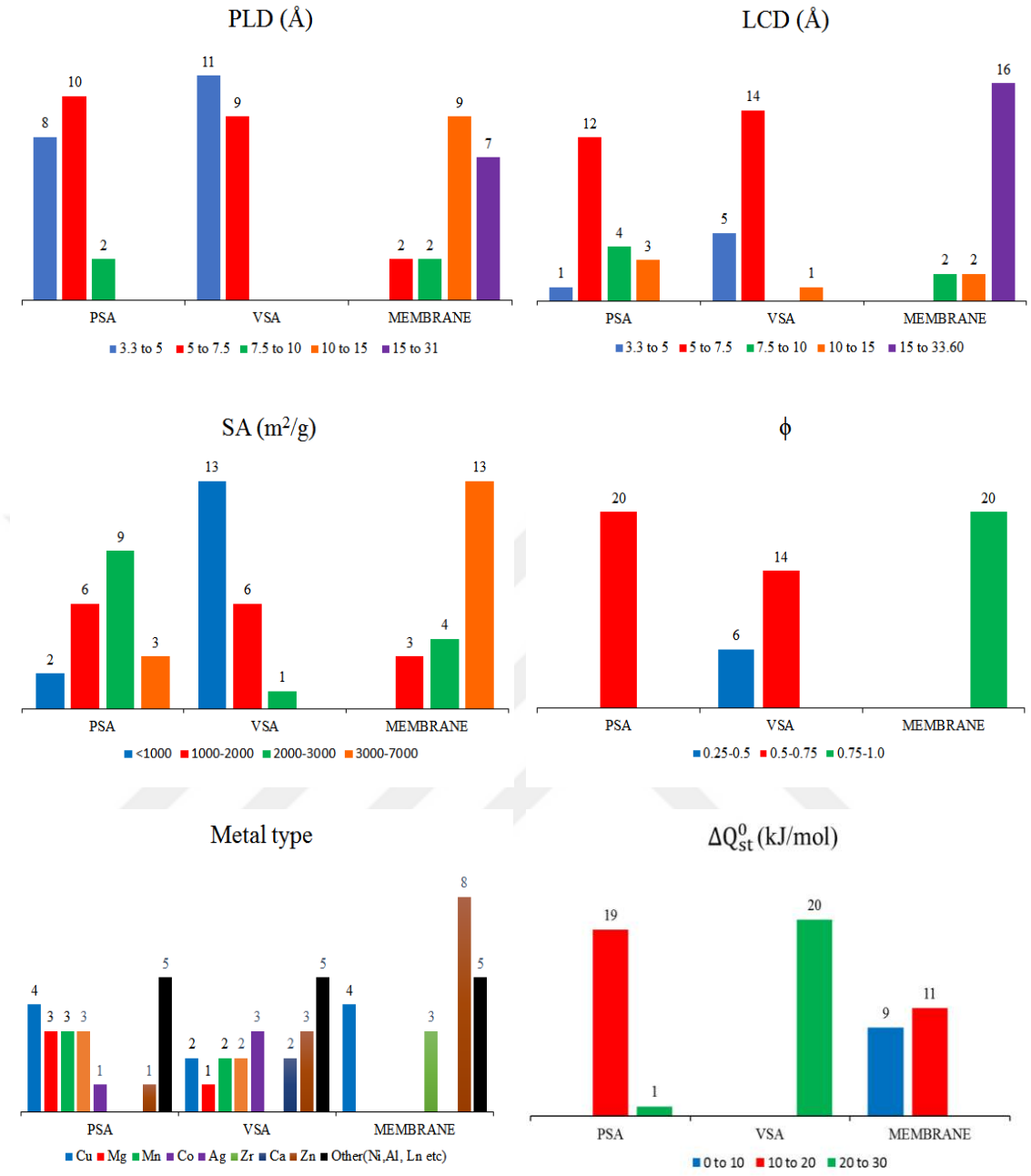

Figure 4.9. Effects of structural properties, PLD, LCD, SA, porosity, metal type, and ΔQ_{st}^0 on the separation performances of the top 20 MOFs for PSA, VSA, and membrane processes.

4.3 Conclusion

High-throughput computational screening was performed to identify the best MOF adsorbents and membranes for CO_2/H_2 separation. Adsorption data was produced with GCMC simulations and CO_2/H_2 mixture data for 3857 MOFs were obtained. The upper limits for MOF selectivity and working capacity were investigated and promising MOFs with APS >2000 mol/kg were identified. Materials having R% >85% were ranked based on their APSs to identify the top 20 adsorbents for PSA and VSA processes. The influence of impurities such as CO, CH_4 and H_2O was investigated. MD simulations were performed to compute permeabilities and selectivities of MOF membranes. A significant number of MOFs (899) exceeds the upper bound defined for polymeric membranes suggesting that MOFs have the potential to replace traditional membranes in selective separation of H_2 from CO_2. The performance of MOFs was compared with experimental data of traditional materials such as zeolites and polymers. Detailed examination of the structural characteristics of the top MOF adsorbents and membranes revealed that MOFs with pore sizes <7.5 Å, $0.5<\phi<0.75$, SA <2000 m^2/g are good adsorbents whereas the top MOF membranes have pore sizes >15 Å, ϕ >0.75 and SA >3000 m^2/g. These structure-performance relationships can serve as a guideline to the development of novel MOFs with high CO_2/H_2 and H_2/CO_2 separation performances.

Chapter 5*

SCREENING THE UPDATED MOF DATABASE FOR CO_2/H_2 SEPARATION

MOFs are a new class of materials and novel types of MOFs with unique properties are synthesized and added to CSD each year. Due to the rapid increase in the number of reported MOFs, the experimental MOF databases are updated, therefore it is essential to perform high throughput computational screening on these novel structures. In this part of the thesis, molecular simulations of 10221 MOFs were performed to identify their adsorbent and membrane-based CO_2/H_2 separation performances. In addition to the PSA and VSA conditions that were investigated for 3857 MOFs in Chapter 4, we also investigated temperature swing adsorption (TSA) process in Chapter 5 and MOFs from the updated database significantly outperformed commercial zeolites and the previously reported MOFs in terms of CO_2 selectivity and adsorbent performance score. Due to the increase in the number of MOFs, rare occurrences in MOF databases were investigated such as: (i) applicability of Ideal Adsorbed Solution Theory (IAST), (ii) effects of inaccessible local pores, (iii) influence of catenation and (iv) presence of impurities in CO_2/H_2 mixture on the adsorbent performance metrics of MOFs. With molecular dynamics simulations, large number of MOF membranes were shown to outperform traditional polymer and porous membranes in terms of H_2 permeability and H_2 selectivity. Results showed that MOFs that are recently added to the updated CSD have higher potentials to be promising in terms of adsorbents and membranes. Structure performance relationships of the results discussed in Chapter 4 were compared with the results obtained for the updated MOF database. Finally, characteristics of structural properties for the best MOF adsorbents and membranes were identified to design novel MOFs for CO_2 capture and H_2 purification.

*The content of this chapter is taken from the published work (*Avci G., Erucar I., and Keskin S. Do New MOFs Perform Better for CO_2 Capture and H_2 purification? Computational Screening of the Updated MOF Database. ACS Applied Materials & Interfaces*, 2020, *2(37), 41567–41579: doi.org/10.1021/acsami.0c12330*) and adapted for this thesis.[66]

5.1 Methodology

We retrieved the most recently deposited and updated 70551 non disordered MOF structures from the CSD.[17] Solvents from the structures were cleaned with the Python code to keep up the consistency with our work discussed in Chapter 4.[17] Physical properties such as SA, non-accessible surface area (NaSA), PLD, LCD, porosity, dimensionality were calculated with Zeo++ software version 0.3.0.[90] A N_2 sized probe was used to calculate the accessible and non-accessible surface areas while a He-sized probe was used to calculate porosity. Since MOFs having PLDs between 3.30 and 3.70 Å have no accessible surface area for a N_2 probe, a CO_2-sized probe was used to compute their SA. MOFs that had zero SA and non-convergence in point charge calculations were omitted. After these elimination procedures, we ended up with 10221 different MOFs.

To test the reliability of IAST for CO_2/H_2 mixture at PSA, VSA, and TSA conditions, single-gas adsorption isotherms were discretized with dual-site Langmuir (DSLangmuir) models. Details of the IAST calculations such as fitting parameters, equations, and Root Mean Square Error (RMS) calculations are shown in **Appendix Table B1.** IAST predictions were then compared with GCMC simulations for CO_2/H_2 mixture at 0.1, 1, 2, 4, 6, 8, and 10 bar, 298 K.

In some MOFs due to the presence of inaccessible local pore pockets, it is essential to computationally block potential gas adsorption in these pockets. We used the probe radius of H_2 (1.48 Å) and spherical probe radius of CO_2 (1.65 Å) to identify and assign blocking spheres as implemented in Zeo++ software. Then, these blocking pocket files were assigned to corresponding GCMC simulations performed with RASPA. 216 MOFs were found to be suitable for this analysis since they had NaSA >100 m^2/g. 82 MOFs out of 216 had nonzero NaSA for just CO_2-sized probe, and 136 out of 216 MOFs were calculated to have nonzero NaSA for both probes.

To simulate the PSA and VSA processes, we used the same simulation conditions as discussed in the methodology part of Chapter 4. For the TSA process, we set the adsorption and desorption temperatures as 298 and 473 K at 1 bar. In addition to selectivity, working capacity, regenerability, adsorbent performance score that was discussed in Chapter 4, we also investigated the separation potential metric. Separation potential metric was used to calculate the upper limits of how much the weakly adsorbing species can be extracted where in our research we focused on how much H_2 can be purified.

5.2 Results and Discussion

Screening the updated MOF databases can provide novel insights and valuable information so we compared the adsorption selectivity and working capacity of 10221 MOFs for PSA, VSA and TSA processes in **Figure 5.1**. Orange dots represent the new MOFs for which CO_2/H_2 selectivities were computed between 4.18-4.24×10^4 for PSA, 1.20-1.19×10^5 for VSA, and 1.20-1.19×10^5 for TSA processes. When we compared these new selectivities with available experimental data, 1762 MOFs had higher CO_2/H_2 selectivity (550-4.09×10^5) at 10 bar, 298 K than NaX (1,510) and NaY (550) at 10 bar, 300 K.[171] Similarly, 5365 and 688 MOFs exhibited higher CO_2 working capacities (1.95-11.66 mol/kg at PSA and 2.03-7.05 mol/kg at VSA conditions), outperforming10-membered ring zeolites (1.95 mol/kg at PSA and 2.03 mol/kg at VSA).[54] Many MOFs with APS >2000 mol/kg outperformed NaX (29.60 mol/kg) and NaY (27.10 mol/kg) at PSA condition.[171] It is important to identify MOFs with both high selectivity and working capacity. CO_2 working capacities were calculated to be between 0.02-11.66 mol/kg for PSA, 1.62×10^{-3}-7.05 mol/kg for VSA, and 1.30×10^{-4}-16.11 mol/kg for TSA conditions. These results indicate that the updated MOF database has new promising MOFs that have higher selectivity and working capacity values which were previously (black dots) not reported by the older version of CSD. Majority of the new MOFs in **Figure 5.1** have both a high CO_2 selectivity >10^4 and high working capacities between 2-4 mol/kg for PSA and VSA processes We did not perform TSA simulations in our previous work thus we omitted the comparison of orange and black dots for TSA condition. TSA condition share the same adsorption condition with VSA process whereas temperature is increased to desorb any residual gas molecules from the framework. MOFs at TSA condition had remarkably high working capacity values mostly between 4-8 mol/kg, indicating that temperature can efficiently extract any adsorbed CO_2 molecules in the framework due to the weak intermolecular interactions present at elevated temperatures. Overall, we observed that MOFs included by the updated database have better CO_2 selectivities and working capacities since the upper limits of CO_2 selectivity was increased by up to 15-times and the upper limits of CO_2 working capacity was increased by up to 1.3-times.

Since both selectivity and working capacity were increased in the MOFs from the updated database, we investigated their APS values. 765, 1181, 1443 MOFs were shown to exceed APS >2000 mol/kg at PSA, VSA, and TSA conditions, respectively. Therefore,

we compared the APS of commonly employed zeolites with our MOFs and many MOFs having APS >2000 mol/kg outperformed NaX (29.60 mol/kg) and NaY (27.10 mol/kg) at PSA condition.[171] These results show MOFs from the updated MOF database have great potential to be identified as promising adsorbents in terms of their adsorption selectivity and working capacity.

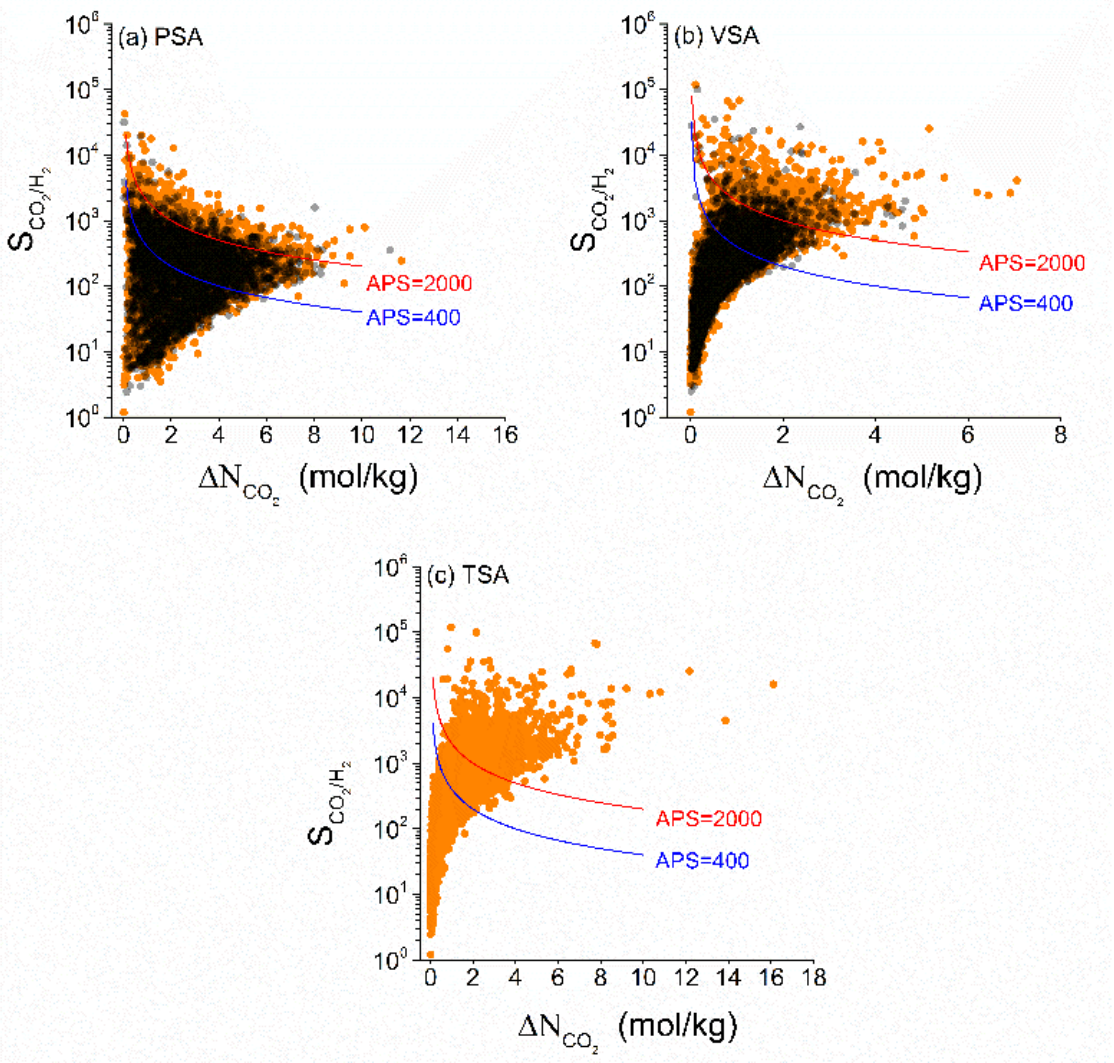

Figure 5.1. Adsorption selectivity, working capacity, and APS of MOFs for separation of CO_2/H_2:15/85 mixture at (a) PSA, (b) VSA, and (c) TSA conditions. Orange points represent the data of new 6364 MOFs studied at PSA and VSA conditions and 10221 MOFs at TSA condition whereas black points represent data of 3857 MOFs from our previous study.[89]

Motivated by the enhancement in both the adsorption selectivity and working capacity for the updated MOF database, we carried on with investigating the relationship between R% and APS in **Figure 5.2**. The same convention of the previous section is used where black dots represent MOFs from the previous study and orange dots represent the

updated MOF database. MOFs with R% >85% are especially desirable since they can be used in processes with a continuous cycle much more efficiently than MOFs with lower regenerabilities. MOFs with the highest APS values have insignificant R% values, however, by screening the updated MOF database, we were able to show that 324 and 829 additional MOFs at PSA and VSA conditions, respectively, had higher APS values at R% >85% condition, than the previously investigated MOFs in our previous work. When we investigate the TSA process, there is a significant number of MOFs (2682) that have APS >400 mol/kg and R% >85% which increases the probability of finding a promising MOF when TSA process is employed. This is mainly due to the increased kinetic energy of CO_2 molecules at 473 K which weakens the interactions between CO_2 molecules and the framework, therefore reducing the amount of energy needed for regeneration.

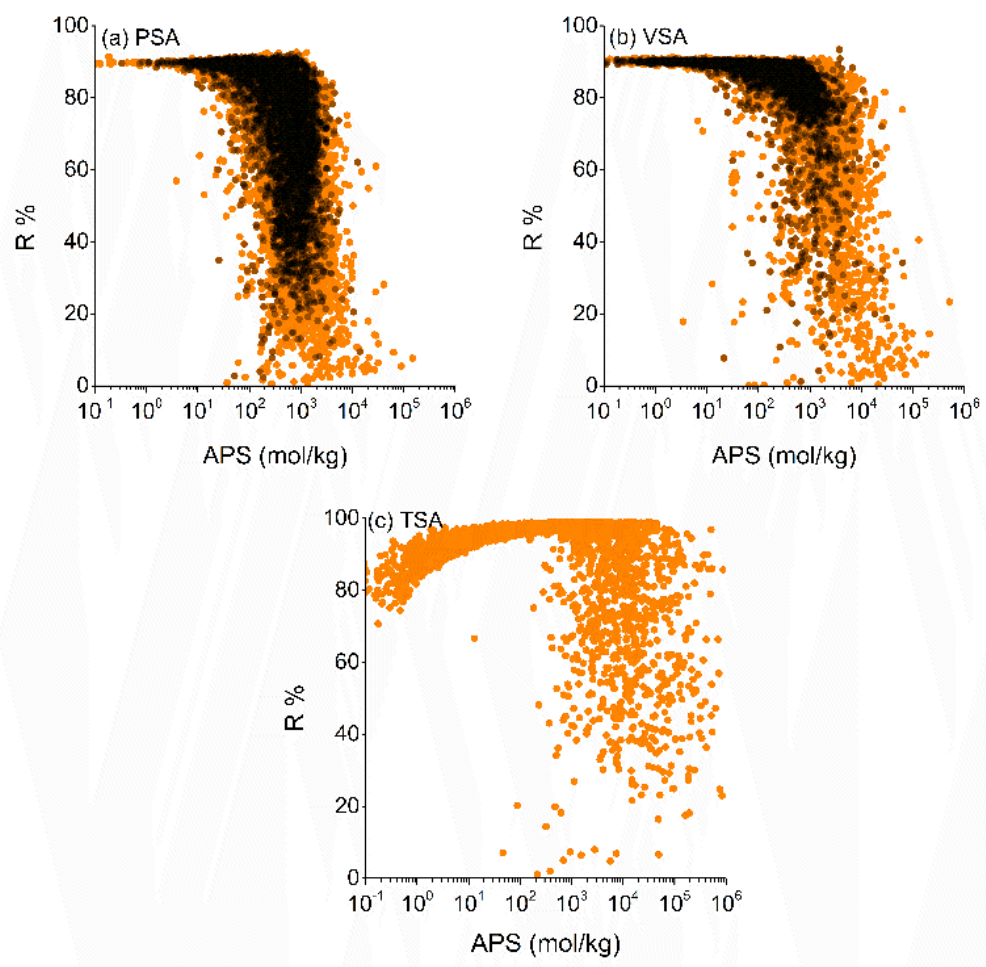

Figure 5.2. R% and APS of MOFs computed for separation of CO_2/H_2:15/85 mixture at (a) PSA, (b) VSA, and (c) TSA conditions. Orange points represent the data of new 6364 MOFs at PSA and VSA conditions and 10221 MOFs at TSA condition whereas black points represent data of 3857 MOFs from our previous study.[89]

In an adsorption process, it is important to quantify how much weakly adsorbed species can be recovered within an adsorbent bed. When a CO_2/H_2 mixture starts to interact with a MOF adsorbent bed, due to the weak interaction between MOF and H_2, H_2 starts to exit the adsorbent bed prior to CO_2. Eventually, the adsorbent bed gets saturated with both molecules and the concentration at the inlet matches the concentration at the outlet. Separation factor (ΔQ) is a metric proposed by Krishna et al.[177] and this performance metric only requires heat of adsorption values and volumetric working capacities as input and separation factor has been shown to predict the recoverable weakly adsorbing gas amount. ΔQ calculations are similar to APS calculations, however, ΔQ is calculated with volumetric gas uptakes whereas APS is calculated with gravimetric gas uptakes. Due to this difference, MOFs with higher densities have slightly higher ΔQ values compared to their APS. Therefore, we color coded ΔQ values with respect to selectivity and working capacities calculated at PSA, VSA, and TSA conditions as shown in **Figure 5.3**. Results showed that PSA condition had the highest ΔQ with 83 mol/L whereas ΔQ values of VSA and TSA conditions were similar due to their identical adsorption conditions. Interestingly, the MOF with the highest ΔQ at PSA condition has a high volumetric working capacity of 6.8 mol/L, which resides at the high working capacity region of the population, and a selectivity of 1204. When compared to the trends observed in **Figure 5.1**, we can see that ΔQ and APS values show similar trends, MOFs with high APS have high ΔQ. When we compared our results with benchmark materials, we observed that zeolite 13X and MgMOF-74 had a calculated ΔQ of 36 and 52 mol/L at an adsorption pressure of 54 and desorption pressure of 14 bar.[178] Since ΔQ metric is determined mainly by working capacity, even though a much larger pressure difference and a much larger adsorption pressure is reported in this study compared to our highest pressure at PSA condition, we were able to observe ΔQ >52 mol/kg. Therefore, MOFs identified in this screening study would be able to recover H_2 much more efficiently than MgMOF74 and zeolite 13X. Overall, our results show that MOFs with APS >2000 mol/kg have a great potential to also have high ΔQ >50 mol/L, therefore they are suitable for next generation adsorbent bed design.

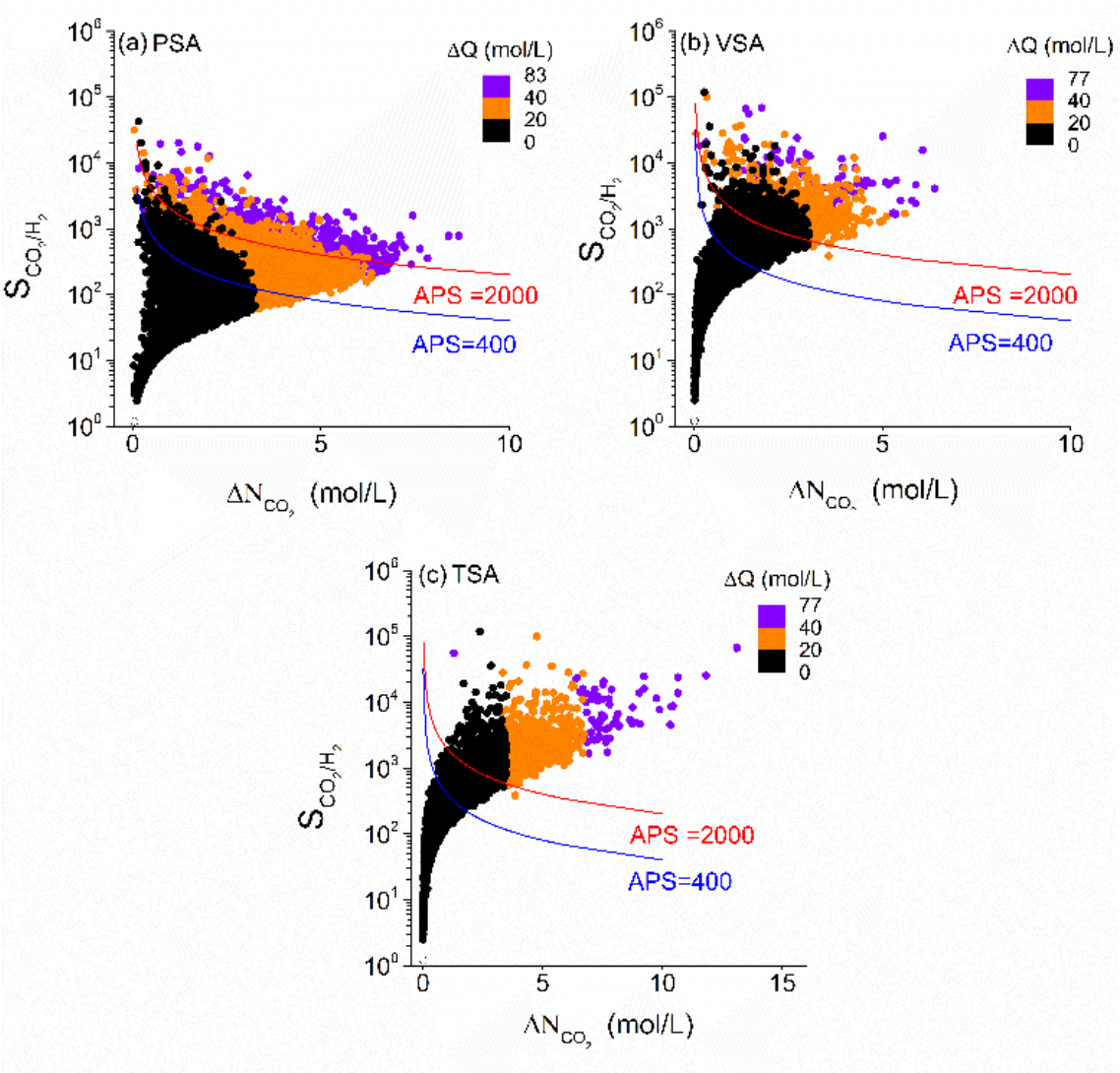

Figure 5.3. Relation between adsorption selectivity, working capacity, and separation potential of 10221 MOFs for separation of CO_2/H_2:15/85 mixture at (a) PSA, (b) VSA, and (c) TSA conditions. Black, orange, and purple regions indicate MOFs with separation potential <20 mol/L, 20-40 mol/L and >40 mol/L.

We distinguished the best 10 MOFs exhibiting the highest APSs among the MOFs having R% >85% and listed them in **Appendix Table B2**. DABWUA having a CO_2/H_2 selectivity of 333, was the best MOF at PSA condition due to its narrow pores providing strong CO_2-MOF interactions.[89] FAQXIF was the best MOF for VSA process with a very high selectivity of 3703. We note that four of the top 10 MOFs at VSA condition, AFEJOK, DATKIU, GUKYUI and OJASOJ, have extra framework ions which enhance the electrostatic interactions between CO_2 molecules and adsorbents, resulting in high selectivities. To understand the impact of extra framework ions, we turned-off the Coulombic interactions between CO_2 and MOFs in molecular simulations and

recalculated selectivities. Selectivities of AFEJOK, DATKIU, GUKYUI, and OJASOJ significantly decreased (from 1262 to 165; 1474 to 40, 1809 to 118, and 1949 to 52, respectively) once the electrostatic interactions were turned-off. JOVLAH10 was determined as the best adsorbent for TSA process with a very high selectivity. The top MOFs identified at TSA condition have exceptionally high selectivities (1.21×10^4-9.91×10^4) and APSs (1.01×10^5-3.07×10^5 mol/kg) and all these MOFs have very narrow PLDs <4.91 Å, exposed metal sites, and/or halogen functional groups which enhance CO_2-MOF electrostatic interactions. These interactions are supported by the favorable adsorption sites of these top 3 MOFs as shown in **Figure 5.4** and the final simulation snapshots as shown in **Figure 5.5**. Overall, we concluded that TSA is the best process option for CO_2/H_2 separation when APS is considered as the main performance metric for MOFs having R% >85%.

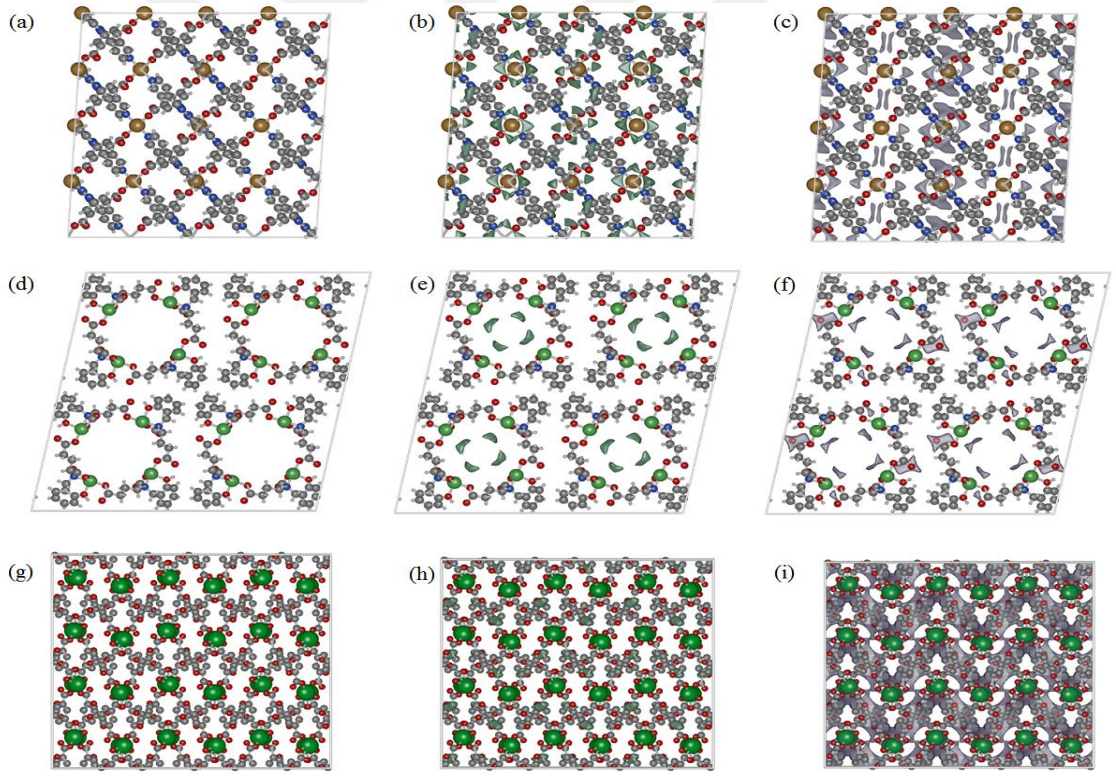

Figure 5.4. Snapshots of the favorable adsorption sites of (a-c) DABWUA, (d-f) FAQXIF and (g-i) JOVLAH10. (a), (d) and (g) illustrate MOFs; (b), (e) and (h) illustrate favorable adsorption sites for CO_2; and (c), (f) and (i) illustrate favorable adsorption sites for H_2.

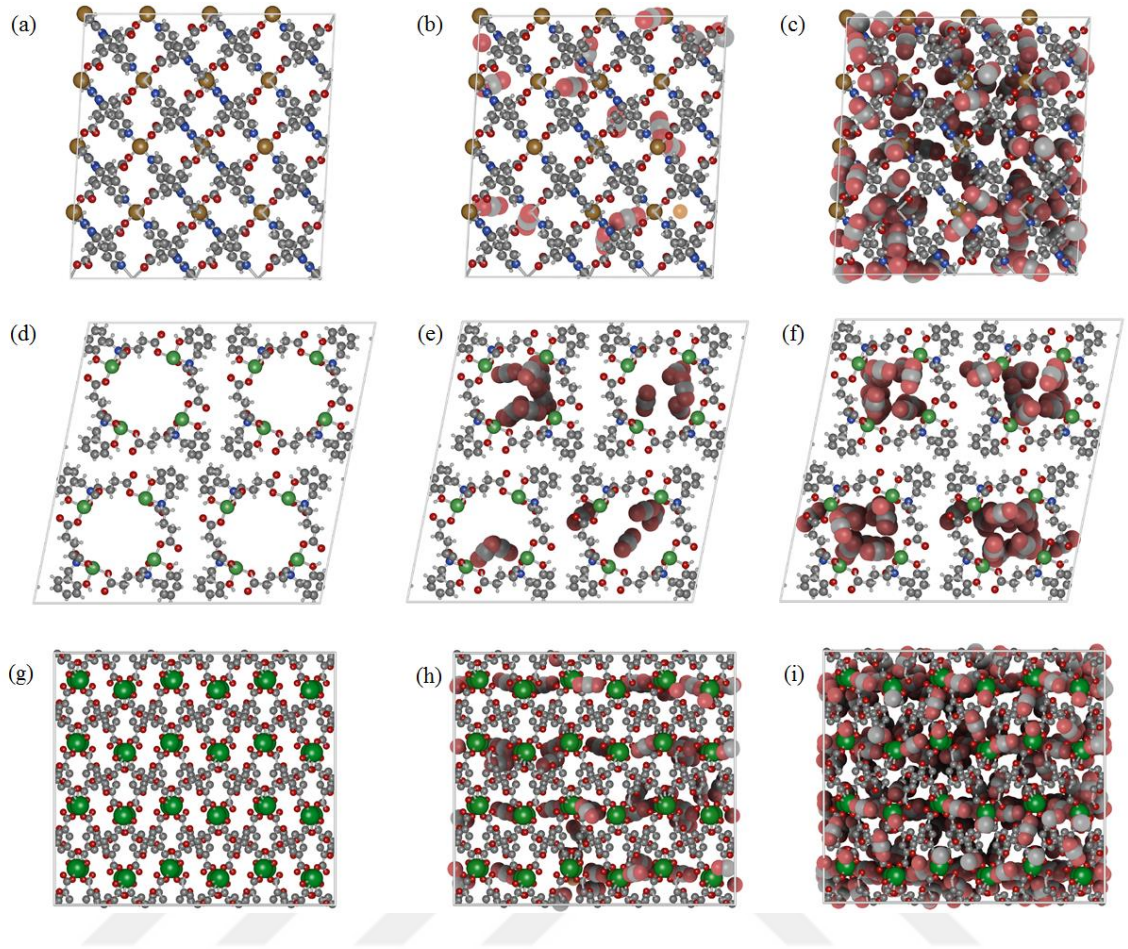

Figure 5.5. GCMC snapshots taken from the last step of molecular simulations for (a-c) DABWUA at PSA, (d-f) FAQXIF at VSA, and (g-i) JOVLAH10 at TSA conditions. (a), (d) and (g) illustrate MOFs; (b), (e) and (h) illustrate desorption conditions; and (c), (f) and (i) illustrate adsorption conditions. CO_2 (H_2) was represented by red and gray (orange) spheres.

Ideal adsorption solution theory (IAST) can be used to make accurate predictions of selectivity in certain physical conditions. IAST can be applied to both computational and experimental studies and the only input required is a well parametrized adsorption isotherm.[179] IAST has been designed for generic adsorbents with homogenous porosity and minimal structural heterogeneity such as common zeolites.[180] As discussed in the methodology, applying IAST to MOFs for gas mixtures such as CO_2/CH_4, CO_2/N_2 and CH_4/H_2 has shown to give good results.[178, 181, 182] CO_2/H_2 mixture IAST predictions are more challenging due to the size and adsorption amount difference of these two gases,[183] therefore we tested IAST for our top 3 MOFs of each condition, namely PSA, VSA and TSA. In **Figure 5.6**, GCMC simulation and IAST predictions for CO_2 and H_2 adsorption, as well as CO_2/H_2 selectivity is shown at 0.1, 1, 2, 4, 6, 8, and 10 bar, 298 K.

We took 10% deviation as an acceptable deviation where QATPUX and GEJRIW fell into these regions in terms of adsorbed CO_2 and H_2. We observed the highest deviation in LACDEY due to its small surface area of 300 m^2/g.

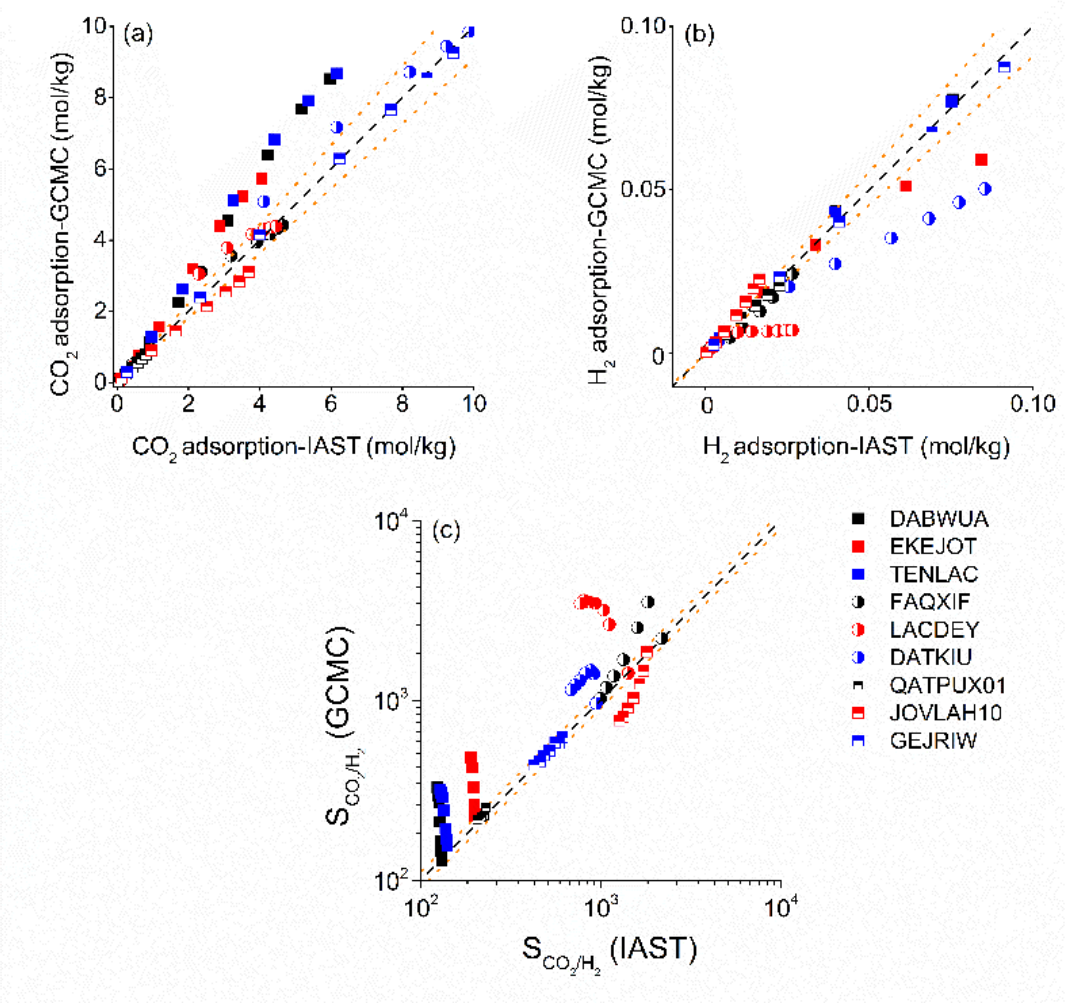

Figure 5.6. Comparison between GCMC simulation results and IAST predictions for (a) CO_2 adsorption, (b) H_2 adsorption, and (c) CO_2/H_2 selectivity at 0.1, 1, 2, 4, 6, 8, 10 bar, 298 K. Black dashed lines are to guide the eye, orange dashed lines represent 10% deviation from parity line.

IAST does not consider for structural influences such as open metal sites present in LACDEY therefore IAST predictions significantly underestimated our GCMC simulations. DATKIU, TENLAC, DABWUA and EKEJOT also had similar disagreements between GCMC simulations and IAST predictions, underscoring the challenges in applying IAST to CO_2/H_2 mixture. TENLAC and DATKIU had polar groups (Cl^- and BF_4^-) which enhanced the heterogeneity of adsorption in GCMC simulations. As a contrast the selectivity of JOVLAH10 was overpredicted by IAST even though it had open metal sites. This was attributed to the probe accessible surface area

difference between CO_2 and H_2 (527 to 810 m^2/g). This implies that JOVLAH10 has a smooth surface curvature with narrow pores which effectively results in a considerable difference of surface areas experienced by each adsorbate. Overall, our results underline that performing GCMC simulations is essential for high-throughput computational studies rather than performing simple IAST calculations since IAST generally underestimates the CO_2/H_2 separation performances of the top MOFs.

MOFs can have a wide variety of structural types and orientation and clustering of ligands and metal linkers can prohibit the entrance of gas molecules to local pores. Probing inaccessible local pores which are by default accessible through our simulation technique can be inaccessible under experimental techniques. Therefore adding an additional step to GCMC simulations and disabling access to these pores with NaSA has been suggested in the literature.[184, 185] Since CO_2 has slightly higher radius than H_2, there can be some cases where H_2 can freely enter a pocket that CO_2 cannot travel into (condition 1), and there are cases where two gas molecules both travel through a local pore (condition 2). Out of 10221 MOFs, 216 MOFs fell into these two special conditions, therefore, we compared the selectivity with and without pore blocking at PSA, VSA and TSA conditions in **Figure 5.7**. Blocking these inaccessible pores lead to lower selectivity and working capacities since these pores have very small volumetric surface area regions which can be extremely favorable sites for CO_2 adsorption due to the strong coulombic interactions between CO_2 and MOF and presence of a quadrupole moment in CO_2 molecule. Performance of MOFs with low SA and large NaSA were greatly diminished since both the available surface for gas molecules were significantly decreased and favorable pockets were left out by the simulation. SAZPIV satisfied both condition 1 and 2 and its selectivity decreased from 434 to 21.5, 1043 to 25, 1483 to 2.8 at PSA, VSA and TSA conditions, respectively. This was mainly due to the high NaSA of 152.72 m^2/g accompanied with a mediocre SA of 428.30 m^2/g. The largest deviation in working capacity was in FECPIM since charge balancing Na^+ ions were at the gates of each pore which resulted with a very high NaSA of 553.44 m^2/g. Although blocking pockets seem to be decreasing the overall performance of MOFs, it is not strictly the case since we assume our frameworks to be rigid and any local framework flexibility within the period of molecular diffusion values of gas molecules can convert NaSA into SA. Physical, and chemical pressure induced by gas adsorption can be strong enough to propagate mobility into charge balancing ions, which were blocking pore entrance as in the case of FECPIM.

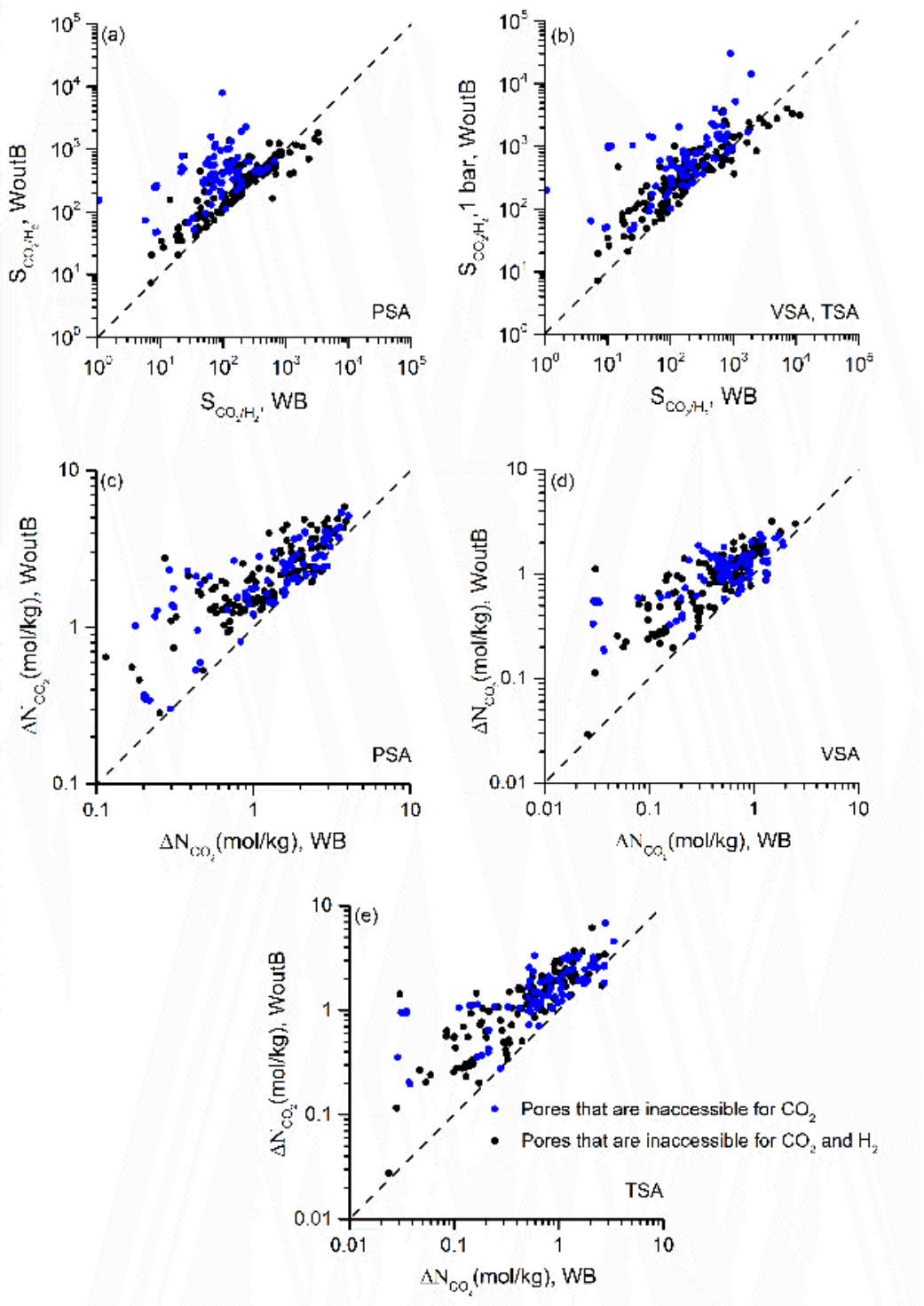

Figure 5.7. Effect of blocking pockets of MOFs on (a-b) CO_2/H_2 selectivities, (c-e) CO_2 working capacities at PSA, VSA, and TSA conditions.

The influence of pore blocking on regenerability is also shown in **Appendix B1** and **B2**. Since the decrease in CO_2 uptakes was greater than the decrease in their CO_2 working capacities, R% values of MOFs were enhanced when the inaccessible pores were blocked.

As a result, blocking local pores of MOFs showed us that high-throughput computational screening method overestimates the performances for these special cases of MOFs if proper blocking techniques are not used. Therefore, in screening studies, blocking pockets should be used, if necessary, since pore blocking can significantly influence the simulation results and performance ranking of a MOF.

It has been shown that catenated IRMOFs outperform their non-catenated counterparts in CO_2/H_2 selectivity due to the strong interaction of CO_2 molecules in the catenated MOFs.[186] We identified 29 catenated MOFs and their non-catenated pairs in our dataset and compared their selectivities, working capacities, and APSs at PSA, VSA, and TSA conditions in **Figure 5.8**. Catenated MOFs have generally higher CO_2/H_2 selectivities due to the stronger MOF-CO_2 interactions caused by the entrapment of CO_2 within a reduced available adsorption surface. Similar results were also discussed in a computational study[187] where six catenated MOFs exhibited higher CO_2/H_2 selectivity compared to their non-catenated pairs up to 20 bar at 298 K, which was attributed to the creation of new adsorption sites for CO_2. Although catenation reduces pore sizes and surface areas of MOFs, CO_2 working capacities of catenated MOFs were found to be higher compared to their non-catenated counterparts. R% values of catenated MOFs and their non-catenated pairs did not significantly change. We note that non-catenated structures of these 29 MOFs have APS <400 mol/kg, thus they are not identified as the top performing MOFs. As a result, by screening a larger dataset of MOFs provided by increasing number of MOFs available in the updated MOF database, we have shown that catenation can increase the CO_2/H_2 separation performances of some catenated MOFs which can make them potentially promising adsorbents.

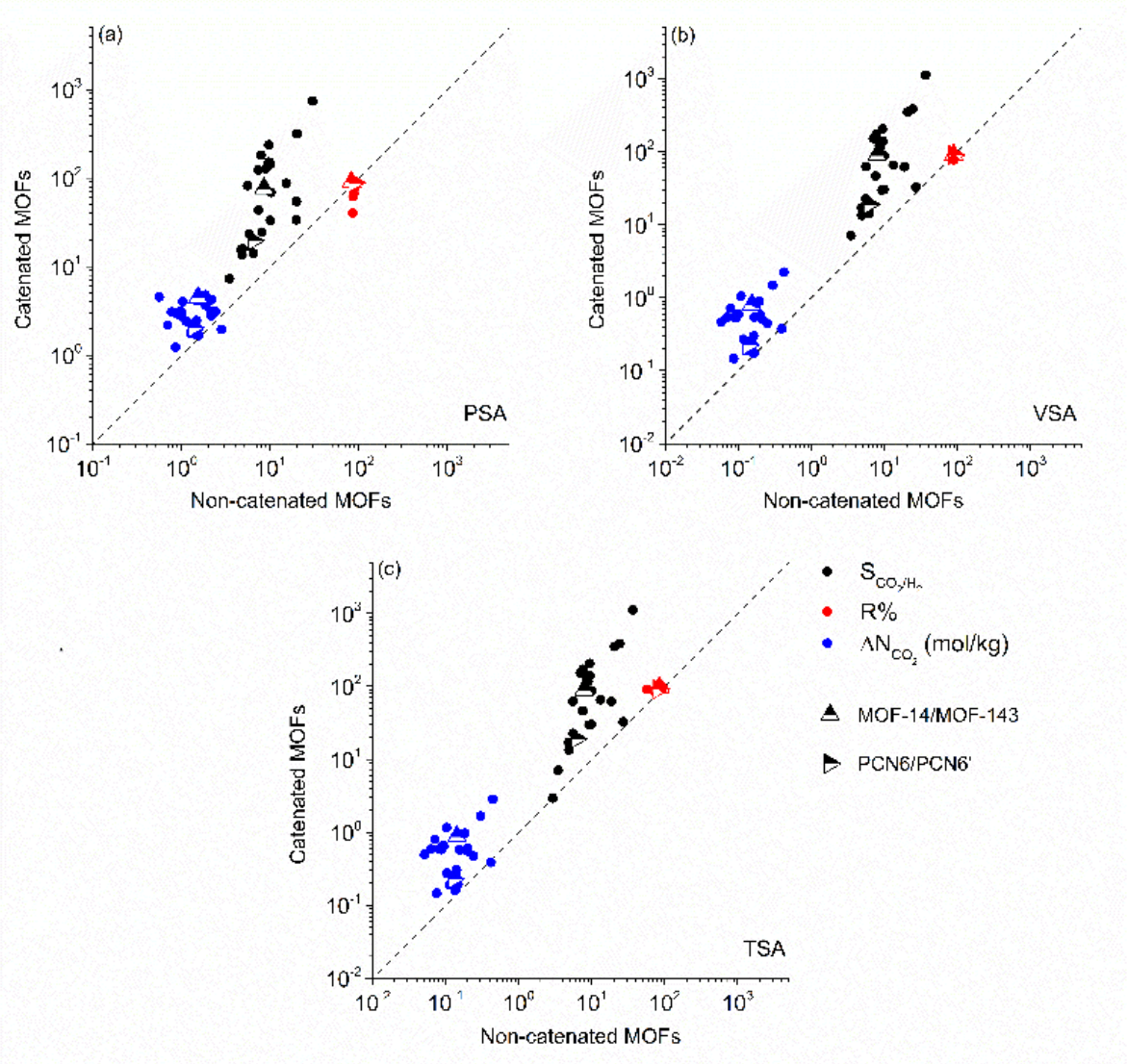

Figure 5.8. Comparison of adsorption selectivities, regenerabilities and working capacities of catenated MOFs with those of their non-catenated pairs at (a) PSA, (b) VSA, and (c) TSA conditions.

CO_2 capture and H_2 purification occur within the presence of impurities such as CO, CH_4, and H_2O in the pre-combustion process plants.[188] Therefore, we studied the effect of impurities in the bulk gas mixture on the performances of the top 20 MOFs at PSA and VSA conditions. GCMC simulations were performed for binary (CO_2/H_2:15/85) and quinary ($CO_2/H_2/CH_4/CO/H_2O$:15/75/5/5/0.1) mixture to compute APS and R% and results are given in **Table 5.1**. To examine the water affinity of MOFs, we also computed the Henry's constants for CO_2 ($K^0_{CO_2}$) and H_2O ($K^0_{H_2O}$). Results showed that APSs of the top performing MOFs significantly decrease in the presence of impurities within the bulk gas mixture. For example, APS of the top performing MOF identified for PSA process,

DABWUA, decreased from 2463 to 1065 mol/kg. CO_2 uptakes of MOFs decreased at PSA and VSA conditions due to the high number of adsorbed H_2O molecules within the pores of MOFs in the quinary mixture simulations, resulting in lower selectivity and working capacity compared to those obtained from the binary mixture simulations. $K^0_{H_2O}/K^0_{CO_2}$ ratio had the most influence since a ratio higher than 1 drastically changed the calculated adsorbent metrics. For example, APS of the 9th best performing MOF, MEKKUL, at PSA condition significantly decreased from 1831 to 337 mol/kg due to its strong affinity towards H_2O with $K^0_{H_2O}/K^0_{CO_2}$ value of 836. The strong affinity of MEKKUL towards H_2O can be attributed to its open Co metal-oxide clusters. Similar results were also discussed in the literature[189] where presence of H_2O as the third component in CO_2/CH_4 and CO_2/N_2 mixtures was shown to remarkably decrease the performance metrics of MOFs having strong affinity towards water due to the presence of specific functional groups. Other impurities such as CO and CH_4 were found to have less impact on the calculated metrics compared to H_2O. We generally did not observe significant changes in R% of the top MOFs in the presence of impurities except for the MOFs having high $K^0_{H_2O}/K^0_{CO_2}$ ratios. Thus, we infer that calculated APSs of hydrophobic MOFs generally decrease in the presence of impurities in CO_2/H_2 mixture.

Updating the screening studies on MOF datasets can provide useful insight upon the general membrane performances of MOFs. **Figure 5.9** shows H_2/CO_2 selectivities and H_2 permeabilities of 10221 MOF membranes with the Robeson's upper bound,[63] designed for polymer membranes to demonstrate the trade-off between their permeability and selectivity. It is important to remember that this upper bound represents the intrinsic permeability and selectivity of the dense polymer membranes.[190] For this reason, membrane community has aimed to enhance gas diffusivity by increasing the gas solubility of polymers to obtain high-performance polymer membranes for H_2/CO_2 separation.[170] However, industrially available polymer membranes are still below the upper bound. On the other hand, we found that MOFs, having a wide range of structural and textural properties, exhibit extremely high H_2 permeabilities (>10^5 Barrer) to overcome that trade-off.

Table 5.1. Performances of the top 10 MOFs (having the highest APSs and R% >85%) for PSA and VSA processes for separation of CO_2/H_2:15/85 binary and $CO_2/H_2/CO/CH_4/H_2O$:15/75/5/5/0.1 quinary mixtures.

MOFs	APS CO_2 binary (mol/kg)	APS CO_2 quinary (mol/kg)	R% binary	R% quinary	$K^0_{H_2O}$ (mol/kg/Pa)	$K^0_{CO_2}$ (mol/kg/Pa)	$K^0_{H_2O}/K^0_{CO_2}$
Pressure Swing Adsorption (PSA)							
DABWUA	2463.17	1065.49	86.72	85.34	2.34×10^{-5}	7.20×10^{-5}	0.33
EKEJOT	2442.44	59.70	85.82	72.64	0.08	4.90×10^{-4}	163.26
TENLAC	2348.93	999.06	85.52	86.43	4.35×10^{-5}	8.21×10^{-5}	0.53
QEBZII	2318.89	460.66	86.79	82.13	1.87×10^{-2}	6.44×10^{-5}	290.37
PIJDIW	2101.27	702.84	85.29	87.24	7.96×10^{-4}	6.38×10^{-5}	12.47
HOWRES	2035.12	734.18	86.58	87.51	1.55×10^{-4}	7.22×10^{-5}	2.15
IJEFUZ	1864.90	247.18	86.53	86.65	1.68×10^{-2}	6.26×10^{-5}	268.37
ENATUJ	1848.82	941.24	87.96	86.20	5.43×10^{-6}	6.93×10^{-5}	0.08
MEKKUL	1831.12	336.92	86.40	72.59	4.58×10^{-2}	5.48×10^{-5}	835.76
VUFHEL	1822.53	270.88	87.59	87.68	7.41×10^{-3}	7.47×10^{-5}	99.20
Vacuum Swing Adsorption (VSA)							
FAQXIF	9834.22	1918.65	85.02	87.67	4.83	3.12×10^{-4}	1.55×10^{4}
LACDEY	7592.04	938.04	85.73	86.20	6.54×10^{-3}	2.86×10^{-4}	2.30×10^{1}
DATKIU	6735.40	9.534	88.30	75.06	9.31	4.19×10^{-4}	2.22×10^{4}
OJASOJ	6249.19	125.31	85.41	80.52	1.71	3.54×10^{-4}	4.83×10^{3}
YUFLOC	5982.71	276.32	86.77	85.88	2.62×10^{-3}	4.36×10^{-4}	6.01
ERAPUK	4560.50	1918.65	85.94	86.74	1.90×10^{-4}	3.90×10^{-4}	4.87×10^{-1}
NIDBOS	4209.17	259.84	88.11	85.45	4.12×10^{-2}	1.72×10^{-4}	2.40×10^{2}
SEHSUU	4161.53	219.52	85.40	86.01	2.78	4.06×10^{-4}	6.85×10^{3}
AFEJOK	4009.79	952.18	86.22	86.74	5.93×10^{-3}	3.48×10^{-4}	1.70×10^{1}
GUKYUI	3880.99	61.00	90.86	86.71	52.62	1.27×10^{-4}	4.14×10^{5}

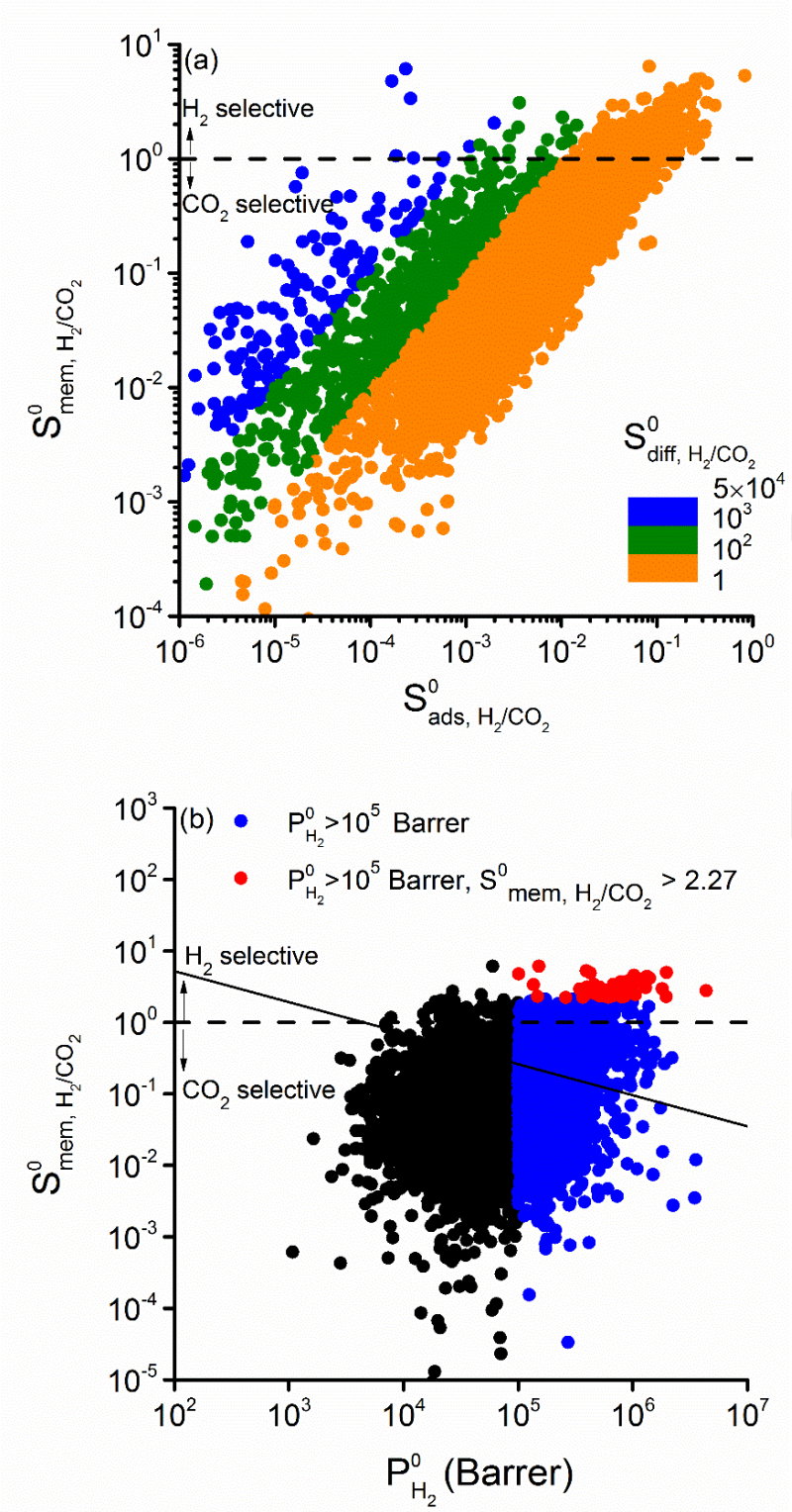

Figure 5.9. (a) Adsorption, diffusion, and membrane selectivities of 10221 MOFs computed at infinite dilution. (b) H_2/CO_2 membrane selectivities and H_2 permeabilities of 10221 MOF membranes. Black solid line represents the Robeson's upper bound for H_2/CO_2 separation whereas black dashed line indicates $S^0_{mem,\,H_2/CO_2} = 1$.

In **Figure 5.9(b)**, $S^0_{mem,\ H_2/CO_2}$ of MOFs was found to be between 2.34×10^{-4}-6.34 whereas $P^0_{H_2}$ was calculated as 1.08×10^3-4.38×10^6 Barrers. 4,234 MOFs exhibited high H_2 permeabilities ($P^0_{H_2}$ >10^5 Barrer) and these materials can decrease the size and cost of membranes for H_2/CO_2 separation. Finally, we note that the number of MOFs (1,854) surpassing the upper bound significantly increased compared to our previous work (899),[89] indicating that new MOF structures deposited into the database have a strong potential as membranes for H_2/CO_2 separation.

Motivated by the promising results from the previous section, we identified the top 10 promising MOF membranes having $S^0_{mem,\ H_2/CO_2}$ >3.80 and $P^0_{H_2}$ >10^5 Barrer and listed their separation performances along with structural properties in **Table 5.2**. Interestingly, 4 out of 10 top MOFs were common with our previous study, showing that high performing MOF membranes have similar characteristics with large pores and large porosities. When we investigated the diffusion characteristics of newly reported MOFs in detail, the newly synthesized MOFs exhibited much higher diffusion selectivities towards H_2, leading to higher membrane selectivities towards H_2 compared to the previously reported MOFs. The number of H_2 selective MOF membranes (397) having $S^0_{mem,\ H_2/CO_2}$ >1 and $P^0_{H_2}$ >10^5 Barrer is much higher than the previously identified MOF membranes (198) having $S^0_{mem,\ H_2/CO_2}$ >1 and $P^0_{H_2}$ >10^5 Barrer, showing the potential of newly synthesized MOFs as membranes for H_2/CO_2 separation.

Up to this point, we derived the membrane performance of MOFs in infinite dilution conditions, but it is also important to consider their behavior at finite pressures. Performing mixture membrane simulations are computationally demanding, for this reason, we carried out mixture MD simulations only for the best performing 10 MOFs and compared the gas permeabilities obtained from these simulations with those calculated at infinite dilution as shown in **Appendix B3**. CO_2 and H_2 permeabilities calculated at infinite dilution agreed reasonably with the permeabilities calculated for the binary gas mixture at both 1 and 10 bar, 298 K. H_2/CO_2 diffusion selectivities calculated at 1 bar were found to be generally higher than those computed at 10 bar. This was attributed to the higher CO_2 uptake at 10 bar, which hinders the transport of H_2, leading to a smaller diffusion coefficient for H_2 in comparison to that obtained at 1 bar. As a result, mixture selectivities of MOF membranes calculated at 1 bar were found to be generally like those calculated at infinite dilution whereas mixture selectivities calculated

at 10 bar were generally lower than those calculated at infinite dilution as indicated in the insets of **Appendix B3(a-b)**. To sum up, infinite dilution simulations can give accurate predictions for H_2 permeability and H_2/CO_2 selectivity of the top performing MOF membranes.

Table 5.2. Separation performances of the top 10 H_2 selective MOF membranes. This list consists of MOFs with $S^0_{mem,\ H_2/CO_2} > 1$ and $P^0_{H_2} > 10^5$ Barrer. MOFs are ranked based on $S^0_{mem,\ H_2/CO_2}$.

MOFs	LCD (Å)	PLD (Å)	ϕ	$D^0_{CO_2}$ (cm^2/s)	$D^0_{H_2}$ (cm^2/s)
FOTNIN	33.63	28.54	0.88	1.78×10^{-4}	1.35×10^{-2}
BAZGAM	42.80	24.23	0.93	8.68×10^{-4}	1.51×10^{-2}
PESSUE	35.69	35.34	0.80	1.99×10^{-4}	3.86×10^{-3}
XANLIJ	26.15	14.45	0.89	6.19×10^{-4}	8.39×10^{-3}
AVAJUE02	37.53	19.54	0.91	5.61×10^{-4}	1.01×10^{-2}
XAHQAA	23.03	21.61	0.91	5.63×10^{-4}	1.06×10^{-2}
KAZSIQ	19.46	17.85	0.88	3.05×10^{-4}	9.08×10^{-3}
CEFNOT	35.04	17.95	0.89	4.14×10^{-4}	8.67×10^{-3}
XAHPUT	21.83	20.59	0.91	4.78×10^{-4}	8.83×10^{-3}
NIBJAK	32.01	17.53	0.90	4.21×10^{-4}	7.65×10^{-3}

MOFs	$P^0_{CO_2}$ (Barrer)	$P^0_{H_2}$ (Barrer)	$S^0_{ads,CO_2/H_2}$	$S^0_{diff,H_2/CO_2}$	$S^0_{mem,H_2/CO_2}$
FOTNIN	2.63×10^5	1.67×10^6	12.00	76.05	6.34
BAZGAM	3.92×10^5	1.97×10^6	3.47	17.42	5.02
PESSUE	8.62×10^4	4.26×10^5	3.93	19.42	4.94
XANLIJ	3.99×10^5	1.83×10^6	2.95	13.55	4.59
AVAJUE02	3.03×10^5	1.33×10^6	4.10	18.06	4.40
XAHQAA	3.37×10^5	1.40×10^6	4.52	18.84	4.17
KAZSIQ	2.94×10^5	1.21×10^6	7.25	29.82	4.11
CEFNOT	2.88×10^5	1.15×10^6	5.25	20.94	3.99
XAHPUT	2.97×10^5	1.16×10^6	4.72	18.47	3.91
NIBJAK	2.70×10^5	1.02×10^6	4.78	18.17	3.80

To benchmark the membrane-based separation performances of the MOFs we investigated we compared them with zeolite and graphene oxide (GO) membranes. NaX[191] and LTA[192] were reported to have H_2 permeabilities of 195.41 and 125.37 Barrer and H_2/CO_2 selectivities of 3.6 and 7.6 at 1 bar, respectively. Most of the top MOF membranes identified in this work exhibited much higher H_2 permeability ranging between 4.87×10^5-1.90×10^6 (1.52×10^5-1.58×10^6) Barrers and almost similar H_2 selectivity between 3.52-5.26 (2.71-4.43) at 1 bar (10 bar). GO membrane[193] exhibited a high H_2 permeability of 5.07×10^3 Barrer and a high H_2/CO_2 selectivity of 48 at 1 bar, 298 K. The best MOF membranes listed in **Table 5.2** can still outperform GO membrane in terms of H_2 permeability. JUC-150[194] and ZIF-8[195] membranes were reported to

exhibit H_2 permeabilities of 1.64×10^4 and 4.48×10^3 Barrers and H_2/CO_2 selectivities of 38.7 and 3.5 at 1 bar, 298 K, respectively. Due to very narrow pores of these MOF membranes, they exhibited two orders of magnitude lower H_2 permeabilities compared to the top MOF membranes we identified in **Table 5.2**. Overall, we can conclude that the top MOF membranes identified in this work can outperform traditional porous membranes in terms of H_2 permeability.

We finally studied structure-performance relations of MOF adsorbents and membranes. **Figures 5.10(a-b)** show the relations between porosity, LCD, and adsorption selectivity of MOFs having 1D, 2D, and 3D structures. Among 10221 MOFs, 5046 MOFs were found to have either 1D or 2D channels whereas 5175 MOFs exhibited 3D channels. As expected, MOFs with small LCDs (5-15 Å) generally exhibited high CO_2/H_2 adsorption selectivities (>1000), regardless of dimensionality due to the strong confinement of gas molecules within small pores. **Figures 5.10(c-d)** show that majority of the top MOF membranes have large LCDs (>20 Å), 3D channels, and high porosities (>0.80). Weakly adsorbed H_2 molecules in these MOFs diffused much faster than the strongly adsorbed CO_2 molecules, resulting in high diffusion selectivities towards H_2. Since MOFs with high porosities and LCDs generally exhibited very low adsorption selectivities <100, their diffusion selectivities toward H_2 governed their membrane selectivities. As a result, MOFs with large pores (>20 Å) and high porosities (>0.80) were identified to be promising for membrane-based H_2/CO_2 separation.

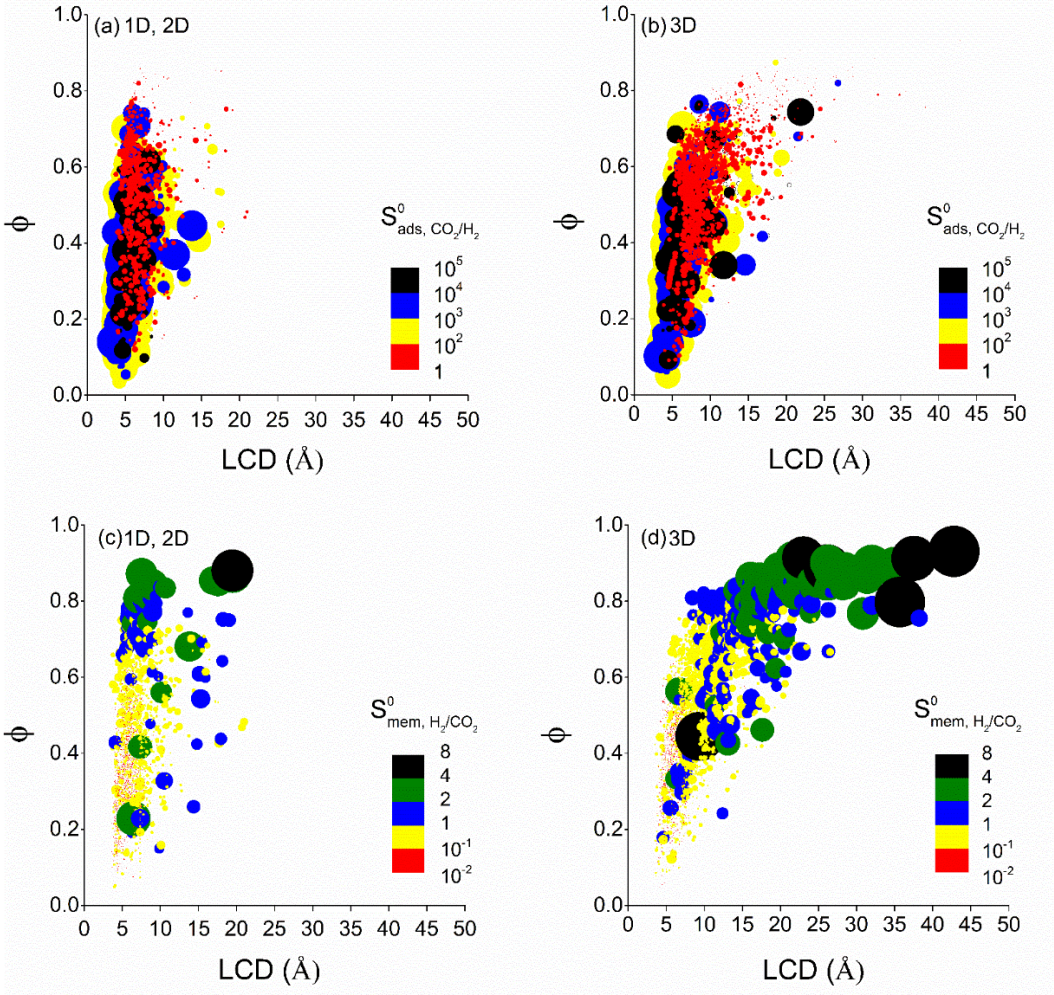

Figure 5.10. Relations between porosities, pore sizes, and CO_2/H_2 adsorption selectivities of (a) 1D-2D MOFs and (b) 3D MOFs. Relations between porosities, pore sizes, and H_2/CO_2 membrane selectivities of (c) 1D-2D MOFs and (d) 3D MOFs. Size of the bubbles represents selectivities of MOFs. Red, yellow, blue, and black regions were scaled with a factor of 4.0×10^{-2}, 2.4×10^{-2}, 2.4×10^{-3} and 2.4×10^{-4}, respectively in (a) and (b); scaling factor of 25 was used in (c) and (d) to have a clear representation.

We also investigated the influence of structural properties, PLD, LCD, SA, and porosity, on the separation performances of the top 100 MOF adsorbents at PSA, VSA, and TSA conditions and the top 100 MOF membranes identified in our previous study[89] in **Figure 5.11(a)** and in our current study in **Figure 5.11(b)**. When the number of MOFs increased from 3857 to 10221, the distributions of most of the textural properties of MOFs exhibited a similar behavior for PSA and VSA processes. The top MOFs at TSA condition showed similar PLDs, and porosities compared to those at VSA whereas the top MOFs at TSA had lower LCDs and porosities compared to the top MOFs at PSA condition. MOFs with small pore sizes (3.30-5.00 Å) and low porosities (0.30-0.60) are the best adsorbent candidates for CO_2/H_2 separation whereas MOFs having high porosities (0.60-1.0) and

large LCD (>15 Å) have high performance as membranes for H_2/CO_2 separation. We also note that newly synthesized MOFs with high PLDs (15-31 Å) are more suitable candidates as membranes in comparison to the previously studied MOFs.[89] These structure-performance relationships can be a useful guidance not only for the selection of MOFs but also for the future synthesis of new MOFs to achieve a high-performance for CO_2 capture and H_2 purification.

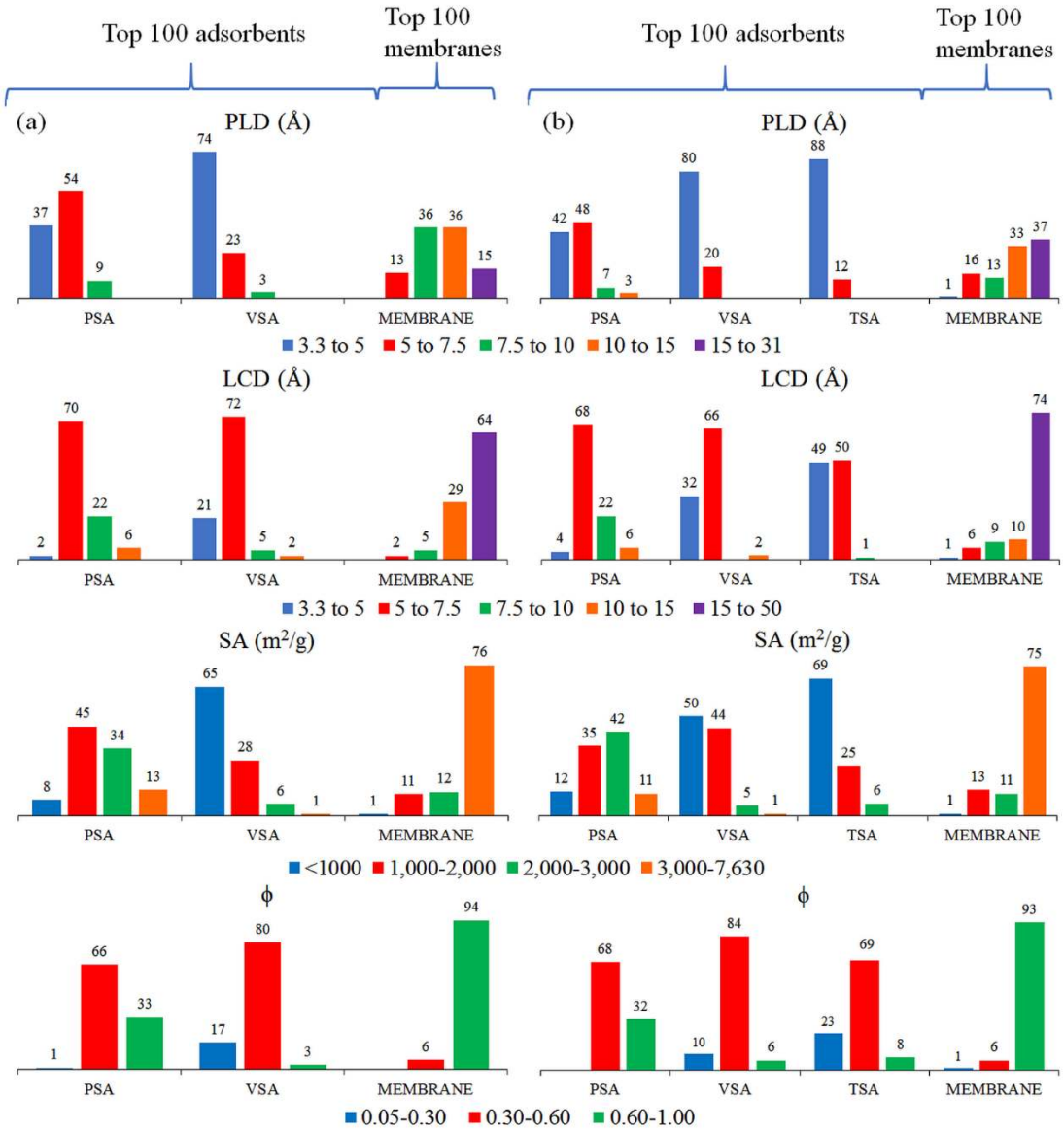

Figure 5.11. Effect of PLD, LCD, SA and ϕ on the separation performance of the % of the top 100 MOF adsorbents at PSA, VSA, and TSA conditions and the % of the top 100 MOF membranes among (a) 3,857 MOFs previously studied and (b) 10,221 MOFs studied in this work.

5.3 Conclusion

In this work, we computationally assessed the performances of 10221 MOF adsorbents and membranes for CO_2 capture and H_2 purification using GCMC and MD simulations. Many MOFs outperformed benchmark zeolites in terms of performance metrics such as CO_2 selectivity, working capacity, APS, and ΔQ. CO_2/H_2 adsorption selectivities of the top performing MOFs were generally underestimated by IAST due to their heterogeneous adsorption sites, underlying the importance of performing mixture GCMC simulations. Blocking of the pores that are inaccessible to CO_2 and H_2 resulted in decreases in CO_2 working capacities and selectivities but increases in R% of MOFs. Results also showed that catenation can significantly improve APSs of MOFs without changing their R%, suggesting that catenation can be a useful design strategy for experiments to obtain high-performance MOF adsorbents for CO_2/H_2 separation. We found that APSs of the top MOFs generally decreased, whereas their R% remained the same in the presence of impurities in CO_2/H_2 mixture. H_2/CO_2 selectivities and H_2 permeabilities of 10221 MOF membranes were computed and many MOF membranes surpassed the upper bound, outperforming polymer membranes. The upper limits of H_2 permeability and H_2/CO_2 selectivity of MOF membranes were computed as 4.38×10^6 Barrer and 6.34, respectively. We finally investigated the influence of structural features of MOFs on their adsorbent and membrane performances. MOFs with small pores (3.30–5.00 Å) and low porosities (0.30–0.60) generally exhibited high adsorption selectivities for CO_2 (>1000), whereas MOFs with large pores (>20 Å) and high porosities (>0.80) exhibited high membrane selectivities for H_2 (3.80–6.34). We showed that the top MOFs identified for adsorption-based CO_2/H_2 separation have narrow pores, exposed metal sites and halogen functional groups which provide favorable adsorption sites for CO_2 molecules due to the strong electrostatic interactions between CO_2 and the MOFs' atoms. However, the top MOF membranes identified for H_2/CO_2 separation have large pores enabling fast and efficient H_2 diffusion which is desired for efficient H_2 purification. We note that all the MOFs we studied including the top ones have been already experimentally synthesized. These results will be useful to guide the future experiments to high-performance MOFs both for adsorption-based CO_2/H_2 separation and membrane-based H_2/CO_2 separation.

Chapter 6*

IMPACT OF METAL EXCHANGE ON CO_2 CAPTURE POTENTIAL OF MOFs

Currently available types of MOFs are generally derivatives of generic MOFs such as Cu-BTC (or synonymously HKUST-1), MOF-74 and UiO-66. Considering the lego-like mix and match approach that can be used to synthesize and design new MOFs, there may be many possible structures with improved adsorbent-based separation performances. To harness these design principles, we used molecular design techniques and molecular simulations, and performed metal exchange on a commonly studied MOF, HKUST-1 and one of the top MOFs identified in the studies from Chapter 4 and Chapter 5, HATGUF. We performed GCMC simulations to investigate the impact of different metal centers on CO_2/H_2 mixture adsorption and separation performances of these M-MOFs where M represents different metals: Cd, Co, Cr, Cu, Fe, Mn, Mo, Ni, Ru, Zn. Many MOFs synthesized to date have nodes with Zn metal and a detailed understanding of their gas separation efficiency upon metal exchange is needed to pave the way for designing next generation of MOFs. Depending on the pore properties and adsorption selectivities, two MOFs from IRMOFs and two MOFs from ZnO-MOFs were selected. The metal atom (Zn) of the selected four MOFs was exchanged with eight different metals (Cd, Co, Cr, Cu, Mn, Ni, Ti, and V) and 32 different M-MOFs were obtained. The influence of metal type on CO_2 capture properties of MOFs were investigated and consequently, adsorbent performance metrics such as selectivity, working capacity, regenerability, and adsorbent performance score of M-MOFs were calculated. Adsorbate density profiles were plotted to identify cooperative and competitive adsorption between CO_2 and H_2 towards the framework. The results presented in this study will serve as a guideline to design new MOFs with exceptional CO_2 separation properties.

*The content of this chapter is taken from the published work (*Avci G., Velioglu S., and Keskin S. In Silico Design of Metal Organic Frameworks with Enhanced CO_2 Separation Performances: Role of Metal Sites. Journal of Physical Chemistry C*, 2019, *123, 28255–28265:doi.org/10.1021/acs.jpcc.9b08581, Avci G., Altintas C., and Keskin S. Metal Exchange Boosts the CO_2 Selectivity of Metal Organic Frameworks Having Zn-Oxide Nodes. Journal of Physical Chemistry C*, 2021, 125*, 17311–17322:* doi.org/10.1021/acs.jpcc.1c03630) and adapted for this thesis.[196] [197]

6.1 Methodology

We first identified the MOFs which could be potentially promising materials for CO_2/H_2 separation after metal exchange. As a prototype MOF, we selected HKUST-1, also called as Cu-BTC since it is the most widely studied MOF in the literature in the field of metal exchange.[80, 82] HATGUF was identified as one of the top promising MOFs at VSA condition from the work discussed at Chapter 5.[66] Both HKUST-1 and HATGUF have similar PLD values (6.65 and 6.67 Å) but their LCD values are different (13.2 and 8.42 Å) since HKUST-1 has tricarboxylate linkers and HATGUF has dicarboxylate linkers that are connected to Cu-paddlewheel nodes. This chemical difference resulted in MOFs with similar structures and different topologies. We removed the coordinated solvent molecules (H_2O) from both cif structures. The distinct pore structures of both MOFs are illustrated in **Figure 6.1**.

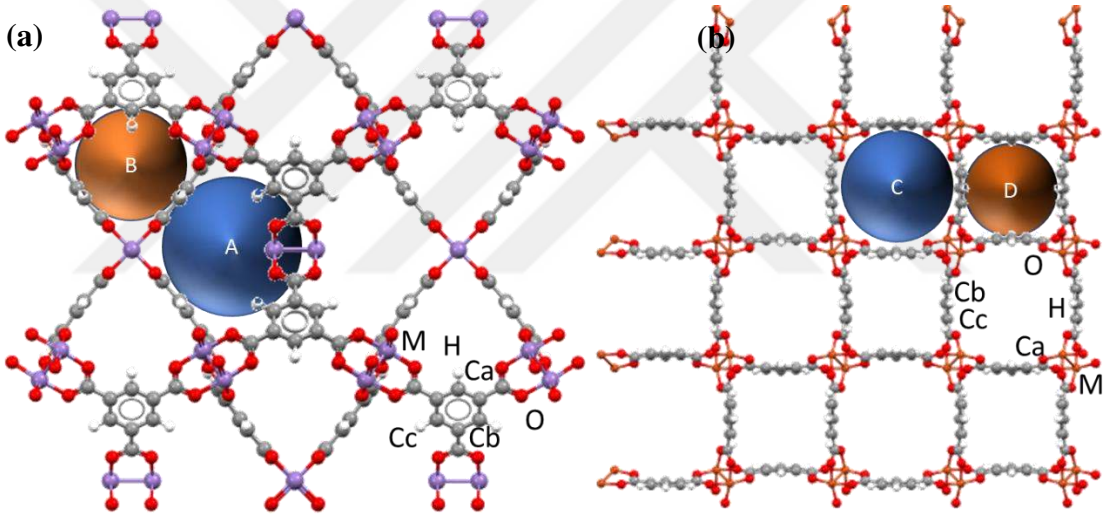

Figure 6.1 Representation of pores existing in (a) M-HKUST-1 and (b) M-HATGUF. A and D represent the largest pores whereas B and C represent the smallest pores.

We proceeded by changing the metals in each MOF by 10 different metals: Cd, Co, Cr, Cu, Fe, Mn, Mo, Ni, Ru and Zn. Cu is the original metal that was present in the structure therefore we ended up with 20 unique MOF structures. We performed the metal exchange procedures in Materials Studio software where we also removed any bound and unbound solvent molecules manually.[95] A maximum number of 1000 iterations were set to satisfy convergence requirements for energy of 10^{-4} kcal/mol. For displacement, energy, and force, 10^{-6} Å, 10^{-5} kcal/mol, and 10^{-4} kcal/mol × A was set, respectively where each simulation converged to minimum energy levels within pre-determined energy threshold values. MOF simulation box was allowed to relax in all three dimensions to

release additional stress caused by larger or smaller replaced metal radii. We used UFF parameters as implemented in Materials Studio to consider for intermolecular interactions. QeQ (charge equilibration method) or EQEq (Extended charge equilibration method) charge assignment methods were implemented depending on the oxidation state that satisfied reasonable electrostatic interactions between MOF atoms and gas molecules.[139, 198] The partial charges for both M-HKUST-1 and M-HATGUF are shown in **Appendix Table C1.**

We used the same high-throughput screening parameters as discussed in methodology part in Chapter 5 to calculate structural properties of MOFs. We set the probe radius as 1.87 Å and 0 Å to calculate the surface area and porosity. We controlled the optimization quality of our geometry optimizations by investigating the PLD and LCD values of each optimized structure. For M-HKUST-1 series, PLD (LCD) ranged from 6.22 to 6.74 Å (6.22-7.36), and for M-HATGUF series PLD (LCD) ranged from 12.02-13.44 Å (7.21-8.78 Å) which showed that MOFs' cell parameters were allowed to relax correctly after metal exchange.

In our further study with metal exchange of MOFs, we utilized CSD ConQuest software[199] and conducted a connectivity search on 10,221 MOFs. The guidelines described in the literature[200] were followed for targeted classification of MOFs and 933 MOFs with Zn-oxide nodes were identified. 933 MOFs were further narrowed down to 769 MOFs after excluding the MOFs that have functional groups and/or more than one type of organic linker. Complete metal-exchange of MOFs severely depends on factors such as the pore size distribution and flexibility of the framework, framework stability, coordination geometry of the metal node, and steric hindrance caused by the linkers.[201] We aimed to work on relatively simple MOF structures and eliminated the MOFs consisting of mixed linkers and/or functional groups due to the following reasons: (i) MOFs designed with mixed linker strategies can have defects,[202, 203] or differing topologies and crystal structures,[204] but we aimed to work on MOFs with similar topologies after metal exchange and with defect-free, homogeneous adsorption surface. (ii) MOFs with functional groups can have strong electrostatic interactions with CO_2 as shown in our previous works[205, 206] but we aimed to isolate the influence of metal exchange on CO_2/H_2 selectivity by omitting the MOFs with functional groups and mixed linkers. 769 MOFs with Zn-oxide nodes, single type of linker, and no functional groups were divided into two final subgroups depending on the shape of the metal cluster

(coordination of the node): 140 IRMOF-like MOFs (IRMOFs) and remaining (629) MOFs with Zn-oxide nodes (ZnO-MOFs). The main difference between IRMOF-like and ZnO-MOFs is the shape of the metal cluster.[200] MOFs with IRMOF-like structures have a 4-connected configuration with oxygen atoms connected to each metal site as shown in **Figure 6.2 (a)**, while MOFs with ZnO-MOF type structures have two metal atoms connected with four oxygen and one Zn atom bonded with six oxygen as shown in **Figure 6.2 (b)**.This classification methodology is shown in **Figure 6.3.** together with the representative MOFs selected for metal exchange from IRMOFs and ZnO-MOFs. Representative MOFs from IRMOFs and ZnO-MOFs which satisfy the following two criteria were selected for metal exchange: (i) MOFs with PLD >4 Å to avoid pore sizes smaller than or very close to the size of the gas molecules after geometry optimization, (ii) MOFs with CO_2/H_2 mixture selectivity (S_{ads})~100 at 1 bar since these materials can have outstanding separation performances upon an increase in their CO_2 uptakes with metal exchange. We also identified a peer-MOF for each selected MOF to compare the change in their gas separation performances upon the metal exchange. 16 IRMOFs and 284 ZnO-MOFs had pore sizes >4 Å and S_{ads} ~100.

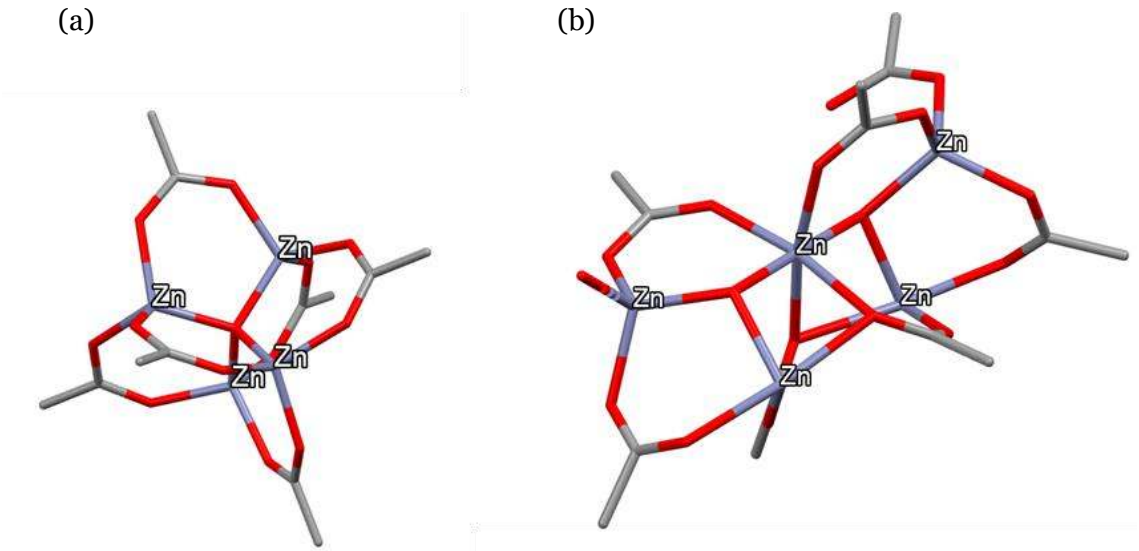

Figure 6.2. Classification of MOF node types according to bonding scheme for a) IRMOFs and b) ZnO-MOFs. Carbon, oxygen, and zinc are represented with gray, red, and purple, respectively.

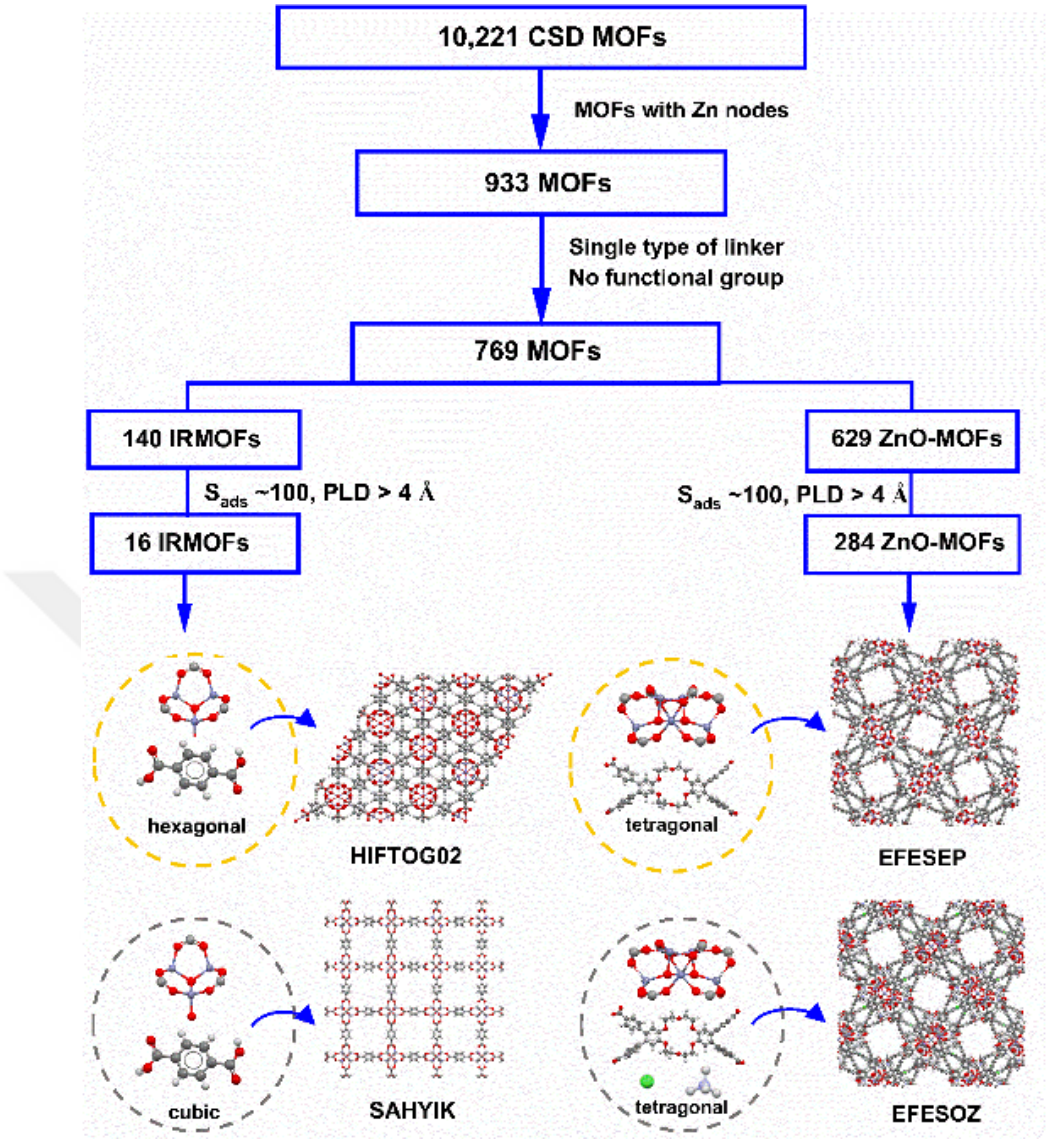

Figure 6.3. Targeted MOF categorization according to the type of the node and building blocks to select the representative MOFs for *in-silico* metal exchange. Carbon, oxygen, hydrogen, zinc, chlorine, and nitrogen are represented with gray, red, white, purple, green and light blue, respectively.

Among 16 IRMOFs, HIFTOG02 (PLD: 4.15 Å, S_{ads}: 119) was selected since it has the same building blocks with SAHYIK (known as IRMOF-1 or MOF-5)[207] but arranged in a hexagonal crystal geometry unlike the cubic geometry of SAHYIK.[208] Although SAHYIK (PLD: 7.8 Å) has a low S_{ads}, 9.5 at 1 bar, it was selected as the peer for HIFTOG02 to compare the influence of catenation on MOF performance upon the metal exchange. Among 629 ZnO-MOFs, EFESEP (SNU-200) with PLD of 6.13 Å and S_{ads} of 160 was selected with its peer EFESOZ (PLD: 6.2 Å, S_{ads}: 160), which has the same crystal structure with EFESEP but with the guest ions Cl^- and NH_4^+,[209] to investigate the influence of the guest ions on the gas separation performances of the metal

exchanged ZnO-MOFs.

We note that the coordination geometry of the node, steric hindrance exposed by the linkers, pore size, and the stability of the framework are the preliminary factors that we considered before selecting the candidate MOFs for metal exchange.[201] The four MOFs we considered in our work for metal exchange (SAHYIK, HIFTOG02, EFESEP, and EFESOZ) have been experimentally reported to be stable with mediocre pore sizes.[208, 209] We considered pore sizes between 3.3 Å and 4 Å as small, 4 Å and 15 Å as mediocre, 15 Å and 45 Å as large by following the convention used in our previous study.[206] We selected SAHYIK as a benchmark MOF since several previous works have both experimentally and computationally performed metal exchange on IRMOF series.[210-213] For example, Ti, V, Cr, Mn, Fe, and Ni variants of MOF-5 were experimentally reported via cation exchange.[210, 211]HIFTOG02[208] is the catenated form of MOF-5, thus we assumed that a metal exchange procedure similar to that of MOF-5 can be easily implemented on this material. We selected SNU-200 variants, EFESEP and EFESOZ, since SNU-200[209] has Zn-oxide nodes in frequently observed coordination geometries (octahedral and tetrahedral), and in a previous work,[214] exchange of Zn with Pd, Cd, Cu, Ni, Co, Mn and Cr has been experimentally reported for a structure which have a similar type of node geometry.

To examine the impact of metal type on the CO_2/H_2 and CO_2/CH_4 separation performances of SAHYIK, HIFTOG02, EFESEP and EFESOZ, we studied eight different metals, Cd, Cu, Co, Cr, Mn, Ni, Ti, and V, which are commonly employed both in computational and experimental metal exchange studies on MOFs,[211, 213, 215] and obtained 32 unique metal-exchanged MOFs (M-MOFs). Prior to metal exchange, bound and unbound solvent molecules were cleaned from structures and metal exchange and geometry optimization were performed with Materials Studio 2020.[216] Original metal (Zn) of the structures were modified using the "modify element" tool implemented in the Materials Studio, and energy of the structure was minimized with a convergence tolerance of ultrafine (10^{-5} kcal/mol). Smart algorithm was employed for geometry optimization with a maximum iteration of 1000 steps. Convergence tolerances for geometry optimization were set as 10^{-6} Å for distance, 10^{-5} kcal/mol for energy and 10^{-4} kcal/mol/Å for force. Unit cell parameters were allowed to relax during geometry optimization, which enabled the bonds between atoms of the MOF relax after the metal exchange step. More details of this method were described in our previous study.[217]

We used the RASPA software for GCMC simulations. UFF was set to identify LJ interactions, which summed up all interaction pairs for gas-gas and gas-MOF interactions. Single-site spherical and three-site rigid 12-6 LJ potentials were established to accurately model H_2 and CO_2, respectively. CH_4 was modeled using the TraPPE model as a unified sphere with van der Waals interactions.[218] Lorentz-Berthelot mixing rules identified the LJ interactions between unlike pairs of atoms. Ewald summation with 10^{-6} precision was set for both real and imaginary parts of the equation. A cutoff radius of 12.5 Å was used rather than 13.0 Å as shown in Chapter 4 and Chapter 5 methodology parts, since some MOFs had smaller unit cell diameters after optimization and cutoff rule was reassigned accordingly. To produce high quality adsorption profiles, we performed 5000 cycles for initialization and 100000 cycles for production. To investigate the influence of gas composition upon adsorption, CO_2/H_2:15/85 and CO_2/H_2:50/50 mixture ratios were investigated at 0.1, 1 and 10 bar, 298 K. To produce adsorption profiles, we used the VTK (The Visualization Toolkit) that was implemented in RASPA.

We used the same adsorbent performance metrics as discussed in Chapter 4 and Chapter 5, namely adsorption selectivity, working capacity, regenerability and adsorbent performance score. We used the fluctuation method to calculate isosteric heat of adsorption values at finite pressure levels.[94]

6.2 Results and Discussion

Assessing the computational accuracy of molecular simulations is essential especially for MOFs with different metals, therefore we compared the available computational and experimental data for M-HKUST-1 with our simulation results. We compared our simulation results with the experimental CO_2 uptakes of Cu-HKUST-1 (at 298 K),[219] Cu-HKUST-1 (at 333 K),[220] Ru-HKUST-1,[221] Cr-HKUST-1,[219] Fe-HKUST-1[220] under the same conditions. Different charge assignment methods can capture different coulombic environments in MOFs, as MOFs with neutral oxidation states will produce better results with QeQ method and MOFs with higher valency metal clusters will produce better results with EQEq method.[198] We compared the readily available experimental data with QeQ method, EQEq method with +2 oxidation state and EQEq method with +3 oxidation state on M-HKUST-1 (M= Cu, Ru, Cr, Fe, Co, Ni and Zn) as shown in **Appendix Figure C1**. QeQ method resulted in best isotherm reproduction for the whole pressure range between 0.1-1 bar whereas Cr-HKUST-1

showed a good agreement between experimental and simulation adsorption isotherms when EQEq method was used with +2 oxidation state. For Ni- and Zn-HKUST-1, the computational DFT data was well reproduced with EQEq +2 oxidation state charges as shown in **Appendix Figure C1**. Although we could not find any experimental data for Cd-HKUST-1, we observed a positive Coulombic energy when EQEq method was used therefore we used the QeQ method for Cd-HKUST-1. For rest of the MOFs that we could not find any experimental or computational isotherms such as Mn- and Mo-HKUST-1, we used the QeQ method. The overall charge assignment is shown in **Appendix Table C2.**

The CO_2 and H_2 uptakes of M-HKUST-1 series for CO_2/H_2:15/85 mixture at 0.1, 1 and 10 bar, 298 K are shown in **Figure 6.4**. In each figure, metal charges of MOFs, difference of heats of adsorption values between CO_2 and H_2, and surface area of MOFs were color-coded to examine their effects on the CO_2 and H_2 adsorption on adsorbents having different metals. **Figure 6.4(a)** shows that as the value of metal charge increases, CO_2 adsorption increases whereas H_2 adsorption decreases for all MOFs except Mo-, Ru- and Cd-HKUST-1. Three MOFs, Mo-, Ru- and Cd-HKUST-1, are located at a different region due to their large ionic radii. **Figure 6.4(b)** shows that M-HKUST-1 materials having high CO_2 uptakes are the ones having the largest difference between the heat of adsorption values of two gases, ($\Delta Q_{st} = Q_{st}^{CO_2} - Q_{st}^{H_2}$). For all MOFs, $Q_{st}^{H_2}$ values were calculated to be almost the same, 5.37-5.75 kJ/mol, but $Q_{st}^{CO_2}$ values were computed to vary from 23.9 to 25.5 kJ/mol, indicating that metal type has a more pronounced effect on the CO_2 uptake than H_2 uptake. **Figure 6.4(c)** represents that there is not a direct relation between the gas uptakes and surface areas of MOFs, in agreement with the literature where it was shown that simple geometrical factors such as surface area and porosity are not sufficient to explain gas adsorption in MOFs.[222] We identified three different regions based on the calculated surface areas of MOFs in **Figure 6.4(c)** and **Figure 6.4(d)** represents the similarities between the pore sizes of MOFs grouped in each region. MOFs with the highest surface areas (Cr-, Cu-, Co-, Mn- and Fe-HKUST-1) exhibit the highest H_2 adsorption but their CO_2 uptakes vary depending on the metal charges as shown in **Appendix Table C2.**

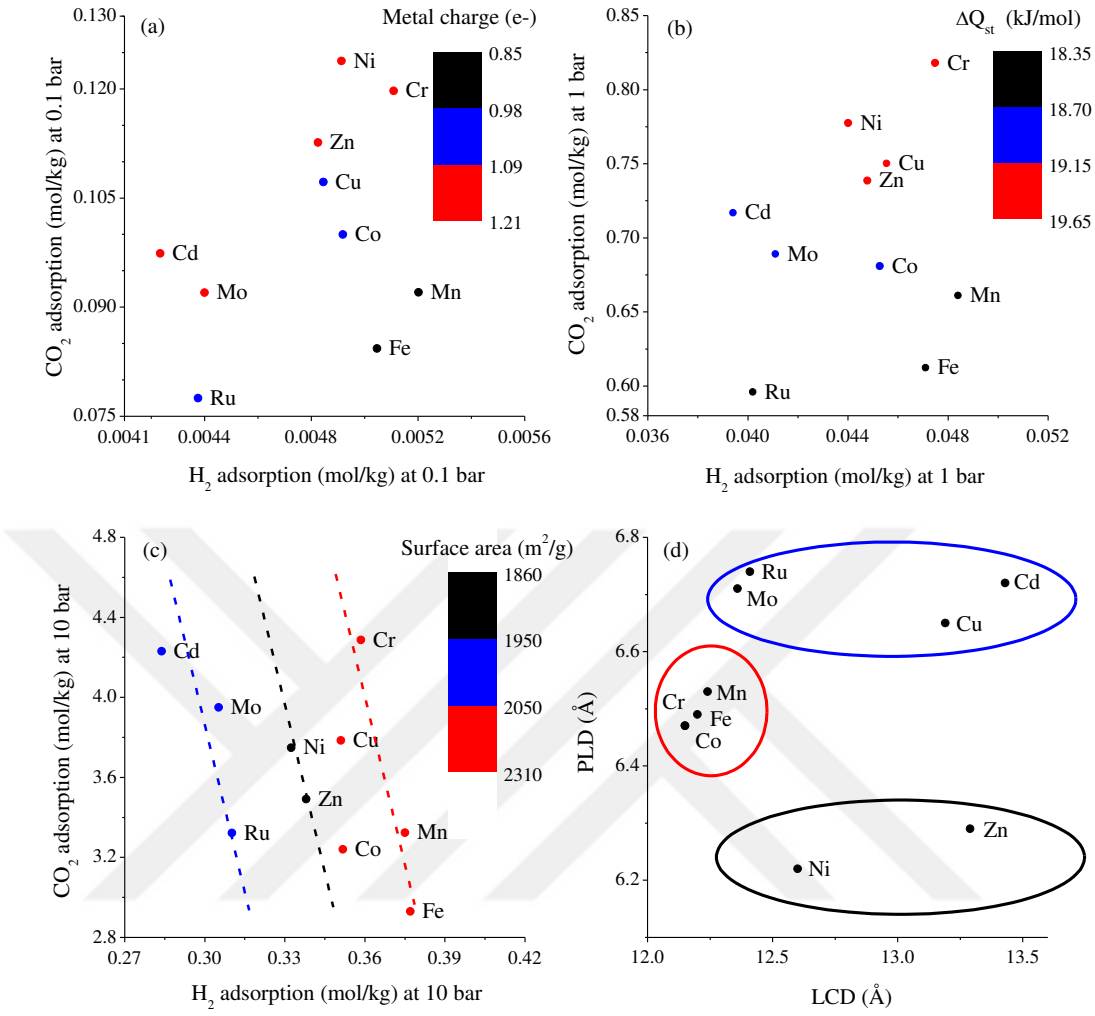

Figure 6.4. CO_2 and H_2 uptakes in M-HKUST-1 series at (a) 0.1, (b) 1, (c) 10 bar and 298 K. (d) PLD and LCD of M-HKUST-1 series.

Figure 6.5 reveals the density plots of adsorbed CO_2 and H_2 positions in M-HKUST-1 materials for CO_2/H_2:15/85 mixture at 298 K, 10 bar. We specifically focused on three MOFs, Fe-, Cu-, and Cd-HKUST-1 since (i) Fe-HKUST-1 has the lowest CO_2 and the highest H_2 adsorption; (ii) Cu is the original metal of HKUST-1; (iii) Cd-HKUST-1 has the highest CO_2 and the lowest H_2 adsorption at 10 bar. The metal change from Fe to Cu and from Cu to Cd alters the regions that CO_2 is adsorbed in the framework due to the change in the electronic environment, as the electronic environment gets more positively charged (calculated partial charges of Fe, Cu, and Cd are 0.85, 0.99, and 1.21 e^-, respectively) along with the decreased surface area (calculated surface areas of Fe, Cu, and Cd-HKUST-1 are 2249, 2160, 1871 m^2/g, respectively). **Figure 6.5(a-c)** shows that as the effect of charge environment dominates and accessible surface area decreases

because of metal change, the second most preferential adsorption site becomes available for the guest molecules, enhancing the CO_2 adsorption. **Figure 6.5(d-f)** shows that H_2 tends to be adsorbed both in small and large pores. As the partial charge of the metal increases from **Figure 6.5(d)** to **(f)**, adsorption of H_2 molecules is hindered due to CO_2 adsorption around the favorable adsorption sites. As a result, in contrast to being adsorbed around the most favorable adsorption sites in pore B as shown in **Figure 6.5(d)**, H_2 molecules are more preferentially adsorbed in pore A as shown in **Figure 6.5(e-f)**. Overall, these density plots of adsorbate positions provided molecular-level information about how the gas adsorption preference of M-HKUST-1 materials changes depending on the identity of metals.

Figure 6.6 shows CO_2 and H_2 adsorption in M-HATGUF series at pressures of 0.1, 1 and 10 bar, 298 K. Like **Figure 6.4** where M-HKUST-1 was studied, metal charges, difference of heats of adsorption values between CO_2 and H_2, and surface areas of M-HATGUF materials were color-coded to examine their impacts on the adsorption of CO_2/H_2 mixture. **Figure 6.6(a)** shows that CO_2 adsorption generally increases with the value of metal charge at low pressure. **Figure 6.6(b)** shows that CO_2 adsorption increases with the values of ΔQ_{st}, whereas H_2 adsorption decreases which can be attributed to the competitive adsorption between two gases in the mixture. We also note that the values of $Q_{st,\,CO_2}$ in M-HKUST-1 were computed to vary between 23.9 and 25.5 kJ/mol whereas they were calculated to range between 24.3 and 34.0 kJ/mol for M-HATGUF series. This result indicates that changing the metal type has a more pronounced effect on the CO_2 affinity of M-HATGUF compared to M-HKUST-1. **Figure 6.6(c)** shows that both CO_2 and H_2 adsorption increase with the surface area of materials whereas pore sizes shown in **Figure 6.6(d)** do not significantly affect the gas adsorption properties of M-HATGUF.

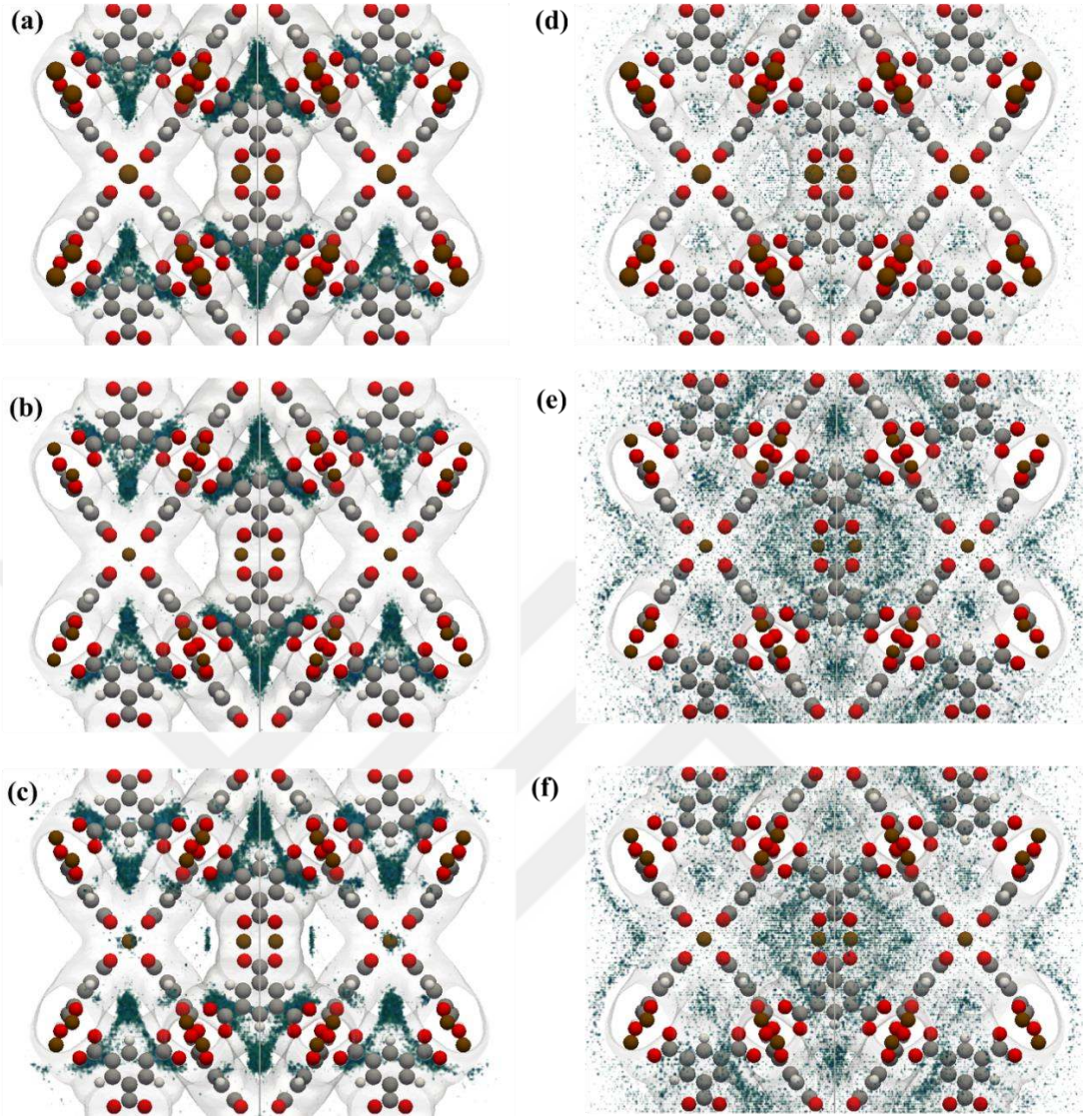

Figure 6.5. Density plots of adsorbed CO_2 positions within the unit cell of M-HKUST-1 where M is (a) Fe, (b) Cu, (c) Cd at 10 bar and 298 K. Density plots of adsorbed H_2 positions within the unit cell of M-HKUST-1 where M is (d) Fe, (e) Cu, (f) Cd at 10 bar and 298 K. Cyan dots show the locations where gas molecules were adsorbed in the GCMC simulations. Carbon, hydrogen, oxygen, and metal in the framework were represented using gray, white, red, and brown colors, respectively.

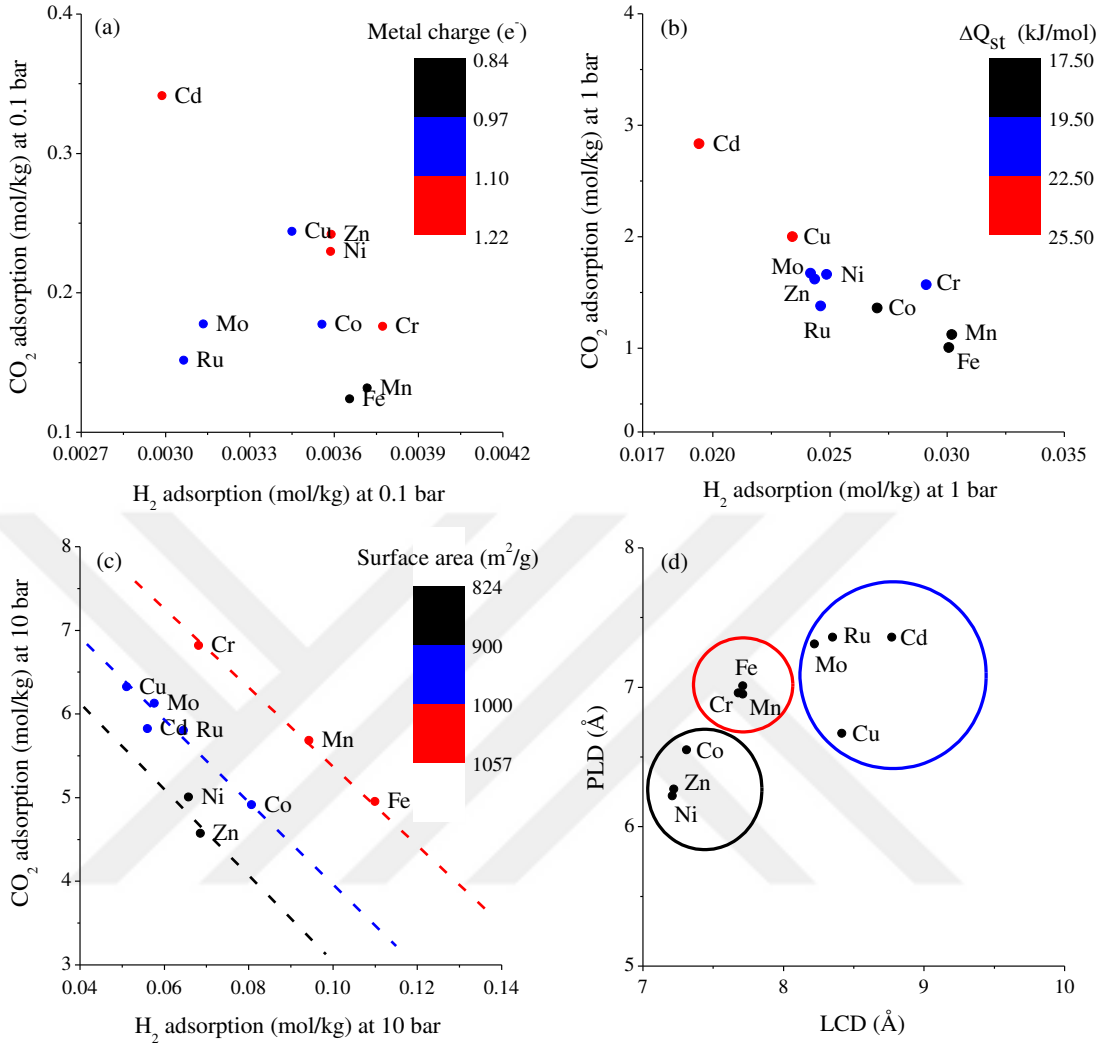

Figure 6.6. CO_2 and H_2 uptakes in M-HATGUF series at (a) 0.1, (b) 1, (c) 10 bar and 298 K. (d) PLD and LCD of M-HATGUF series.

Figure 6.7 shows the density plots of adsorbed CO_2 and H_2 positions in Zn-, Cu-, and Cr-HATGUF at 10 bar, 298 K. Zn and Cr were specifically compared with Cu (the original metal of HATGUF) since the former represents the MOF having the lowest CO_2 adsorption and the latter represent the MOF having the highest CO_2 adsorption. **Figure 6.7** shows that CO_2 and H_2 are preferentially adsorbed on the same adsorption sites. For this reason and because of its lower surface area, Zn-HATGUF revealed the lowest CO_2 adsorption capacity among Zn-, Cu-, and Cr-HATGUF. CO_2 molecules preferred both pores for adsorption in Zn-HATGUF (**Figure 6.7(a)**) while they preferred the adsorption sites available in the small pore in Cu- and Cr-HATGUF as shown in **Figure 6.7(b)** and **(c)**, respectively. On the other hand, adsorbed H_2 molecules were more concentrated

around the favorable sorption sites of Zn- and Cr-HATGUF (**Figure 6.7(d)** and **(f)**) leading to higher H_2 adsorption compared to Cu-HATGUF (**Figure 6.7(e)**).

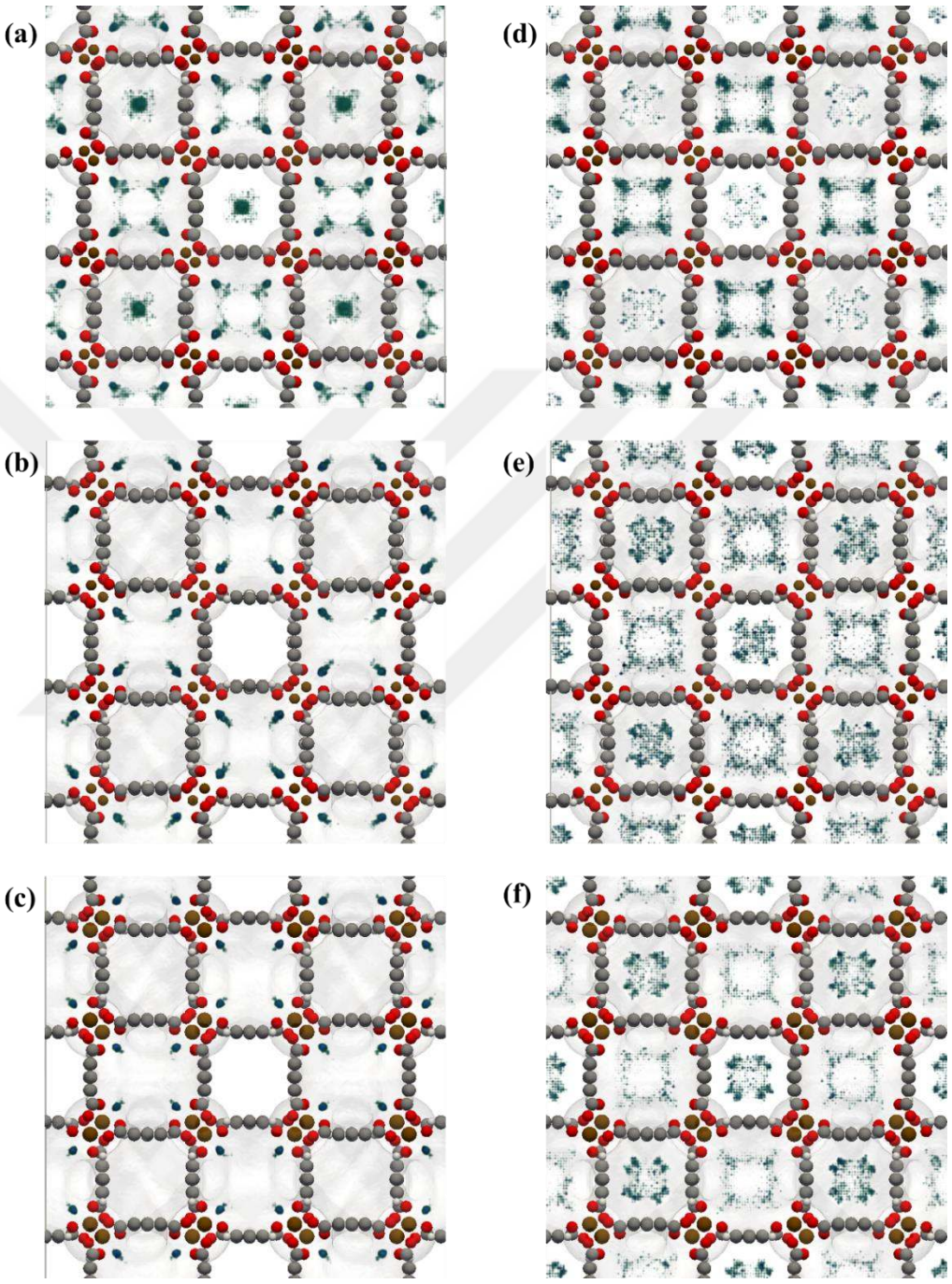

Figure 6.7. Density plots of adsorbed CO_2 positions within the unit cell of M-HATGUF where M is (a) Zn, (b) Cu, (c) Cr at 10 bar and 298 K. Density plots of adsorbed H_2 positions within the unit cell of M-HKUST-1 where M is (d) Zn, (e) Cu, (f) Cr at 10 bar and 298 K. Cyan dots show the locations where gas molecules were adsorbed in the GCMC simulations. Carbon, hydrogen, oxygen, and metal in the framework were represented using circles with gray, white, red, and brown colors, respectively.

The main purpose of designing new MOFs with metal exchange is to improve CO_2/H_2 separation performances of M-HKUST-1 and M-HATGUF materials. Therefore, after evaluating CO_2/H_2 mixture adsorption in M-HKUST-1 and M-HATGUF series, we focused on how the adsorbent performance metrics of these materials change depending on the metal type of MOFs. **Figure 6.8** shows CO_2/H_2 adsorption selectivity and CO_2 working capacity at VSA and PSA conditions for M-HKUST-1 (**Figure 6.8(a-b)**) and M-HATGUF (**Figure 6.8(c-d)**). Cu-HKUST-1 and Cu-HATGUF are the reference MOFs for the comparison of adsorbent performance metrics of M-HKUST-1 and M-HATGUF materials and therefore their locations are marked with dotted lines in each figure. CO_2/H_2 selectivity and CO_2 working capacity of Cu-HKUST-1 were calculated as 93.34 and 0.64 mol/kg at VSA condition, and 61.11 and 3.03 mol/kg at PSA condition, respectively. Cr-HKUST-1 (selectivity of 97.64 and working capacity of 0.70 mol/kg) and Ni-HKUST-1 (100.10 and 0.65 mol/kg) outperform the original Cu-HKUST-1 at VSA condition as shown in **Figure 6.8(a)**. At PSA conditions, Mo-HKUST-1 (73.33 and 3.26 mol/kg), Cr-HKUST-1 (67.75 and 3.47 mol/kg), and Cd-HKUST-1 (84.43 and 3.51 mol/kg) outperform the original Cu-HKUST-1 as shown in **Figure 6.9(b)**. CO_2/H_2 selectivity and CO_2 working capacity of Cu-HATGUF were computed as 484.57 and 1.76 mol/kg at VSA condition, and 701.23 and 4.32 mol/kg at PSA condition, respectively. Only Cd-HATGUF (827.40 and 2.49 mol/kg) outperforms the original HATGUF at VSA condition (**Figure 6.9(c)**). Cd atom has the highest epsilon value and the highest metal charge among all the metals we studied for M-HATGUF series as shown in **Appendix Table C1**, therefore both electrostatic and van der Walls interactions strongly favored adsorption of CO_2 over H_2, resulting in a significant selectivity improvement when Cd was used as the metal in the framework. At PSA condition (**Figure 6.9(d)**), metal change in HATGUF led to improvements only in the CO_2 working capacities. Mo-HATGUF (4.46 mol/kg), Ru-HATGUF (4.42 mol/kg), Mn-HATGUF (4.56 mol/kg), and Cr-HATGUF (5.25 mol/kg) were found to have higher CO_2 working capacities than Cu-HATGUF but none of them resulted in a selectivity enhancement.

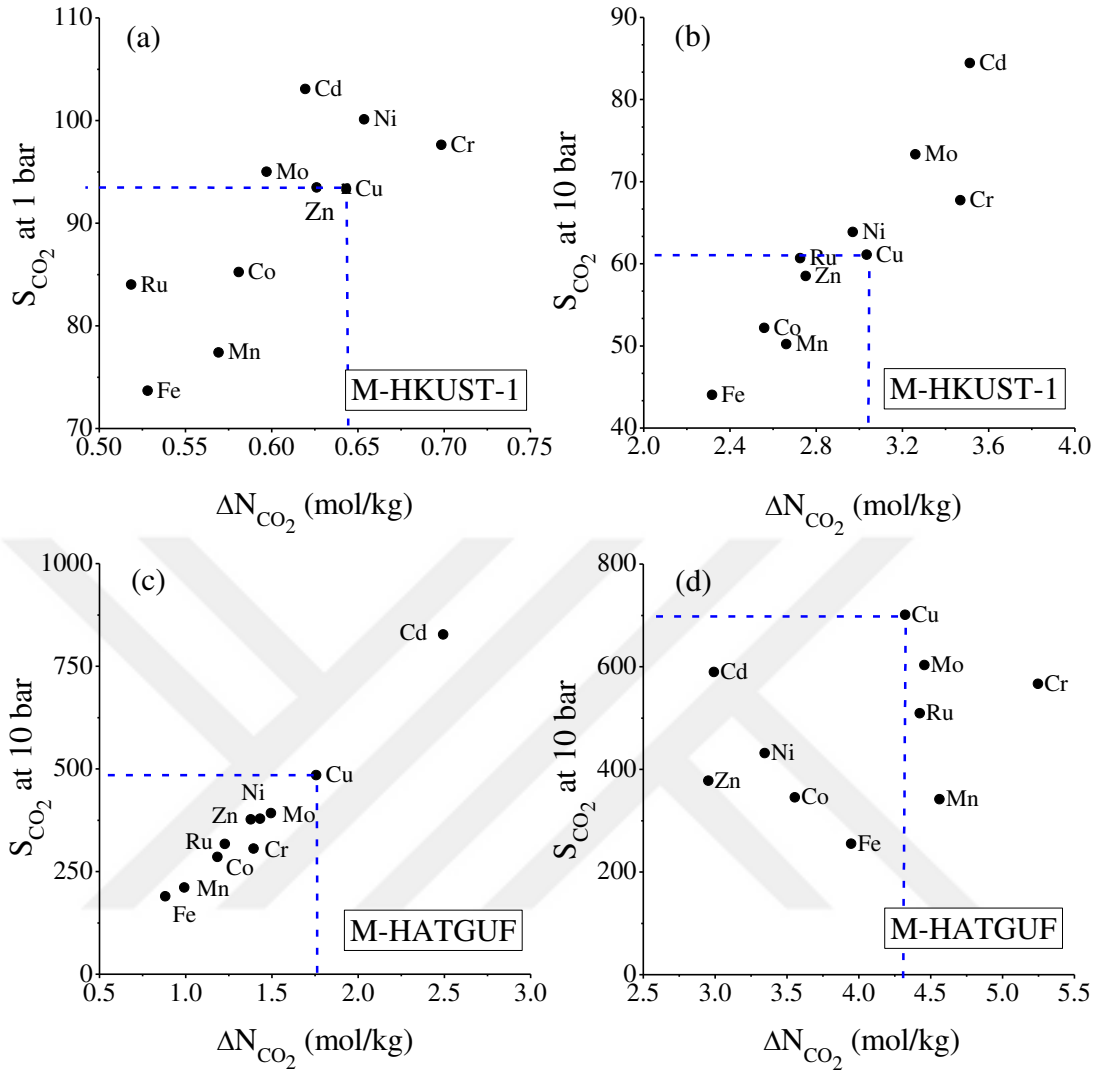

Figure 6.8. Calculated selectivity and working capacity for M-HKUST-1 series at (a) VSA, (b) PSA conditions. Calculated selectivity and working capacity for M-HATGUF series at (c) VSA, (d) PSA conditions.

To compare CO_2/H_2 selectivity and working capacity of M-HKUST-1 and M-HATGUF series, we investigated the gas-gas and gas-MOF interaction energies of MOFs in **Appendix Figure C3.** We showed the Coulomb and LJ energies separately. Lennard-Jones energies between adsorbates and M-HKUST-1 series were comparable with those between adsorbates and M-HATGUF series at every pressure. However, Coulomb energies between CO_2 and M-HATGUF series were greater than those between CO_2 and M-HKUST-1 series at each pressure. Higher CO_2 adsorption capacity of M-HATGUF series compared to M-HKUST-1 series can be explained by the higher CO_2-MOF Coulomb energy and because of this, higher adsorption capacity, higher selectivity and higher working capacity values were calculated for M-HATGUF series compared to M-

HKUST-1 series.

We so far focused on CO_2/H_2:15/85 mixture since it is the relevant composition for the pre-combustion CO_2 capture. To explore the effect of composition on our results, we also studied adsorption of CO_2/H_2:50/50 mixture and compared simulated CO_2 uptakes and selectivities of M-HKUST-1 and M-HATGUF with those calculated for CO_2/H_2:15/85 gas mixtures in **Appendix Figure C1.** At low pressures, 0.1 and 1 bar, changing the composition did not significantly affect selectivities of MOFs. At 10 bar, CO_2/H_2 adsorption selectivities were calculated to increase for M-HKUST-1 series while they were computed to slightly decrease for M-HATGUF series when the composition was changed from 15/85 to 50/50. The rankings of M-HKUST-1 and M-HATGUF series based on their CO_2 uptakes and CO_2/H_2 selectivities were found to be very similar for CO_2/H_2:15/85 and CO_2/H_2:50/50 mixtures. We computed the Spearman correlation coefficients (SRCC) which shows the relationship between two independent ranking lists (one for CO_2/H_2:15/85 mixture and the other for CO_2/H_2:50/50 mixture). If the correlation between two independent rankings agrees well, SRCC reaches to 1. SRCC values for CO_2 uptakes of M-HKUST-1 and M-HATGUF series were calculated to be in the range of 0.88-0.96 and 0.75-0.99, respectively whereas SRCC values for CO_2/H_2 selectivity of M-HKUST-1 and M-HATGUF series were computed as 0.93-0.99 and 0.89-0.99, respectively, depending on the pressure.

Although selectivity and working capacity are widely used to assess the gas separation performance of MOF adsorbents, a recent approach in identifying the most promising MOFs is to rank the materials having R%>85% based on their APS values.[223] **Figure 6.9** shows calculated R% and APS of M-HKUST-1 (**Figure 6.9(a-b)**) and M-HATGUF (**Figure 6.9(c-d)**) at VSA and PSA conditions. We computed R% and APS of original HKUST-1 as 85.71% and 60.03 mol/kg at VSA condition, and 80.18% and 185.44 mol/kg at PSA condition. Enhancement in both metrics (R% and APS) was observed at VSA condition when the metal was changed from Cu to Cd as shown in **Figure 6.9(a)**. Cd-HKUST-1 was calculated to have R% of 86.41% and APS of 63.85 mol/kg. **Figure 6.9(b)** shows that improvements in both metrics were achieved when Cd, Mo and Cr were used as metals in HKUST-1. Cd-HKUST-1 (R% of 83.05% and APS of 296.63 mol/kg), Mo-HKUST-1 (R% of 82.55% and APS of 239.11 mol/kg) and Cr-HKUST-1 (R% of 80.92% and APS of 235.01 mol/kg) outperform Cu-HKUST-1 at PSA condition. We note that APS of Cd-HKUST-1 was 1.6 times greater than that

of Cu-HKUST-1, and Cd-HKUST-1 was also estimated to have the highest R% among all M-HKUST-1 materials. These results show that using Cd as the metal center in HKUST-1 leads to an adsorbent offering higher APS and R% at both VSA and PSA conditions.

R% and APS of Cu-HATGUF were computed as 87.80% and 851.35 mol/kg at VSA, and 68.36% and 3030.98 mol/kg at PSA conditions, respectively. **Figure 6.9(c)** shows that there is a dramatic enhancement in APS of HATGUF when Cu was changed with Cd at VSA condition.

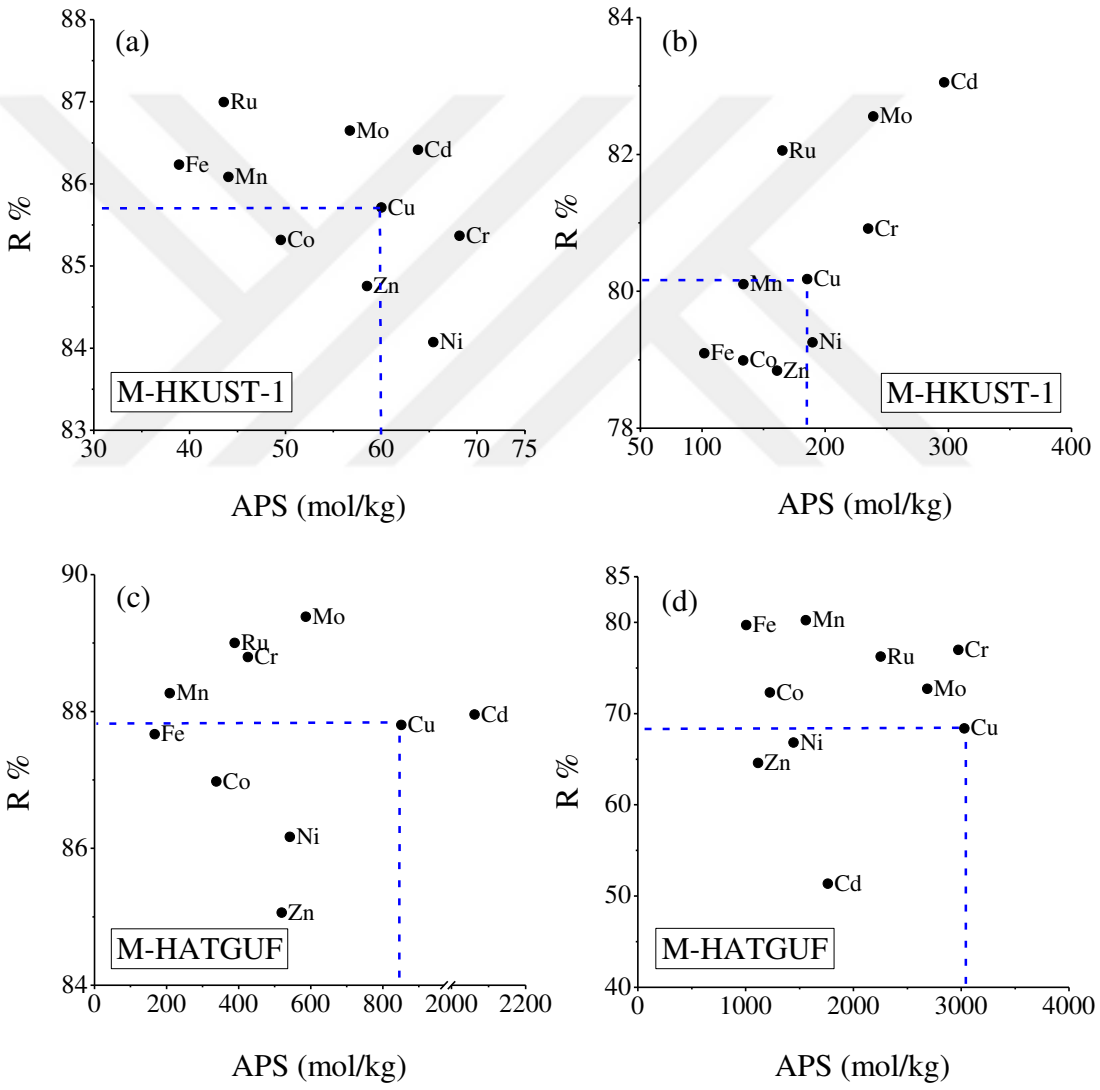

Figure 6.9. Calculated R% and APS for M-HKUST-1 series at (a) VSA, (b) PSA conditions. Calculated R% and APS for M-HATGUF series at (c) VSA, (d) PSA conditions.

Specifically, APS of Cd-HATGUF (2062.63 mol/kg) was more than double of Cu-

HATGUF with a slightly improvement in R%. The high APS of Cd-HATGUF is due to its high CO_2/H_2 selectivity as we discussed above. The highest epsilon value and the highest metal charge value of Cd-HATGUF lead to strong interactions between CO_2 molecules and framework atoms which result in an increase in the CO_2 adsorption and a decrease in H_2 adsorption. Therefore, Cd-HATGUF revealed better separation performance than the original Cu-HATGUF that we identified to be highly promising at VSA condition in our previous computational screening study.[223] On the other hand, **Figure 6.9(d)** shows that using different metal sites can improve only R% without offering an enhancement in APS of HATGUF at PSA condition.

Results so far indicate the huge potential of tuning the adsorbent performance metrics of MOFs through metal change. To reveal the role of metal change in the adsorbent selection metrics of M-HKUST-1 and M-HATGUF, we showed the best MOFs having improvements over the original MOFs (Cu-HKUST-1 and Cu-HATGUF) in **Figure 6.10**. The first column represents the calculated value of the metrics, and the other columns represent the percentage improvements in the metric upon the metal change. For example, using Cr instead of Cu in HKUST-1 improves CO_2/H_2 selectivity, CO_2 working capacity and APS about 5%, 9% and 14%, respectively, without changing R% of the MOF at VSA condition. At PSA condition, using Cd or Cr significantly improves selectivity, working capacity, APS and R% of HKUST-1. For example, Cd-HKUST-1 has 38%, 16%, 4%, and 60% enhanced CO_2/H_2 selectivity, CO_2 working capacity, R% and APS, respectively, compared to original HKUST-1. Although there was not any MOF that exceed the performance of Cu-HATGUF at PSA condition, excellent improvement at each metric was observed by Cd-HATGUF at VSA condition. Using Cd in HATGUF resulted in 71%, 42%, and 142% of increase in selectivity, working capacity and APS of MOF, respectively, without any change in R%. We note that computed adsorbent performance metrics of Cd-HATGUF are significantly higher than those of M-HKUST-1 series. Our results so far showed that changing metals can provide significantly promising results in terms of adsorbent performance improvements of HATGUF, but it is important to note that the stability of M-HATGUF materials should be further examined by experimental studies.

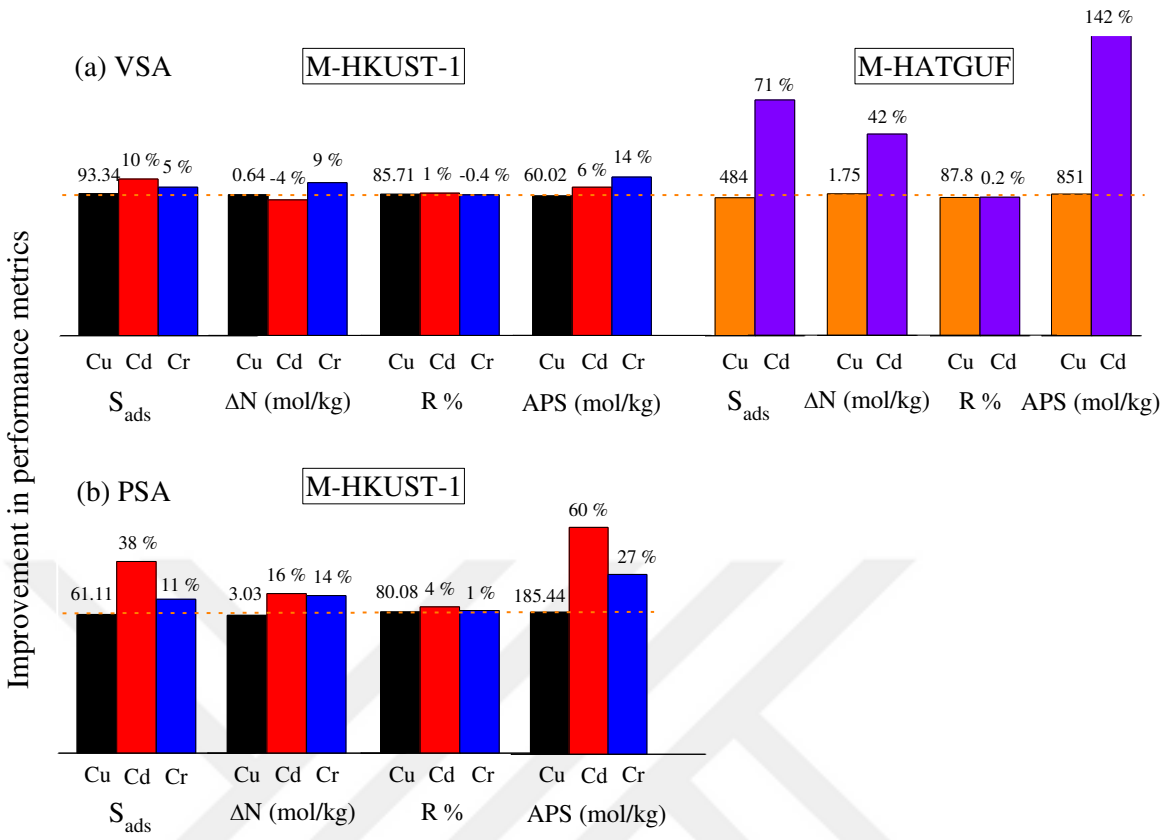

Figure 6.10. Percentage increase in selectivity, working capacity, R%, and APS of M-HKUST-1 and M-HATGUF. Columns in black represent calculated values of the adsorbent performance metrics for Cu-HKUST-1 and Cu-HATGUF whereas red and blue columns represent the percentage enhancement in the metrics upon the metal change.

The investigation on the influence of metal exchange for the gas separation performance was progressed for Zn-MOFs. We first compared the effect of metal exchange on CO_2/H_2 mixture uptakes of IRMOFs and ZnO-MOFs. CO_2 and H_2 uptakes of 140 IRMOFs and 629 ZnO-MOFs computed at 0.1, 1, and 10 bar are shown in **Figure 6.11**. We color-coded and scaled the size of the data points according to the largest charge (LC) assigned to the framework atoms and pore limiting diameter (PLD) of the MOFs, respectively. Most of the IRMOFs and ZnO-MOFs had LC between 0.4 and 0.8 e^-, and IRMOFs had relatively larger pores (PLD range: 3.9-25.1 Å, LCD range: 5.5-26.1 Å) compared to ZnO-MOFs (PLD range: 3.7-19.2 Å, LCD range:4.2-21.6 Å). Mixture CO_2 uptakes of ZnO-MOFs were higher than IRMOFs at 0.1, 1, and 10 bar, while IRMOFs had slightly higher H_2 uptakes than ZnO-MOFs as pressure increased. Therefore, without metal exchange, ZnO-MOFs were potentially more promising in terms of their CO_2 capture performance from the CO_2/H_2 mixture compared to IRMOFs. IRMOFs and ZnO-MOFs with small pore sizes (shown with the smallest symbols) generally had the highest

CO_2 uptakes at all pressures as shown in **Figure 6.11(a-f)**. In MOFs having small pores, CO_2 molecules have increased interactions with the framework atoms due to the strong confinement.[224] We note that most of the IRMOFs and ZnO-MOFs had small pore sizes and low LCs, and metal exchange can intensify the CO_2-MOF interactions, making these materials promising due to the high CO_2 uptake.

The CO_2 and H_2 uptakes of M-MOFs that we focused on were also shown in **Figure 6.11**. For the group of IRMOFs, we compared the gas adsorption performances of M-HIFTOG02 (stars) and M-SAHYIK (triangles) with 140 IRMOFs (circles) in **Figure 6.11(a-c)**. The ranges of PLD for M-HIFTOG02 and M-SAHYIK were computed as 4.1-4.6 Å and 7.8-8.2 Å, respectively. M-HIFTOG02 is the catenated form of M-SAHYIK,[208] therefore the former series had narrower pore sizes, smaller S_{acc}, and lower porosity than the latter (given in **Appendix Table C3**). As shown in **Figure 6.11(a-c)**, the metal exchange in M-HIFTOG02 had a strong influence on the CO_2 uptakes while H_2 uptakes remained almost the same. We observed the greatest improvement in the CO_2 uptake of M-HIFTOG02 at 0.1 bar (**Figure 6.11(a)**) where CO_2 uptake of the original Zn-HIFTOG02 increased from 0.08 mol/kg to 0.18, 0.21, 0.34, and 0.52 mol/kg for Cr, Ti-, Ni-, and V-HIFTOG02, respectively. Ti, Ni, Cr, and V had the highest LC (1.40, 1.58, 2.07, and 2.33 e^- for Ti, V, Cr, and Ni, respectively) among the M-HIFTOG02 series. Since CO_2-MOF electrostatic interactions are important at low pressures,[224] high LCs of these metals led to enhanced CO_2 uptakes in these MOFs. Thus, at 0.1 bar, CO_2 uptakes of V-HIFTOG02 and Ni-HIFTOG02 even exceeded those of all IRMOFs. The effect of metal exchange on the CO_2 uptakes of M-IRMOFs was weaker but still observable at 10 bar compared to 0.1 bar. At 10 bar, Ti-HIFTOG02 with an exceptional CO_2 uptake of 6.12 mol/kg surpassed the CO_2 uptakes of all IRMOFs. This is a significant finding because the IRMOF with the highest CO_2 uptake in our subset had a CO_2 uptake value of 5.94 mol/kg and Ti-HIFTOG02 surpassed even this limit. This demonstrates that by exchanging Zn with V and Ti, we can build MOFs with exceptional CO_2 uptakes that exceed the upper limits of CO_2 uptake for all the existing IRMOFs.

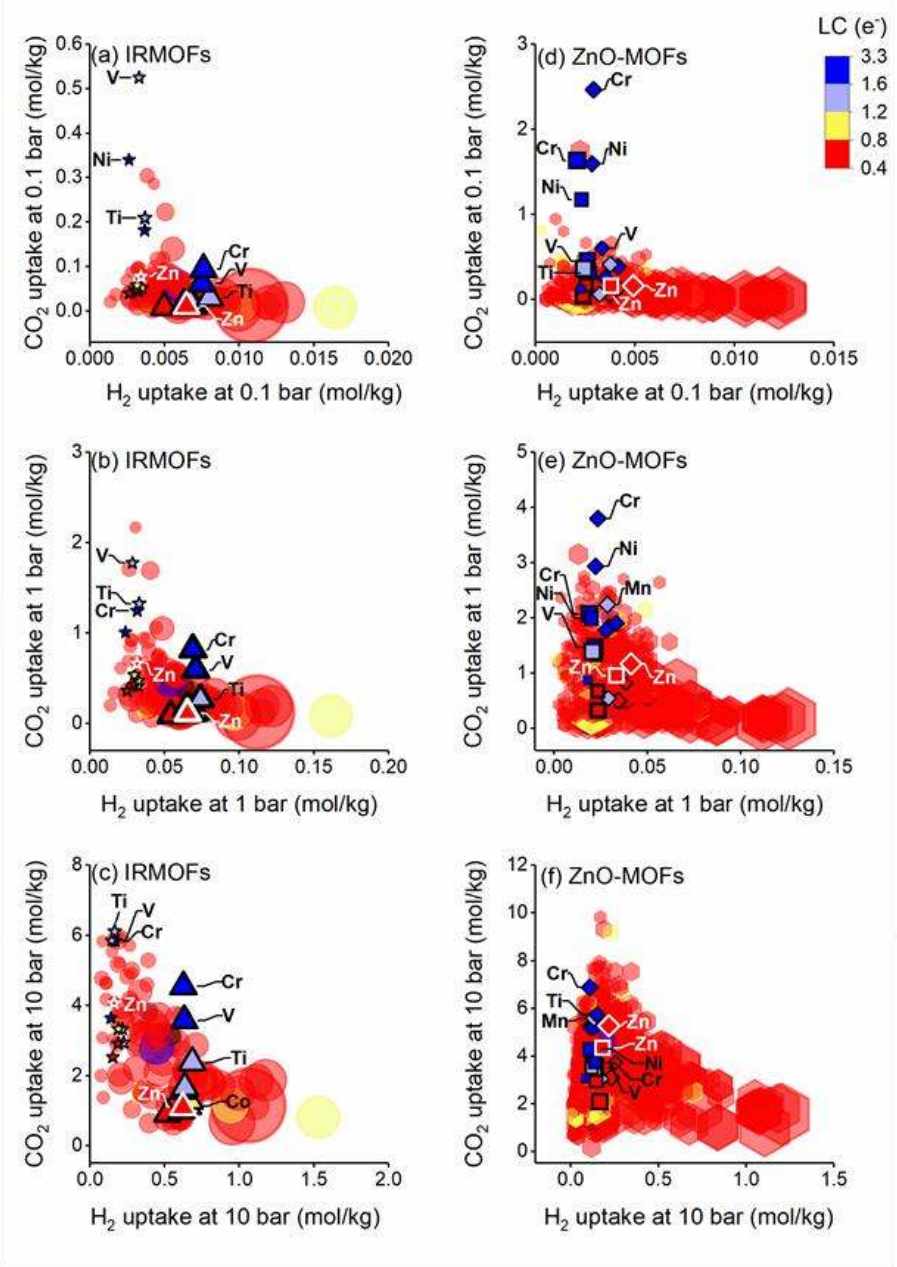

Figure 6.11. (a-c) CO_2 and H_2 uptakes of 140 IRMOFs (circles), M-HIFTOG02 (stars), M-SAHYIK (triangles) at 0.1, 1, and 10 bar. (d-f) CO_2 and H_2 uptakes of 629 ZnO-MOFs (hexagonals), M-EFESEP (diamonds), and M-EFESOZ (squares) at 0.1, 1, and 10 bar. Color and size of symbols represent the largest charge (LC) and pore limiting diameter (PLD) of MOFs, respectively.

Zn-SAHYIK had higher H_2 uptakes and lower CO_2 uptakes compared to Zn-HIFTOG02. CO_2 uptakes of SAHYIK increased up to nine times, from 0.01 mol/kg to 0.09 mol/kg at 0.1 bar, when Zn is exchanged with Cr and the CO_2 uptake of Cr-SAHYIK even overcame the CO_2 uptake of Zn-HIFTOG02. However, the upper limit for CO_2 uptakes of M-SAHYIK was lower than that of M-HIFTOG02, as catenated MOFs (M-HIFTOG02 in this work) have been shown to have higher CO_2 adsorption due to increased framework densities and lower porosities when compared to their non-catenated counterparts (M-SAHYIK in this work).[187, 206] This can be supported with the higher Q_{st,CO_2} values that we calculated for M-HIFTOG02 (ranging from -23 to -37 kJ/mol) than those for M-SAHYIK (ranging from -13 to -29 kJ/mol) at 0.1 bar. At 1 bar and 10 bar (**Figure 6.11(b-c)**), CO_2 uptakes of M-SAHYIK almost reached to those of M-HIFTOG02. At high pressures, the impact of physical properties such as surface area and porosity of MOFs on gas uptakes is more pronounced.[225] M-HIFTOG02 series were easily saturated with CO_2 molecules due to their lower porosities and surface areas (as shown in **Appendix Table C3**) compared to M-SAHYIK series, which have larger pores and higher surface area providing more space for gas adsorption.

We compared the gas adsorption performances M-EFESEP (diamonds) and M-EFESOZ (squares) with 629 ZnO-MOFs (hexagonals) in **Figure 6.11(d-f)**. Similar to M-IRMOFs, metal exchange did not remarkably change the H_2 uptakes of M-ZnO-MOFs but altered their CO_2 uptakes. As shown in **Figure 6.11(d)**, high LC assigned to Cr-EFESEP and Cr-EFESOZ provided the maximum CO_2 uptakes observed both for the M-EFESEP and M-EFESOZ series, followed by Ni and V. With Cr-EFESEP (Cr-EFESOZ), CO_2 uptakes increased by 15 (10) fold compared to the original Zn-EFESEP (Zn-EFESOZ) at 0.1 bar. Smaller PLDs of M-EFESEP (3.9-6.1 Å) lead to slightly higher CO_2 uptakes compared to M-EFESOZ (PLD:3.7-6.8 Å). Due to the presence of guest ions in the pores of M-EFESOZ, it had a smaller surface area compared to M-EFESEP (given in **Appendix Table C4**), therefore the available space for CO_2 and H_2 molecules was less in M-EFESOZ compared to that in M-EFESEP. Moreover, the presence of anions (Cl^-) has been shown to reduce CO_2-CO_2 interactions,[226] both Lennard Jones (LJ) and Coulomb, in the narrow pores of M-EFESOZ, which lead to lower CO_2 adsorption compared to M-EFESEP. For example, changing the metal from Zn to Cr increased the CO_2 uptake of M-EFESEP from 0.17 mol/kg to 2.47 mol/kg at 0.1 bar, while for M-EFESOZ the CO_2 uptake increased from 0.16 mol/kg to 1.63 mol/kg. The CO_2 uptake of

Cr-EFESEP is even higher than the CO_2 uptakes of all ZnO-MOFs at 0.1 bar. At 1 bar (**Figure 6.11(e)**), Cr still had a positive impact on the CO_2 uptakes, and CO_2 uptake of Zn-EFESEP (Zn-EFESOZ) increased from 1.17 mol/kg to 3.80 mol/kg (from 0.95 mol/kg to 2.07 mol/kg) when Cr was used. At 10 bar, exchanging Zn with Cr in EFESEP slightly increased CO_2 uptake from 5.28 to 6.88 mol/kg (**Figure 6.11(f)**).

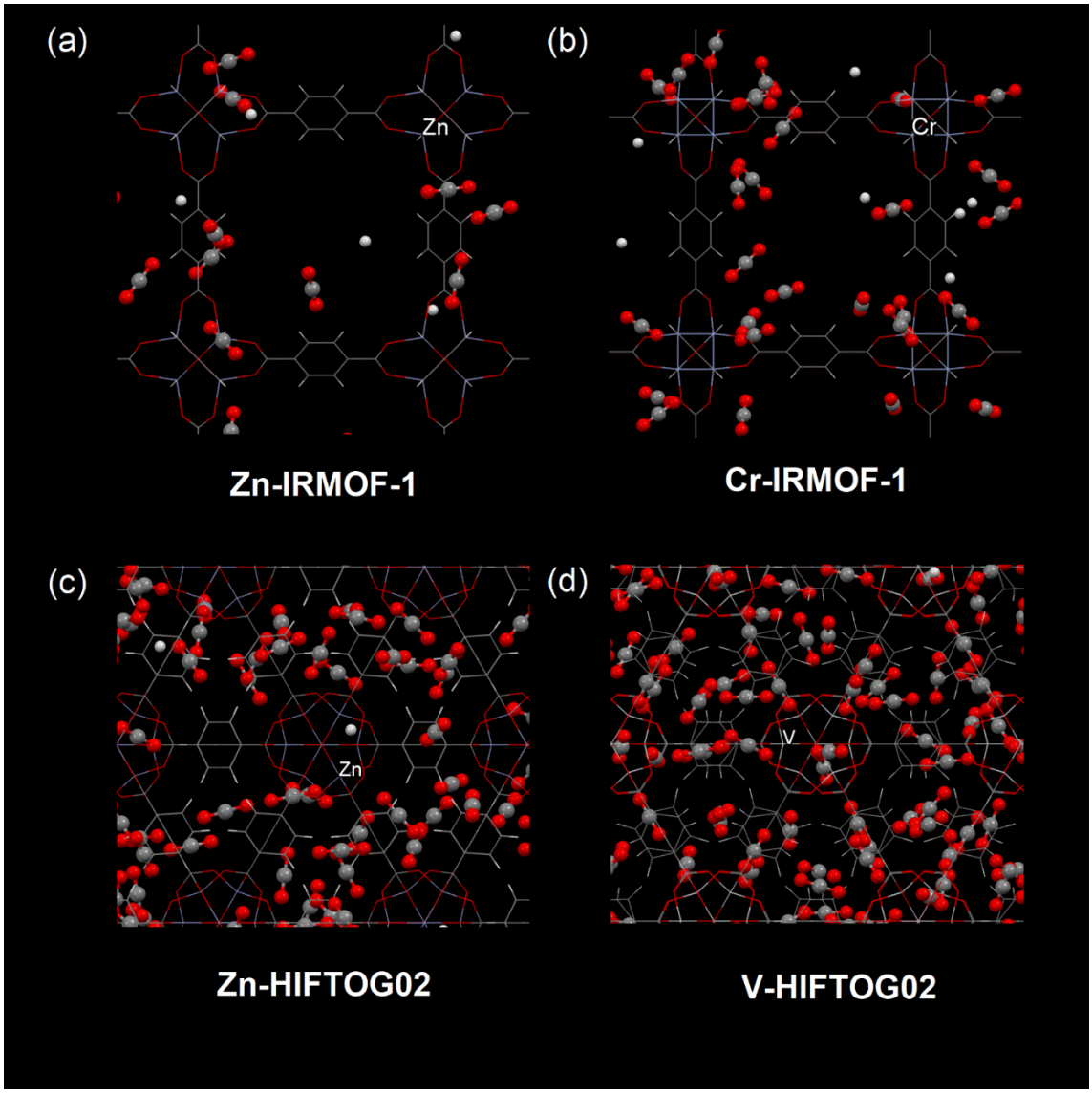

Figure 6.12. CO_2 and H_2 adsorption snapshots of (a) Zn-SAHYIK, (b) Cr-SAHYIK, (c) Zn- HIFTOG02, (d) V-HIFTOG02 at 10 bar. Framework is represented as wireframe and gas molecules are represented with ball and stick. Red: oxygen, gray: carbon, white: hydrogen. Type of the metal atom in the MOF is shown with the label.

We compared the increase in CO_2 uptakes of M-IRMOFs and M-ZnO-MOFs between 0.1 and 10 bar. At low pressure, CO_2 uptakes of M-ZnO-MOFs were found to be more affected from the metal exchange compared to M-IRMOFs. For example, at 0.1 bar, CO_2 uptake of M-HIFTOG02, increased up to 7-fold when Zn was exchanged with

V (**Figure 6.11(a)**), whereas CO_2 uptakes of M-EFESEP, increased up to 15-fold when Zn was exchanged with Cr (**Figure 6.11(d)**). Surface area and porosity of MOFs, and proximity of gas molecules to metal centers became important factors in determining the gas adsorption properties of M-MOFs with increased pressure.[213] At 10 bar, with the enhancement in the CO_2 uptake, Ti-HIFTOG02 surpassed all IRMOFs (**Figure 6.11(c)**), while Cr-EFESEP and Cr-EFESOZ surpassed most of the ZnO-MOFs (**Figure 6.11(f)**). Overall, we observed that exchange of Zn with Cr significantly increased the CO_2 uptakes of both M-IRMOFs and M-ZnO-MOFs.

To explain the change in the gas uptakes of MOFs upon the metal exchange, we examined the contribution of LJ interaction energies (E_{LJ}) for MOF-H_2, MOF-CO_2, CO_2-CO_2, H_2-H_2, CO_2-H_2, and the contribution of the Coulombic interaction energies ($E_{Coulomb}$) for MOF-CO_2 and CO_2-CO_2 to the total energy. **Appendix Figure C4** shows that the highest contributions to total energy were by $E_{LJ,\ MOF\text{-}CO_2}$ and $E_{Coulomb,\ MOF\text{-}CO_2}$ for M-SAHYIK and M-HIFTOG02 while the gas-gas interaction energies $E_{LJ,\ H_2\text{-}H_2}$ and $E_{LJ,\ CO_2\text{-}H_2}$ had almost no contribution at any pressure. MOF-H_2 LJ interaction energy, $E_{LJ,\ MOF\text{-}H_2}$, in M-SAHYIK were more effective compared to that in M-HIFTOG02 (**Appendix Figure C4(a-c)**) which can be explained by the size and geometry of the structures. Large rectangular pores of M-SAHYIK did not favor CO_2 adsorption as much as small triangular pores of M-HIFTOG02 which resulted in lower MOF-CO_2 interaction energies and higher MOF-H_2 interaction energies. Thus, higher H_2 adsorption was observed in M-SAHYIK (0.09-0.59 mol/kg) compared to M-HIFTOG02 (0.36-1.78 mol/kg) at 1 bar. As pressure increased from 0.1 to 10 bar, contribution of $E_{Coulomb,\ MOF\text{-}CO_2}$ in M-HIFTOG02 decreased whereas contributions of $E_{LJ,\ MOF\text{-}CO_2}$ and $E_{LJ,\ CO_2\text{-}CO_2}$ increased as shown in **Appendix Figure C4(d-f)**. This was due to the presence of high CO_2 loading in the pores of M-HIFTOG02 at 10 bar which can be observed from the adsorption snapshots given in **Figure 6.12**. The contribution of $E_{Coulomb,\ MOF\text{-}CO_2}$ to the total energy was higher for V, Ni, Ti, and Cr-exchanged versions of M-SAHYIK and M-HIFTOG02 as the higher LC enhanced the calculated CO_2-MOF electrostatic interactions compared to those in Zn-SAHYIK and Zn-HIFTOG02.

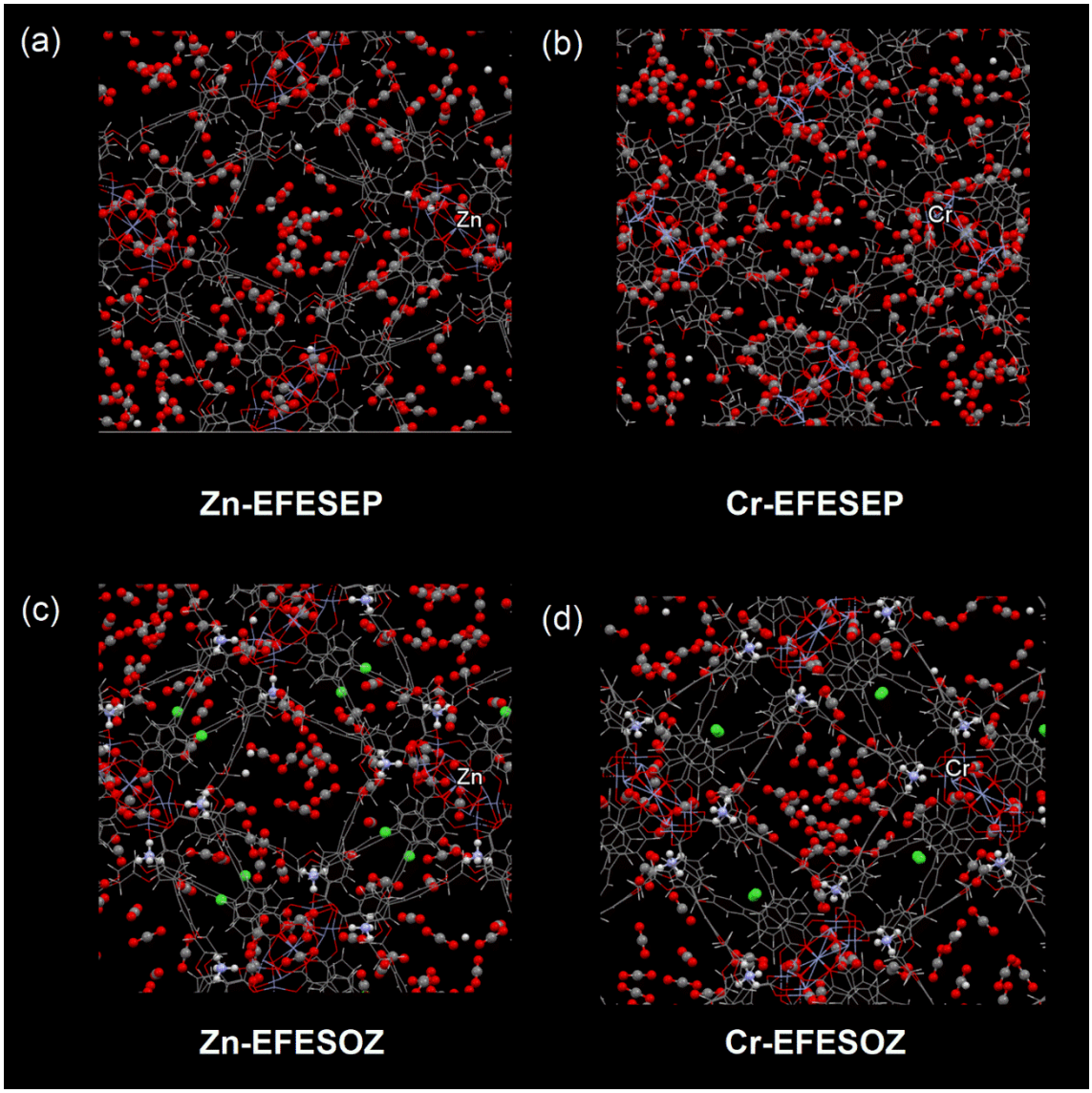

Figure 6.13. CO_2 and H_2 adsorption snapshots of (a) Zn-EFESEP, (b) Cr-EFESEP, (c) Zn-EFESOZ, (d) Cr-EFESOZ at 10 bar. Framework is represented as wireframe and gas molecules and ions are represented with ball and stick. Red: oxygen, gray: carbon, white: hydrogen. Green spheres represent Cl^- ions and blue spheres represent NH_4^+ ions in (c) and (d). Type of the metal atom in the MOF is shown with the label.

In **Appendix Figure C5**, slightly higher contribution of $E_{LJ,\ CO_2\text{-}CO_2}$ and $E_{Coulomb,\ CO_2\text{-}CO_2}$ to total interaction energy in M-EFESEP compared to M-EFESOZ is shown. Simulation snapshots given in **Figure 6.13**. also indicate that all pores provide adsorption sites in M-EFESEP whereas in M-EFESOZ mainly the large pore was preferred by both gases. As a result, MOFs with V, Ti, Ni and Cr which have LC >1.4 e^- and PLD <5 Å led to a stronger confinement of CO_2 at low pressure, as supported by high contribution of $E_{Coulomb,\ MOF\text{-}CO_2}$ to total interaction energy, and as a result these MOFs

had the highest CO_2 uptakes (the largest improvement in CO_2 uptake was observed for Cr-EFESEP, from 0.17 to 2.47 mol/kg at 0.1 bar). As the pressure increased to 10 bar, Cr-EFESEP had the highest improvement in CO_2 uptake from 3.72 to 6.88 mol/kg, followed by Ti-HIFTOG02 with the improved CO_2 uptake from 2.92 to 6.12 mol/kg. This increase was attributed to the tight packing of CO_2 molecules inside the MOF pores as shown by decreased $E_{Coulomb,\ MOF\text{-}CO_2}$ and increased $E_{LJ,\ MOF\text{-}CO_2}$, $E_{LJ,\ CO_2\text{-}CO_2}$. Overall, MOFs with V, Ti, Ni and Cr metals in M-HIFTOG02 series had higher CO_2 uptakes than M-SAHYIK series at all pressures due to the catenated structure of M-HIFTOG02, and MOFs with V, Ti, Ni and Cr in M-EFESEP series had higher CO_2 uptakes than M-EFESOZ series due to the empty space left by the absence of guest ions.

The aim of our work was to determine the effect of metal exchange on the adsorption-based gas separation performances of MOFs. In **Figure 6.14.**, S_{ads} and ΔN_{CO_2} of IRMOFs and ZnO-MOFs for CO_2/H_2 mixture separation were shown at VSA and PSA conditions. Effects of metal exchange on adsorbent performance score (APS) was shown with the color of the symbols and adsorbent regenerability (R%) was shown with the size of the symbols in **Figure 6.14.** At VSA and PSA conditions, ZnO-MOFs had higher adsorption selectivity (S_{ads}) and CO_2 working capacity (ΔN_{CO_2}), than IRMOFs, which was expected due to the higher CO_2 uptakes of ZnO-MOFs. As **Figure 6.14(a-b)** show, M-HIFTOG02 materials (stars) had higher S_{ads} and ΔN_{CO_2} compared to M-SAHYIK series (triangles). S_{ads} and ΔN_{CO_2} of original Zn-HIFTOG02 were computed as 119 and 0.58 mol/kg, respectively, whereas with changing the metal from Zn to V, S_{ads} and ΔN_{CO_2} increased to 355 and 1.25 mol/kg, respectively, leading to a 6-fold increase in APS at VSA condition. At PSA condition, V and Ti increased the S_{ads} of Zn-HIFTOG02 from 144 to 229 and 211, respectively, while its ΔN_{CO_2} increased from 3.4 to 4 mol/kg and 4.79 mol/kg, respectively. A trade-off between S_{ads} and ΔN_{CO_2} has been commonly observed for MOFs with different physical properties[227] whereas here we showed that S_{ads} and ΔN_{CO_2} can be improved simultaneously with metal exchange. We also considered the change in R% values upon the metal exchange since R% is a significant metric for the efficiency of adsorbents in cyclic processes. All M-HIFTOG02 except Ni-HIFTOG02 had R% values equal to or larger than 70%, which is a good range of R% values for an industrial gas separation process.

Exchange of Zn with Cr in M-SAHYIK (triangles) increased the S_{ads} of Zn-

SAHYIK from 10 to 67 at 1 bar, and from 10 to 41 at 10 bar, in addition to an enhanced ΔN_{CO_2} from 0.1 to 0.7 mol/kg at VSA condition, and from 1 to 3.7 mol/kg at PSA condition as shown in **Figure 6.14**. Therefore, upon the metal exchange, APS of Cr-SAHYIK increased 50-times at VSA condition, and 15-times at PSA condition compared to the APS of Zn-SAHYIK. M-SAHYIK series also preserved their high R% (represented by the size of the triangles) at VSA condition upon the metal exchange, which made them highly promising materials. Overall, the metal exchange had a greater impact on the adsorbent performance evaluation metrics of M-SAHYIK than M-HIFTOG02, and the separation performance of Cr-SAHYIK even approached to that of Zn-HIFTOG02 in terms of both S_{ads} and ΔN_{CO_2} at VSA condition, and in terms of ΔN_{CO_2} at PSA condition. At this point, we compared the performances of M-SAHYIK and M-HIFTOG02 which had the highest APS and R% >70% with the performances of all IRMOFs. At VSA (PSA) condition APS of V-HIFTOG02 is higher than 98% (98%) of all IRMOFs, whereas APS of Cr-SAHYIK is higher than 85% (75%) of all IRMOFs, indicating that metal exchange significantly extended the current adsorbent performance limits of IRMOFs both at VSA and PSA conditions.

In **Figure 6.14(c-d)**, S_{ads} and ΔN_{CO_2} trends of M-EFESEP (diamonds) and M-EFESOZ (squares) were compared with the results of ZnO-MOFs (hexagonals) at VSA and PSA conditions. At VSA condition, both S_{ads} and ΔN_{CO_2} of Zn-EFESEP and Zn-EFESOZ were improved with the metal exchange, while the improvement in S_{ads} was more pronounced compared to the improvement in ΔN_{CO_2}. Changing the metal from Zn to Cr increased S_{ads} of EFESEP 6-times (from 161 to 921) and of EFESOZ 4 times (from 160 to 613) at VSA condition. Moreover, Zn-EFESEP exhibited ΔN_{CO_2}, S_{ads}, and R% of 1.01 mol/kg, 160, and 86%, respectively, whereas Mn-EFESEP led to a more promising combination of ΔN_{CO_2}, S_{ads}, and R% as 1.83 mol/kg, 446, and 81%, respectively, at VSA condition. Similarly, ΔN_{CO_2}, S_{ads}, and R% values of Zn-EFESOZ were computed as 0.79 mol/kg, 160, and 83%, and these values were improved to 1.02 mol/kg, 378, and 74%, respectively, for Co-EFESOZ. We note that the metal exchange with Cr raised the APS of Zn-EFESEP exceptionally from 162 to 1233 mol/kg, while Ni raised the APS of Zn-EFESOZ from 126 to 462 mol/kg, at VSA condition. Upon the exchange of Zn with V, Ni, and Cr, a decrease was observed in ΔN_{CO_2} of M-EFESEP and M-EFESOZ at PSA condition, which was due to the more significant increase in their CO_2 uptakes upon metal

exchange at 1 bar compared to at 10 bar. Still, with the increase in the S_{ads} (from 137 to 359), APS of Zn-EFESEP increased from 562 mol/kg to 1104 mol/kg with Cr at PSA condition. Overall, metal-exchange with Cr, Ni, and V led to a good combination of ΔN_{CO_2} and S_{ads} for M-EFESEP and M-EFESOZ at VSA condition while at PSA condition an improvement in S_{ads} was achievable.

It is important to compare the calculated CO_2 uptake and CO_2/H_2 selectivity of the metal-exchanged MOFs with existing MOFs constructed from the same metals to better situate the results of our work. Gagliardi and coworkers investigated single component CO_2 adsorption in M-IRMOF-10 (M= Mg, Ca, Fe, Cu, Zn, Ge, Se, Cd, Sn, Ba) and compared the CO_2 adsorption isotherms of M-IRMOF-10 with IRMOF-1, IRMOF-7, IRMOF-16, and MOF-200.[213] At 1 bar, 298 K, single component CO_2 uptake of the best performing metal exchanged MOF (Ba-IRMOF-10) was computed as 0.84 mol/kg; while IRMOF-1, IRMOF-7, IRMOF-16, and MOF-200 had CO_2 uptakes of 1.82 mol/kg, 1.79 mol/kg, 0.56 mol/kg, and 0.59 mol/kg, respectively. In this study, we computed the highest CO_2 uptake with Cr-SAHYIK (Cr-IRMOF-1) as 0.82 mol/kg. We note that this CO_2 uptake was computed for CO_2/H_2:15/85 mixture at 1 bar, 298 K, therefore the performance of Cr-SAHYIK can be considered as promising. We compared the CO_2 uptake and CO_2/H_2 selectivity of the top MOFs identified in this work with the top candidates of M-HKUST-1 series where M=Cd, Co, Cr, Cu, Fe, Mn, Mo, Ni, Ru and Zn in our previous study.[217] At 1 bar, 298 K, Ni-HKUST-1 had a simulated CO_2 uptake of 0.12 mol/kg and CO_2/H_2 selectivity of 100.21, while at 10 bar, 298 K, Cr-HKUST-1 was the top performer among other metal exchanged M-HKUST-1 with a simulated CO_2 uptake of 4.21 mol/kg and selectivity of 85.23. In this work, Cr-EFESEP had the highest CO_2/H_2 selectivity and CO_2 uptake of 921.25 and 3.8 mol/kg, respectively, at 1 bar, 298 K, and 358.72 and 6.88 mol/kg, respectively, at 10 bar, 298 K. These comparisons showed that metal exchange in Zn-MOFs led to superior performances compared to the performances of M-HKUST-1 for CO_2/H_2 mixture separation.

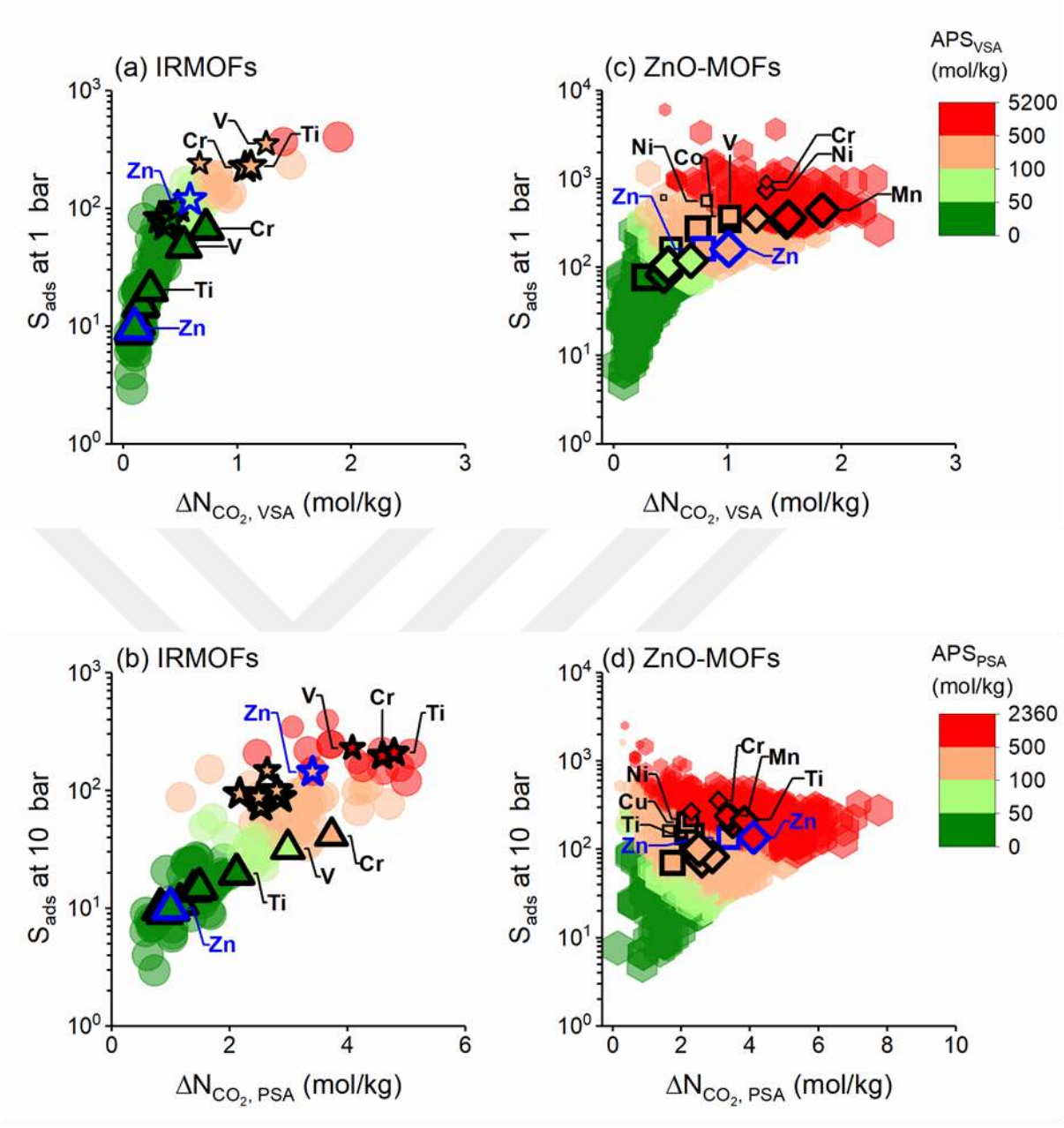

Figure 6.14 (a, b) ΔN_{CO_2} and S_{ads} of M-HIFTOG02 (stars), M-SAHYIK (triangles), and 140 IRMOFs (circles) (c, d) ΔN_{CO_2} and S_{ads} of M-EFESEP (stars), M-EFESOZ (triangles), and 629 ZnO-MOFs (circles) are shown for CO_2/H_2 mixture separation at VSA and PSA conditions. Size of symbols represents R%, color of symbols represents APS at the corresponding working condition.

Finally, in **Figure 6.15,** we summarized the overall effect of metal exchange on the CO_2/H_2 separation performances of M-SAHYIK, M-HIFTOG02, M-EFESEP, and M-EFESOZ series both at VSA and PSA conditions. The intensity of the blue color shifting

from low to high represents the improvement in S_{ads} or APS, while the color of the circles reflects the most promising (green), the least promising (red), and in-between (yellow) performances (S_{ads} or APS) of M-MOFs. **Figure 6.15(a)** represents that exchange of Zn with Cr in M-SAHYIK increased both S_{ads} and APS at VSA and PSA conditions, and this was followed by V, uplifting the performance of Zn-SAHYIK to one of the highest performances. Similarly, changing the metal from Zn to Cr, Mn, or Ni enhanced the S_{ads} and APS of M-HIFTOG02 at VSA condition, while Ti increased the APS of M-HIFTOG02 as much as Cr at PSA condition as shown in **Figure 6.15(b)**.

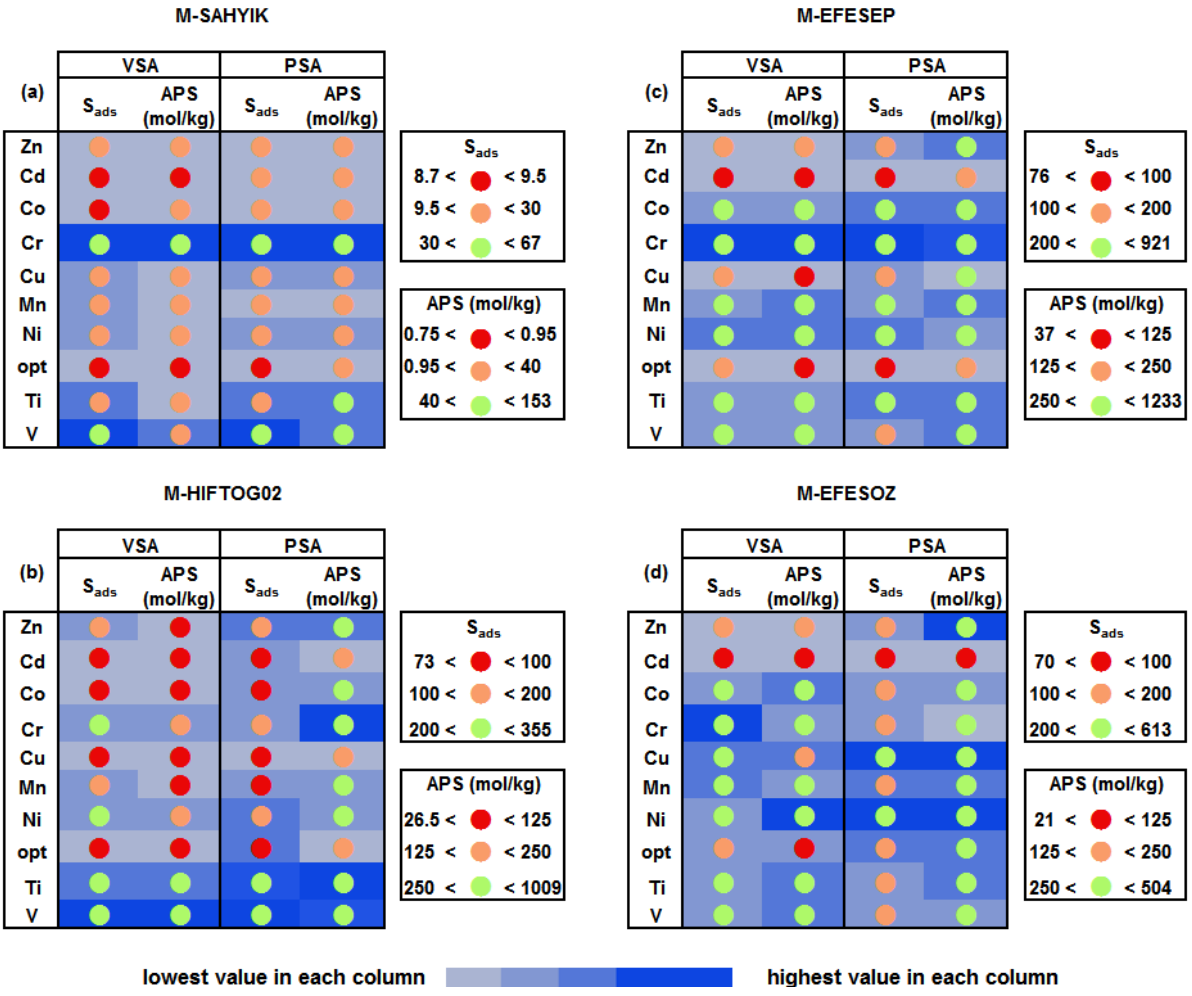

Figure 6.15. Infographic representing the effect of metal exchange on S_{ads} and APS of (a) M-SAHYIK (b) M-HIFTOG02 (c) M-EFESEP and (d) M-EFESOZ for CO_2/H_2 mixture separation at VSA and PSA conditions. "opt" represents the "geometry optimized version of the original MOF".

For M-EFESEP, significant improvements in the S_{ads} and APS both at VSA and PSA conditions were observed when the original metal (Zn) was changed to V or Ti as

shown in **Figure 6.15(c)**. As shown in **Figure 6.15(d)**, for M-EFESOZ exchange of Zn with a wide range of metals, Co, Cr, Mn, Ni, Ti and V, could double the S_{ads} and APS of the MOF. These findings suggest that a major improvement in the gas separation efficiency of MOFs can be obtained by changing the metal from Zn to especially Cr or V, therefore, the synthesis and/or post-synthetic modification of MOFs with these metals warrants further studies.

Since we obtained improved CO_2/H_2 separation performances with M-IRMOFs and M-ZnO-MOFs, we also tested their separation performances for equimolar CO_2/CH_4 mixture. In **Figure 6.16.**, we represented the effect of exchanging Zn with different metals on S_{ads} and APS of M-HIFTOG02, M-SAHYIK, M-EFESEP, and M-EFESOZ for CO_2/CH_4 separation at VSA and PSA conditions. As shown in **Figure 6.16(a,b)**, similar to CO_2/H_2 separation, superior S_{ads} and APS values were obtained with V- and Ti-HIFTOG02 compared to Zn-HIFTOG02 for CO_2/CH_4 separation at both conditions. With the improvement in its S_{ads}, Cr-SAHYIK had a similar S_{ads} compared to V-HIFTOG02 at VSA condition. Zn-HIFTOG02 and Zn-SAHYIK had S_{ads} of 3.9 and 1.8, respectively, for CO_2/CH_4 separation at VSA condition, which increased to 13.5 with V-HIFTOG02 and to 13.2 with Cr-SAHYIK. This is due to the significantly higher CO_2 uptakes and lower CH_4 uptakes of V-HIFTOG02 and Cr-SAHYIK compared to that of their Zn-versions as shown in **Appendix Figure C6.** For example, CO_2 uptake of Zn-HIFTOG02 increased from 0.25 to 1.06 mol/kg (~4 fold) with V and CO_2 uptake of Zn-SAHYIK increased from 0.04 to 0.33 mol/kg (~9 fold) with Cr at 0.1 bar. At 1 bar, CO_2 uptake of Zn-HIFTOG02 increased from 1.80 to 3.47 mol/kg (~2 fold) with V, and CO_2 uptake of Zn-SAHYIK increased from 0.36 to 2.39 mol/kg (~6 fold) with Cr. Thus, V-HIFTOG02 and Cr-SAHYIK significantly outperformed all IRMOFs at VSA condition. This was followed by Cr- and Ni-HIFTOG02, and V-SAHYIK, which also had high CO_2 uptakes close to the maximum of the CO_2 uptakes of all IRMOFs. In **Appendix Figure C7,** we provided S_{ads} and ΔN_{CO_2} of M-IRMOFs and M-ZnO-MOFs for CO_2/CH_4 separation. As shown, both the selectivity and working capacity of MOFs increased with metal exchange. A remarkable increase in the ΔN_{CO_2} of Zn-SAHYIK, from 0.33 to 2.06 mol/kg at VSA condition, was observed when Cr was used. Both V-HIFTOG02 and Cr-SAHYIK had the highest APS values and surpassed the performances of all IRMOFs at VSA condition. At PSA condition, V-HIFTOG02 and Ti-HIFTOG02 had outstanding separation performances compared to all IRMOFs while Cr-SAHYIK competed with the

best performing IRMOFs due to its high S_{ads}, ΔN_{CO_2}, and high APS.

For M-ZnO-MOFs, as shown in **Appendix Figure C6**, exchanging Zn with Cr increased the CO_2 uptake of Zn-EFESEP from 0.46 to 2.95 mol/kg, and of Zn-EFESOZ from 0.40 to 1.86 mol/kg, at 0.1 bar. Cr-EFESEP had a CO_2 uptake higher than that of all ZnO-MOFs at 0.1 bar. At 1 and 10 bar, metal exchange contributed less to CO_2 uptakes but was still distinctive, and Cr-EFESEP had as high CO_2 uptakes as the best performing ZnO-MOFs at 1 bar. Cr significantly increased the S_{ads} of Zn-EFESEP from 3.8 to 10.5 for CO_2/CH_4 separations and APS increased from 7.7 to 21.7 mol/kg at VSA condition as shown in **Figure 6.16(c)**. **Figure 6.16(d)** shows that S_{ads} of Zn-EFESOZ increased from 4.1 to 12.6 when Zn was changed to Cr, and Cr-EFESOZ had a high S_{ads} close to the highest S_{ads} observed for ZnO-MOFs (shown in **Appendix Figure C7)**. Ni followed Cr and increased the S_{ads} of Zn-EFESOZ from 4.1 to 11.3 at VSA condition while its APS also increased from 6.7 to 15.7 mol/kg. Although we selected the MOFs for *in-silico* metal exchange by considering their pore sizes and S_{ads} for CO_2/H_2 separation, M-MOFs considered in this work performed well both for CO_2/H_2 and CO_2/CH_4 mixtures. We observed significant increases in both S_{ads} and APS of MOFs especially when Zn was exchanged with V, Cr, and Ni. This is an important result signaling that the MOFs carefully selected for metal exchange for CO_2/H_2 separation can have improved separation performances also for other gas mixtures such as CO_2/CH_4.

Finally, it is important to note that the M-MOFs we examined in this work are hypothetically produced with computational methods and with the assumption of successful exchange of all metals in the framework. Combination of several factors, such as the MOF topology, coordination geometry of the metal node, pore sizes, size and shape of the linkers determine the extent of metal exchange of MOFs in experimental studies.[201] These factors may lead to partially metal exchanged MOFs which eventually influence the CO_2 capture performance of materials. Our results can be considered as useful guidelines to achieve upper limits of CO_2 separation performances of metal exchanged M-IRMOFs and M-ZnO-MOFs under industrially applicable conditions for CO_2/H_2 and CO_2/CH_4 mixture separations.

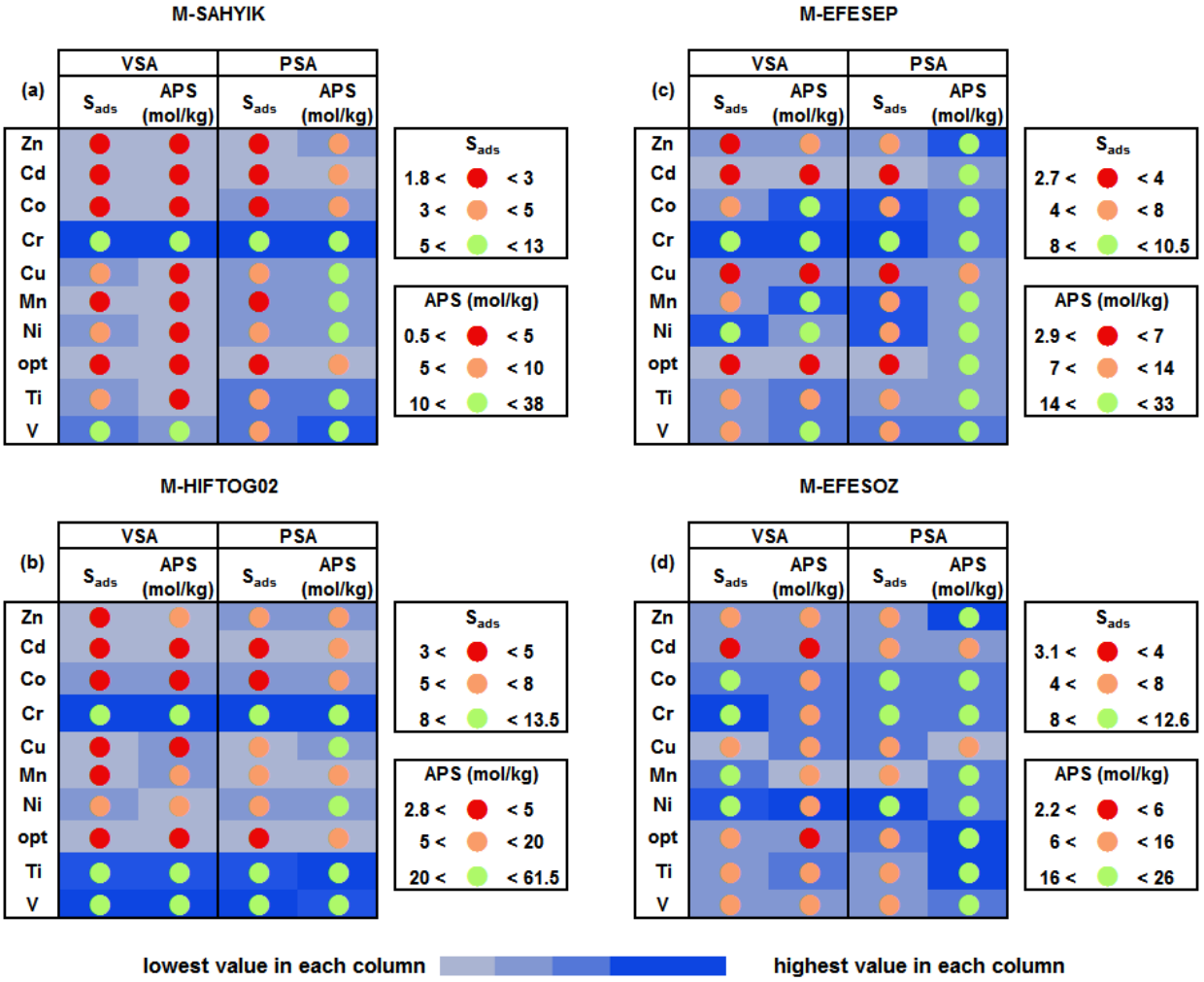

Figure 6.16. Infographic representing the effect of metal exchange on S_{ads} and APS of (a) M-SAHYIK (b) M-HIFTOG02 (c) M-EFESEP and (d) M-EFESOZ for CO_2/CH_4 mixture separation at VSA and PSA conditions. "opt" represents the "geometry optimized version of the original MOF".

6.3 Conclusion

In this work, we investigated the new possibilities brought by metal exchange techniques in M-HKUST-1 and M-HATGUF to design new MOFs with exceptional CO_2/H_2 mixture separation performances. We illustrated that by changing the metal type, the adsorption dynamics of CO_2 and H_2 can be modulated such that a significant improvement in several adsorbent performance metrics can be observed. We observed the greatest improvements in performance metrics with Cr-HKUST-1 and Cd-HKUST-1 that could even outperform HKUST-1 both at VSA and PSA conditions. Cd-HKUST-1 had the highest enhancements with 38%, 16%, 4% and 60% increase in selectivity, working capacity, R%, and APS, respectively, compared to original HKUST-1 at PSA

condition. Cd-HATGUF more than doubled its APS with a 142% increase at VSA condition, which has been explained by competitive adsorption between CO_2 and H_2 towards the small pores of the MOF. As a result, the CO_2/H_2 selectivity of Cd-HATGUF was almost doubled with metal exchange.

Out of 10,221 MOFs, we first identified 769 MOFs containing Zn nodes and single type of linker without any functional groups (140 IRMOFs and 629 ZnO-MOFs), then targeted the MOFs providing S_{ads}~100 and PLD> 4 Å (16 IRMOFs and 284 ZnO-MOFs) and selected the candidate MOFs and their peer MOFs for metal exchange (two IRMOFs, M-SAHYIK and M-HIFTOG02, and two ZnO-MOFs, M-EFESEP and M-EFESOZ). We exchanged the metal atom (Zn) of the selected four MOFs with eight different metals (Cd, Co, Cr, Cu, Mn, Ni, Ti, and V) and 32 unique metal-exchanged MOFs (16 M-IRMOFs and 16 M-ZnO-MOFs) were obtained. Molecular-level insight obtained from atomically detailed simulations showed that higher contributions of MOF-CO_2 electrostatic interactions in MOFs with Cr, V, Ni, and Ti metals led to higher CO_2 uptakes. We compared the CO_2 separation performances of 32 *in-silico* designed M-MOFs with 629 ZnO-MOFs and 140 IRMOFs. Our results showed that the most significant improvement in the CO_2/H_2 and CO_2/CH_4 selectivities of MOFs were obtained with Cr, V, Ni, and Ti metals. After the exchange of Zn with V, CO_2/H_2 selectivity of HIFTOG02 (355 at 1 bar) exceeded the selectivity of 138 out of 140 IRMOFs. The exchange of Zn with Cr improved the selectivity of EFESEP (921 at 1 bar) and surpassed the selectivities of 602 ZnO-MOFs out of 629 ZnO-MOFs. These increases in selectivities were accompanied by an increase in working capacity of MOFs resulting in improved APSs. Thus, metal exchange was shown to significantly extend the current adsorbent performance limits of ZnO-MOFs. These results show that designing new MOFs with simulation techniques can be a time efficient way to guide and direct experimentalists to synthesize new generation of exceptional adsorbents for CO_2 capture.

We hope the results of this chapter will inspire computational and experimental studies that investigate the influence of metal exchange on CO_2 separation performances of MOFs with different MOF topologies or rich amount of guest ion pairs and will serve as a catalyst to identify novel metal exchanged MOFs with exceptional CO_2 capture performances.

Chapter 7

OUTLOOK

Novel gas adsorption and separation technologies with MOFs have been rapidly developing over this decade and identification of the most promising MOF adsorbents and membranes can be facilitated by high-throughput computational screening and molecular design methods. The results of this thesis showed that MOFs are exceptionally promising materials for CO_2 capture and H_2 purification both as adsorbents and membranes.

In Chapter 4, adsorption data of binary CO_2/H_2 mixtures in 3857 MOFs was obtained using GCMC simulations and the top 20 MOF adsorbents for PSA and VSA processes were identified. CO_2/H_2 adsorption selectivities of MOFs at PSA and VSA conditions were calculated to be in the range of 2.5−25000 and 2.5−85000, respectively, outperforming many zeolite adsorbents. MD simulation results showed that a significant number of MOFs (899) exceeded the Robeson's upper bound for polymeric membranes, suggesting that MOFs have a tremendous potential to replace traditional polymeric membranes for CO_2 purification. Detailed analysis of the structural characteristics of the top MOF adsorbents and membranes showed that MOFs with pore sizes <7.5 Å, 0.5< ϕ <0.75 and SA <2000 m^2/g are good adsorbents whereas the top MOF membranes have pore sizes >15 Å, ϕ >0.75, and SA >3000 m^2/g.

In Chapter 5, the performances of 10221 MOF adsorbents and membranes have been computationally assessed for CO_2 capture and H_2 purification using GCMC and MD simulations. 765, 1181, and 1443 MOFs out of 10221 were identified as promising adsorbents at PSA, VSA, and TSA conditions, respectively, since they exceeded APS > 2000 mol/kg. CO_2/H_2 adsorption selectivities of the top performing MOFs were generally underestimated by IAST calculations (6 out of 9 MOFs) due to the heterogenous adsorption sites of MOFs. The largest decrease in selectivity for a MOF upon blocking of pores that are inaccessible to CO_2 and H_2 was from 434 to 21.5, 1043 to 25, 1483 to 2.6 at PSA, VSA and TSA conditions, respectively. Upper limits of H_2/CO_2 selectivities and H_2 permeabilities of 10221 MOF membranes were computed as 6.34 and 4.38×10^6 Barrer,

respectively. MOFs with small pores (3.30−5.00 Å) and low porosities (0.30-0.60) generally exhibited high adsorption selectivities for CO_2 (>1000), whereas MOFs with large pores (>20 Å) and high porosities (>0.80) exhibited high membrane selectivities for H_2 (3.80-6.34). The top MOFs, identified for adsorption-based CO_2/H_2 separation, were shown to have narrow pores, exposed metal sites and halogen functional groups which provide favorable adsorption sites for CO_2 molecules due to the strong electrostatic interactions between CO_2 and the MOFs' atoms. The top MOF membranes identified for H_2/CO_2 separation have large pores enabling fast and efficient H_2 diffusion which is desired for efficient H_2 purification. Results revealed the importance of enriching the number of MOFs in high-throughput computational screening studies for the discovery of new promising materials for CO_2/H_2 separation.

In Chapter 6, the influence of metal type in M-HKUST-1 and M-HATGUF materials on their CO_2/H_2 mixture separation performances was investigated using molecular simulations. Cr-HKUST-1 and Cd-HKUST-1 were identified to outperform Cu-HKUST-1 in terms of selectivity and APS at both VSA and PSA conditions. For example, Cd-HKUST-1 was computed to have 38%, 16%, 4%, and 60% enhanced CO_2/H_2 selectivity, CO_2 working capacity, R%, and APS, respectively, compared to original Cu-HKUST-1 at PSA condition. Cd-HATGUF was identified to offer a significant enhancement in APS, 142% increase, compared to Cu-HATGUF, which made it a very promising MOF for a VSA process. CO_2/H_2 selectivity of HATGUF was also found to be almost doubled by changing the metal from Cu to Cd. Results revealed that CO_2/H_2 mixture separation performances of materials can be significantly improved via metal exchange. 769 MOFs with Zn nodes and single type of linker without any functional groups (140 IRMOFs and 629 ZnO-MOFs) were identified, then MOFs providing S_{ads}~100 and PLD> 4 Å (16 IRMOFs and 284 ZnO-MOFs) were selected. These candidate MOFs were paired with their peer MOFs for metal exchange (two IRMOFs, M-SAHYIK and M-HIFTOG02, and two ZnO-MOFs, M-EFESEP and M-EFESOZ). We exchanged the metal atom (Zn) of the selected four MOFs with eight different metals (Cd, Co, Cr, Cu, Mn, Ni, Ti, and V) and 32 unique metal-exchanged MOFs (16 M-IRMOFs and 16 M-ZnO-MOFs) were obtained. Contributions of MOF-CO_2 electrostatic interactions in MOFs with Cr, V, Ni, and Ti metals led to higher CO_2 uptakes. We compared the CO_2 separation performances of 32 *in-silico* designed M-MOFs with 629 ZnO-MOFs and 140 IRMOFs. Our results showed that the most significant improvement in the CO_2/H_2 and CO_2/CH_4 selectivities

of MOFs were obtained with Cr, V, Ni, and Ti metals. These results show that the effect of metal exchange on the gas separation performance is influenced by both the MOF type and the metal type.

Several issues discussed below can be considered as a guideline for the future directions of the field:

- The top MOFs considered in this work are assumed to be in their pristine state, so they represent a perfect crystal with no defects and no solvents with full activation of the MOF. These structural features can influence the adsorption and diffusion properties of MOFs which can hinder or enhance their performance.[77] The top MOFs identified in this thesis are promising candidates for detailed experimental investigations and simulation results from this thesis can serve as a guideline for future experimental and computational studies.
- The adsorption process is exothermic, and the dissipated heat must be dispersed efficiently. If heat builds up in the adsorbent bed, then due to the increasing temperature, the gas adsorption capacity of the MOF will decline, therefore adsorbent performance scores will be negatively affected.[228] MOFs also have a varying degree of mechanical stabilities and certain types of polar gases such as H_2S and H_2O can react with the MOF and change its chemical and physical properties.[229] Pre-combustion gas capture can also reach high pressures up to 10 bar in which mechanical stability of the MOF becomes increasingly important.[57] Additional stress tests for chemical and mechanical stability for the top MOF candidates can be performed before scaling up for potential mass production and adoption in industrial processes.
- For MOF membranes, diffusion characteristics can be influenced by the geometry and topology of MOFs. Gas diffusion in a single crystal MOF is calculated with EMD simulations in this thesis. The EMD simulations within this thesis does not take into account the surface effects, non-equilibrium MD simulations can be performed to investigate the gas diffusion characteristics with taking surface effects into account for CO_2/H_2 separation.[230]
- The metal exchange procedures shown in this thesis can be extended to the rest of the metals in the periodic system, however, chemical design limitations should be considered for metal exchange as the structure might collapse or lose its porosity partially if the oxidation state of the metal is different than the original

precursor.[79] UFF was used to represent the interatomic potentials in this thesis however, fine-tuned force fields can present a better representation of interatomic potentials for lanthanides or group 1A metals.[83]

- The immense amount of data produced in this thesis can be used to make machine learning predictions with supervised and non-supervised algorithms. Machine learning techniques have been shown to make good predictions for CH_4, H_2 and CO_2 storage capacities of MOFs.[231] Given that the simulation and adsorption results for 10221 MOFs are a good representation of future MOFs that will be added to the CSD, a performance prediction algorithm can be employed to accelerate the discovery of new promising MOFs.

We hope that the results of this thesis will solidify and accelerate the future of MOF research to address solutions to the global problems we are facing right now, such as global warming, green energy production, and CO_2 sequestration and it is hoped that the outcomes of this thesis will foster further interdisciplinary collaboration between chemical engineers, materials scientist, chemists, and computer/data scientists.

BIBLIOGRAPHY

1. Caro, J., *Quo Vadis, MOF?* Chemie Ingenieur Technik, 2018. **90**(11): p. 1759-1768.
2. Jansen, D., et al., *Pre-combustion CO_2 capture.* International Journal of Greenhouse Gas Control, 2015. **40**: p. 167-187.
3. Fairbanks, D.F. and C.R. Wilke, *Diffusion Coefficients in Multicomponent Gas Mixtures.* Industrial & Engineering Chemistry, 1950. **42**(3): p. 471-475.
4. Bui, M., et al., *Carbon capture and storage (CCS): the way forward.* Energy & Environmental Science, 2018. **11**(5): p. 1062-1176.
5. Langmuir, I., *The Adsorption of Gases on Plane Surfaces of Glass, Mica and Aluminum.* Journal of the American Chemical Society, 1918. **40**(9): p. 1361-1403.
6. Helfferich, F.G., *Principles of adsorption & adsorption processes, by D. M. Ruthven, John Wiley & Sons, 1984, xxiv + 433 pp.* AIChE Journal, 1985. **31**(3): p. 523-524.
7. Sumer, Z. and S. Keskin, *Ranking of MOF Adsorbents for CO_2 Separations: A Molecular Simulation Study.* Industrial & Engineering Chemistry Research, 2016. **55**(39): p. 10404-10419.
8. Keskin, S. and D.S. Sholl, *Screening Metal−Organic Framework Materials for Membrane-based Methane/Carbon Dioxide Separations.* The Journal of Physical Chemistry C, 2007. **111**(38): p. 14055-14059.
9. Bet-moushoul, E., et al., *TiO2 nanocomposite based polymeric membranes: A review on performance improvement for various applications in chemical engineering processes.* Chemical Engineering Journal, 2016. **283**: p. 29-46.
10. Yamato, N., et al., *Difference in membrane fouling in membrane bioreactors (MBRs) caused by membrane polymer materials.* Journal of Membrane Science, 2006. **280**(1): p. 911-919.
11. Ding, M., et al., *Carbon capture and conversion using metal–organic frameworks and MOF-based materials.* Chemical Society Reviews, 2019. **48**(10): p. 2783-2828.
12. Wang, Z. and S.M. Cohen, *Postsynthetic modification of metal–organic frameworks.* Chemical Society Reviews, 2009. **38**(5): p. 1315-1329.
13. Moghadam, P.Z., et al., *Targeted classification of metal–organic frameworks in the Cambridge structural database (CSD).* Chemical Science, 2020. **11**(32): p. 8373-8387.
14. Gangu, K.K., et al., *A review on contemporary Metal–Organic Framework materials.* Inorganica Chimica Acta, 2016. **446**: p. 61-74.
15. Moosavi, S.M., et al., *Understanding the diversity of the metal-organic framework ecosystem.* Nature Communications, 2020. **11**(1): p. 4068.
16. Allen, F., *The Cambridge Structural Database: a Quarter of a Million Crystal Structures and Rising.* Acta Crystallogr. B., 2002. **58**(3 Part 1): p. 380−388.
17. Moghadam, P.Z., et al., *Development of a Cambridge Structural Database Subset: A Collection of Metal–Organic Frameworks for Past, Present, and Future.* Chem. Mater., 2017. **29**(7): p. 2618−2625.

18. Farha, O.K., et al., *Metal–Organic Framework Materials with Ultrahigh Surface Areas: Is the Sky the Limit?* J. Am. Chem. Soc., 2012. **134**(36): p. 15016−15021.
19. Stock, N. and S. Biswas, *Synthesis of Metal-Organic Frameworks (MOFs): Routes to Various MOF Topologies, Morphologies, and Composites.* Chemical Reviews, 2012. **112**(2): p. 933-969.
20. Klinowski, J., et al., *Microwave-Assisted Synthesis of Metal–Organic Frameworks.* Dalton Transactions, 2011. **40**(2): p. 321-330.
21. Willems, T.F., et al., *Algorithms and Tools for High-throughput Geometry-based Analysis of Crystalline Porous Materials.* Micropor. Mesopor. Mat., 2012. **149**(1): p. 134−141.
22. Dubbeldam, D., et al., *RASPA: Molecular Simulation Software for Adsorption and Diffusion in Flexible Nanoporous Materials.* Mol. Simulat., 2015: p. 1−21.
23. Li, A., et al., *Enabling efficient exploration of metal–organic frameworks in the Cambridge Structural Database.* CrystEngComm, 2020.
24. Mishra, P., et al., *Adsorption of Lower Alkanes on a Zinc Based Metal Organic Framework.* Journal of Chemical & Engineering Data, 2012. **57**(9): p. 2610-2613.
25. Li, X., et al., *Synthesis of amino-functionalized MIL-101(Cr) with large surface area.* Materials Letters, 2017. **197**: p. 192-195.
26. Tranchemontagne, D.J., J.R. Hunt, and O.M. Yaghi, *Room temperature synthesis of metal-organic frameworks: MOF-5, MOF-74, MOF-177, MOF-199, and IRMOF-0.* Tetrahedron, 2008. **64**(36): p. 8553-8557.
27. Xiang, S., et al., *Exceptionally High Acetylene Uptake in a Microporous Metal−Organic Framework with Open Metal Sites.* Journal of the American Chemical Society, 2009. **131**(34): p. 12415-12419.
28. Hungerford, J. and K.S. Walton, *Room-Temperature Synthesis of Metal–Organic Framework Isomers in the Tetragonal and Kagome Crystal Structure.* Inorganic Chemistry, 2019. **58**(12): p. 7690-7697.
29. Freund, R., et al., *25 years of Reticular Chemistry.* Angewandte Chemie International Edition, 2021. **n/a**(n/a).
30. Altintas, C., et al., *An extensive comparative analysis of two MOF databases: high-throughput screening of computation-ready MOFs for CH4 and H2 adsorption.* Journal of Materials Chemistry A, 2019. **7**(16): p. 9593-9608.
31. Chung, Y.G., et al., *Computation-Ready, Experimental Metal–Organic Frameworks: A Tool To Enable High-Throughput Screening of Nanoporous Crystals.* Chemistry of Materials, 2014. **26**(21): p. 6185-6192.
32. Chen, T. and T.A. Manz, *Identifying misbonded atoms in the 2019 CoRE metal–organic framework database.* RSC Advances, 2020. **10**(45): p. 26944-26951.
33. Altintas, C., et al., *Database for CO_2 Separation Performances of MOFs Based on Computational Materials Screening.* ACS Applied Materials & Interfaces, 2018. **10**(20): p. 17257-17268.
34. Lin, C.-K., et al., *A global perspective on coal-fired power plants and burden of lung cancer.* Environmental Health, 2019. **18**(1): p. 9.
35. van Renssen, S., *The hydrogen solution?* Nature Climate Change, 2020. **10**(9): p. 799-801.
36. Ahn, H., et al., *Process simulation of a dual-stage Selexol unit for pre-combustion carbon capture at an IGCC power plant.* Energy Procedia, 2014. **63**: p. 1751-1755.
37. Wang, X., L. Chen, and Q. Guo, *Development of hybrid amine-functionalized MCM-41 sorbents for CO2 capture.* Chemical Engineering Journal, 2015. **260**: p.

573-581.
38. Banerjee, R., et al., *High-Throughput Synthesis of Zeolitic Imidazolate Frameworks and Application to CO_2 Capture.* Science, 2008. **319**(5865): p. 939.
39. *Pre-Combustion Carbon Capture*, in *Handbook of Clean Energy Systems*. p. 1-28.
40. Kenarsari, S.D., et al., *Review of recent advances in carbon dioxide separation and capture.* RSC Advances, 2013. **3**(45): p. 22739-22773.
41. Jansen, D., et al., *Pre-combustion CO_2 Capture.* Int. J. Greenh. Gas. Con., 2015. **40**: p. 167−187.
42. Sircar, S. and T.C. Golden, *Purification of Hydrogen by Pressure Swing Adsorption.* Sep. Sci. Technol., 2000. **35**(5): p. 667−687.
43. Smit, B., *Carbon Capture and Storage: introductory lecture.* Faraday Discussions, 2016. **192**(0): p. 9-25.
44. Belmabkhout, Y., V. Guillerm, and M. Eddaoudi, *Low Concentration CO_2 Capture using Physical Adsorbents: Are Metal–organic Frameworks Becoming the New Benchmark Materials?* Chem. Eng. J., 2016. **296**: p. 386−397.
45. Langmi, H.W., et al., *Hydrogen Storage in Metal-Organic Frameworks: A Review.* Electrochimica Acta, 2014. **128**: p. 368-392.
46. Sumida, K., et al., *Carbon Dioxide Capture in Metal–Organic Frameworks.* Chemical Reviews, 2012. **112**(2): p. 724-781.
47. Lee, Y.G., et al., *A comparison of the H_2 sorption capacities of isostructural metal-organic frameworks with and without accessible metal sites: [{Zn2(abtc)(dmf)2}3] and [{Cu2(abtc)(dmf)2}3] versus [{Cu2(abtc)}3].* Angew Chem Int Ed Engl, 2008. **47**(40): p. 7741-5.
48. Bao, Z., et al., *Adsorption of CO2 and CH4 on a magnesium-based metal organic framework.* J Colloid Interface Sci, 2011. **353**(2): p. 549-56.
49. Aprea, P., et al., *Modeling Carbon Dioxide Adsorption on Microporous Substrates: Comparison between Cu-BTC Metal−Organic Framework and 13X Zeolitic Molecular Sieve.* Journal of Chemical & Engineering Data, 2010. **55**(9): p. 3655-3661.
50. Zhao, Z., Z. Li, and Y.S. Lin, *Adsorption and Diffusion of Carbon Dioxide on Metal−Organic Framework (MOF-5).* Industrial & Engineering Chemistry Research, 2009. **48**(22): p. 10015-10020.
51. Yazaydın, A.Ö., et al., *Screening of Metal−Organic Frameworks for Carbon Dioxide Capture from Flue Gas Using a Combined Experimental and Modeling Approach.* Journal of the American Chemical Society, 2009. **131**(51): p. 18198-18199.
52. Britt, D., et al., *Highly efficient separation of carbon dioxide by a metal-organic framework replete with open metal sites.* Proceedings of the National Academy of Sciences, 2009. **106**(49): p. 20637.
53. Liang, Z., M. Marshall, and A.L. Chaffee, *CO2 Adsorption-Based Separation by Metal Organic Framework (Cu-BTC) versus Zeolite (13X).* Energy & Fuels, 2009. **23**(5): p. 2785-2789.
54. Fang, H., et al., *Identification of High-CO_2-capacity Cationic Zeolites by Accurate Computational Screening.* Chem. Mater., 2016. **28**(11): p. 3887−3896.
55. Herm, Z.R., et al., *Metal−Organic Frameworks as Adsorbents for Hydrogen Purification and Precombustion Carbon Dioxide Capture.* Journal of the American Chemical Society, 2011. **133**(15): p. 5664-5667.
56. Chung, Y.G., et al., *In Silico Discovery of Metal-organic Frameworks for*

Precombustion CO_2 Capture using a Genetic Algorithm. Sci. Adv., 2016. **2**(10): p. 1−9.
57. Dureckova, H., et al., *Robust Machine Learning Models for Predicting High CO_2 Working Capacity and CO_2/H_2 Selectivity of Gas Adsorption in Metal Organic Frameworks for Precombustion Carbon Capture.* J. Phys. Chem. C., 2019. **123**(7): p. 4133−4139.
58. Korelskiy, D., et al., *Efficient Ceramic Zeolite Membranes for CO_2/H_2 Separation.* J. Mater. Chem. A, 2015. **3**(23): p. 12500−12506.
59. Daglar, H., I. Erucar, and S. Keskin, *Exploring the performance limits of MOF/polymer MMMs for O2/N2 separation using computational screening.* Journal of Membrane Science, 2021. **618**: p. 118555.
60. Qiu, S., M. Xue, and G. Zhu, *Metal–organic framework membranes: from synthesis to separation application.* Chemical Society Reviews, 2014. **43**(16): p. 6116-6140.
61. Zhang, M., et al., *Approaches to Suppress CO2-Induced Plasticization of Polyimide Membranes in Gas Separation Applications.* Processes, 2019. **7**(1).
62. Scholes, C.A., et al., *CO2 capture from pre-combustion processes—Strategies for membrane gas separation.* International Journal of Greenhouse Gas Control, 2010. **4**(5): p. 739-755.
63. Robeson, L.M., *The Upper Bound Revisited.* J. Membr. Sci., 2008. **320**(1-2): p. 390−400.
64. Rezac, M.E. and B. Schöberl, *Transport and thermal properties of poly(ether imide)/acetylene-terminated monomer blends.* Journal of Membrane Science, 1999. **156**(2): p. 211-222.
65. Nagai, K., A. Higuchi, and T. Nakagawa, *Gas permeability and stability of poly(1-trimethylsilyl-1-propyne-co-1-phenyl-1-propyne) membranes.* Journal of Polymer Science Part B: Polymer Physics, 1995. **33**(2): p. 289-298.
66. Avci, G., I. Erucar, and S. Keskin, *Do New MOFs Perform Better for CO2 Capture and H2 Purification? Computational Screening of the Updated MOF Database.* ACS Applied Materials & Interfaces, 2020. **12**(37): p. 41567-41579.
67. Goldsmith, J., et al., *Theoretical Limits of Hydrogen Storage in Metal–Organic Frameworks: Opportunities and Trade-Offs.* Chemistry of Materials, 2013. **25**(16): p. 3373-3382.
68. Nazarian, D., J.S. Camp, and D.S. Sholl, *A Comprehensive Set of High-Quality Point Charges for Simulations of Metal–Organic Frameworks.* Chem. Mater., 2016. **28**(3): p. 785-793.
69. Manz, T.A. and D.S. Sholl, *Chemically Meaningful Atomic Charges That Reproduce the Electrostatic Potential in Periodic and Nonperiodic Materials.* J. Chem. Theory Comput., 2010. **6**(8): p. 2455-2468.
70. Nazarian, D., et al., *Large-Scale Refinement of Metal-Organic Framework Structures Using Density Functional Theory.* Chemistry of Materials, 2017. **29**(6): p. 2521-2528.
71. Simon, C.M., et al., *The materials genome in action: identifying the performance limits for methane storage.* Energy & Environmental Science, 2015. **8**(4): p. 1190-1199.
72. Chung, Y.G., et al., *Advances, Updates, and Analytics for the Computation-Ready, Experimental Metal–Organic Framework Database: CoRE MOF 2019.* Journal of Chemical & Engineering Data, 2019. **64**(12): p. 5985-5998.
73. Altintas, C., et al., *An extensive comparative analysis of two MOF databases:*

high-throughput screening of computation-ready MOFs for CH4 and H2 adsorption. J. Mater. Chem. A., 2019. **7**(16): p. 9593−9608.

74. Hoskins, B.F. and R. Robson, *Design and construction of a new class of scaffolding-like materials comprising infinite polymeric frameworks of 3D-linked molecular rods. A reappraisal of the zinc cyanide and cadmium cyanide structures and the synthesis and structure of the diamond-related frameworks [N(CH3)4][CuIZnII(CN)4] and CuI[4,4',4'',4'''-tetracyanotetraphenylmethane]BF4.xC6H5NO2.* Journal of the American Chemical Society, 1990. **112**(4): p. 1546-1554.
75. Ryan, P., L.J. Broadbelt, and R.Q. Snurr, *Is catenation beneficial for hydrogen storage in metal–organic frameworks?* Chemical Communications, 2008(35): p. 4132-4134.
76. Sezginel, K.B., T. Feng, and C.E. Wilmer, *Discovery of Hypothetical Hetero-interpenetrated MOFs with Arbitrarily Dissimilar Topologies and Unit Cell Shapes.* CrystEngComm, 2017. **19**(31): p. 4497−4504.
77. Chong, S., G. Thiele, and J. Kim, *Excavating Hidden Adsorption Sites in Metal-organic Frameworks using Rational Defect Engineering.* Nat. Commun., 2017. **8**(1): p. 1539−1549.
78. Kim, M., et al., *Postsynthetic ligand exchange as a route to functionalization of 'inert' metal–organic frameworks.* Chemical Science, 2012. **3**(1): p. 126-130.
79. Lalonde, M., et al., *Transmetalation: routes to metal exchange within metal–organic frameworks.* Journal of Materials Chemistry A, 2013. **1**(18): p. 5453-5468.
80. Wu, Y., et al., *Adsorptive Separation of Methanol-Acetone on Isostructural Series of Metal-Organic Frameworks M-BTC (M = Ti, Fe, Cu, Co, Ru, Mo): A Computational Study of Adsorption Mechanisms and Metal-Substitution Impacts.* ACS Appl Mater Interfaces, 2015. **7**(48): p. 26930-40.
81. Yu, J., Y. Wu, and P.B. Balbuena, *Response of metal sites toward water effects on postcombustion CO_2 capture in metal-organic frameworks.* ACS Sustainable Chem. Eng., 2016. **4**(4): p. 2387-2394.
82. Koh, H.S., et al., *Predicting Methane Storage in Open-Metal-Site Metal–Organic Frameworks.* The Journal of Physical Chemistry C, 2015. **119**(24): p. 13451-13458.
83. Borycz, J., et al., *CO2 Adsorption in M-IRMOF-10 (M = Mg, Ca, Fe, Cu, Zn, Ge, Sr, Cd, Sn, Ba).* The Journal of Physical Chemistry C, 2016. **120**(23): p. 12819-12830.
84. Park, J., et al., *Tuning metal-organic frameworks with open-metal sites and its origin for enhancing CO_2 affinity by metal substitution.* J. Phys. Chem. Lett., 2012. **3**(7): p. 826-829.
85. Canepa, P., et al., *High-throughput screening of small-molecule adsorption in MOF.* J. Mater. Chem. A, 2013. **1**(43): p. 13597-13604.
86. Zarabadi-Poor, P. and R. Marek, *In silico study of (Mn, Fe, Co, Ni, Zn)-BTC metal-organic frameworks for recovering xenon from exhaled anesthetic gas.* ACS Sustainable Chem. Eng., 2018. **6**(11): p. 15001-15006.
87. You, W., et al., *Tuning binding tendencies of small molecules in metal-organic frameworks with open metal sites by metal substitution and linker functionalization.* J. Phys. Chem. C, 2018. **122**(48): p. 27486-27494.
88. Yuan, J., et al., *Computer simulations for the adsorption and separation of CH4/H2/CO2/N2 gases by hybrid ultramicroporous materials.* Materials Today

Communications, 2021. **26**: p. 101987.
89. Avci, G., S. Velioglu, and S. Keskin, *High-Throughput Screening of MOF Adsorbents and Membranes for H_2 Purification and CO_2 Capture.* ACS Appl. Mater. Interfaces., 2018. **10**(39): p. 33693−33706.
90. Pinheiro, M., et al., *Characterization and comparison of pore landscapes in crystalline porous materials.* Journal of Molecular Graphics and Modelling, 2013. **44**: p. 208-219.
91. Plimpton, S., *Fast Parallel Algorithms for Short-Range Molecular Dynamics.* Journal of Computational Physics, 1995. **117**: p. 1.
92. Metropolis, N., et al., *Equation of State Calculations by Fast Computing Machines.* The Journal of Chemical Physics, 1953. **21**(6): p. 1087-1092.
93. Frenkel, D., *Understanding molecular simulation from algorithms to applications*. 2nd ed. ed. Computational science series ; 1, ed. B. Smit. 2002, San Diego: Academic Press.
94. Karavias, F. and A.L. Myers, *Isosteric heats of multicomponent adsorption: thermodynamics and computer simulations.* Langmuir, 1991. **7**(12): p. 3118-3126.
95. *Dassault Systemes BIOVIA, B. W. Release 2020; BIOVIA Pipeline Plot, Release 2020; Dasault Systemes, San Diego, CA.*
96. Dubbeldam, D., A. Torres-Knoop, and K.S. Walton, *On the inner workings of Monte Carlo codes.* Molecular Simulation, 2013: p. 1-40.
97. Dubbeldam, D., et al., *RASPA: molecular simulation software for adsorption and diffusion in flexible nanoporous materials.* Molecular Simulation, 2016. **42**(2): p. 81-101.
98. Allen, M.P. and D.J. Tildesley, *Computer simulation of liquids*. 2017: Oxford university press.
99. Barthel, S., et al., *Distinguishing Metal-Organic Frameworks.* Crystal growth & design, 2018. **18**(3): p. 1738-1747.
100. Dubbeldam, D., et al., *Design, parameterization, and implementation of atomic force fields for adsorption in nanoporous materials.* Advanced Theory and Simulations, 2019. **2**(11).
101. Sturluson, A., et al., *The role of molecular modelling and simulation in the discovery and deployment of metal-organic frameworks for gas storage and separation.* Mol. Simul., 2019. **45**(14-15): p. 1082-1121.
102. Buch, V., *Path Integral Simulations of Mixed Para-D_2 and ortho-D_2 Clusters: The Orientational Effects.* J. Chem. Phys., 1994. **100**(10): p. 7610−7629.
103. Rappe, A.K., et al., *UFF, a Full Periodic Table Force Field for Molecular Mechanics and Molecular Dynamics Simulations. (Universal Force Field).* J. Am. Chem. Soc., 1992. **114**(25): p. 10024−10035.
104. Babarao, R., M. Eddaoudi, and J.W. Jiang, *Highly Porous Ionic rht Metal−Organic Framework for H2 and CO2 Storage and Separation: A Molecular Simulation Study.* Langmuir, 2010. **26**(13): p. 11196-11203.
105. Ongari, D., et al., *Evaluating charge equilibration methods to generate electrostatic fields in nanoporous materials.* J. Chem. Theory Comput., 2018. **15**(1): p. 382-401.
106. Evans, D.J. and B.L. Holian, *The Nose–Hoover thermostat.* The Journal of Chemical Physics, 1985. **83**(8): p. 4069-4074.
107. Andersen, H.C., *Molecular dynamics simulations at constant pressure and/or temperature.* The Journal of Chemical Physics, 1980. **72**(4): p. 2384-2393.

108. Widom, B., *Some topics in the theory of fluids.* The Journal of Chemical Physics, 1963. **39**(11): p. 2808-2812.
109. Swisher, J.A., et al., *Evaluating mixture adsorption models using molecular simulation.* AIChE Journal, 2013. **59**(8): p. 3054-3064.
110. Adatoz, E. and S. Keskin, *Application of MD Simulations to Predict Membrane Properties of MOFs.* J. Nanomater., 2015. **16**(1): p. 193.
111. Braun, E., S.M. Moosavi, and B. Smit, *Anomalous Effects of Velocity Rescaling Algorithms: The Flying Ice Cube Effect Revisited.* Journal of Chemical Theory and Computation, 2018. **14**(10): p. 5262-5272.
112. Einstein, A., *Investigations on the Theory of the Brownian Movement.* Courier Corporation. 1956.
113. Bae, Y.S. and R.Q. Snurr, *Development and evaluation of porous materials for carbon dioxide separation and capture.* Angew Chem Int Ed Engl, 2011. **50**(49): p. 11586-96.
114. Gao, W.-Y., et al., *In Operando Analysis of Diffusion in Porous Metal-Organic Framework Catalysts.* Chemistry – A European Journal, 2019. **25**(14): p. 3465-3476.
115. Bae, Y.S. and R.Q. Snurr, *Development and evaluation of porous materials for carbon dioxide separation and capture.* Angewandte Chemie International Edition, 2011. **50**(49): p. 11586-11596.
116. Rege, S.U. and R.T. Yang, *A simple parameter for selecting an adsorbent for gas separation by pressure swing adsorption.* Separation Science and Technology, 2001. **36**(15): p. 3355-3365.
117. Chung, Y.G., et al., *In silico discovery of metal-organic frameworks for precombustion CO₂ capture using a genetic algorithm.* Science Advances, 2016. **2**(10): p. e1600909.
118. Trickett, C.A., et al., *The chemistry of metal–organic frameworks for CO_2 capture, regeneration and conversion.* Nat. Rev. Mater., 2017. **2**: p. 1-16.
119. Cui, X., R.M. Bustin, and G. Dipple, *Selective transport of CO_2, CH_4, and N_2 in coals: insights from modeling of experimental gas adsorption data.* Fuel, 2004. **83**(3): p. 293-303.
120. García, E.J., et al., *Sketching a portrait of the optimal adsorbent for CO_2 separation by pressure swing adsorption.* Industrial & Engineering Chemistry Research, 2017. **56**(16): p. 4818-4829.
121. Walton, K.S., *110th anniversary: Commentary: Perspectives on adsorption of complex mixtures.* Industrial & Engineering Chemistry Research, 2019. **58**(37): p. 17100-17105.
122. Myers, A.L. and J.M. Prausnitz, *Thermodynamics of mixed-gas adsorption.* Aiche Journal, 1965. **11**(1): p. 121-127.
123. Walton, K.S. and D.S. Sholl, *Predicting multicomponent adsorption: 50 years of the ideal adsorbed solution theory.* Aiche Journal, 2015. **61**(9): p. 2757-2762.
124. García, E.J., et al., *Tuning the adsorption properties of zeolites as adsorbents for CO_2 separation: Best compromise between the working capacity and selectivity.* Industrial & Engineering Chemistry Research, 2014. **53**(23): p. 9860-9874.
125. Wiersum, A.D., et al., *An adsorbent performance indicator as a first step evaluation of novel sorbents for gas separations: application to metal-organic frameworks.* Langmuir, 2013. **29**(10): p. 3301-9.
126. Park, J., et al., *How well do approximate models of adsorption-based CO_2 capture processes predict results of detailed process models?* Industrial & Engineering

Chemistry Research, 2019.
127. Keskin, S. and D.S. Sholl, *Assessment of a metal-organic framework membrane for gas separations using atomically detailed calculations: CO_2, CH_4, N_2, H_2 mixtures in MOF-5.* Ind. Eng. Chem. Res., 2009. **48**(2): p. 914-922.
128. Krishna, R. and D. Paschek, *Self-Diffusivities in Multicomponent Mixtures in Zeolites.* Phys. Chem. Chem. Phys., 2002. **4**(10): p. 1891−1898.
129. Coupry, D.E., M.A. Addicoat, and T. Heine, *Extension of the Universal Force Field for Metal–Organic Frameworks.* Journal of Chemical Theory and Computation, 2016. **12**(10): p. 5215-5225.
130. Yu, J. and P.B. Balbuena, *Water Effects on Postcombustion CO2 Capture in Mg-MOF-74.* The Journal of Physical Chemistry C, 2013. **117**(7): p. 3383-3388.
131. Dokur, D. and S. Keskin, *Effects of Force Field Selection on the Computational Ranking of MOFs for CO2 Separations.* Ind. Eng. Chem. Res., 2018. **57**(6): p. 2298−2309.
132. Fang, Z., et al., *Defect-Engineered Metal-Organic Frameworks.* Angewandte Chemie (International ed. in English), 2015. **54**(25): p. 7234-7254.
133. Rogge, S.M.J., et al., *Modeling Gas Adsorption in Flexible Metal–Organic Frameworks via Hybrid Monte Carlo/Molecular Dynamics Schemes.* Advanced Theory and Simulations, 2019. **2**(4): p. 1800177.
134. Chang, Z., et al., *Flexible metal-organic frameworks: Recent advances and potential applications.* Adv Mater, 2015. **27**(36): p. 5432-41.
135. Coudert, F.X., *Responsive metal-organic frameworks and framework materials: Under pressure, taking the heat, in the spotlight, with friends.* Chemistry of Materials, 2015. **27**(6): p. 1905-1916.
136. Li, W., S. Henke, and A.K. Cheetham, *Research update: Mechanical properties of metal-organic frameworks - influence of structure and chemical bonding.* Apl Materials, 2014. **2**(12): p. 123902.
137. Moghadam, P.Z., et al., *Structure-mechanical stability relations of metal-organic frameworks via machine learning.* Matter, 2019. **1**(1): p. 219-234.
138. Bahr, D.F., et al., *Mechanical properties of cubic zinc carboxylate IRMOF-1 metal-organic framework crystals.* Physical Review B, 2007. **76**(18): p. 184106.
139. Rappe, A.K. and W.A. Goddard, *Charge Equilibration for Molecular Dynamics Simulations.* J. Phys. Chem. , 1991. **95**(8): p. 3358−3363.
140. Basdogan, Y. and S. Keskin, *Simulation and Modelling of MOFs for Hydrogen Storage.* CrystEngComm, 2015. **17**(2): p. 261−275.
141. Hefti, M., et al., *Adsorption equilibrium of binary mixtures of carbon dioxide and nitrogen on zeolites ZSM-5 and 13X.* Microporous and Mesoporous Materials, 2015. **215**: p. 215-228.
142. Potoff, J.J. and J.I. Siepmann, *Vapor–liquid Equilibria of Mixtures Containing Alkanes, Carbon Dioxide, and Nitrogen.* AIChE J., 2001. **47**(7): p. 1676−1682.
143. Martin, M.G. and J.I. Siepmann, *Transferable Potentials for Phase Equilibria. 1. United-atom Description of N-alkanes.* J. Phys. Chem. B., 1998. **102**(14): p. 2569−2577.
144. Jorgensen, W.L., et al., *Comparison of Simple Potential Functions for Simulating Liquid Water.* J. Chem. Phys., 1983. **79**(2): p. 926−935.
145. Hufton, J., S. Mayorga, and S. Sircar, *Sorption-enhanced reaction process for hydrogen production.* AIChE Journal, 1999. **45**(2): p. 248-256.
146. Krishna, R., *Screening Metal–organic Frameworks for Mixture Separations in Fixed-bed Adsorbers using a Combined Selectivity/Capacity Metric.* RSC Adv.,

2017. **7**(57): p. 35724−35737.
147. Krishna, R. and J.M. van Baten, *In silico screening of metal–organic frameworks in separation applications.* Physical Chemistry Chemical Physics, 2011. **13**(22): p. 10593-10616.
148. Tong, M., Q. Yang, and C. Zhong, *Computational screening of covalent organic frameworks for CH_4/H_2, CO_2/H_2 and CO_2/CH_4 separations.* Microporous and Mesoporous Materials, 2015. **210**: p. 142-148.
149. Ozturk, T.N. and S. Keskin, *Predicting Gas Separation Performances of Porous Coordination Networks Using Atomistic Simulations.* Ind. Eng. Chem., 2013. **52**(49): p. 17627−17639.
150. Zhang, K., A. Nalaparaju, and J. Jiang, *CO 2 capture in rht metal–organic frameworks: multiscale modeling from molecular simulation to breakthrough prediction.* Journal of Materials Chemistry A, 2015. **3**(31): p. 16327-16336.
151. Chung, Y.G., et al., *In silico discovery of metal-organic frameworks for precombustion CO2 capture using a genetic algorithm.* Sci Adv, 2016. **2**(10): p. e1600909.
152. Nandi, S., et al., *A single-ligand ultra-microporous MOF for precombustion CO_2 capture and hydrogen purification.* Science advances, 2015. **1**(11): p. e1500421.
153. Jia, J., et al., *Twelve-connected porous metal–organic frameworks with high H2 adsorption.* Chemical Communications, 2007(8): p. 840-842.
154. Fang, H., et al., *Identification of high-CO2-capacity cationic zeolites by accurate computational screening.* Chemistry of Materials, 2016. **28**(11): p. 3887-3896.
155. Krishna, R., *Methodologies for Screening and Selection of Crystalline Microporous Materials in Mixture Separations.* Separation and Purification Technology, 2017. **194**: p. 281-300.
156. Dantas, T.L., et al., *Carbon dioxide–nitrogen separation through pressure swing adsorption.* Chemical engineering journal, 2011. **172**(2-3): p. 698-704.
157. Shirani, B. and M. Eic, *Novel Differential Column Method for Measuring Multicomponent Gas Adsorption Isotherms in NaY Zeolite.* Industrial & Engineering Chemistry Research, 2017. **56**(4): p. 1008-1018.
158. Chung, Y.G., et al., *In silico discovery of metal-organic frameworks for precombustion CO_2 capture using a genetic algorithm.* Science advances, 2016. **2**(10): p. e1600909.
159. Gurdal, Y. and S. Keskin, *A new approach for predicting gas separation performances of MOF membranes.* Journal of Membrane Science, 2016. **519**: p. 45-54.
160. Lässig, D., et al., *A microporous copper metal–organic framework with high H_2 and CO_2 adsorption capacity at ambient pressure.* Angewandte Chemie International Edition, 2011. **50**(44): p. 10344-10348.
161. Qian, J., et al., *Highly selective carbon dioxide adsorption in a water-stable indium–organic framework material.* Chemical Communications, 2012. **48**(78): p. 9696-9698.
162. Huang, H., et al., *Understanding the effect of trace amount of water on CO_2 capture in natural gas upgrading in metal–organic frameworks: a molecular simulation study.* Industrial & Engineering Chemistry Research, 2012. **51**(30): p. 10031-10038.
163. Liu, B. and B. Smit, *Comparative molecular simulation study of CO_2/N_2 and CH_4/N_2 separation in zeolites and metal− organic frameworks.* Langmuir, 2009. **25**(10): p. 5918-5926.

164. Li, J., et al., *An rht-type metal–organic framework constructed from an unsymmetrical ligand exhibiting high hydrogen uptake capability.* RSC Advances, 2014. **4**(96): p. 53975-53980.
165. Altintas, C., I. Erucar, and S. Keskin, *High-throughput Computational Screening of the MOF Database for CH_4/H_2 Separations.* ACS applied materials & interfaces.
166. Li, Y., et al., *Zeolitic imidazolate framework ZIF-7 based molecular sieve membrane for hydrogen separation.* Journal of Membrane Science, 2010. **354**(1-2): p. 48-54.
167. Fan, L., et al., *Electrospinning technology applied in zeolitic imidazolate framework membrane synthesis.* Journal of Materials Chemistry, 2012. **22**(48): p. 25272-25276.
168. Zhang, X., et al., *New Membrane Architecture with High Performance: ZIF-8 Membrane Supported on Vertically Aligned ZnO Nanorods for Gas Permeation and Separation.* Chemistry of Materials, 2014. **26**(5): p. 1975-1981.
169. Sanders, D.F., et al., *Energy-efficient Polymeric Gas Separation Membranes for a Sustainable Future: a Review.* Polymer, 2013. **54**(18): p. 4729−4761.
170. Galizia, M., et al., *50^{th} Anniversary Perspective: Polymers and Mixed Matrix Membranes for Gas and Vapor Separation: A Review and Prospective Opportunities.* Macromolecules, 2017. **50**(20): p. 7809−7843.
171. Krishna, R., *Methodologies for Screening and Selection of Crystalline Microporous Materials in Mixture Separations.* Separation and Purification Technology, 2017.
172. Feng, D., et al., *A highly stable zeotype mesoporous zirconium metal–organic framework with ultralarge pores.* Angewandte Chemie International Edition, 2015. **54**(1): p. 149-154.
173. Oisaki, K., et al., *A Metal− Organic Framework with Covalently Bound Organometallic Complexes.* Journal of the American Chemical Society, 2010. **132**(27): p. 9262-9264.
174. Feng, D., et al., *Kinetically tuned dimensional augmentation as a versatile synthetic route towards robust metal–organic frameworks.* Nature communications, 2014. **5**: p. 5723.
175. Altintas, C., et al., *Computer simulations of 4240 MOF membranes for H 2/CH 4 separations: insights into structure–performance relations.* Journal of Materials Chemistry A, 2018. **6**(14): p. 5836-5847.
176. Martin, R.L., B. Smit, and M. Haranczyk, *Addressing challenges of identifying geometrically diverse sets of crystalline porous materials.* Journal of chemical information and modeling, 2011. **52**(2): p. 308-318.
177. Krishna, R., *Metrics for Evaluation and Screening of Metal–Organic Frameworks for Applications in Mixture Separations.* ACS Omega, 2020. **5**(28): p. 16987-17004.
178. García-Pérez, E., et al., *A Computational Study of CO_2, N_2, and CH_4 Adsorption in Zeolites.* Adsorption, 2007. **13**(5-6): p. 469−476.
179. Simon, C.M., B. Smit, and M. Haranczyk, *pyIAST: Ideal Adsorbed Solution Theory (IAST) Python Package.* Comput. Phys. Commun., 2016. **200**: p. 364−380.
180. Walton, K.S. and D.S. Sholl, *Predicting Multicomponent Adsorption: 50 Years of the Ideal Adsorbed Solution Theory.* AIChE J., 2015. **61**(9): p. 2757−2762.
181. Dickey, A.N., et al., *Screening CO_2/N_2 Selectivity in Metal-organic Frameworks using Monte Carlo Simulations and Ideal Adsorbed Solution Theory.* Can. J.

Chem. Eng., 2012. **90**(4): p. 825−832.
182. Keskin, S., *Molecular Simulation Study of CH_4/H_2 Mixture Separations Using Metal Organic Framework Membranes and Composites.* J. Phys. Chem. C., 2010. **114**(30): p. 13047−13054.
183. Keskin, S. and D.S. Sholl, *Efficient Methods for Screening of Metal Organic Framework Membranes for Gas Separations using Atomically Detailed Models.* Langmuir, 2009. **25**(19): p. 11786−11795.
184. Gómez-Álvarez, P., et al., *Importance of Blocking Inaccessible Voids on Modeling Zeolite Adsorption: Revisited.* J. Phys. Chem. C., 2017. **121**(8): p. 4462−4470.
185. Zhang, K., et al., *Crucial Role of Blocking Inaccessible Cages in the Simulation of Gas Adsorption in a Paddle-wheel Metal–organic Framework.* RSC Adv., 2013. **3**(36): p. 16152−16158.
186. Yang, Q., et al., *Molecular Simulation of CO_2/H_2 Mixture Separation in Metal-organic Frameworks: Effect of Catenation and Electrostatic Interactions.* Chin. J. Chem. Eng., 2009. **17**(5): p. 781−790.
187. Han, S.S., D.-H. Jung, and J. Heo, *Interpenetration of Metal Organic Frameworks for Carbon Dioxide Capture and Hydrogen Purification: Good or Bad?* J. Phys. Chem. C., 2013. **117**(1): p. 71−77.
188. Leung, D.Y.C., G. Caramanna, and M.M. Maroto-Valer, *An Overview of Current Status of Carbon Dioxide Capture and Storage Technologies.* Renew. Sust. Eneg. Rev., 2014. **39**: p. 426−443.
189. Erucar, I. and S. Keskin, *Unlocking the Effect of H_2O on CO_2 Separation Performance of Promising MOFs Using Atomically Detailed Simulations.* Ind. Eng. Chem., 2020. **59**(7): p. 3141−3152.
190. Song, Q., et al., *Photo-oxidative Enhancement of Polymeric Molecular Sieve Membranes.* Nat. Commun., 2013. **4**(1): p. 1918−1926.
191. Lai, L.S., et al., *Zeolitic Imidazolate Frameworks (ZIF): A Potential Membrane for CO_2/CH_4 Separation.* Sep. Sci. Technol., 2014. **49**(10): p. 1490−1508.
192. Huang, A., et al., *Neutral and Cation-free LTA-type Aluminophosphate ($AlPO_4$) Molecular Sieve Membrane with High Hydrogen Permselectivity.* J. Am. Chem. Soc., 2010. **132**(7): p. 2140−2141.
193. Chi, C., et al., *Facile Preparation of Graphene Oxide Membranes for Gas Separation.* Chem. Mater., 2016. **28**(9): p. 2921−2927.
194. Kang, Z., et al., *Highly Selective Sieving of Small Gas Molecules by Using an Ultra-microporous Metal–organic Framework Membrane.* Energy Environ. Sci., 2014. **7**(12): p. 4053−4060.
195. Bux, H., et al., *Zeolitic Imidazolate Framework Membrane with Molecular Sieving Properties by Microwave-Assisted Solvothermal Synthesis.* J. Am. Chem. Soc., 2009. **131**(44): p. 16000−16001.
196. Avci, G., S. Velioglu, and S. Keskin, *In Silico Design of Metal Organic Frameworks with Enhanced CO2 Separation Performances: Role of Metal Sites.* The Journal of Physical Chemistry C, 2019. **123**(46): p. 28255-28265.
197. Avci, G., C. Altintas, and S. Keskin, *Metal Exchange Boosts the CO2 Selectivity of Metal Organic Frameworks Having Zn-Oxide Nodes.* The Journal of Physical Chemistry C, 2021. **125**(31): p. 17311-17322.
198. Wilmer, C.E., K.C. Kim, and R.Q. Snurr, *An Extended Charge Equilibration Method.* The Journal of Physical Chemistry Letters, 2012. **3**(17): p. 2506-2511.
199. Bruno, I.J., et al., *New software for searching the Cambridge Structural Database*

and visualizing crystal structures. Acta Crystallogr., Sect. B: Struct. Sci, 2002. **58**(3): p. 389-397.
200. Moghadam, P.Z., et al., *Targeted classification of metal-organic frameworks in the Cambridge structural database (CSD).* Chem. Sci., 2020. **11**(32): p. 8373-8387.
201. Lalonde, M., et al., *Transmetalation: routes to metal exchange within metal-organic frameworks.* J. Mater. Chem. A, 2013. **1**(18): p. 5453-5468.
202. Li, S., et al., *High-throughput computational screening of multivariate metal–organic frameworks (MTV-MOFs) for CO_2 capture.* J. Phys. Chem. Lett., 2017. **8**(24): p. 6135-6141.
203. Qin, J.-S., et al., *Mixed-linker strategy for the construction of multifunctional metal–organic frameworks.* J. Mater. Chem. A, 2017. **5**(9): p. 4280-4291.
204. Wang, Y., et al., *Topology exploration in highly connected rare-earth metal–organic frameworks via continuous hindrance control.* J. Am. Chem. Soc., 2019. **141**(17): p. 6967-6975.
205. Erucar, I. and S. Keskin, *High CO_2 selectivity of an amine-functionalized metal organic framework in adsorption-based and membrane-based gas separations.* Ind. Eng. Chem. Res., 2013. **52**(9): p. 3462-3472.
206. Avci, G., I. Erucar, and S. Keskin, *Do new MOFs perform better for CO_2 capture and H_2 purification? Computational screening of the updated MOF database.* ACS Appl. Mater. Interfaces, 2020. **12**(37): p. 41567-41579.
207. Li, H., et al., *Design and synthesis of an exceptionally stable and highly porous metal-organic framework.* Nature, 1999. **402**(6759): p. 276-279.
208. Hafizovic, J., et al., *The inconsistency in adsorption properties and powder XRD data of MOF-5 is rationalized by framework interpenetration and the presence of organic and inorganic species in the nanocavities.* J. Am. Chem. Soc., 2007. **129**(12): p. 3612-3620.
209. Lim, D.W., S.A. Chyun, and M.P. Suh, *Hydrogen storage in a potassium-ion-bound metal-organic framework incorporating crown ether struts as specific cation binding sites.* Angew. Chem. Int. Ed., 2014. **53**(30): p. 7819-7822.
210. Brozek, C.K. and M. Dincă, *Lattice-imposed geometry in metal–organic frameworks: lacunary Zn_4O clusters in MOF-5 serve as tripodal chelating ligands for Ni^{2+}.* Chem. Sci., 2012. **3**(6): p. 2110-2113.
211. Brozek, C.K. and M. Dincă, *Ti^{3+}-, $V^{2+/3+}$-, $Cr^{2+/3+}$-, Mn^{2+}-, and Fe^{2+}-substituted MOF-5 and redox reactivity in Cr- and Fe-MOF-5.* J. Am. Chem. Soc., 2013. **135**(34): p. 12886-12891.
212. Brozek, C.K. and M. Dincă, *Thermodynamic parameters of cation exchange in MOF-5 and MFU-4l.* Chem. Commun., 2015. **51**(59): p. 11780-11782.
213. Borycz, J., et al., *CO_2 adsorption in M-IRMOF-10 (M = Mg, Ca, Fe, Cu, Zn, Ge, Sr, Cd, Sn, Ba).* J. Phys. Chem. C., 2016. **120**(23): p. 12819-12830.
214. Li, J., et al., *Study on the reaction of polymeric zinc ferrocenyl carboxylate with Pb(II) or Cd(II).* Cryst. Growth Des., 2009. **9**(10): p. 4504-4513.
215. Wu, Y., et al., *Adsorptive separation of methanol-acetone on isostructural series of metal-organic frameworks M-BTC (M = Ti, Fe, Cu, Co, Ru, Mo): A computational study of adsorption mechanisms and metal-substitution impacts.* ACS Appl. Mater. Interfaces, 2015. **7**(48): p. 26930-40.
216. Li, Y.L., Y.S. Liu, and X. Yang, *A new safety enrichment method for low concentration coal bed methane-proportion pressure swing adsorption.* Adv. Mat. Res., 2011. **233-235**: p. 2276-2280.

217. Avci, G., S. Velioglu, and S. Keskin, *In silico design of metal organic frameworks with enhanced CO_2 separation performances: Role of metal sites.* J. Phys. Chem. C., 2019. **123**(46): p. 28255-28265.
218. Martin, M.G. and J.I. Siepmann, *Transferable potentials for phase equilibria. 1. United-atom description of n-alkanes.* J. Phys. Chem. B., 1998. **102**(14): p. 2569-2577.
219. Wade, C.R. and M. Dinca, *Investigation of the synthesis, activation, and isosteric heats of CO_2 adsorption of the isostructural series of metal-organic frameworks $M_3(BTC)_2$ (M = Cr, Fe, Ni, Cu, Mo, Ru).* Dalton Trans., 2012. **41**(26): p. 7931-8.
220. Du, M., et al., *Adsorption mechanism on metal organic frameworks of Cu-BTC, Fe-BTC and ZIF-8 for CO_2 capture investigated by X-ray absorption fine structure.* RSC Adv., 2016. **6**(67): p. 62705-62716.
221. Zhang, W., et al., *Ruthenium metal-organic frameworks with different defect types: Influence on porosity, sorption, and catalytic properties.* Chem. Eur. J., 2016. **22**(40): p. 14297-14307.
222. Dureckova, H., et al., *Robust Machine Learning Models for Predicting High CO2 Working Capacity and CO2/H2 Selectivity of Gas Adsorption in Metal Organic Frameworks for Precombustion Carbon Capture.* The Journal of Physical Chemistry C, 2019. **123**(7): p. 4133-4139.
223. Avci, G., S. Velioglu, and S. Keskin, *High-Throughput Screening of MOF Adsorbents and Membranes for H2 Purification and CO2 Capture.* ACS Applied Materials & Interfaces, 2018. **10**(39): p. 33693-33706.
224. Li, Z., et al., *Porous metal-organic frameworks for carbon dioxide adsorption and separation at low pressure.* ACS Sustainable Chem. Eng., 2020. **8**(41): p. 15378-15404.
225. Zhang, Z., et al., *Perspective of microporous metal-organic frameworks for CO_2 capture and separation.* Energy Environ. Sci., 2014. **7**(9): p. 2868-2899.
226. Sokhanvaran, V. and S. Yeganegi, *Multiscale computational study on the adsorption and separation of CO_2/CH_4 and CO_2/H_2 on Li^+-doped mixed-ligand metal-organic framework $Zn_2(NDC)_2(diPyNI)$.* ChemPhysChem, 2016. **17**(24): p. 4124-4133.
227. Daglar, H. and S. Keskin, *Recent advances, opportunities, and challenges in high-throughput computational screening of MOFs for gas separations.* Coord. Chem. Rev., 2020. **422**: p. 213470.
228. Krishna, R. and J.R. Long, *Screening Metal–Organic Frameworks by Analysis of Transient Breakthrough of Gas Mixtures in a Fixed Bed Adsorber.* The Journal of Physical Chemistry C, 2011. **115**(26): p. 12941-12950.
229. Liu, J., et al., *Selective H2S/CO2 Separation by Metal–Organic Frameworks Based on Chemical-Physical Adsorption.* The Journal of Physical Chemistry C, 2017. **121**(24): p. 13249-13255.
230. Adatoz, E., A.K. Avci, and S. Keskin, *Opportunities and challenges of MOF-based membranes in gas separations.* Separation and Purification Technology, 2015. **152**: p. 207-237.
231. Altintas, C., et al., *Machine Learning Meets with Metal Organic Frameworks for Gas Storage and Separation.* Journal of Chemical Information and Modeling, 2021. **61**(5): p. 2131-2146.
232. Herm, Z.R., et al., *Metal−organic Frameworks as Adsorbents for Hydrogen Purification and Precombustion Carbon Dioxide Capture.* J. Am. Chem. Soc., 2011. **133**(15): p. 5664−5667.

233. Keskin, S., *Gas adsorption and diffusion in a highly CO2 selective metal–organic framework: molecular simulations.* Molecular Simulation, 2013. **39**(1): p. 14-24.
234. Guo, H., et al., *"Twin copper source" growth of metal− organic framework membrane: Cu3 (BTC) 2 with high permeability and selectivity for recycling H2.* Journal of the American Chemical Society, 2009. **131**(5): p. 1646-1647.

APPENDIX A

Table A.1. Potential parameters of H_2O, N_2, CO_2 and H_2 molecules used in the simulations

Molecule	ε/k_b (K)	σ (Å)	Bond length (Å)	Partial charge (e^-)
H_2O	108.0	3.76	1.54	-
H_2	92.8	3.68	1.33	-
CO_2	27.0	2.80	1.16	0.70
	79.0	3.05		-0.35
CH_4	148	3.73	-	-

Table A.2. Experimental adsorption selectivity data of MOFs.

MOF	P (bar)	T (K)	Mixture	Method	Reference
Ni-4PyC	10/35	313	CO_2/H_2	Single gas adsorption+IAST*	[152]
MOF177	10/35	313	CO_2/H_2	Single gas adsorption+IAST	[232]
Be-BTB	10/35	313	CO_2/H_2	Single gas adsorption+IAST	[232]
VEXTUO	10/20	313	CO_2/H_2	Single gas adsorption+IAST	[158]
NOTT-101/OeT	10/20	313	CO_2/H_2	Single gas adsorption+IAST	[158]
ZIF-8**	1	298	CO_2/H_2	Mixture GCMC	[233]
PCN-66	1	298	CO_2/H_2	Mixture GCMC	[150]
PCN-68	1	298	CO_2/H_2	Mixture GCMC	[150]
NU-111	1	298	CO_2/H_2	Mixture GCMC	[150]
CU-TDPAT*	1	298	CO_2/H_2	Mixture GCMC	[233]

*IAST: Ideal Adsorbed Solution Theory

All adsorption selectivity data belong to CO_2/H_2:15/85 mixtures except in ** where the composition is equimolar.

Table A.3. Experimental gas permeance data of MOF membranes.

MOF	T (K)	P_{feed} (bar)	$P_{permeate}$ (bar)	Membrane thickness (µm)	Method	Reference
MOF-5	298	1.06	Vacuum	25	Single gas	[110]
Ni-MOF-74	303	1.8	1	25	Single gas	[110]
ZIF-90	473	1	Vacuum	20	Single gas	[110]
Cu-BTC	298	1	Vacuum	60	Single gas+ equimolar mixture	[234]
ZIF-95	598	1	Vacuum	30	equimolar mixture	[110]

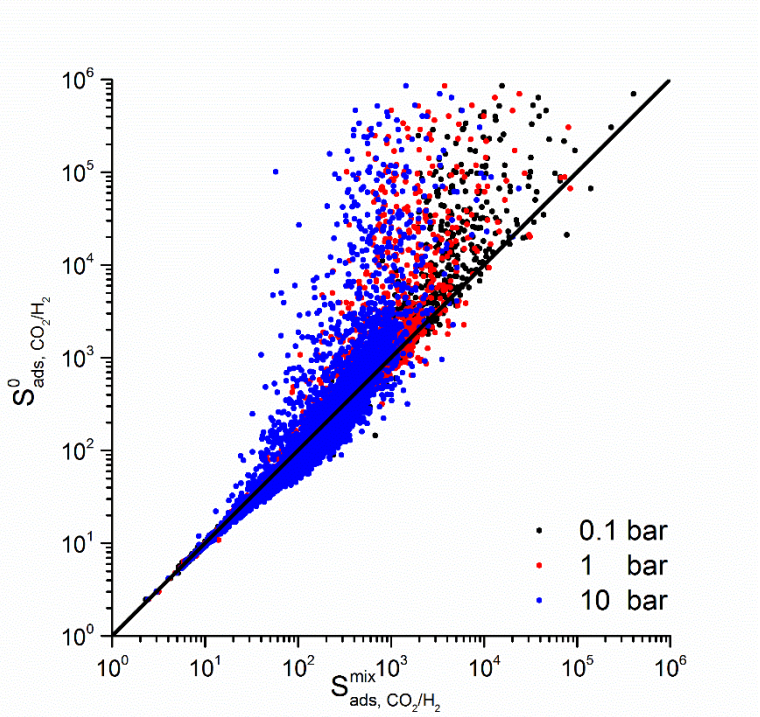

Figure A.1. Comparison of selectivity computed at infinite dilution and CO_2/H_2:15/85 mixture selectivity computed at 0.1, 1 and 10 bar and 298 K. Black line represents x=y to guide the eye.

	AFEJOK	AMOYOR	BUHJUL	CUSDIE	DATKIU	EBIDAW	EGELUY	GUKYUI	HISJIE	NIDBOS	OTAQUW	PEJMOH	RAVNAE	RIGVOU	TIXVON	UBIPAY	WOBQEL	YARFII02	YAZFOW	YEVPIZ
AFEJOK	1.00	0.71	0.76	0.66	0.70	0.79	0.75	0.73	0.70	0.73	0.80	0.72	0.69	0.72	0.78	0.74	0.76	0.75	0.75	0.77
AMOYOI	0.71	1.00	0.78	0.58	0.58	0.77	0.60	0.83	0.84	0.81	0.74	0.65	0.84	0.84	0.73	0.81	0.76	0.82	0.61	0.78
BUHJUL	0.76	0.78	1.00	0.59	0.62	0.82	0.66	0.79	0.77	0.79	0.79	0.71	0.74	0.77	0.78	0.81	0.82	0.80	0.66	0.81
CUSDIE	0.66	0.58	0.59	1.00	0.64	0.64	0.63	0.60	0.58	0.59	0.63	0.61	0.57	0.58	0.64	0.61	0.61	0.62	0.63	0.62
DATKIU	0.70	0.58	0.62	0.64	1.00	0.64	0.72	0.59	0.57	0.60	0.67	0.69	0.56	0.58	0.68	0.60	0.62	0.61	0.72	0.62
EBIDAW	0.79	0.77	0.82	0.64	0.64	1.00	0.69	0.79	0.77	0.78	0.82	0.74	0.75	0.77	0.82	0.81	0.81	0.82	0.69	0.83
EGELUY	0.75	0.60	0.66	0.63	0.72	0.69	1.00	0.63	0.61	0.64	0.70	0.69	0.57	0.61	0.72	0.63	0.67	0.64	0.76	0.66
GUKYUI	0.73	0.83	0.79	0.60	0.59	0.79	0.63	1.00	0.84	0.82	0.77	0.67	0.81	0.81	0.74	0.83	0.78	0.83	0.63	0.79
HISJIE	0.70	0.84	0.77	0.58	0.57	0.77	0.61	0.84	1.00	0.81	0.74	0.64	0.84	0.82	0.72	0.81	0.75	0.82	0.62	0.77
NIDBOS	0.73	0.81	0.79	0.59	0.60	0.78	0.64	0.82	0.81	1.00	0.78	0.67	0.79	0.81	0.73	0.81	0.78	0.82	0.64	0.78
OTAQUW	0.80	0.74	0.79	0.63	0.67	0.82	0.70	0.77	0.74	0.78	1.00	0.75	0.71	0.73	0.79	0.79	0.80	0.79	0.72	0.81
PEJMOH	0.72	0.65	0.71	0.61	0.69	0.74	0.69	0.67	0.64	0.67	0.75	1.00	0.62	0.65	0.74	0.69	0.72	0.68	0.71	0.72
RAVNAE	0.69	0.84	0.74	0.57	0.56	0.75	0.57	0.81	0.84	0.79	0.71	0.62	1.00	0.82	0.71	0.80	0.72	0.80	0.59	0.75
RIGVOU	0.72	0.84	0.77	0.58	0.58	0.77	0.61	0.81	0.82	0.81	0.73	0.65	0.82	1.00	0.72	0.80	0.76	0.81	0.62	0.77
TIXVON	0.78	0.73	0.78	0.64	0.68	0.82	0.72	0.74	0.72	0.73	0.79	0.74	0.71	0.72	1.00	0.77	0.76	0.76	0.75	0.81
UBIPAY	0.74	0.81	0.81	0.61	0.60	0.81	0.63	0.83	0.81	0.81	0.79	0.69	0.80	0.80	0.77	1.00	0.81	0.84	0.64	0.82
WOBQEL	0.76	0.76	0.82	0.61	0.62	0.81	0.67	0.78	0.75	0.78	0.80	0.72	0.72	0.76	0.76	0.81	1.00	0.80	0.68	0.80
YARFII02	0.75	0.82	0.80	0.62	0.61	0.82	0.64	0.83	0.82	0.82	0.79	0.68	0.80	0.81	0.76	0.84	0.80	1.00	0.64	0.80
YAZFOW	0.75	0.61	0.66	0.63	0.72	0.69	0.76	0.63	0.62	0.64	0.72	0.71	0.59	0.62	0.75	0.64	0.68	0.64	1.00	0.67
YEVPIZ	0.77	0.78	0.81	0.62	0.62	0.83	0.66	0.79	0.77	0.78	0.81	0.72	0.75	0.77	0.81	0.82	0.80	0.80	0.67	1.00

	AQEKUD	CAXTEC	CECJAW	COQTEJ	DABWUA	ENATUJ	FOJWOS	HAFVUH	HASSUR	HOWRES	HUFHUN	IJEFUZ	LEYGIH	LONVIV	NULHEJ	QUQQUP	TUBTOB	UWOWEJ	VARJEF	XUNGIX
AQEKUD	1.00	0.61	0.75	0.64	0.61	0.57	0.62	0.58	0.61	0.57	0.55	0.67	0.68	0.61	0.51	0.75	0.69	0.68	0.58	0.61
CAXTEC	0.61	1.00	0.62	0.63	0.70	0.73	0.67	0.69	0.73	0.67	0.66	0.70	0.73	0.65	0.66	0.59	0.67	0.69	0.68	0.74
CECJAW	0.75	0.62	1.00	0.63	0.61	0.58	0.65	0.59	0.61	0.59	0.57	0.69	0.67	0.62	0.55	0.72	0.68	0.70	0.59	0.62
COQTEJ	0.64	0.63	0.63	1.00	0.58	0.66	0.64	0.54	0.64	0.55	0.53	0.70	0.67	0.58	0.51	0.65	0.71	0.66	0.56	0.72
DABWUA	0.61	0.70	0.61	0.58	1.00	0.73	0.69	0.76	0.78	0.78	0.71	0.69	0.75	0.67	0.71	0.57	0.67	0.69	0.77	0.67
ENATUJ	0.57	0.73	0.58	0.66	0.73	1.00	0.70	0.67	0.79	0.70	0.66	0.70	0.75	0.66	0.64	0.56	0.69	0.69	0.69	0.74
FOJWOS	0.62	0.67	0.65	0.64	0.69	0.70	1.00	0.68	0.72	0.69	0.64	0.73	0.71	0.64	0.65	0.60	0.68	0.72	0.67	0.70
HAFVUH	0.58	0.69	0.59	0.54	0.76	0.67	0.68	1.00	0.71	0.77	0.75	0.64	0.68	0.65	0.77	0.52	0.61	0.64	0.76	0.64
HASSUR	0.61	0.73	0.61	0.64	0.78	0.79	0.72	0.71	1.00	0.75	0.69	0.74	0.78	0.67	0.68	0.59	0.71	0.72	0.74	0.74
HOWRES	0.57	0.67	0.59	0.55	0.78	0.70	0.69	0.77	0.75	1.00	0.74	0.65	0.70	0.65	0.76	0.52	0.61	0.65	0.77	0.65
HUFHUN	0.55	0.66	0.57	0.53	0.71	0.66	0.64	0.75	0.69	0.74	1.00	0.60	0.66	0.68	0.75	0.50	0.59	0.60	0.73	0.61
IJEFUZ	0.67	0.70	0.69	0.70	0.69	0.70	0.73	0.64	0.74	0.65	0.60	1.00	0.75	0.64	0.60	0.66	0.74	0.74	0.65	0.75
LEYGIH	0.68	0.73	0.67	0.67	0.75	0.75	0.71	0.68	0.78	0.70	0.66	0.75	1.00	0.68	0.63	0.65	0.74	0.74	0.70	0.73
LONVIV	0.61	0.65	0.62	0.58	0.67	0.66	0.64	0.65	0.67	0.65	0.68	0.64	0.68	1.00	0.62	0.58	0.66	0.66	0.66	0.63
NULHEJ	0.51	0.66	0.55	0.51	0.71	0.64	0.65	0.77	0.68	0.76	0.75	0.60	0.63	0.62	1.00	0.47	0.56	0.60	0.74	0.62
QUQQUP	0.75	0.59	0.72	0.65	0.57	0.56	0.60	0.52	0.59	0.52	0.50	0.66	0.65	0.58	0.47	1.00	0.69	0.67	0.53	0.61
TUBTOB	0.69	0.67	0.68	0.71	0.67	0.69	0.68	0.61	0.71	0.61	0.59	0.74	0.74	0.66	0.56	0.69	1.00	0.74	0.63	0.70
UWOWEJ	0.68	0.69	0.70	0.66	0.69	0.69	0.72	0.64	0.72	0.65	0.60	0.74	0.74	0.66	0.60	0.67	0.74	1.00	0.65	0.71
VARJEF	0.58	0.68	0.59	0.56	0.77	0.69	0.67	0.76	0.74	0.77	0.73	0.65	0.70	0.66	0.74	0.53	0.63	0.65	1.00	0.65
XUNGIX	0.61	0.74	0.62	0.72	0.67	0.74	0.70	0.64	0.74	0.65	0.61	0.75	0.73	0.63	0.62	0.61	0.70	0.71	0.65	1.00

	DEJMOV	GUGNON	HESJOE	HONCIY	KAXQOR	KIPJUQ	LACFOM	LIFWON	LOYMET	LUPQES	NADZID	NEWWAP	NURVAZ	PEMGIZ	PEXROB	PEXSES	SAJFEO	VAJTOR	VOJMIS	VUHJAK
DEJMOV	1.00	0.77	0.81	0.85	0.83	0.73	0.83	0.73	0.85	0.66	0.80	0.76	0.52	0.76	0.75	0.75	0.52	0.87	0.73	0.87
GUGNON	0.77	1.00	0.81	0.75	0.73	0.78	0.73	0.81	0.73	0.77	0.77	0.83	0.59	0.66	0.83	0.83	0.59	0.74	0.82	0.77
HESJOE	0.81	0.81	1.00	0.78	0.76	0.77	0.76	0.79	0.76	0.72	0.83	0.80	0.57	0.68	0.80	0.81	0.57	0.77	0.79	0.80
HONCIY	0.85	0.75	0.78	1.00	0.84	0.70	0.85	0.72	0.85	0.65	0.79	0.76	0.53	0.76	0.73	0.72	0.53	0.86	0.71	0.85
KAXQOR	0.83	0.73	0.76	0.84	1.00	0.69	0.86	0.70	0.87	0.65	0.76	0.74	0.52	0.79	0.72	0.71	0.52	0.86	0.71	0.84
KIPJUQ	0.73	0.78	0.77	0.70	0.69	1.00	0.67	0.79	0.70	0.76	0.74	0.81	0.60	0.61	0.81	0.80	0.60	0.69	0.80	0.71
LACFOM	0.83	0.73	0.76	0.85	0.86	0.67	1.00	0.70	0.86	0.64	0.75	0.73	0.51	0.81	0.71	0.70	0.52	0.86	0.70	0.85
LIFWON	0.73	0.81	0.79	0.72	0.70	0.79	0.70	1.00	0.69	0.76	0.76	0.82	0.61	0.63	0.81	0.81	0.60	0.70	0.80	0.73
LOYMET	0.85	0.73	0.76	0.85	0.87	0.70	0.86	0.69	1.00	0.63	0.76	0.73	0.51	0.81	0.71	0.71	0.51	0.89	0.70	0.86
LUPQES	0.66	0.77	0.72	0.65	0.65	0.76	0.64	0.76	0.63	1.00	0.71	0.79	0.66	0.56	0.80	0.79	0.66	0.64	0.81	0.67
NADZID	0.80	0.77	0.83	0.79	0.76	0.74	0.75	0.76	0.76	0.71	1.00	0.78	0.56	0.67	0.78	0.77	0.56	0.76	0.76	0.79
NEWWAP	0.76	0.83	0.80	0.76	0.74	0.81	0.73	0.82	0.73	0.79	0.78	1.00	0.61	0.66	0.85	0.85	0.61	0.73	0.84	0.76
NURVAZ	0.52	0.59	0.57	0.53	0.52	0.60	0.51	0.61	0.51	0.66	0.56	0.61	1.00	0.46	0.61	0.61	0.98	0.50	0.63	0.52
PEMGIZ	0.76	0.66	0.68	0.76	0.79	0.61	0.81	0.63	0.81	0.56	0.67	0.66	0.46	1.00	0.65	0.64	0.46	0.81	0.63	0.81
PEXROB	0.75	0.83	0.80	0.73	0.72	0.81	0.71	0.81	0.71	0.80	0.78	0.85	0.61	0.65	1.00	0.88	0.61	0.72	0.86	0.75
PEXSES	0.75	0.83	0.81	0.72	0.71	0.80	0.70	0.81	0.71	0.79	0.77	0.85	0.61	0.64	0.88	1.00	0.61	0.72	0.86	0.75
SAJFEO	0.52	0.59	0.57	0.53	0.52	0.60	0.52	0.60	0.51	0.66	0.56	0.61	0.98	0.46	0.61	0.61	1.00	0.50	0.63	0.52
VAJTOR	0.87	0.74	0.77	0.86	0.86	0.69	0.86	0.70	0.89	0.64	0.76	0.73	0.50	0.81	0.72	0.72	0.50	1.00	0.70	0.88
VOJMIS	0.73	0.82	0.79	0.71	0.71	0.80	0.70	0.80	0.70	0.81	0.76	0.84	0.63	0.63	0.86	0.86	0.63	0.70	1.00	0.73
VUHJAK	0.87	0.77	0.80	0.85	0.84	0.71	0.85	0.73	0.86	0.67	0.79	0.76	0.52	0.81	0.75	0.75	0.52	0.88	0.73	1.00

	BOGFIM	ECOKAJ	FOTNIN	GESVAC	HEXVEM	IZOWAW	JULDAV	MOVPEU	RUBDUP	RUBYUK	RUTNOK	SAPBIW	SONKAI	SOVGUF	TOVKOG	TURFIX	WIDNEC	XANLEF	XANLIJ	XIJNUA
BOGFIM	1.00	0.48	0.40	0.82	0.46	0.75	0.77	0.73	0.52	0.54	0.55	0.44	0.40	0.51	0.57	0.43	0.78	0.67	0.44	0.65
ECOKAJ	0.48	1.00	0.57	0.48	0.65	0.45	0.49	0.51	0.67	0.67	0.67	0.60	0.25	0.34	0.62	0.69	0.46	0.60	0.64	0.61
FOTNIN	0.40	0.57	1.00	0.40	0.58	0.38	0.40	0.46	0.59	0.59	0.56	0.63	0.26	0.33	0.56	0.61	0.38	0.51	0.63	0.55
GESVAC	0.82	0.48	0.40	1.00	0.47	0.73	0.79	0.73	0.52	0.55	0.55	0.45	0.40	0.49	0.58	0.44	0.76	0.67	0.45	0.67
HEXVEM	0.46	0.65	0.58	0.47	1.00	0.43	0.50	0.47	0.73	0.72	0.67	0.67	0.26	0.33	0.74	0.75	0.43	0.58	0.74	0.62
IZOWAW	0.75	0.45	0.38	0.73	0.43	1.00	0.70	0.63	0.48	0.47	0.49	0.38	0.46	0.57	0.51	0.41	0.75	0.60	0.41	0.57
JULDAV	0.77	0.49	0.40	0.79	0.50	0.70	1.00	0.67	0.54	0.58	0.58	0.44	0.36	0.46	0.60	0.46	0.70	0.67	0.47	0.66
MOVPEU	0.73	0.51	0.46	0.73	0.47	0.63	0.67	1.00	0.55	0.53	0.56	0.48	0.31	0.43	0.53	0.47	0.70	0.64	0.47	0.63
RUBDUP	0.52	0.67	0.59	0.52	0.73	0.48	0.54	0.55	1.00	0.71	0.75	0.64	0.27	0.33	0.74	0.75	0.47	0.67	0.70	0.63
RUBYUK	0.54	0.67	0.59	0.55	0.72	0.47	0.58	0.53	0.71	1.00	0.72	0.64	0.27	0.33	0.76	0.71	0.51	0.66	0.73	0.74
RUTNOK	0.55	0.67	0.56	0.55	0.67	0.49	0.58	0.56	0.75	0.72	1.00	0.59	0.27	0.34	0.74	0.69	0.50	0.72	0.65	0.68
SAPBIW	0.44	0.60	0.63	0.45	0.67	0.38	0.44	0.48	0.64	0.64	0.59	1.00	0.23	0.31	0.62	0.69	0.39	0.52	0.74	0.58
SONKAI	0.40	0.25	0.26	0.40	0.26	0.46	0.36	0.31	0.27	0.27	0.27	0.23	1.00	0.52	0.30	0.25	0.42	0.31	0.25	0.33
SOVGUF	0.51	0.34	0.33	0.49	0.33	0.57	0.46	0.43	0.33	0.33	0.34	0.31	0.52	1.00	0.34	0.31	0.54	0.38	0.31	0.39
TOVKOG	0.57	0.62	0.56	0.58	0.74	0.51	0.60	0.53	0.74	0.76	0.74	0.62	0.30	0.34	1.00	0.67	0.53	0.71	0.67	0.73
TURFIX	0.43	0.69	0.61	0.44	0.75	0.41	0.46	0.47	0.75	0.71	0.69	0.69	0.25	0.31	0.67	1.00	0.39	0.57	0.80	0.59
WIDNEC	0.78	0.46	0.38	0.76	0.43	0.75	0.70	0.70	0.47	0.51	0.50	0.39	0.42	0.54	0.53	0.39	1.00	0.63	0.41	0.62
XANLEF	0.67	0.60	0.51	0.67	0.58	0.60	0.67	0.64	0.67	0.66	0.72	0.52	0.31	0.38	0.71	0.57	0.63	1.00	0.56	0.72
XANLIJ	0.44	0.64	0.63	0.45	0.74	0.41	0.47	0.47	0.70	0.73	0.65	0.74	0.25	0.31	0.67	0.80	0.41	0.56	1.00	0.61
XIJNUA	0.65	0.61	0.55	0.67	0.62	0.57	0.66	0.63	0.63	0.74	0.68	0.58	0.33	0.39	0.73	0.59	0.62	0.72	0.61	1.00

Figure A.2. Structural similarity indexes (SI) of the top 20 most promising MOFs identified based on the highest APSs and R%>85% for (a) PSA process (b) VSA process (c) H_2 selective membranes (d) CO_2 selective membranes. Green, light green, yellow, orange, and red colors correspond to the most similar materials, highly similar, similar, slightly similar, and dissimilar materials having SI of 0.8-1.0, 0.7-0.8, 0.5-0.7, 0.3-0.5 and 0-0.3, respectively.

APPENDIX B

Table B.1. Parameters for Dual-site Langmuir isotherms of CO_2 adsorption.

MOFs	Model	M_1	K_1	M_2	K_2	R^2
DABWUA	DSLangmuir	8.99	0.39	7.13	0.39	0.79
EKEJOT	DSLangmuir	4.08	0.40	6.64	0.40	0.80
TENLAC	DSLangmuir	8.74	0.43	6.93	0.43	0.79
FAQXIF	DSLangmuir	4.09	7.05	1.18	1.05	0.97
LACDEY	DSLangmuir	3.50	6.95	1.19	1.06	0.81
DATKIU	DSLangmuir	12.09	3.25	1.02	0.20	0.88
JOVLAH10	DSLangmuir	3.47	1.46	1.92	1.45	0.93
GEJRIW	DSLangmuir	13.16	1.23	1.22	1.23	0.88
QATPUX01	DSLangmuir	0.50	0.31	1.77	0.38	0.92

Table B.2. Parameters for Dual-site Langmuir isotherms of H_2 adsorption.

MOFs	Model	M_1	K_1	M_2	K_2	R^2
DABWUA	DSLangmuir	61.25	3.80×10^{-5}	18.04	2.60×10^{-3}	0.99
EKEJOT	DSLangmuir	4.43	2.50×10^{-4}	12.26	1.70×10^{-4}	0.99
TENLAC	DSLangmuir	11.05	3.20×10^{-4}	19.80	2.20×10^{-3}	0.99
FAQXIF	DSLangmuir	5.93	3.20×10^{-4}	7.57	1.60×10^{-3}	0.94
LACDEY	DSLangmuir	4.62	5.90×10^{-4}	4.21	4.50×10^{-3}	0.90
DATKIU	DSLangmuir	10.04	3.70×10^{-3}	45.33	1.40×10^{-4}	0.92
JOVLAH10	DSLangmuir	5.47	1.65×10^{-4}	8.00	4.26×10^{-4}	0.97
GEJRIW	DSLangmuir	22.90	1.03×10^{-3}	23.47	2.77×10^{-4}	0.98
QATPUX01	DSLangmuir	1.81	7.11×10^{-4}	2.48	9.90×10^{-4}	0.99

Table B.2. Performances of the top 10 MOFs (having the highest APSs and R% >85%) for

PSA, VSA, and TSA processes for separation of CO_2/H_2:15/85 binary mixture.

MOFs	APS (mol/kg)	$S^{mix}_{ads,CO_2/H_2}$	R%	LCD (Å)	PLD (Å)	ϕ	SA (m^2/g)
Pressure Swing Adsorption (PSA)							
DABWUA	2463.17	332.97	86.72	6.31	3.85	0.59	1339.41
EKEJOT	2442.44	490.30	85.82	6.08	5.90	0.42	1456.43
TENLAC	2348.93	317.55	85.52	5.59	4.52	0.64	2379.07
QEBZII	2318.89	339.79	86.79	5.93	5.43	0.58	2494.12
PIJDIW	2101.27	370.24	85.29	5.72	5.14	0.48	1171.33
HOWRES	2035.12	308.57	86.58	5.93	5.12	0.51	1541.54
IJEFUZ	1864.90	294.48	86.53	6.19	5.40	0.56	2077.14
ENATUJ	1848.82	238.76	87.96	5.93	5.35	0.63	2605.48
MEKKUL	1831.12	367.91	86.40	5.48	4.08	0.49	882.66
VUFHEL	1822.53	217.32	87.59	6.59	4.66	0.68	3330.39
Vacuum Swing Adsorption (VSA)							
FAQXIF	9834.22	3703.39	85.02	7.26	7.13	0.31	452.43
LACDEY	7592.04	2845.71	85.73	4.40	3.85	0.28	300.79
DATKIU	6735.40	1474.34	88.30	5.74	4.50	0.54	2138.70
OJASOJ	6249.19	1949.30	85.41	5.32	4.09	0.42	963.62
YUFLOC	5982.71	1353.18	86.77	5.97	4.46	0.59	2125.42
ERAPUK	4560.50	1283.27	85.94	7.36	7.24	0.52	1032.02
NIDBOS	4209.17	1928.53	88.11	5.46	5.27	0.31	564.20
SEHSUU	4161.53	1232.59	85.40	5.48	4.60	0.58	1311.18
AFEJOK	4009.79	1261.52	86.22	5.98	5.12	0.47	1240.72
GUKYUI	3880.99	1809.03	90.86	5.99	5.23	0.26	532.52
Temperature Swing Adsorption (TSA)							
JOVLAH10	3.07×10^5	5.55×10^4	85.95	4.86	3.75	0.54	299.56
GEJRIW	2.58×10^5	1.60×10^4	86.93	5.00	4.13	0.57	2061.75
QATPUX01	2.13×10^5	9.91×10^4	94.41	4.33	4.02	0.29	131.54
XUNHAQ	1.78×10^5	2.69×10^4	95.63	4.43	3.93	0.37	802.72
HAYTAE	1.57×10^5	2.37×10^4	86.92	4.16	3.84	0.55	423.62
YURRUY	1.30×10^5	1.21×10^4	87.68	4.87	4.44	0.59	1682.46
VIFBOD	1.28×10^5	2.44×10^4	89.89	5.74	4.36	0.55	606.52
VILWIX	1.27×10^5	1.38×10^4	91.25	5.24	4.24	0.66	1667.72
XIBXIP	1.17×10^5	1.37×10^4	90.22	6.55	4.91	0.67	1857.78
OMODAW	1.01×10^5	3.64×10^4	92.72	4.69	4.17	0.21	343.91

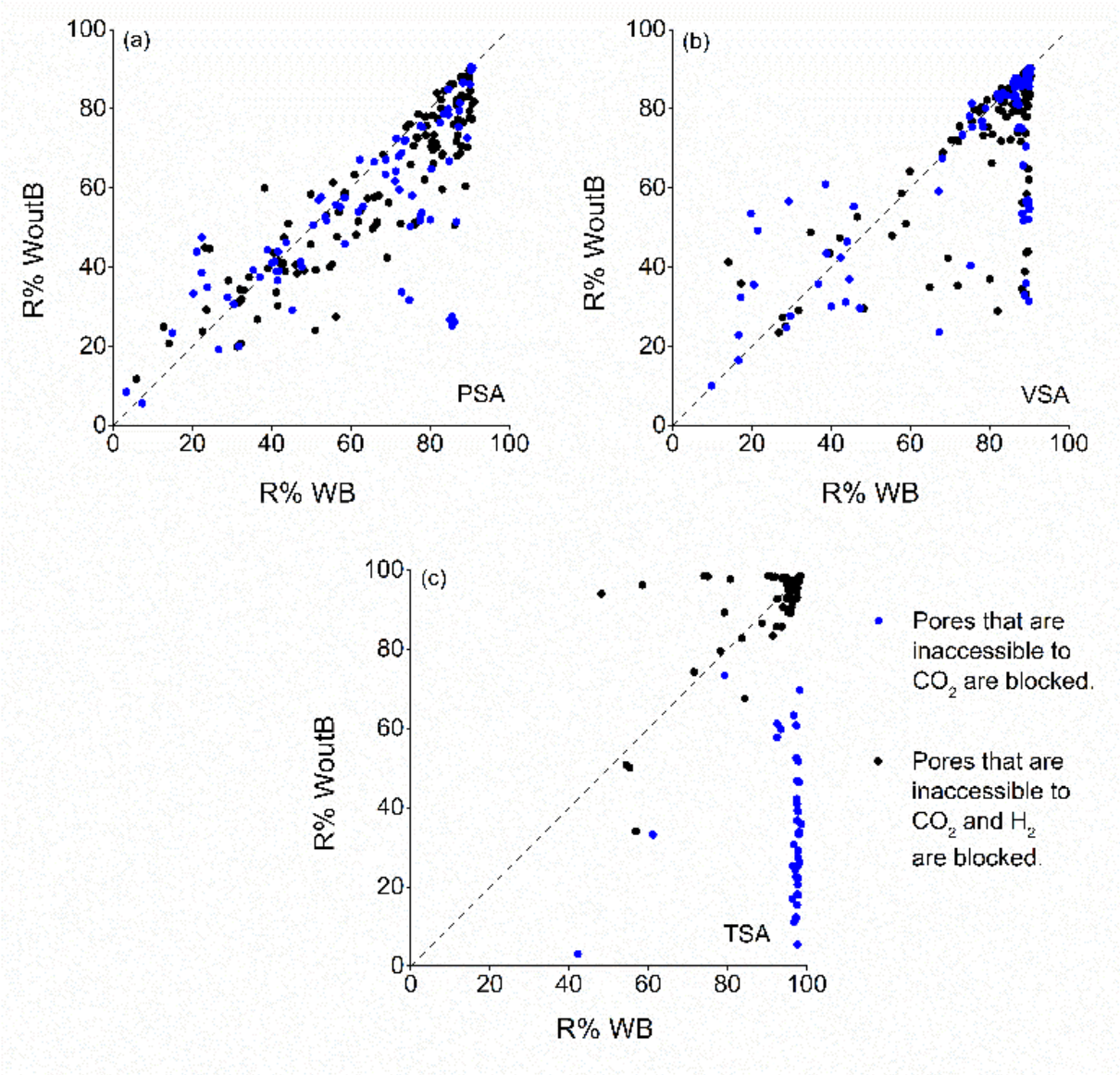

Figure B1. Effect of blocking pockets on R% of MOFs at (a) PSA, (b) VSA and (c) TSA conditions.

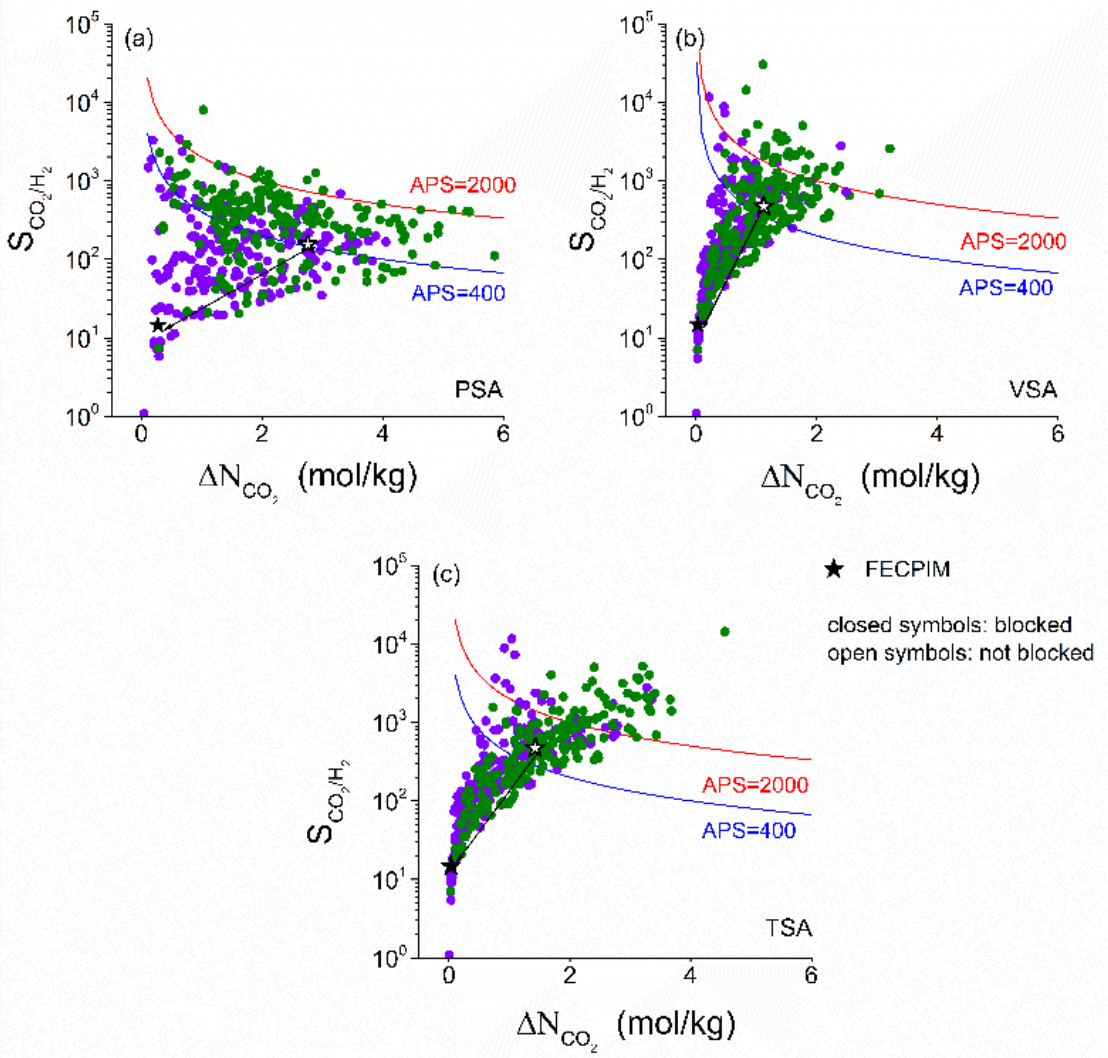

Figure B2. Effect of blocking pockets on selectivities and working capacities of MOFs at (a) PSA, (b) VSA, and (c) TSA conditions. Purple points represent the results obtained from simulations of MOFs where the pores that are inaccessible to CO_2 and H_2 were blocked. Green points represent the results obtained from simulations where the pores that are inaccessible to CO_2 and H_2 were not blocked.

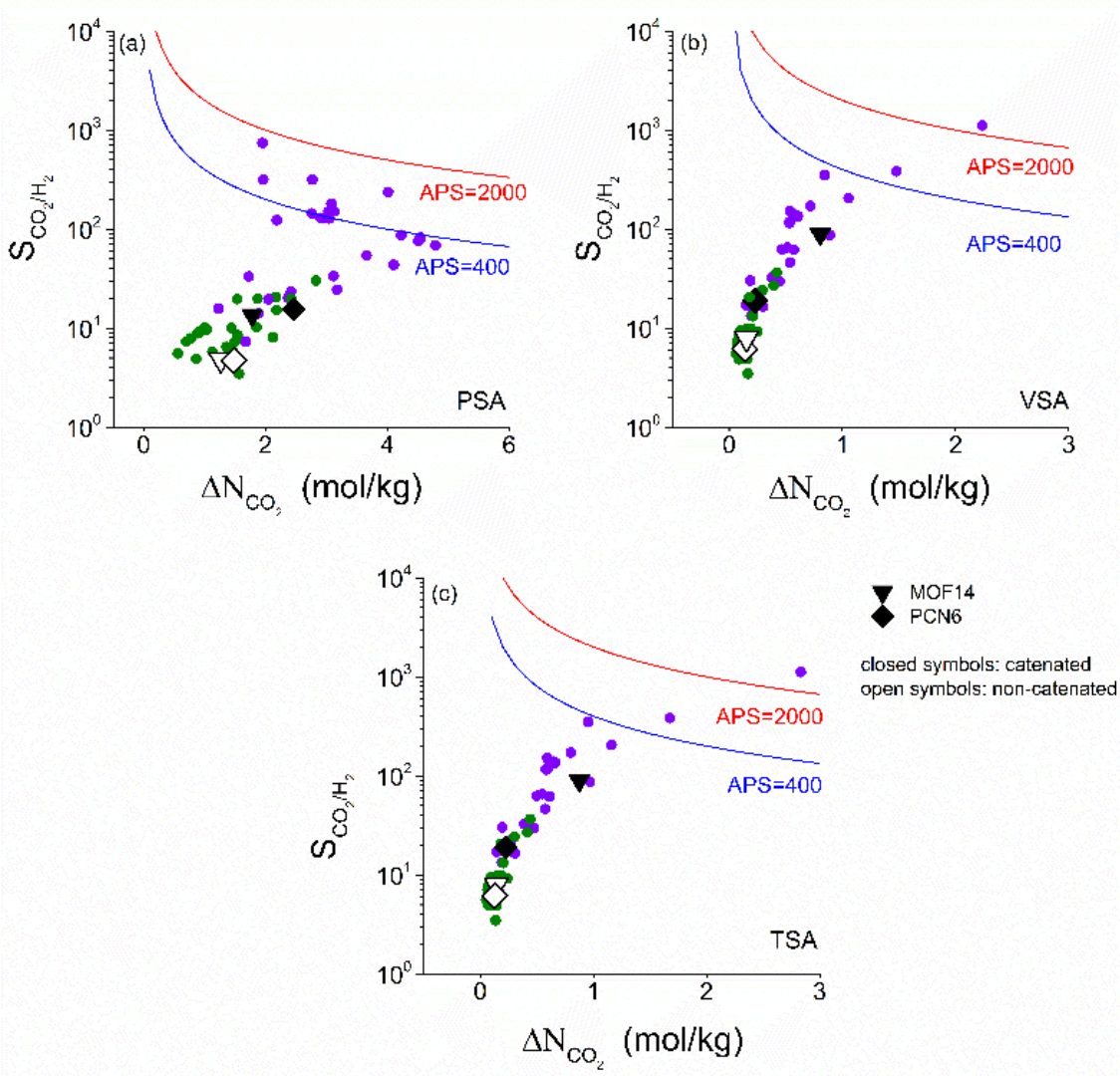

Figure B3. Effect of catenation on adsorption selectivity and working capacity of MOFs at (a) PSA, (b) VSA, and (c) TSA conditions. Green points represent the simulation results of non-catenated MOFs whereas purple points represent the simulation results of catenated MOFs.

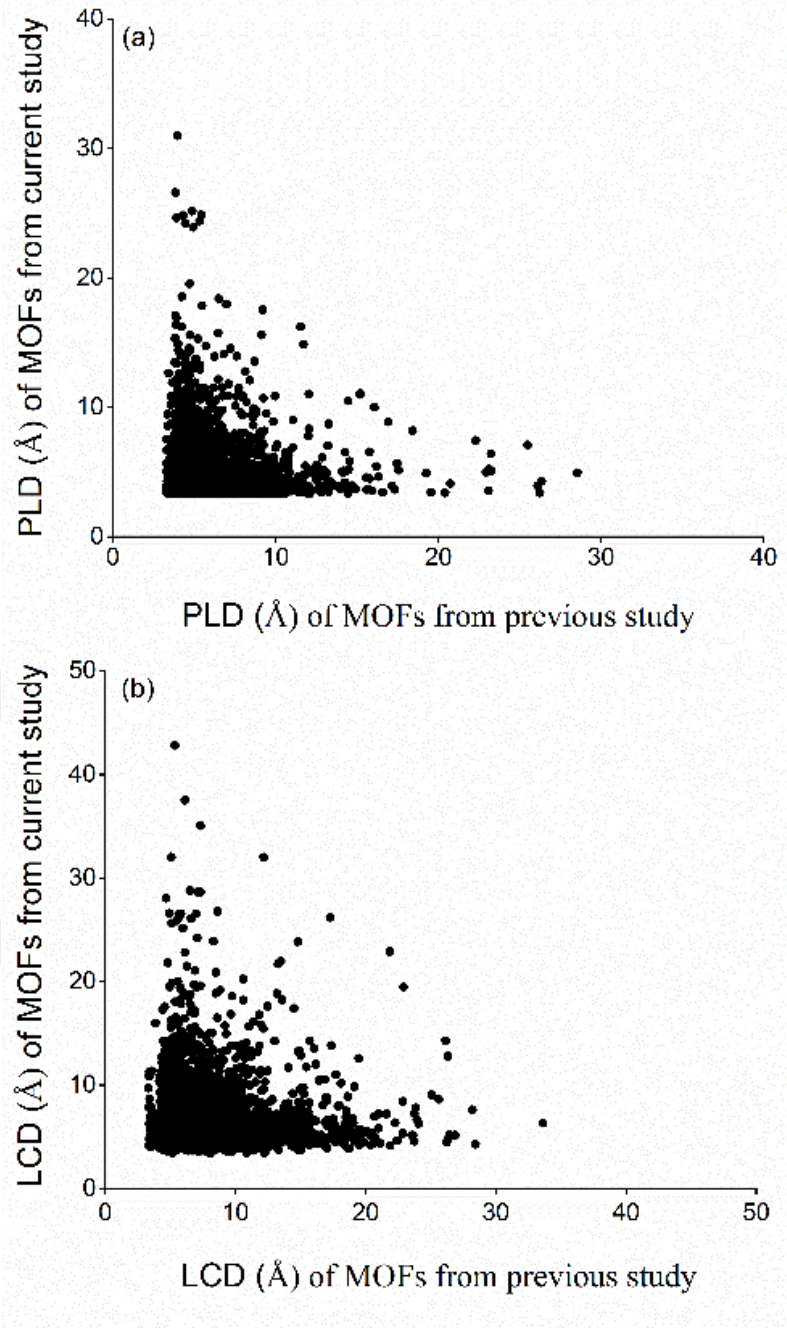

Figure B4. Comparison of (a) PLDs and (b) the LCDs of MOFs from this study and MOFs from our previous study.[89]

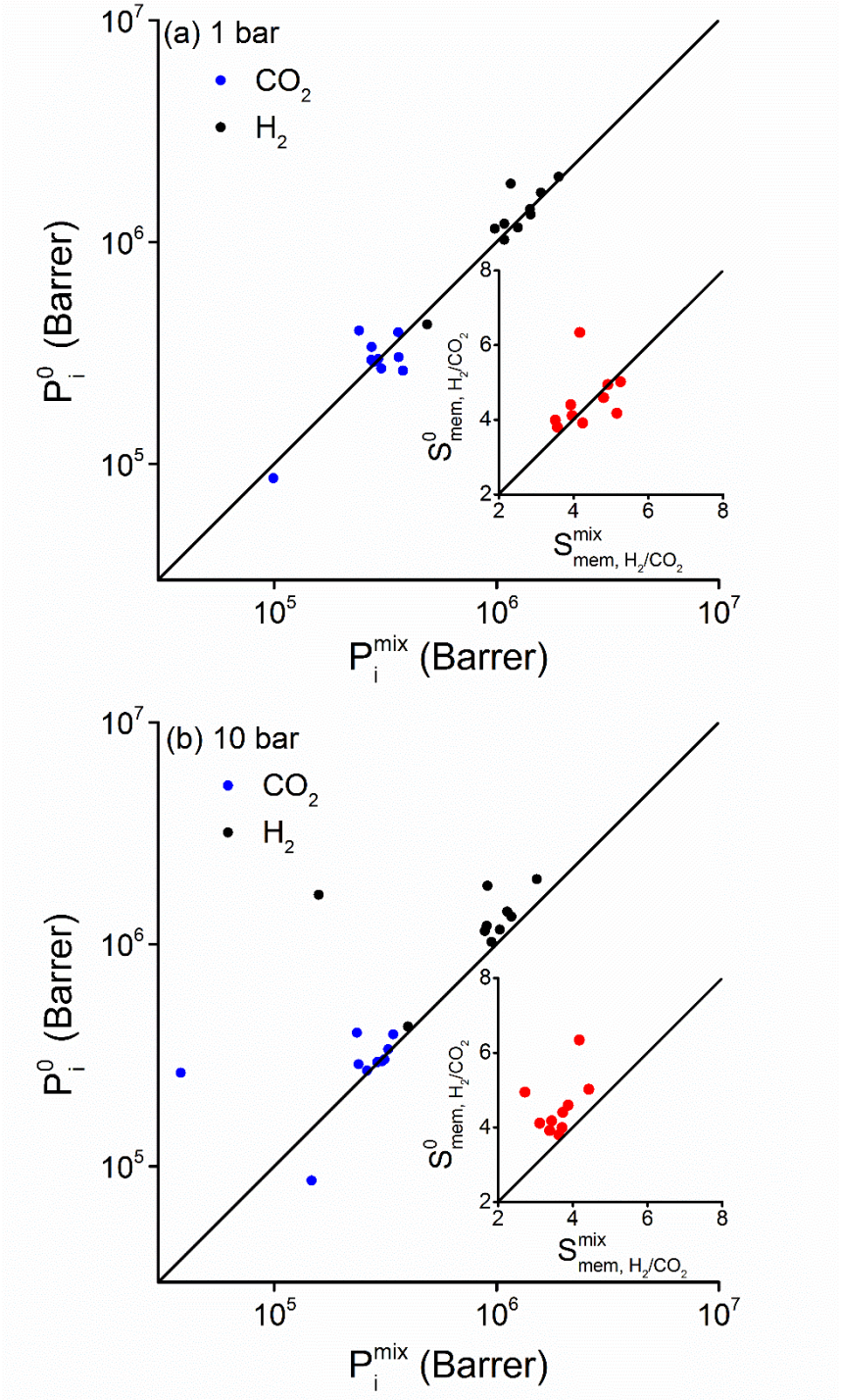

Figure B5. Comparison of gas permeabilities computed at infinite dilution ($P^0_{H_2}$ and $P^0_{CO_2}$) with the permeabilities computed for CO_2/H_2:15/85 mixture ($P^{mix}_{H_2}$ and $P^{mix}_{CO_2}$) at (a) 1 bar, (b) 10 bar. Inset shows the comparison of the selectivities computed at infinite dilution, $S^0_{mem,\ CO_2/H_2}$ with the mixture selectivities $S^{mix}_{mem,\ H_2/CO_2}$ at (a) 1 bar, (b) 10 bar.

APPENDIX C

Table C.1. Non-bonded interaction parameters of metals and structural properties of M-HKUST-1 and M-HATGUF materials.

MOF	ε_{metal}/k_B (K)	σ_{metal} (Å)	q_{metal} (e^-)	PLD (Å)	LCD (Å)	Surface area (m^2/g)	Pore volume (cm^3/g)
Cd-HKUST-1	114.8	2.54	1.21	6.72	13.44	1870.8	0.70
Co-HKUST-1	7.04	2.56	1.00	6.34	12.02	2095.5	0.77
Cr-HKUST-1	7.55	2.69	1.13	6.47	12.15	2292.7	0.83
Cu-HKUST-1	3.11	2.51	0.99	6.65	13.19	2159.7	0.82
Fe-HKUST-1	6.54	2.59	0.85	6.49	12.20	2248.9	0.82
Mn-HKUST-1	6.54	2.63	0.97	6.53	12.24	2309.4	0.84
Mo-HKUST-1	28.19	2.71	1.12	6.71	12.36	2032.4	0.73
Ni-HKUST-1	7.55	2.52	1.12	6.22	12.60	1898.3	0.75
Ru-HKUST-1	28.19	2.64	1.03	6.74	12.41	2015.4	0.72
Zn-HKUST-1	62.44	2.46	1.19	6.29	13.29	1861.0	0.75
Cd-HATGUF	114.8	2.54	1.21	7.36	8.78	913.2	0.46
Co-HATGUF	7.04	2.56	1.01	6.55	7.31	926.3	0.47
Cr-HATGUF	7.55	2.69	1.15	6.95	7.71	1054.0	0.53
Cu-HATGUF	3.11	2.51	0.99	6.67	8.42	918.1	0.50
Fe-HATGUF	6.54	2.59	0.84	6.96	7.68	1041.8	0.52
Mn-HATGUF	6.54	2.63	0.96	7.01	7.71	1056.9	0.53
Mo-HATGUF	28.19	2.71	1.09	7.31	8.22	931.1	0.48
Ni-HATGUF	7.55	2.52	1.15	6.27	7.22	878.8	0.46
Ru-HATGUF	28.19	2.64	0.99	7.36	8.35	921.0	0.47
Zn-HATGUF	62.44	2.46	1.21	6.22	7.21	824.9	0.43

Table C.2. Partial atomic charges (e^-) of atoms in M-HKUST-1 and M-HATGUF series. Different carbon atoms (Ca, Cb, and Cc) in the framework were labeled in Figure 6.1.

MOF	Metal	Oxygen	Ca	Cb	Cc	H
Cd-HKUST-1	1.21	-0.49	0.38	-0.14	0.07	0.04
Co-HKUST-1	1.00	-0.45	0.41	-0.14	0.09	0.04
Cr-HKUST-1	1.13	-0.48	0.37	-0.15	0.07	0.04
Cu-HKUST-1	0.99	-0.46	0.38	-0.13	0.11	0.04
Fe-HKUST-1	0.85	-0.39	0.38	-0.13	0.08	0.05
Mn-HKUST-1	0.97	-0.43	0.39	-0.14	0.08	0.03
Mo-HKUST-1	1.12	-0.46	0.39	-0.14	0.08	0.03
Ni-HKUST-1	1.12	-0.48	0.38	-0.14	0.08	0.05
Ru-HKUST-1	1.03	-0.43	0.38	-0.13	0.07	0.03
Zn-HKUST-1	1.19	-0.49	0.35	-0.12	0.08	0.07
Cd-HATGUF	1.21	-0.47	0.37	-0.08	0.06	0.05
Co-HATGUF	1.01	-0.46	0.41	-0.13	0.04	0.04
Cr-HATGUF	1.15	-0.47	0.37	-0.13	0.07	0.04
Cu-HATGUF	0.99	-0.44	0.43	-0.15	0.06	0.03
Fe-HATGUF	0.84	-0.39	0.38	-0.13	0.03	0.05
Mn-HATGUF	0.96	-0.43	0.39	-0.12	0.04	0.04
Mo-HATGUF	1.09	-0.45	0.38	-0.12	0.03	0.04
Ni-HATGUF	1.15	-0.49	0.39	-0.13	0.07	0.05
Ru-HATGUF	0.99	-0.44	0.43	-0.10	0.06	0.03
Zn-HATGUF	1.21	-0.50	0.36	-0.10	0.06	0.05

Table C3. S_{ads} of M-IRMOFs at 0.1, 1, and 10 bar, their physical properties (LCD, PLD, S_{acc}, ϕ) and chemical properties (ε, σ and the largest charge (LC) assigned in the framework).

M-IRMOF	$S_{ads,\ 0.1\ bar}$	$S_{ads,\ 1\ bar}$	$S_{ads,\ 10\ bar}$	LCD (Å)	PLD (Å)	S_{acc} (m^2/g)	ϕ	LC (e^-)	ε_{metal}/k_B (K)	σ_{metal} (Å)
V-HIFTOG02	906.2	354.8	228.9	7.9	4.2	1330.0	0.6	1.6	8.07	2.80
Ni-HIFTOG02	739.7	241.2	148.3	8.5	4.1	1005.6	0.6	2.3	7.55	2.52
Ti-HIFTOG02	323.8	228.8	210.7	7.4	4.6	1694.9	0.6	1.4	8.56	2.83
Cr-HIFTOG02	281.6	223.8	197.7	7.5	4.3	1669.7	0.6	2.1	7.55	2.69
Zn-HIFTOG02	129.3	119.2	143.6	6.3	4.2	1128.9	0.5	0.5	62.44	2.46
Mn-HIFTOG02	104.2	102.7	99.7	7.7	4.3	1410.6	0.6	1.1	6.54	2.63
Co-HIFTOG02	84.7	82.8	87.6	7.6	4.2	1574.1	0.6	1.1	7.04	2.56
Cd-HIFTOG02	85.7	82.5	94.0	7.8	4.3	1109.3	0.6	0.6	114.8	2.54
opt-HIFTOG02*	87.8	81.3	87.9	7.8	4.3	1253.3	0.6	0.5	62.44	2.46
Cu-HIFTOG02	79.8	72.6	73.9	7.4	4.4	1331.8	0.6	1.3	2.51	3.11
Cr-SAHYIK	70.5	67.3	41.2	15.4	8.1	4121.6	0.8	1.8	7.55	2.69
V-SAHYIK	47.0	47.4	32.1	15.4	8.2	4167.3	0.8	1.6	8.07	2.80
Ti-SAHYIK	21.0	20.3	19.7	15.4	8.2	4239.5	0.8	1.4	8.56	2.83
Ni-SAHYIK	14.7	15.0	14.8	15.2	8.1	3901.0	0.8	1.5	7.55	2.52
Cu-SAHYIK	14.6	14.8	14.2	15.2	8.0	3812.8	0.8	1.9	2.51	3.11
Mn-SAHYIK	10.3	10.5	10.9	15.3	8.1	4046.1	0.8	1.1	6.54	2.63
Zn-SAHYIK	9.6	9.6	10.0	15.0	7.8	3599.7	0.8	0.5	62.44	2.46
Co-SAHYIK	10.0	9.4	9.8	15.3	8.1	3932.6	0.8	1.1	7.04	2.56
Cd-SAHYIK	10.2	9.3	9.9	15.2	8.0	2999.6	0.8	0.6	114.8	2.54
opt-SAHYIK*	8.7	8.7	9.2	15.0	7.9	3638.6	0.8	0.5	62.44	2.46

*opt indicates the "geometry optimized version of the original MOF".

Table C4. S_{ads} of M-ZnO-MOFs at 0.1, 1, and 10 bar, their physical properties (LCD, PLD, S_{acc}, ϕ) and chemical properties (ε, σ and the largest charge (LC) assigned in the framework).

M-ZnO-MOF	$S_{ads,\ 0.1\ bar}$	$S_{ads,\ 1\ bar}$	$S_{ads,\ 10\ bar}$	LCD (Å)	PLD (Å)	S_{acc} (m^2/g)	ϕ	LC (e^-)	ε_{metal}/k_B (K)	σ_{metal} (Å)
Cr-EFESEP	4788.1	921.3	358.7	7.4	4.8	1199.7	0.6	3.3	7.55	2.69
Ni-EFESEP	3184.4	749.4	265.9	7.3	4.7	1014.4	0.6	3.0	7.55	2.52
Mn-EFESEP	623.1	446.4	240.4	7.2	4.8	1220.8	0.6	1.5	6.54	2.63
Co-EFESEP	404.1	359.8	231.2	7.2	4.7	1155.7	0.6	1.7	7.04	2.56
V-EFESEP	1018.6	356.3	191.9	8.0	4.2	1231.3	0.6	2.2	8.07	2.80
Ti-EFESEP	528.3	323.6	216.3	7.3	4.5	1500.9	0.6	2.0	8.56	2.83
Zn-EFESEP	190.2	161.1	136.9	10.3	6.1	1394.1	0.6	0.5	62.44	2.46
opt-EFESEP*	182.3	119.6	82.5	10.3	3.9	1519.7	0.6	0.7	62.44	2.46
Cu-EFESEP	113.9	106.4	100.4	8.5	4.6	1126.5	0.6	1.5	2.51	3.11
Cd-EFESEP	94.9	83.3	76.2	9.8	4.8	1380.9	0.6	0.6	114.8	2.54
Cr-EFESOZ	4390.7	613.4	161.1	9.1	6.8	862.1	0.6	3.0	7.55	2.69
Ni-EFESOZ	2862.7	565.0	220.0	8.9	5.7	967.6	0.6	3.0	7.55	2.52
Co-EFESOZ	831.3	378.2	147.7	9.8	6.7	800.6	0.6	1.5	7.04	2.56
V-EFESOZ	977.4	376.7	141.0	9.3	6.6	925.0	0.6	2.2	8.07	2.80
Mn-EFESOZ	723.3	375.7	163.2	8.9	5.1	824.4	0.6	1.4	6.54	2.63
Ti-EFESOZ	639.1	332.5	153.0	9.7	5.3	898.6	0.6	1.8	8.56	2.83
Cu-EFESOZ	309.4	270.8	202.5	7.5	3.7	765.6	0.6	2.1	2.51	3.11
opt-EFESOZ*	371.2	163.1	115.7	10.2	5.8	864.4	0.6	0.7	62.44	2.46
Zn-EFESOZ	237.6	160.2	133.8	10.4	6.2	1152.3	0.6	0.5	62.44	2.46
Cd-EFESOZ	92.2	76.3	69.8	10.0	6.5	808.4	0.6	0.6	114.8	2.54

*opt indicates the "geometry optimized version of the original MOF".

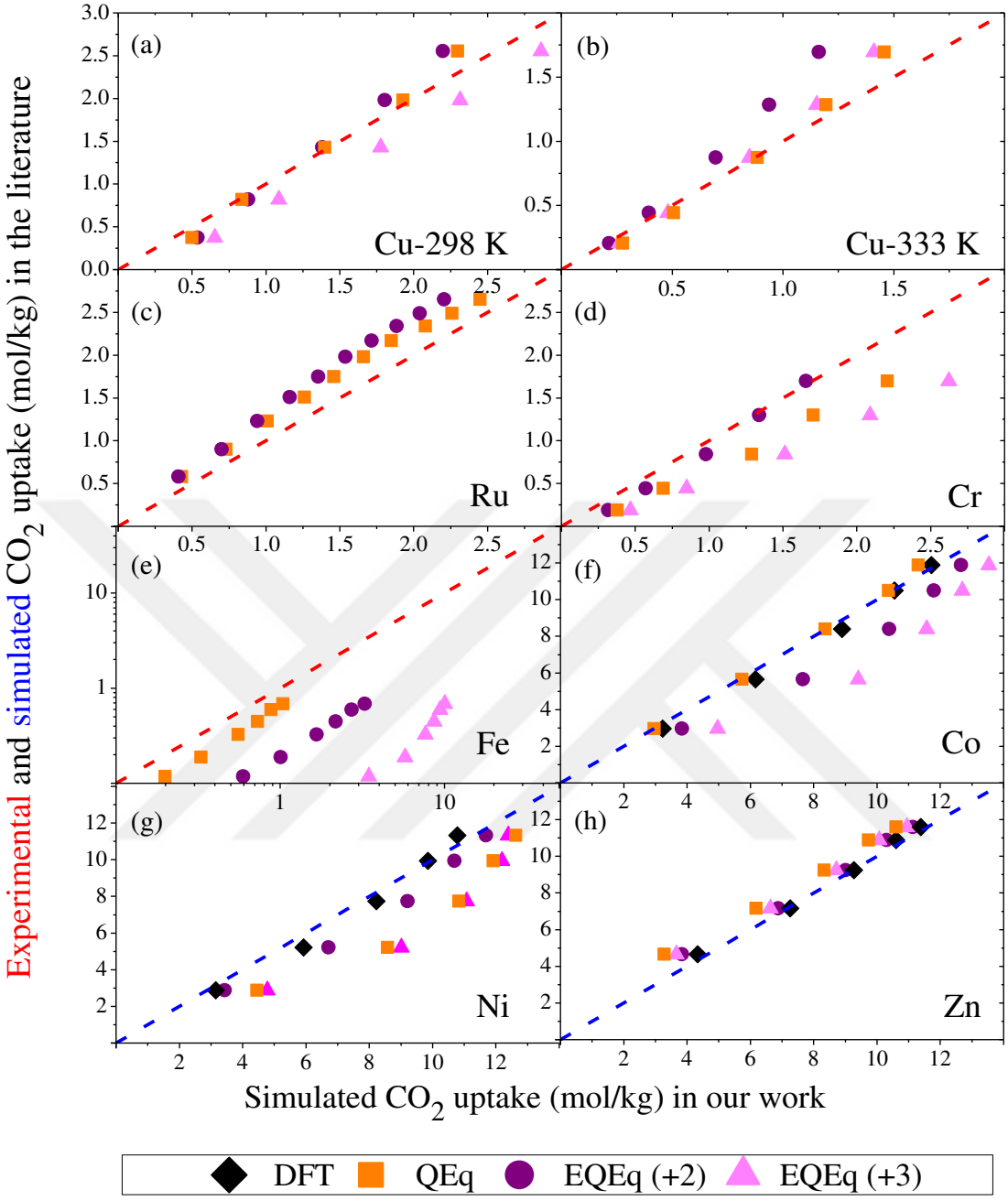

Figure C1. Comparison of our simulated CO_2 uptakes in M-HKUST-1 materials with the available experimental and simulation data at 0.1-1 bar, 298 K unless otherwise stated in the figure. Red and blue dotted diagonal lines represent experimental and simulated data comparison, respectively. Orange, purple, pink and black data points represent the simulated CO_2 uptakes obtained by using QEq, EQEq method with +2 oxidation state, EQEq method with +3 oxidation state, DFT charges provided in the literature,[81] respectively.

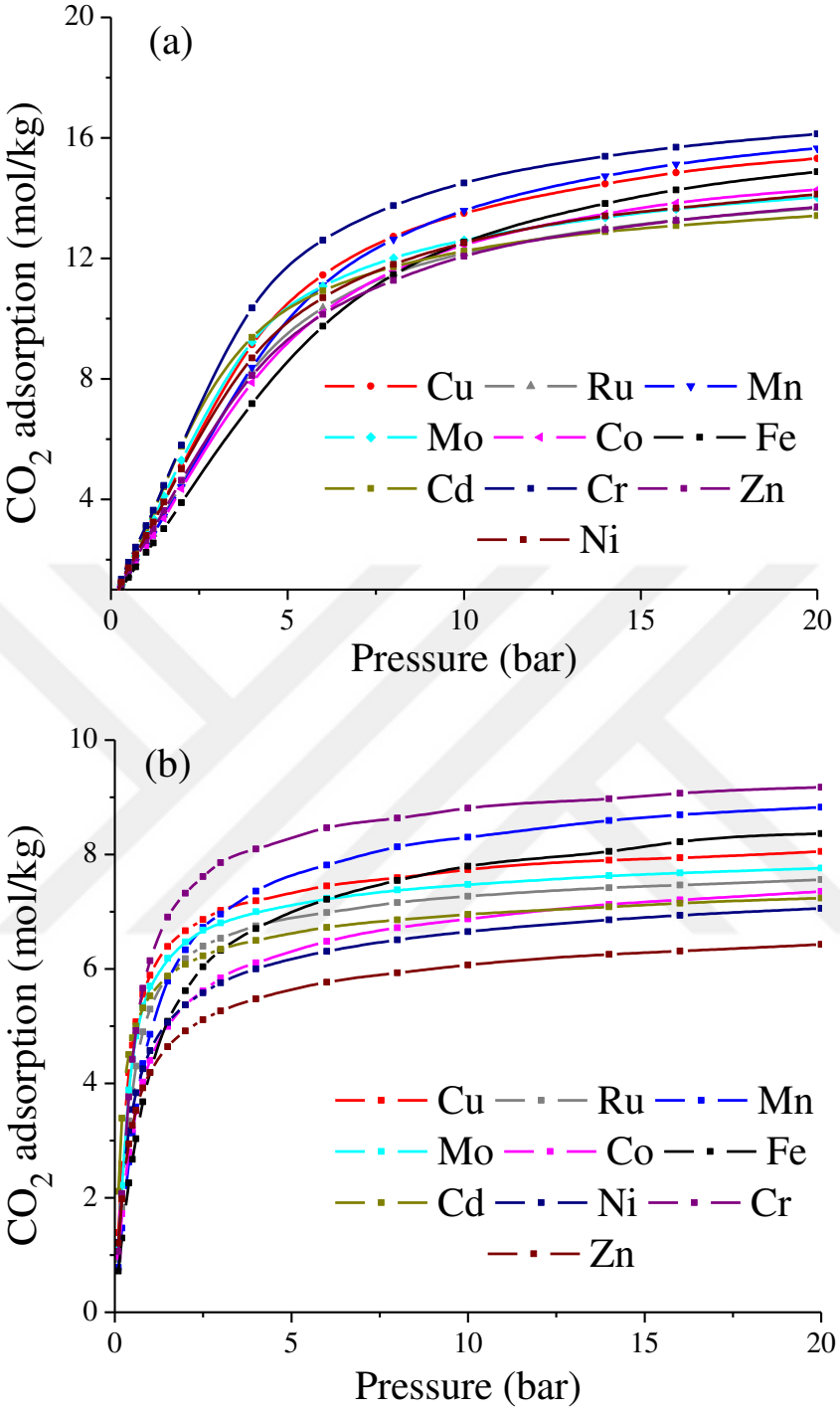

Figure C2. CO_2 adsorption isotherms of (a) M-HKUST-1 and (b) M-HATGUF series at 298 K.

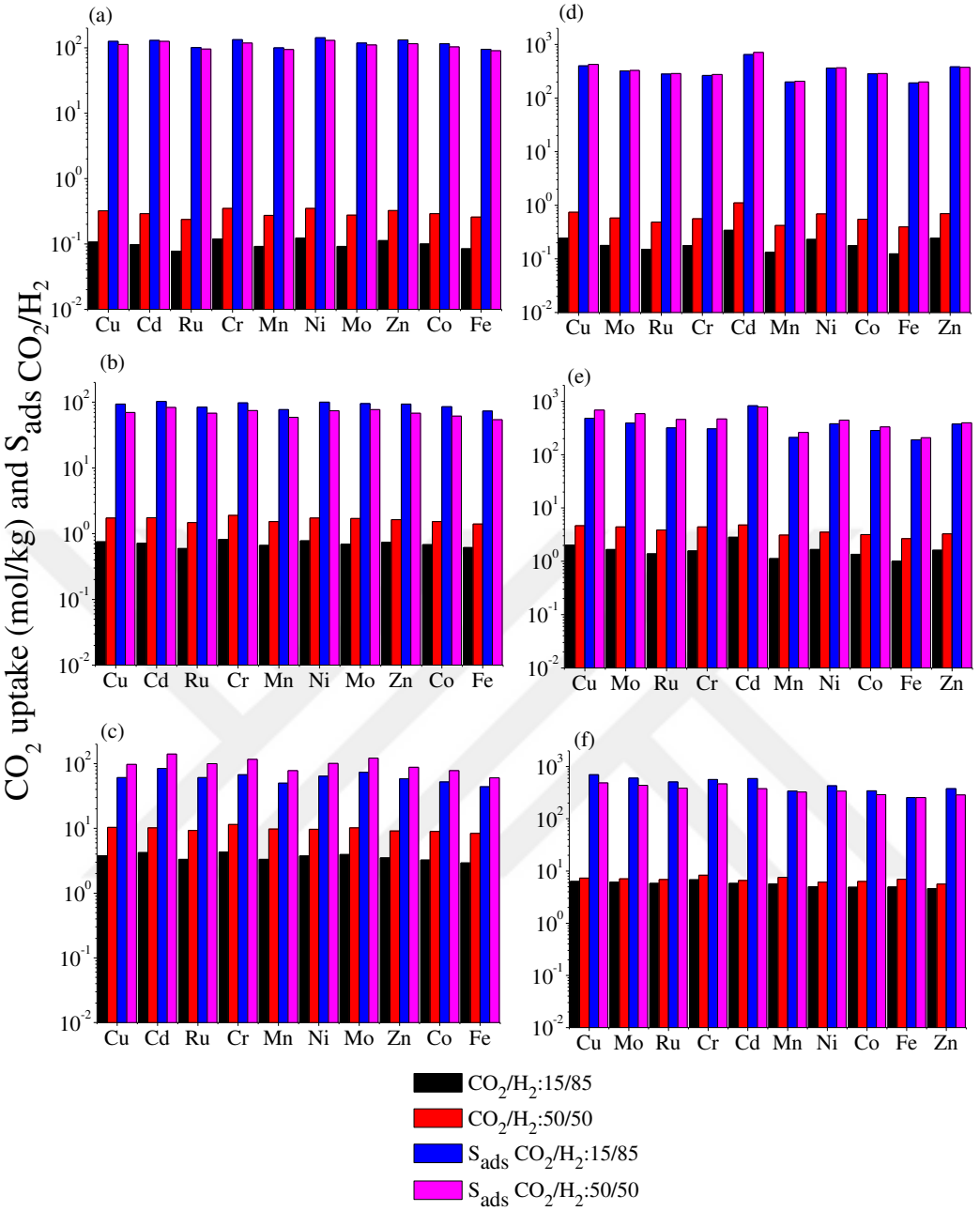

Figure C3. CO_2 uptake and CO_2/H_2 selectivity for CO_2/H_2:50/50 and CO_2/H_2:15/85 mixtures of M-HKUST-1 at (a) 0.1, (b) 1, and (c) 10 bar at 298 K, and M-HATGUF at (d) 0.1, (e) 1, and (f) 10 bar and 298 K.

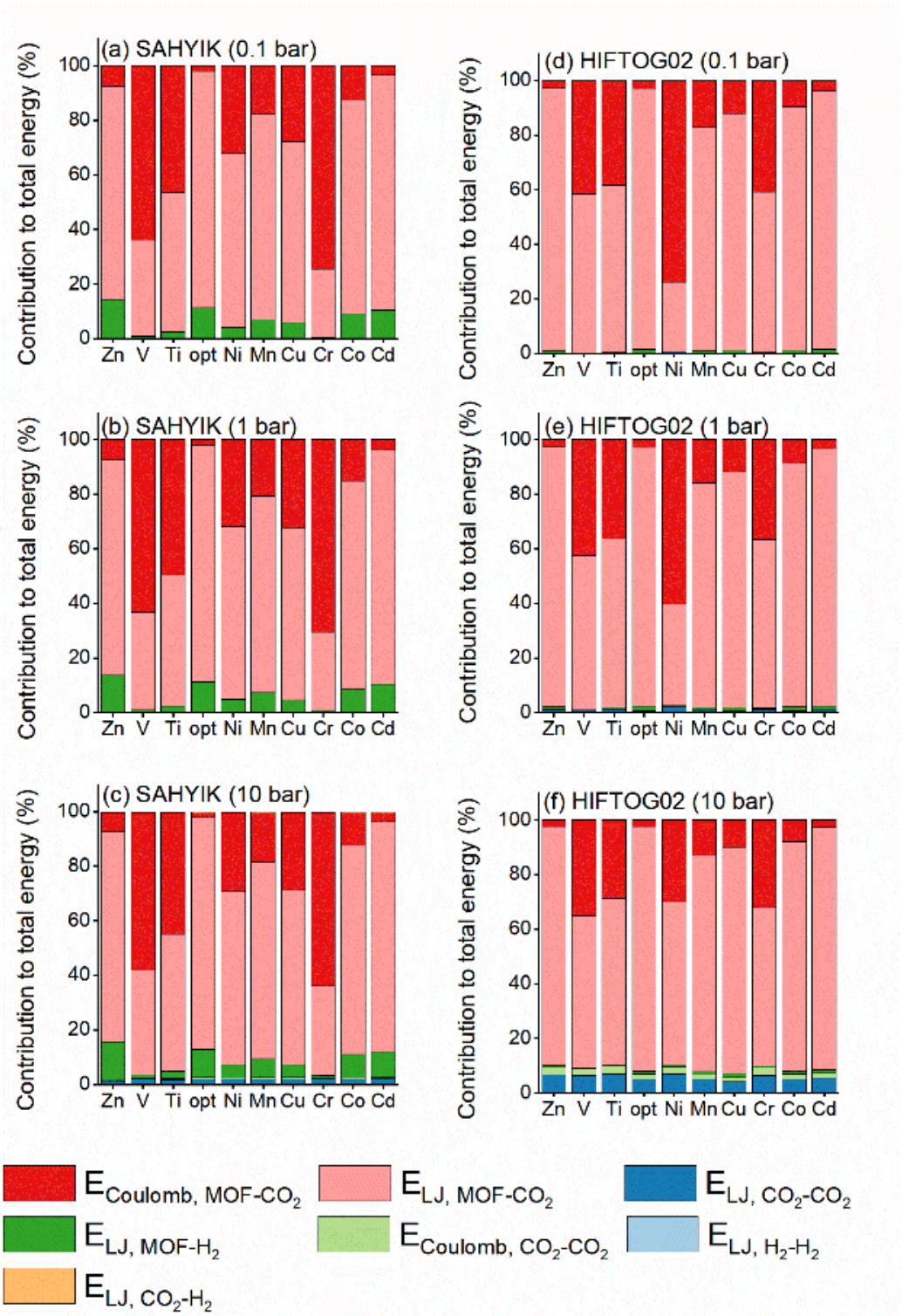

Figure C4. The contribution percentage of LJ interaction energies (E_{LJ}) for MOF-H_2, MOF-CO_2, CO_2-CO_2, H_2-H_2, and CO_2-H_2, and Coulomb interaction energies ($E_{Coulomb}$) for MOF-CO_2 and CO_2-CO_2, to total energy in (a-c) M-SAHYIK and (d-f) M-HIFTOG02. "opt" represents the "geometry optimized version of the original MOF".

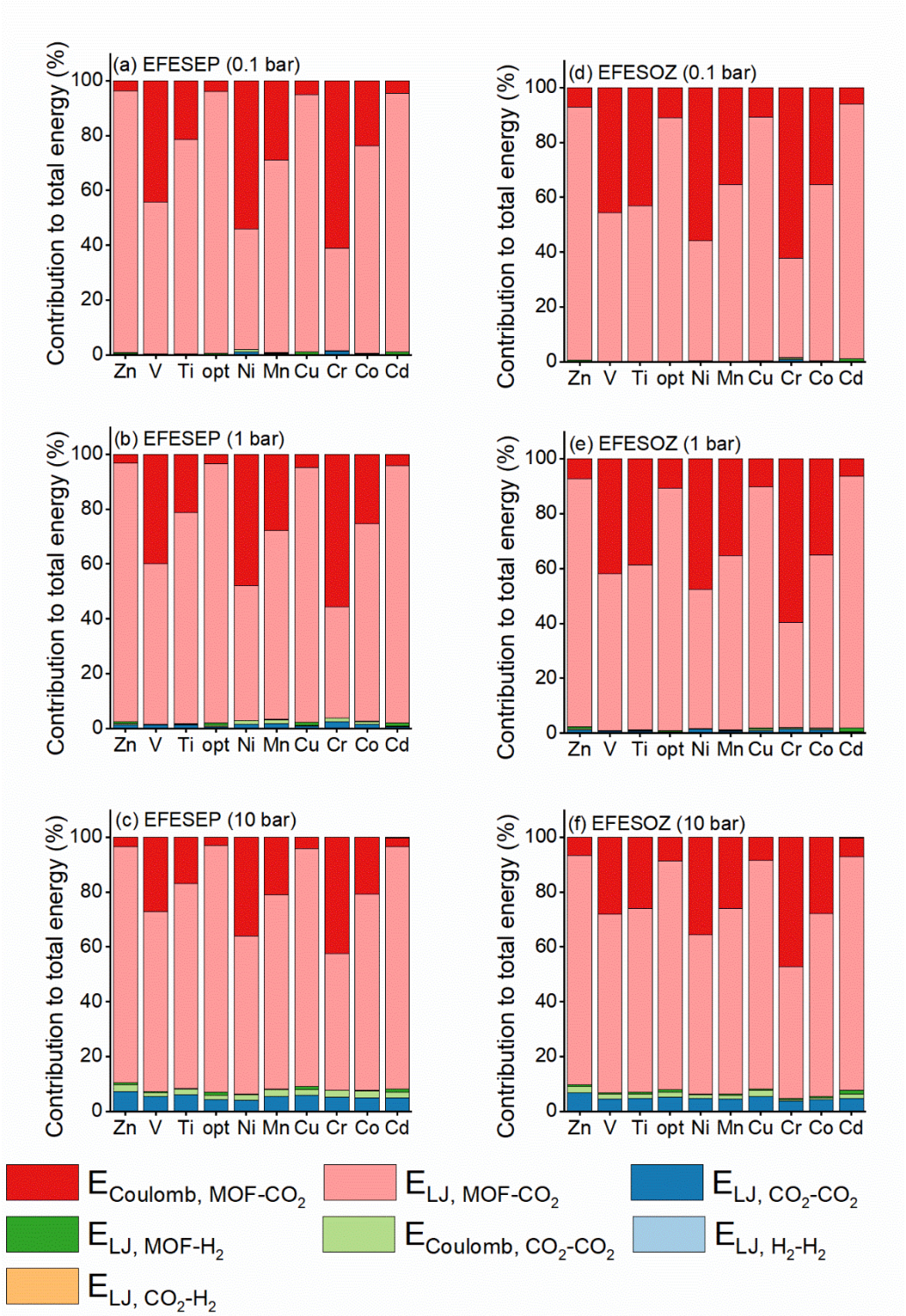

Figure C5. The contribution percentage of LJ interaction energies (E_{LJ}) for MOF-H_2, MOF-CO_2, CO_2-CO_2, H_2-H_2, and CO_2-H_2, and Coulomb interaction energies ($E_{Coulomb}$) for MOF-CO_2 and CO_2-CO_2, to total energy in (a-c) M-EFESEP and (d-f) M-EFESOZ. "opt" represents the "geometry optimized version of the original MOF".

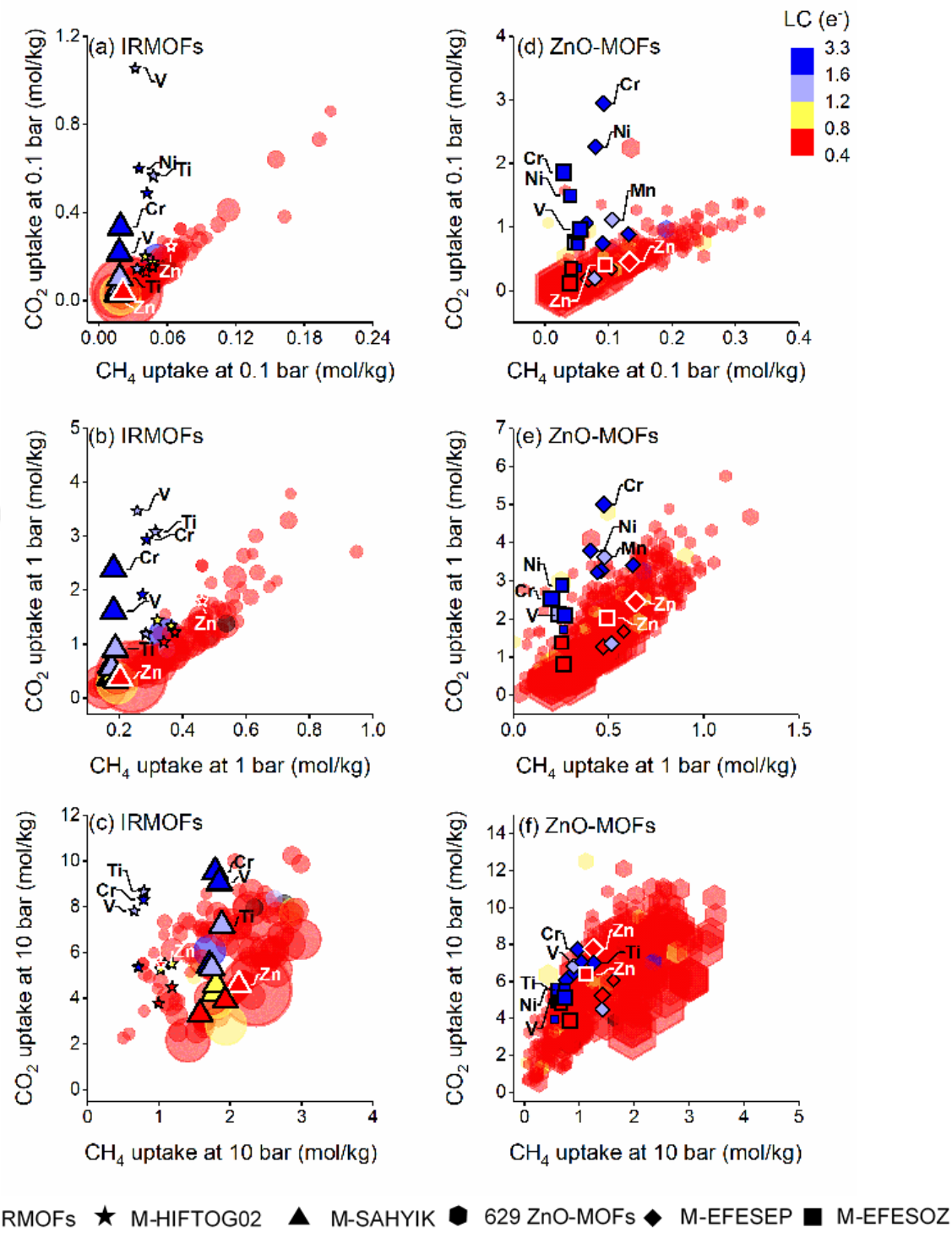

Figure C6. (a-c) CO_2 and CH_4 uptakes of 140 IRMOFs (circles), M-HIFTOG02 (stars), M-SAHYIK (triangles) at 0.1, 1, and 10 bar. (d-f) CO_2 and H_2 uptakes of 629 ZnO-MOFs (hexagonals), M-EFESEP (diamonds), and M-EFESOZ (squares) at 0.1, 1, and 10 bar. Color and size of symbols represent the largest charge (LC) assigned in the framework and pore limiting diameter (PLD) of MOFs, respectively.

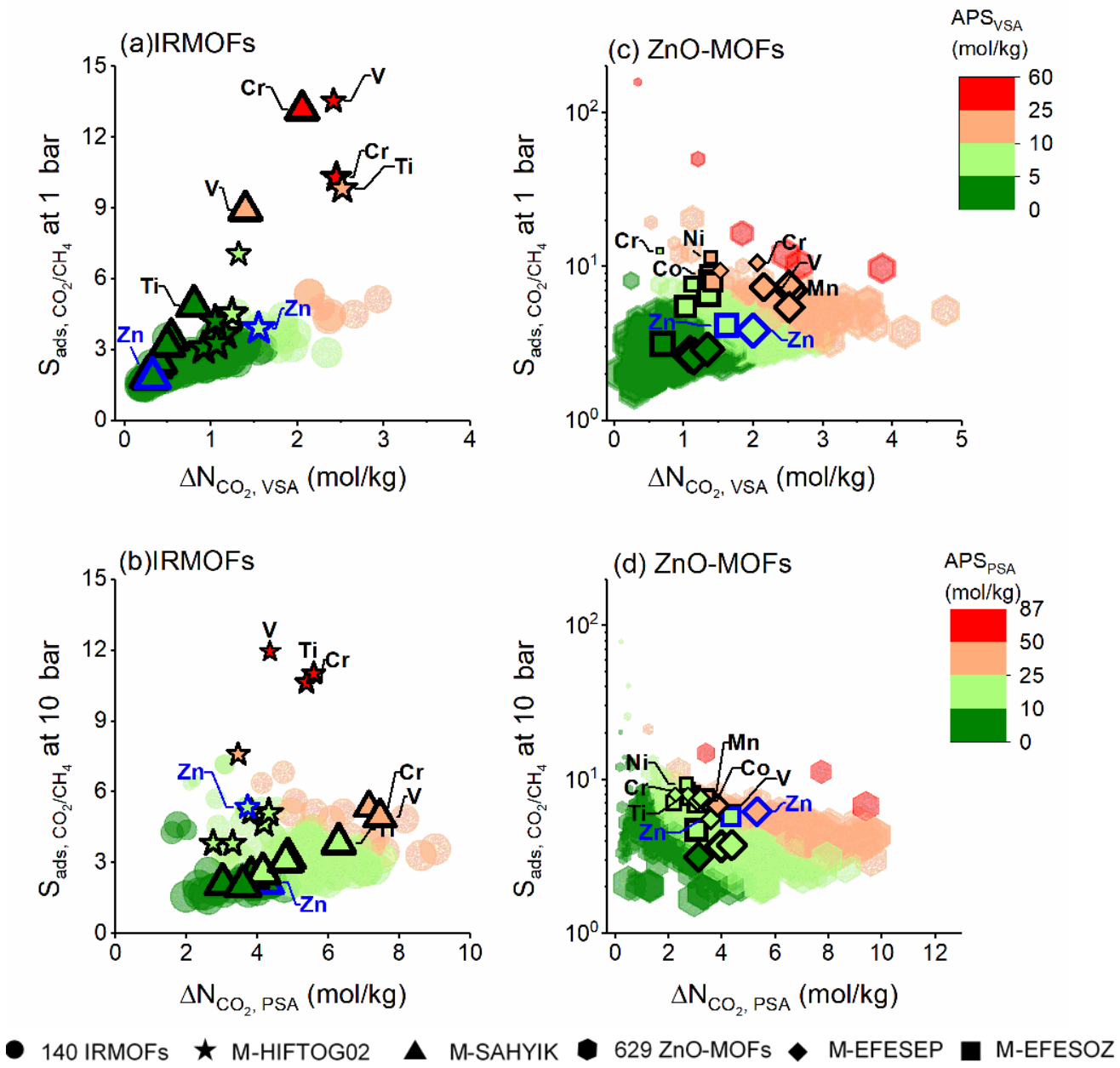

Figure C7. (a, b) ΔN_{CO_2} and S_{ads} of M-HIFTOG02 (stars), M-SAHYIK (triangles), and 140 IRMOFs (circles) (c, d) ΔN_{CO_2} and S_{ads} of M-EFESEP (stars), M-EFESOZ (triangles), and 629 ZnO-MOFs (circles) are shown for CO_2/CH_4 mixture separation at VSA and PSA conditions. Size of symbols represents R%, color of symbols represents APS at the corresponding working condition.

LIST OF PUBLICATIONS

Publications included in this thesis:

Avci G., Altintas C. and Keskin S. "Metal Exchange Boosts the CO_2 selectivity of MOFs having Zn-oxide Node" *Journal of Physical Chemistry C. 125, 17311-17322,* (2021).

Avci G., Erucar I. and Keskin S. "Do New MOFs Perform Better for CO_2 Capture and H_2 Purification? Computational Screening of the Updated MOF Database" *ACS Applied Materials & Interfaces. 12, 41567-41579,* (2020).

Avci G., Velioglu S. and Keskin S. "In-silico Design of MOFs with Enhanced CO_2 Separation Performances: Role of Metal Sites" *Journal of Physical Chemistry C, 123, 28255-28265,* (2019).

Avci G., Velioglu S. and Keskin S. "High-throughput Screening of MOF Adsorbents and Membranes for H_2 Purification and CO_2 Capture" *ACS Applied Materials & Interfaces. 10, 33693-33706,* (2018).

Participations in other projects:

Daglar H., Gulbalkan H.C., Avci G., Aksu G.O., Altundal O.F., Altintas C., Erucar I. and Keskin S. "Effect of MOF Database Selection on the Assessment of Gas Storage and Separation Potentials of MOFs" *Angewandte Chemie. 14, 7828-7837,* (2021).

Altintas C., Avci G., Daglar H., Azar A., Erucar I., Velioglu S. and Keskin S. "An Extensive Comparative Analysis of Two MOF Databases: High-Throughput Screening of Computation-Ready MOFs for CH_4 and H_2 Adsorption" *Journal of Materials Chemistry A, 7, 9593-9608,* (2019).

Altintas C., Avci G., Daglar H., Azar A., Velioglu S., Erucar I. and Keskin S. "Database for CO_2 Separation Performances of MOFs Based on Computational Materials Screening" *ACS Applied Materials & Interfaces, 10, 17257-17268,* (2018).

Altintas C., Avci G., Daglar H., Gulcay E., Erucar I. and Keskin S. "Computer Simulations of 4,240 MOF Membranes for H_2/CH_4 Separations: Insights into Structure-Performance Relations" *Journal of Materials Chemistry A, 6, 5836-5847,* (2018).